POLITECNICO DI TORINO

DOCTORATE SCHOOL

Course in Information and System Engineering – XXI Cycle

A dissertation submitted for the degree of
Doctor of Philosophy

Control of Tethered Airfoils for High–Altitude Wind Energy Generation

Advanced control methods as key technologies for a breakthrough in renewable energy generation

LORENZO FAGIANO

Advisors
ing. Massimo Canale
prof. Mario Milanese

PhD course Co–ordinator
prof. Pietro Laface

Complex System Modeling and Control Group
Head of the research group
prof. Mario Milanese

2009

A Maria

Note from the author

I would like to point out here that the research activities that I've carried out during my Ph.D. studies have nothing to share with the company named "KiteGen Research s.r.l.". The name "KiteGen" has been coined at Politecnico di Torino, well before the foundation of KiteGen Research s.r.l., and it has been the name of the first research project, funded by Regione Piemonte and coordinated by Politecnico di Torino, aimed to investigate high-altitude wind energy using power kites. This is the reason why I referred to this technology as "KiteGen" in my Ph.D. thesis. KiteGen Research s.r.l. gave no contribution to my research activities and to the related publications. In order to avoid confusion, I've decided to modify my thesis and to refer to the technology with the acronym "HAWE" (High Altitude Wind Energy).

October 19th, 2010

Lorenzo Fagiano

Abstract

This thesis is concerned with the development of an innovative technology of high–altitude wind energy generation and with the investigation of the related advanced automatic control techniques. Indeed, the problems posed by the actual energy situation are among the most urgent challenges that have to be faced today, on a global scale. One of the key points to reduce the world dependance on fossil fuels and the emissions of greenhouse gases is the use of a suitable combination of alternative and green energy sources. Renewable energies like hydropower, biomass, wind, solar and geothermal could meet the whole global energy needs, with minor environmental impact in terms of pollution and global warming. However, they are not economically competitive without incentives, mainly due to the high costs of the related technologies, their discontinuous and nonuniform availability and the low generated power density per unit area. Focusing the attention on wind energy, recent studies showed that there is enough potential in the total world wind power to sustain the global needs. Nevertheless, such energy can not be harvested by the actual technology, based on wind towers, which has nearly reached its economical and technological limits. The first part of this dissertation is aimed at evaluating the potential of an innovative high–altitude wind energy technology to overcome some of these limitations. In particular, a class of generators denoted as HAWE (High Altitude Wind Energy) is considered, which exploits the aerodynamical forces generated by the flight of tethered airfoils to produce electric energy. Numerical simulations, theoretical studies, control optimization, prototype experiments and wind data analyses are employed to show that the HAWE technology, capturing the energy of wind at higher elevation than the actual wind towers, has the potential of generating renewable energy available in large quantities almost everywhere, with a cost even lower than that of fossil energy.

Though the idea of exploiting tethered airfoils to generate energy is not new, it is practicable today thanks to recent advancements in several science and engineering fields like materials, aerodynamics, mechatronics and control theory. In particular, the latter is of paramount importance in HAWE technology, since the system to be controlled is nonlinear, open loop unstable, subject to operational constraints and with relatively fast dynamics. Nonlinear Model Predictive Control techniques offer a powerful tool to deal with this problems, since they allow to stabilize and control nonlinear systems while explicitly

taking into account state and input constraints. However, an efficient implementation is needed, since the computation of the control input, which requires the real–time solution of a constrained optimization problem, can not be performed at the employed "fast" sampling rate. This issue motivates the research efforts devoted in the last decade to devise more efficient implementations of predictive controllers. Among the possible solutions proposed in the literature, in this thesis Set Membership theory is employed to derive off–line a computationally efficient approximated control law, to be implemented on–line instead of solving the optimization. The second part of this thesis investigates the methodological aspects of such a control strategy. Theoretical results regarding guaranteed approximation accuracy, closed loop stability and performance and constraint satisfaction are obtained. Moreover, optimal and suboptimal approximation techniques are derived, allowing to achieve a tradeoff between computational efficiency, approximation accuracy and memory requirements. The effectiveness of the developed techniques is tested, besides the HAWE application, on several numerical and practical examples.

Acknowledgements

The studies and research activities underlying this dissertation have been funded in part by Ministero dell'Istruzione, dell'Università e della Ricerca under the Projects "Advanced control and identification techniques for innovative applications" and "Control of advanced systems of transmission, suspension, steering and braking for the management of the vehicle dynamics" and by Regione Piemonte under the Projects "Controllo di aquiloni di potenza per la generazione eolica di energia" and "Power kites for naval propulsion".

Contents

List of Tables

List of Figures

Part I

High–altitude wind energy generation using controlled airfoils

Chapter 1

Introduction

The problem of sustainable energy generation is one of the most urgent challenges that mankind is facing today. On the one hand, the world energy consumption is continuously growing, mainly due to the development of non–OECD (Organization for Economic Co–operation and Development, see Appendix A) countries, and an increase of about 45–50% in energy consumption, with respect to the actual value, is estimated for year 2030 [1, 2]. On the other hand, the problems related to the actual and projected distribution of energy production among the different sources are evident and documented by many studies (see e.g. [3]). Most of the global energy needs are actually covered by fossil sources (i.e. oil, coal and natural gas), accounting for about 81% of the global primary energy demand in 2006 [1]. Fossil sources are supplied by few producer countries [1, 2], which own limited reservoirs, and the average cost of energy obtained from such sources is continuously increasing due to the increasing demand, related to the rapid economy growth of the highly populated non–OECD countries [3]. Moreover, the negative effects of energy generation from fossil sources on global warming and climate change, due to excessive carbon dioxide emissions, and the negative impact of fossil energy on the environment are recognized worldwide and lead to additional indirect costs [3, 4]. Such a situation gives rise to serious geopolitical and economical problems, affecting almost all of the world's countries.
One of the key points to solve these issues is the use of a suitable combination of alternative and renewable energy sources. In early 2007, the European Union (EU) heads of state endorsed an integrated energy/climate change plan that addresses the issues of energy supply, climate change and industrial development [5]. One of the points of the plan is the target of increasing the proportion of renewable energies in the EU energy mix to 20% by year 2020 (starting from about 8% of 2006, [1]). However, the actual renewable technologies (hydropower, solar, wind, biomass, geothermal) seem to have little potential to reach this target. Indeed, according to the projections given in [2], if no political and economical measures will be adopted only about 8.9% of the energy consumption in European countries will be supplied by renewable energies in 2020. A fairly more optimistic estimate is given in [1], with about 13% of primary energy demand covered by

renewables in EU in 2020. Similar estimates are obtained for all of the OECD countries, while for non–OECD countries according to [2] it is expected that a constant fraction of about 7.5% of the whole energy consumption will be supplied by renewable energies for the next 20 years. Excluding hydropower (which is not likely to increase substantially in the future, because most major sites are already being exploited or are unavailable for technological and/or environmental reasons), the main issues that hamper the growth of renewable energies are the high investment costs of the related technologies, their non–uniform availability and the low generated power density per unit area.

Focusing the attention on wind energy, it is interesting to note that recent studies [6] showed that by exploiting 20% of the global land sites of "class 3" or more (i.e. with average wind speed greater than 6.9 m/s at 80 m above the ground), the entire world's energy demand could be supplied. However, such potential can not be harvested with competitive costs by the actual wind technology, based on wind towers which require heavy foundations and huge blades, with massive investments, and have a limited operating height of about 150 meters from the ground, where wind flows are weaker and more variable. A comprehensive overview of the present wind technology is given in [7], where it is also pointed out that no dramatic improvement is expected in this field. All the mentioned issues lead to wind energy production costs that are higher than those of fossil sources. Therefore, a quantum leap would be needed in wind technology to overcome the present limits and boost its application, providing green energy with competitive costs with respect to those of the actual fossil sources, thus no more requiring economic incentives.

Such a breakthrough in wind energy generation can be realized by capturing high–altitude wind power. A possible viable approach is to use airfoils (like power kites used for surfing or sailing), linked to the ground with one or more cables. The latter are employed to control the airfoil flight and to convert the aerodynamical forces into mechanical and electrical power, using suitable rotating mechanisms and electric generators kept at ground level. Such airfoils are able to exploit wind flows at higher altitudes (up to 1000 m) than those of wind towers. At such elevations, stronger and more constant wind can be found basically everywhere in the world: thus, this technology can be used in a much larger number of locations. The potential of this concept has been theoretically investigated almost 30 years ago [8], showing that if the airfoils are driven to fly in "crosswind" conditions, the resulting aerodynamical forces can generate surprisingly high power values. However, only in recent years more intensive studies have been carried out by quite few research groups in the world, to deeply investigate this idea from the theoretical, technological and experimental point of views. In particular, at Politecnico di Torino (Italy), a project named KiteGen started in 2006, aimed at studying and develop the technology of high–altitude wind energy using controlled airfoils.

Part I of this dissertation collects all the main advances of the project KiteGen. The outcome of the theoretical and numerical analyses performed in the last three years (2006–2008) and presented in this thesis, together with the results of the first experimental tests, indicate that high–altitude wind energy has the potential to overcome the limits of the

actual wind turbines and to generate large quantities of renewable energy, available practically everywhere in the world, with competitive costs with respect to fossil sources. Such results have been partly published in [9, 10, 11, 12, 13, 14].
The remaining of this Chapter is organized as follows. Section 1.1 gives a concise overview of the actual and projected global energy situations, while Section 1.2 briefly resumes the main characteristics of the actual wind power technology and the existing concepts of high–altitude wind generators. Finally, Section 1.3 states the contributions given in this Part of the thesis.

1.1 Global energy situation

This Section resumes the latest available data, related to 2006, as well as future projections, until 2030, of the global marketed energy consumption. Indeed, to perform an accurate and deep study of the actual situation of global energy and of the projected scenario is an hard task, outside the scope of this dissertation, and only some concise analyses are reported, to better describe the context, the motivations and the potential of the presented research. Since the HAWE technology regards mainly the field of electric energy production, particular attention is given to the distribution, among the different sources, of the global energy consumption for electricity generation. Moreover, the actual and projected values of energy–related carbon dioxide emissions, by source and by end–use sector, are also resumed, since the potential impact of high–altitude wind energy involves also the abatement of such a greenhouse gas.

1.1.1 Actual global energy situation

Information on the global energy panorama in the last years can be found in several sources (see e.g. [1, 2, 15, 16]), in which the data on energy consumption are usually grouped by fuel, by geographical region and by end–use sector. Most studies consider both the Total Primary Energy Demand (TPED), i.e. the demand of raw fuels and other forms of energy that have not been subjected to any conversion or transformation process, and the Total Final Consumption (TFC), which embraces the consumption of "refined" energy sources in the various end–use sectors like transportation, industry, residential, etc.. The analyses are mostly focused on fossil energy (i.e. oil, coal and natural gas), which accounts for about 81% of TPED and 59% of TFC (according to [1]). The collected data are usually put into relation with demographic and economic indicators like population and Gross Domestic Product (GDP) growth, which are considered to be the most influential factors on energy consumption.
Although some discrepancy (of the order of few percent points) can be noticed in the data given by the different sources, the actual global energy situation is quite clear and it is

now briefly resumed, using the data related to 2006. Table 1.1 shows the world total primary energy demand in 2006 by region[1] and by source, expressed in trillions of MJ. The considered sources are the three main categories of fossil fuels (i.e. oil, coal and natural gas), nuclear power, hydro, biomass and waste and "other" sources, which include all the non–hydro renewable sources, i.e. solar, geothermal, wind, tide and wave energy[2]. Figures 1.1 and 1.2 show the percent distribution of energy consumption by source and by region respectively. It can be clearly noted that more than 80% of TPED is covered by

Table 1.1. World total primary energy demand in 2006 by region and source (trillion MJ). Data taken from [1].

Region	**Fossil sources**			**Nuclear**	**Biomass and waste**	**Hydro**	**Other**	**Total**
	Oil	Natural gas	Coal					
OECD North America	47.43	26.33	24.57	10.10	4.22	2.42	0.75	115.85
OECD Europe	29.14	18.76	13.86	10.67	3.93	1.71	0.75	78.83
OECD Pacific	15.91	5.56	9.25	4.94	0.67	0.46	0.25	37.05
Total OECD	**92.48**	**50.66**	**47.69**	**25.70**	**8.83**	**4.60**	**1.75**	**231.74**
Europe and Eurasia	9.75	23.02	9.00	3.14	0.79	1.09	0.04	46.85
Asia	31.56	9.83	65.60	1.25	23.61	2.42	0.79	135.11
Middle East	11.72	9.58	0.37	0	0.04	0.08	0.04	21.85
Africa	5.52	3.22	4.31	0.12	12.18	0.33	0.04	25.75
Latin America	9.92	4.44	0.92	0.25	4.22	2.34	0.08	22.19
Total Non–OECD	**68.49**	**50.11**	**80.21**	**4.77**	**40.86**	**6.28**	**1.00**	**251.75**
World	**160.98**	**100.77**	**127.90**	**30.47**	**49.69**	**10.88**	**2.76**	**483.49**

fossil sources and that almost 50% of TPED is related to OECD countries, whose population, about $1.17\,10^9$ people, correspond to only about 18% of the world total population. Thus, the distribution of energy demand among the various sources and over the world's regions is all but well balanced. Moreover, the production of fossil fuels is concentrated in few countries, since for example about 42% of oil, which covers about 15% of TPED, is produced in OPEC[3] countries and about 22% of natural gas (i.e. about 5% of TPED) is supplied by Russia.

[1]The considered regions are: OECD North America, OECD Europe , OECD Pacific, Europe and Eurasia, Asia, Middle East, Africa and Latin America. For a complete list of the countries included in each region, see Appendix A.

[2]For a more complete definition of the considered energy sources, see Appendix B

[3]Organization of the Petroleum Exporting Countries. Includes Algeria, Angola, Ecuador, Indonesia, Iran, Iraq, Kuwait, Libya, Nigeria, Qatar, Saudi Arabia, the United Arab Emirates and Venezuela

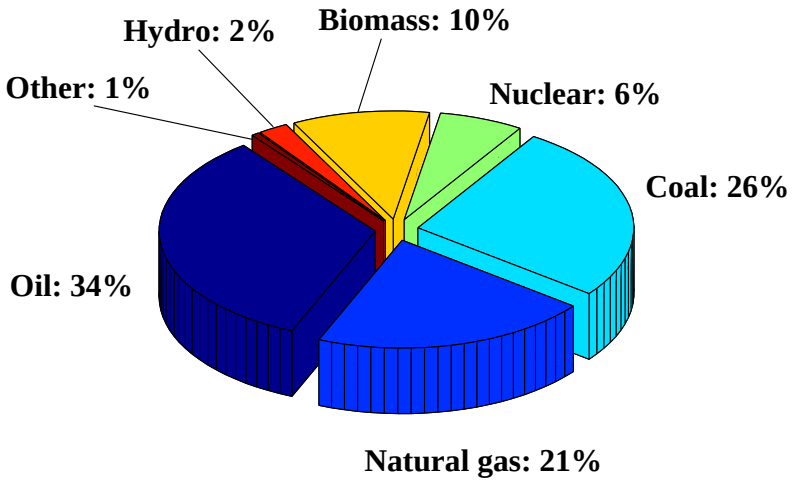

Figure 1.1. Percent distribution of the total primary energy demand by source in 2006.

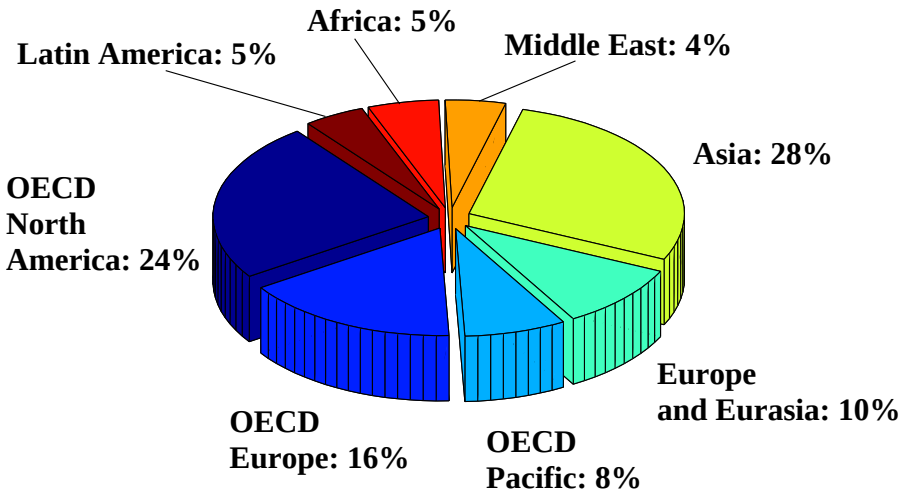

Figure 1.2. Percent distribution of the total primary energy demand by region in 2006.

As regards electric power generation, Table 1.2 shows the global electricity produced in 2006 by region and by source; the related distribution among the various fuels is depicted in Figure 1.3. OECD countries produce about 55% of the total electricity, using mainly coal (38%), natural gas (20%) and nuclear power (22%). Non–OECD countries generate the remaining 45% of global electricity, relying mainly on coal (45%), natural gas and hydro (20% each). Thus fossil sources, particularly coal, account for 67% of the global electricity generation and, considering also nuclear power, the share of non–renewable sources in electric power generation is 82%. Indeed, the amount of coal employed in thermal power plants corresponds to about 66% of the total coal consumption and about

Table 1.2. World total electricity generated in 2006 by region and source (trillion MJ). Data taken from [1].

Source	OECD	Non–OECD	World
Oil	1.50	2.44	3.94
Natural gas	7.55	6.15	13.7
Coal	14.15	13.77	27.92
Nuclear	8.48	1.57	10.05
Biomass and waste	0.73	0.12	0.85
Hydro	4.62	6.29	10.91
Wind	0.41	0.05	0.46
Geothermal	0.13	0.07	0.21
Total electricity	**37.60**	**30.49**	**68.10**

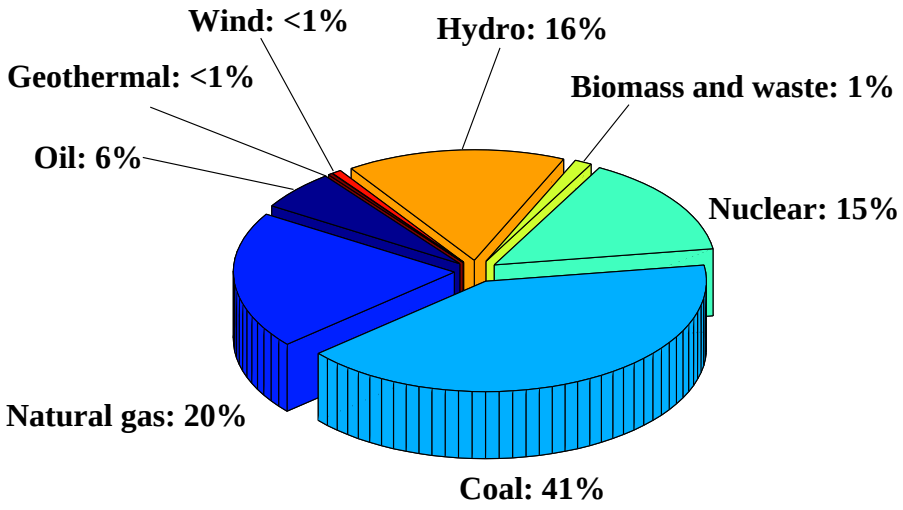

Figure 1.3. Electricity generated in 2006 by fuel.

18% of TPED. Note that wind power covers less than 1% of the total electricity generation: such a situation derives from the limits of the actual wind technology, as it is pointed out in Section 1.2. The production of electricity using wind energy in OECD countries is eight times higher than that of non–OECD countries, but still almost negligible with respect to the total production of electricity.
Finally, to conclude this brief overview of the present energy situation, the data of energy–related carbon dioxide emissions in 2006 are given in Table 1.3 and in Figure 1.4, that shows the distribution of CO_2 emissions by region, by fuel and by sector. In particular,

the considered fields are power generation[4], industry, transportation and other sectors[5]. Coherently with the distribution of TPED, OECD countries account for almost 50% of the global CO_2 emissions. Note that the sector of power generation alone accounts for 45% of the global emissions, due to the massive usage of coal, which is the most carbon–intensive fuel [17], since its combustion releases about 112 gCO_2/MJ, i.e. almost twice the amount of CO_2 per energy unit with respect to natural gas (62 gCO_2/MJ). Non–OECD countries employ more coal–fired thermal plants than OECD countries, where a much higher share of nuclear power is present. Oil is the second source of carbon dioxide emissions (36%), mainly in the transportation sector (which accounts for 67% of oil share of global CO_2 emissions). Indeed, oil covers practically 100% of the whole transportation sector while its use in power generation, industry and other sectors is relatively low.

Table 1.3. Energy–related carbon dioxide emissions in 2006 by region, fuel and sector (Gt). Data taken from [1].

Source and end–use sector	**OECD**	**Non–OECD**	**World**
Oil total	**5.59**	**4.19**	**9.78**
Power generation	0.30	0.58	0.88
Industry	0.44	0.56	1.00
Transport	3.77	2.03	5.80
Other sectors	0.70	0.72	1.42
Natural gas total	**2.80**	**2.64**	**5.44**
Power generation	0.95	1.26	2.21
Industry	0.61	0.56	1.53
Transport	0	0	0
Other sectors	1.02	0.55	1.22
Coal total	**4.39**	**7.28**	**11.67**
Power generation	3.72	4.61	8.33
Industry	0.51	2.07	1.79
Transport	0	0	0
Other sectors	0.08	0.45	1.33
Total CO_2 emissions	**12.79**	**14.12**	**26.91**

[4]Power generation refers to fuel use in electricity plants, heat plants and Combined Heat and Power (CHP) plants. Both main activity producer plants and small plants that produce fuel for their own use (autoproducers) are included.

[5]Other sectors include residential use, commercial and public services, agriculture/forestry and fishing.

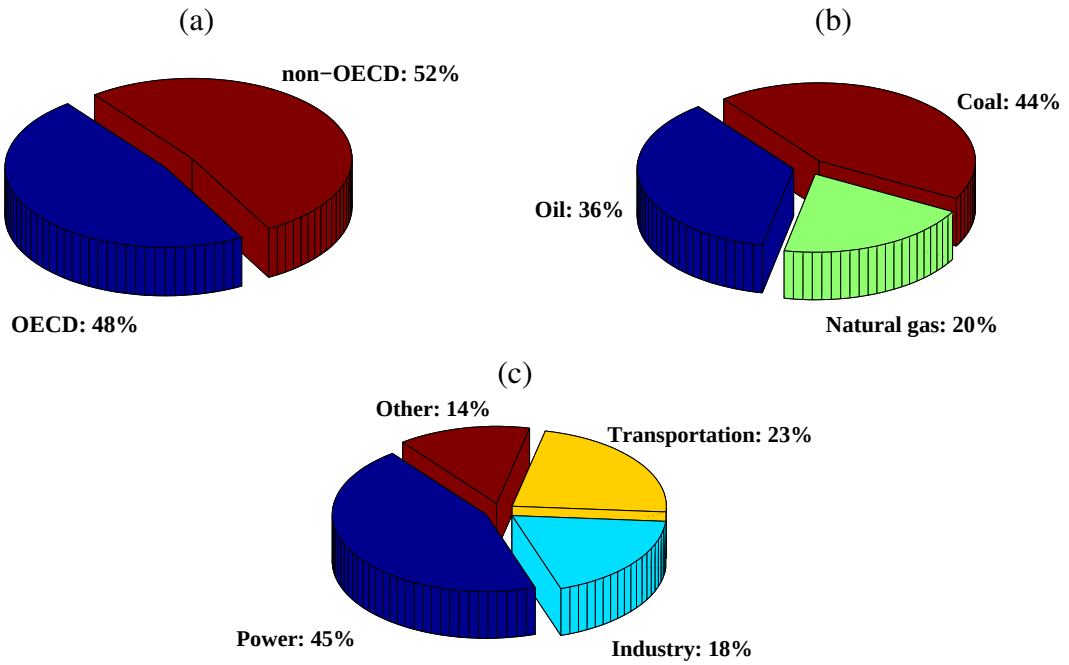

Figure 1.4. Energy–related carbon dioxide emissions in 2006 by (a) region, (b) fuel and (c) sector.

1.1.2 Global energy outlook to 2030

Energy forecasting on both short and long horizons is a task of great interest for a large variety of subjects, including governments, finance companies, investors, enterprises operating in every sector, economists, scientists, etc.. Energy is required for any human activity and consequently any noticeable change in the production, trade and consumption of energy influences all of the world societies. The evolution of the global energy system is continuously being studied by many public and private institutions and some of the resulting outlooks and reports are made available every year (see e.g. [1, 2, 18]). However, to perform a relatively accurate estimate of the future course of the global energy situation is a hard (impossible?) task, which typically fails due to the system complexity and the presence of large uncertainty sources and external factors[6]. Nevertheless, some general trends in global energy production and consumption can be captured with some approximation and are now resumed. In particular, most of the information reported here derive from the outlooks [1, 2]. The projections presented in both [1] and [2] have been computed considering a reference future scenario in which the current laws and policies remain unchanged throughout the projection period (i.e. 2005–2030). Indeed, such projections are subject to several sources of uncertainty, like the economy growth rate of the

[6] An interesting example of failed forecast and an analysis of the causes of failure can be found in [19]).

various world's regions, in terms of GDP (Gross Domestic Product), the variation of energy prices, the change of energy intensity (i.e. the link between economic growth and energy consumption), the adoption of political measures that influence energy production and use and other geopolitical factors. In order to evaluate the effects of such uncertainty sources, in [2] four different alternatives have been considered in addition to the reference scenario. These scenarios differ by the assumed GDP growth rates and trends of oil price, which are considered to be the most influent factors on energy consumption. In the reference case, the considered GDP growth rates are reported in Table 1.4 and the oil price is supposed to reach around $70 per barrel in 2015 and to rise steadily to $113 per barrel in 2030 (i.e. $70 per barrel in inflation-adjusted 2006 dollars). The variations considered in the alternative scenarios are listed below.

I) *High economic growth case*. Average GDP growth increased by +0.5% per year for each country, oil price as in the reference case.

II) *Low economic growth case*. Average GDP growth decreased by -0.5% per year for each country, oil price as in the reference case.

III) *High oil price case*. Average GDP growth as in the reference case, oil price increasing from the initial value of about 105 $/barrel (September 2008) to about 186 $/barrel in 2030.

IV) *Low oil price case*. Average GDP growth as in the reference case, oil price declining from the initial value of about 105 $/barrel (September 2008) to about 46 $/barrel in 2016, then increasing to 68 $/barrel in 2030.

Table 1.4. Average annual growth of gross domestic product by region considered in [2], 2006–2030 (Percent per Year)

	History		**Projections**		
Region	2006	2007	2008	2008–2015	2015–2030
OECD North America	3.0	2.3	1.9	2.8	2.5
OECD Europe	3.3	3.1	2.7	2.3	2.1
OECD Asia	2.7	2.6	2.9	2.2	1.5
Non–OECD Europe and Eurasia	7.9	7.9	7.1	5.1	3.4
Non–OECD Asia	9.2	9.3	8.7	6.6	4.7
Middle East	5.0	4.6	5.0	4.4	3.7
Africa	5.5	6.0	5.8	4.9	4.1
Central and South America	5.4	5.4	5.1	4.1	3.6

According to [2], the different assumptions on oil price and economy growth do not influence the projections substantially, resulting in a variation of $\pm 10\%$ of the global energy

Table 1.5. Total primary energy demand (trillion MJ) projection over the years 1990–2030 by source and region. Data taken from [1].

Source and region	1990	2006	2015	2020	2025	2030	Ave. yearly % change
OECD							
Oil	79.38	92.48	90.10	89.64	88.34	86.66	-0.3
Natural gas	35.16	50.66	56.94	58.57	60.62	63.26	0.9
Coal	44.50	47.69	50.61	50.86	51.41	49.90	0.2
Nuclear	18.84	25.70	26.33	26.29	26.71	26.21	0.1
Biomass and waste	5.90	8.83	12.76	14.61	16.62	18.42	3.1
Hydro	4.23	4.60	5.06	5.27	5.44	5.56	0.8
Other	1.21	1.75	4.23	5.73	7.16	8.75	6.9
OECD Total	**189.20**	**231.74**	**246.10**	**250.95**	**256.31**	**258.74**	**0.5**
non–OECD							
Oil	50.61	68.49	90.97	100.23	109.23	117.64	2.3
Natural gas	34.87	50.11	64.60	72.80	81.09	90.39	2.5
Coal	48.39	80.21	117.77	132.26	146.16	155.58	2.8
Nuclear	3.14	4.77	7.87	8.96	10.38	11.55	3.8
Biomass and waste	31.86	40.86	44.80	46.72	48.77	51.12	0.9
Hydro	3.51	6.28	8.37	9.50	10.63	11.76	2.6
Other	0.29	1.00	2.38	3.30	4.39	5.90	7.7
non–OECD Total	**172.70**	**251.75**	**336.78**	**373.46**	**410.68**	**443.96**	**2.4**
World							
Oil	134.73	160.98	189.45	198.62	206.74	213.90	1.0
Natural gas	70.04	100.77	121.54	131.04	141.68	153.65	1.8
Coal	92.90	127.90	168.43	183.13	197.57	205.49	2.0
Nuclear	21.98	30.47	34.20	35.25	37.09	37.72	0.9
Biomass and waste	37.76	49.69	57.56	61.33	65.39	69.58	1.4
Hydro	7.74	10.88	13.43	14.77	16.03	17.33	1.9
Other	1.50	2.76	6.61	9.00	11.55	14.65	7.2
World Total	**366.63**	**483.49**	**591.21**	**633.16**	**676.12**	**712.34**	**1.6**

consumption in 2030. Indeed, it can be noted that even with the lowest value of GDP growth considered in [2] (i.e. the values of Table 1.4, decreased by 0.5%), the assumed GDP growth rates are actually highly optimistic, since for example the United States registered a GDP growth of 1.3% at the end of 2008 with respect to the end of 2007, with -0.5% GDP in the fourth quarter of 2008 [20], and the short term projections for 2009 forecast a further decrease, due to the present global financial crisis. However, according to [1] the actual crisis is not expected to affect long–term investments in the energy sector, but could lead to delays in the completion of the current projects, especially in the high capital–intensive field of power generation. The reference scenario obtained in

[1], which takes into account the government policies and measures adopted up to mid–2008, is similar to that of [2], except for some minor differences in the TPED share of biomass and waste. The highlights of these projections can be deduced by the trends of energy supply and consumption reported in Table 1.5 and Figure 1.5. An average yearly

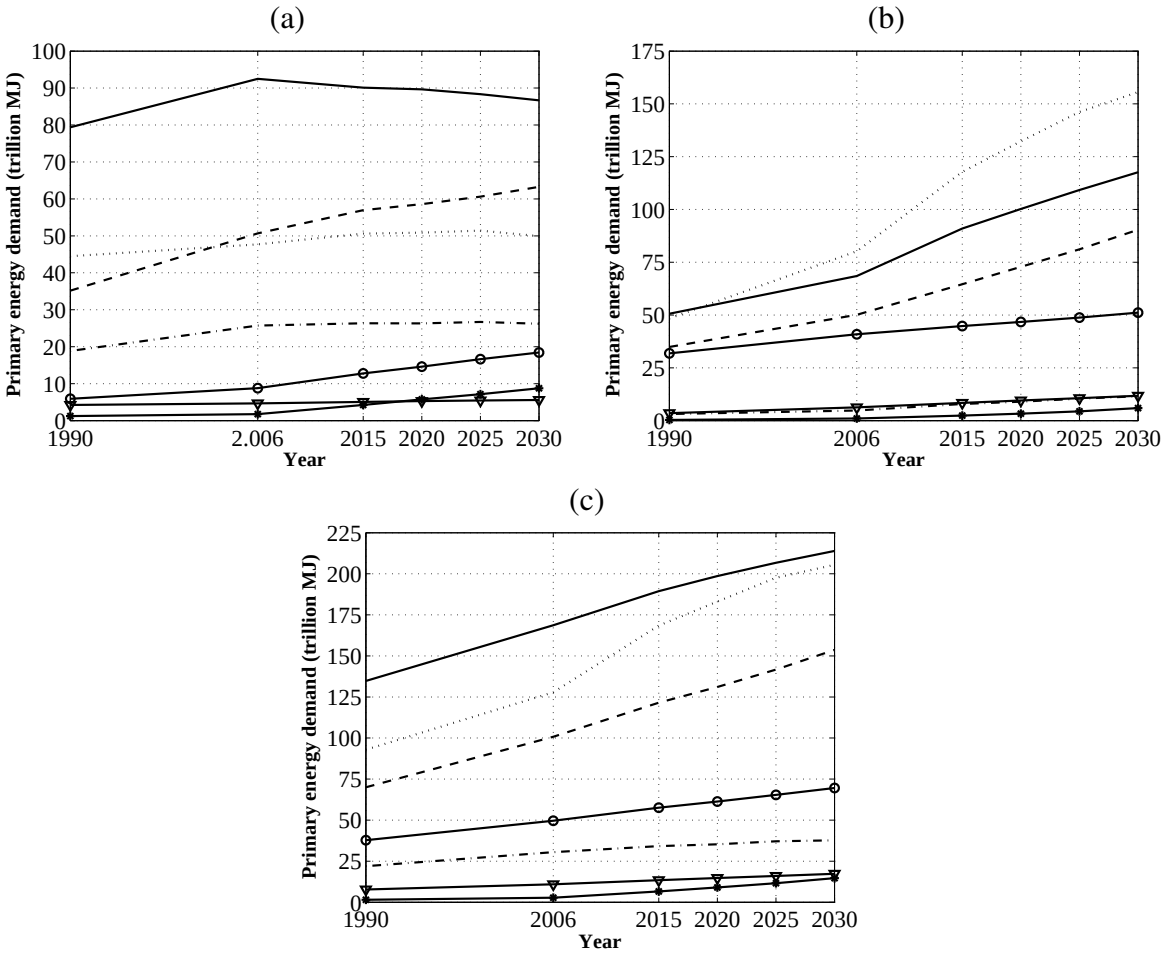

Figure 1.5. Projections of primary energy demand up to 2030 by source: oil (solid), natural gas (dashed), coal (dotted), nuclear (dash–dot), biomass and waste (solid line with circles), hydro (solid line with triangles) and other renewables (solid line with asterisks). Projections for (a) OECD countries, (b) non–OECD countries and (c) world total.

growth of 1.6% of TPED is estimated, leading to an overall increase of about 47% in 2030 with respect to 2006. About 87% of such a growth is accounted for by non–OECD countries, and about 50% by China and India. In these regions, a continuous increase of the demand of every kind of primary energy is expected, with the highest growth rate of renewables but also noticeable percent increase of nuclear energy and fossil energies. Yet, the amount of consumed energy per person of OECD countries will still be higher than

that of non–OECD. Demand for oil and coal energy in OECD countries is expected to plateau and even to slightly decrease, while the consumption of the other non–renewable energies continue to increase at a slow pace. The growth rate of global renewable energy, excluding hydropower, is projected to be the highest among all of the sources, however the TPED share of green energies in 2030 is estimated to be only about 2%, due to the low starting base in 2006. Thus, in the reference scenarios of [1, 2], which practically describe the course on which the world energy system is actually set, fossil sources still account for 80% of the global primary energy demand in 2030, with a growth of 50% in absolute terms with respect to 2006.
Figure 1.6 shows the projected distribution of global electricity generation by fuel in 2030. It can be noted that the electricity share of renewable energy, excluding hydropower, is

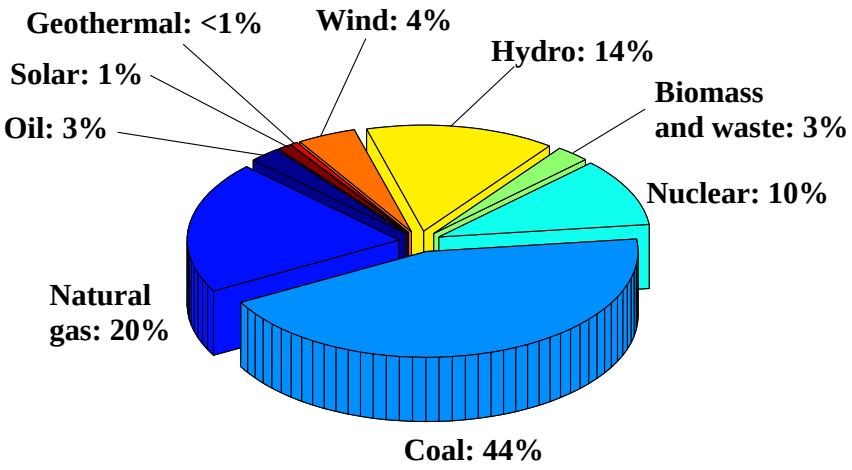

Figure 1.6. Projected electricity generation in 2030 by fuel.

projected to increase from about 1% of 2006 (see Figure 1.3) to some 6%. Such increase is mainly at the expense of nuclear power, which falls from 15% in 2006 to 10% in 2030. Thus, according to the reference scenario in 2030 fossil sources will still account for 67% of electricity generation, with coal being the largest electricity source.
As it can be expected, the energy–related carbon dioxide emissions (see Table 1.6) in the reference scenarios grow with an average rate of 1.6%, following the increase of energy demand, with practically the same distribution by source as that of 2006. Such a course of the global CO_2 emissions is reported in Figure 1.7: an increase of 45% in 2030 with respect to 2006 is expected, i.e. from about 26 Gt to about 40 Gt. Some 75% of the increase of CO_2 emissions arises in China, and approximately 97% is accounted for by non–OECD countries. The power generation sector will still account for most of the carbon dioxide emissions (about 30%), followed by the transportation sector (20%). Clearly, higher CO_2 emissions lead to higher atmospheric CO_2 concentration. The negative effects of such increase of CO_2 concentration on global warming and climate change are widely

Table 1.6. Projected energy–related carbon dioxide emissions in 2030 by region, fuel and sector (Gt). Data taken from [1].

Source and end–use sector	**OECD**	**Non–OECD**	**World**
Oil total	**5.15**	**7.15**	**12.30**
Power generation	0.11	0.58	0.69
Industry	0.34	0.81	1.15
Transport	3.77	4.23	8.00
Other sectors	0.56	1.12	1.68
Natural gas total	**3.49**	**4.75**	**8.24**
Power generation	1.38	1.26	2.64
Industry	0.64	0.99	1.63
Transport	0	0	0
Other sectors	1.20	0.88	2.08
Coal total	**4.51**	**14.11**	**18.62**
Power generation	3.90	4.60	8.50
Industry	0.44	3.59	4.03
Transport	0	0	0
Other sectors	0.04	0.88	0.92
Total CO_2 emissions	**13.15**	**26.01**	**39.16**

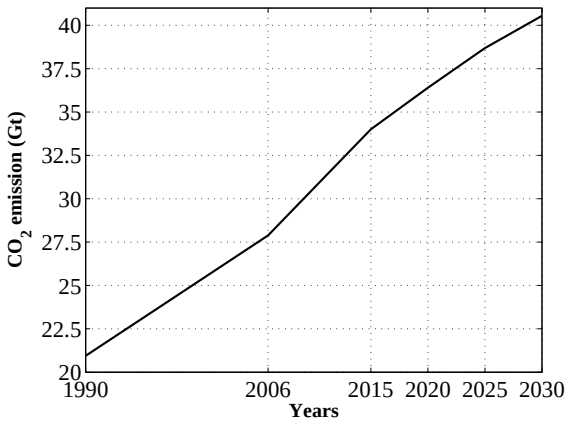

Figure 1.7. Projected carbon dioxide emissions (Gt) in the period 1990–2030.

recognized today and they will be briefly recalled in Section 1.3. For more information and deepening, the interested reader is referred e.g. to the assessment report [21, 22, 23] of the Intergovernmental Panel on Climate Change (IPCC).
On the basis of the data and concise considerations presented so far, a general framework can be easily depicted, where the actual and projected global energy consumption is based on fossil sources. Renewable energies account for a negligible part of the energy

mix, though they have enough potential to cover the world needs. The main causes of such a situation are the high costs of renewable energy technologies, their nonuniform and variable availability and their low power density per unit area.
The next Section focuses the attention on wind energy, describing the state of the art of the present technology and highlighting in particular the technical limitations that reduce its competitiveness.

1.2 Wind energy technology: state of the art and innovative concepts

According to relatively recent studies [6], global wind power has the potential to supply the whole global energy need. In particular it has been shown that by exploiting only 20% of the global land sites of "class 3" or more (i.e. with average wind speed greater than 6.9 m/s at 80 m above the ground), the entire world's energy demand could be supplied. However, such potential can not be harvested with competitive costs by the actual technology, based on wind towers. In this Section, the key points of the actual wind technology are briefly summarized, to complete the context that motivates the present dissertation. Moreover, the actual innovative concepts of high–altitude wind energy generation, that are being studied in few research groups and companies in the world, are also surveyed.

1.2.1 Actual wind energy technology

An interesting overview of the present wind power technology can be found in the recent paper [7], where the characteristics of modern wind turbines are described, together with the current lines of research for future improvements. Other information and details can be largely found in the literature (see e.g. [24, 25]). Development of modern wind technology started in the late 1970s and dramatic improvements have been obtained since that time. The present commercial wind turbines have three-bladed rotors with diameters up to 90–100 m, installed atop towers with 60–100 m of height (see Figure 1.8(a)). The turbine's drive train (i.e. the gearbox, the electric generator and the power converter) is placed inside the nacelle and linked to the rotor's hub. Large commercial turbines can typically produce 1.5–3 MW of electricity depending on the hub height, the rotor size and the electric equipment (see e.g. [26]). The amount of energy in the wind available for extraction by the turbine increases with the cube of wind speed, however such increase is exploited only to some extent, since the operation of a turbine is suitably controlled in order to not exceed the power level for which the electrical system has been designed (referred to as the "rated power"). The turbine power output is controlled by rotating the blades about their long axis to change the angle of attack with respect to the relative wind as the blades spin about the rotor hub (see Section 3.1 for further details on the influence

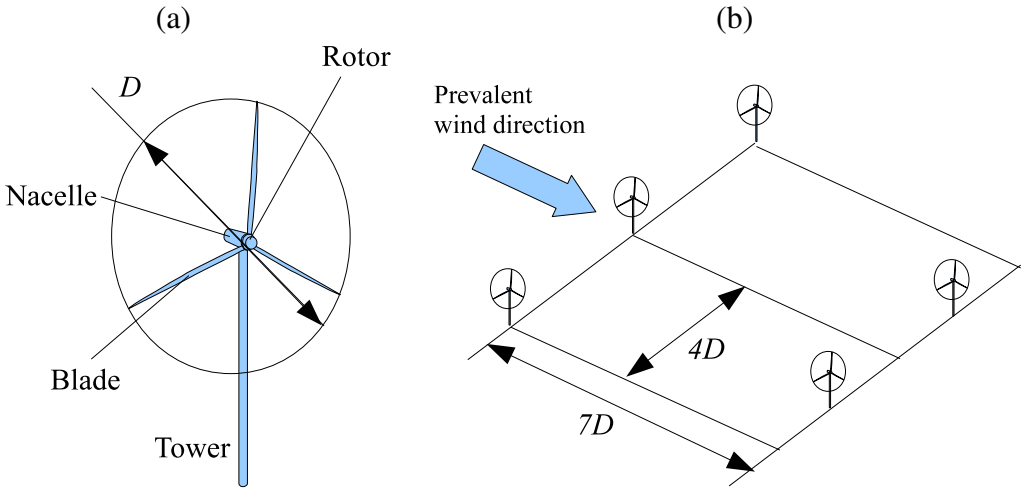

Figure 1.8. (a) Sketch of a modern three–bladed wind tower. (b) Deployment of wind towers in actual wind farms

of the airfoil's attack angle on aerodynamical forces). Moreover, the turbine is pointed into the wind by a control system that rotates the nacelle about the tower, on the basis of measurements of the wind speed and direction. Almost all modern turbines operate with the rotor positioned on the windward side of the tower. Typically, a turbine starts producing power with about 3.5–m/s wind speed and reaches the rated power output at about 15 m/s [26], according to a power curve (i.e. the relationship between wind speed and generated power) like the one depicted in Figure 1.9, related to a commercial 90–m diameter, 2–MW rated power wind turbine. If the wind speed exceeds the "cut–out" value (i.e. about 25 m/s), the blades are pitched to stop power production and rotation, in order to avoid possible breaking due to the excessive forces.
It is important to note that the wind energy potential is a function of the height above the ground due to the presence of the so–called "wind shear", i.e. the growth of wind speed with elevation [6]. An example of wind shear curve for a site near Brindisi, Italy, obtained from wind speed measurements collected daily[7] in the period 1996–2006, is reported in Figure 1.10 (see Section 6.1 for other examples and further details on wind data analyses). The height and the size of wind turbines have increased in the past years to capture the more energetic winds at higher elevations (see Table 1.7, which reports some data related to commercial land turbines [26]). However, actually the limits of such a dimension growth have been almost reached, from both economical and technological points of view. In fact, in general the costs of larger turbines grow linearly with the volume of the employed material (i.e. with the cube of the diameter), while the related increase of energy output is proportional to the rotor–swept area (the diameter squared). Therefore,

[7]Data retrieved from the database RAOB (RAwinsonde OBservation) of the National Oceanic & Atmospheric Administration, see [27].

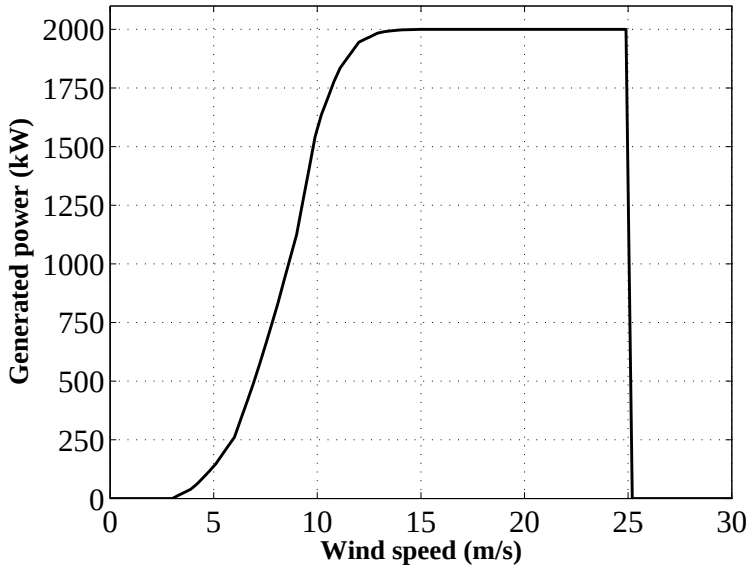

Figure 1.9. Power curve of a commercial 90–m diameter, 2–MW rated power wind turbine.

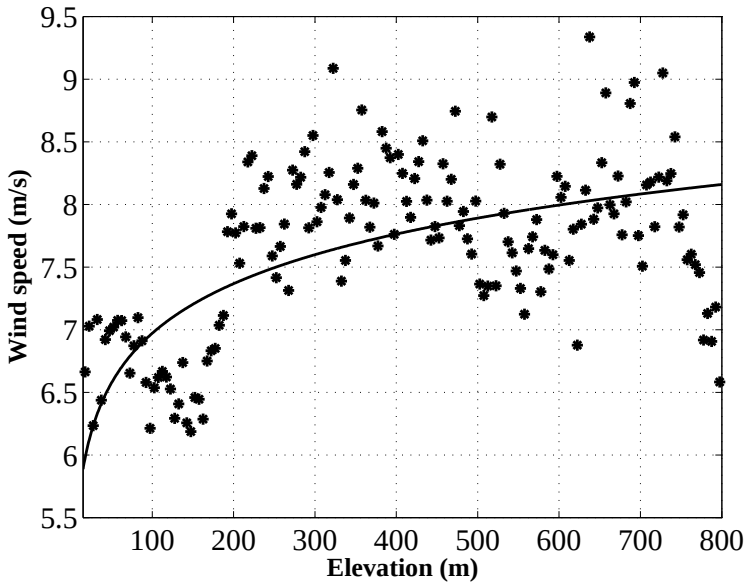

Figure 1.10. Wind shear related to the site of Brindisi, Italy. Solid line: wind shear model, asterisks: averaged wind speed measurements

at some size the cost for a larger turbine will grow faster than the resulting energy output revenue, making scaling not economically profitable. In practice, studies have shown that in recent years blade mass has been scaling at roughly an exponent of 2.3 versus the expected 3, thus delaying the achievement of dimension limit from the economical point of

Table 1.7. Actual wind energy technology: rated power, weight and size of modern commercial turbines.

Rated power	Hub height	Rotor diameter	Total weight	Tower weight	Nacelle weight	Rotor weight
0.85 MW	44 m	52 m	77 t	45 t	22 t	10 t
0.85 MW	49 m	52 m	82 t	50 t	22 t	10 t
0.85 MW	55 m	52 m	92 t	60 t	22 t	10 t
0.85 MW	65 m	52 m	104 t	72 t	22 t	10 t
0.85 MW	74 m	52 m	127 t	95 t	22 t	10 t
1.65 MW	70 m	82 m	200 t	105 t	52 t	43 t
1.65 MW	78 m	82 m	210 t	115 t	52 t	43 t
1.65 MW	80 m	82 m	220 t	125 t	52 t	43 t
2.0 MW	80 m	90 m	256 t	150 t	68 t	38 t
2.0 MW	95 m	90 m	306 t	200 t	68 t	38 t
2.0 MW	105 m	90 m	331 t	225 t	68 t	38 t
3.0 MW	80 m	90 m	271 t	160 t	70 t	41 t
3.0 MW	105 m	90 m	346 t	235 t	70 t	41 t

view. However, it has to be also considered that much higher operation, mobilization, and demobilization costs incur to build bigger turbines. Moreover, serious constraints to size growth have been reached, related to land transportation and turbine construction. Transportation of bigger turbine parts is not cost–effective and crane requirements are quite stringent because of the large nacelle mass in combination with the height of the lift and the required boom extension. For all these reasons, it is not expected that land–based turbines will become much larger than about 100 m in diameter, with corresponding power outputs of about 3–5 MW (see [7] for more details).

Other important aspects of wind energy technology are the generation efficiency and the average yearly generated power. As regards efficiency, according to Betz limit [24], a device can extract a theoretically maximum 59% of the energy in a stream with the same area as the working area of the device. The aerodynamic performance of a modern wind turbine has improved dramatically over the past 20 years and the rotor system can be expected to capture about 80% of such a theoretical upper bound. However, actually the turbine overall efficiency is such that about 40–50% of Betz limit is achieved. Furthermore, due to wind intermittency, any wind generator cannot produce continuously its rated power, thus the average power generated over the year is only a fraction, indicated as Capacity Factor (CF), of the rated one. For a given wind generator on a specific site, the CF can be evaluated knowing the generator power curve and the probability density distribution function of wind speed that flows in through the area spanned by the blades (see Section 6.2). The issue of wind energy density per unit area of occupied land is also of paramount importance. In order to generate a noticeable amount of energy, wind turbines

can be arranged in the so–called "wind farms", i.e. tens or hundreds of turbines built in the same location. According to [6, 25], the usual rule to deploy wind turbines of a given diameter D in a wind farm is to keep a distance of $7D$ in the wind prevalent direction and $4D$ in the transverse direction (see Figure 1.8(b)). This way, considering 90–m diameter, 2–MW rated power turbines, a density of about 4.4 turbines per km^2 is obtained, with a corresponding rated power density of 8.8 MW/km^2. Considering a good windy site (i.e. CF=0.4), a consequent average power density of 3.52 MW/km^2 is achieved. Thus, in order to generate an average power of 1000 MW (i.e. the power supplied by medium–to–large thermal plants), a land occupation of about 280 km^2 would be required, where more than 1200 turbines should be deployed. Such power density values are much lower than those given by thermal plants. For example, a coal–fired power plant like the "Federico II" in Brindisi, Italy, has a land occupation of 270 hectare (i.e. 2.7 km^2) and a rated power of 2640 MW: the corresponding rated power density is 984 MW per km^2, i.e. 100 times higher than a wind farm. Moreover, the CF of a thermal plant is close to 1, thus its average power density is about 270 times higher than that of a wind farm placed in a good location.
As regards future improvements of the present wind technology, studies on advanced rotors and drive trains and innovative towers are undergoing to try to push forward the actual technical limitations. Moreover, offshore wind turbines are being deployed at water depths of up to 30 m and research activities are undergoing to develop deep–water technologies (i.e. wind turbines placed in the sea with 60–90 m of depth). However, according to [7], it is clear that no single component improvement in cost or efficiency can achieve significant cost reductions or dramatically improved performance in the present wind technology and it is estimated that all the projected advancements can cumulatively bring no more than 30–40% improvement in the cost effectiveness of wind energy over the next decade.

1.2.2 Concepts of high–altitude wind power

As already anticipated, in this dissertation the idea of high–altitude wind energy is investigated. In particular, in the present research a precise concept [28, 29] of high–altitude power generation (generically denoted as "HAWE") has been considered. Such a concept will be thoroughly presented and analyzed in Chapters 2–6. At present, quite few research groups and companies in the world are studying and developing similar ideas of exploiting high–altitude wind flows, with conceptual and practical realizations that are either similar to HAWE (see e.g. [30, 31]) or very different [32]. The main research activities on this subject undergoing around the world, to the best of the author's knowledge, are briefly resumed and referenced in this Section.
As already noted, the research groups of the Katholieke Universiteit of Leuven (Belgium) [30] and of the Technical University of Delft (The Netherlands) [31] are studying and developing a concept that is very close to HAWE, i.e. the use of controlled tethered airfoils

to extract energy from high–altitude wind flows. Therefore, the description of HAWE technology included in Chapter 2 of this dissertation is valid also for the projects [30, 31] and the existing differences will be highlighted when appropriate (see Section 2.3.1).
A different concept is being investigated by Sky Wind Power Corporation [32, 33], using the so–called Flying Electric Generators (FEG), i.e. generators mounted on tethered rotorcrafts that levitate at altitudes of the order of 4600 m. Differently from [32], in the HAWE technology the airfoils fly at elevations of at most 800–1000 m above the ground, and the bulkier mechanical and electrical parts of the generator are kept at ground level.
In California, a company named Makani is currently working on wind generation using tethered airfoils or power kites. However, Makani does not release any information on its undergoing projects.
Finally, in the field of marine transportation, the company Skysails GmbH (Hamburg, Germany) [34] is developing a towing kite system that should be able to exploit the aerodynamical forces as auxiliary propulsion for large mercantile ships, achieving an estimated reduction of fuel consumption up to 30%.

1.3 Contributions of this dissertation

The data and concise analyses described in Sections 1.1–1.2 are sufficient to delineate the motivations and the objectives of this dissertation. The analyses of the actual and projected global energy situation of Section 1.1 clearly indicate the two major challenges that mankind is facing today: the supply of reliable, cheap energy in large quantities and the abatement of greenhouse gas emissions.
The dependance of the global energy system on fossil sources owned by few producer countries leads to economical instability, prevents millions of people from having access to energy and gives rise to delicate geopolitical equilibria. Non–OECD countries growing at fast rates like China and India will account for a 50% increase of energy demand in the next two decades. Such an increment has to be covered by an increase of energy supply: considering the current situation, fossil sources are the first candidates to fuel the growth of non–OECD world. As a consequence, the present problems of high concentration of fossil sources in few countries will be more acute, energy costs will continuously increase on average and pronounced short–term swings of oil price will remain the norm in the next 20 years.
The issue of climate change due to excessive concentration of greenhouse gases in the atmosphere, that is clearly related to the predominance of fossil sources in the global energy mix, may be even more serious than geopolitics. In fact, if no measure is undertaken to contain the emissions of carbon dioxide, a doubling of CO_2 concentration is expected to be reached by 2100, with a consequent global average temperature increase of up to 6° C [1, 21, 22, 23]. Almost all of the increase of emissions in the next twenty years is

accounted for by non–OECD countries.
In [1], two alternative climate–policy scenarios are considered (in addition to the reference one), in which the undertaking of political measures and investments aimed at reducing CO_2 emissions is assumed. Both scenarios lead to a long–term stabilization of carbon–dioxide emissions and they differ on the basis of the amount of efforts and investments employed to reach such a goal. Without entering into details (the interested reader is referred to [1]), the alternative scenarios clearly indicate two key points:

- **power generation is a critical sector since it is the less expensive field for CO_2 reduction**. As showed in Section 1.1, power generation accounts for 45% of energy–related CO_2 emissions. A shift to carbon–free electricity and heat generation would significantly contribute to reduce the emissions of greenhouse gases with relatively low costs and timings as compared to those needed to renew the transportation system, which is heavily oil dependent and would require expensive and slow transformation. Moreover, electricity is the most refined form of energy and it can be used to replace the use of fossil sources in every sector.

- **Given the actual situation, policy intervention will be necessary, through appropriate financial incentives and regulatory frameworks, to foster the development of renewable and carbon–free electricity generation**. One of the key points to reduce the dependance on fossil fuels is the use of a suitable combination of alternative energy sources. Nuclear energy actually represents the fourth contribution to the world's power generation sector (with a 15% share, see Section 1.1) and it avoids the problems related to carbon dioxide emissions. However, the issues related to safe nuclear waste management have not been solved yet, despite the employed strong efforts. Moreover, the cost of nuclear energy is likely to increase, due to massive investments of emerging countries [35, 36] and uranium shortage [37]. Renewable energy sources like hydropower, biomass, wind, solar and geothermal actually cover 19% of global electricity generation (with hydro alone accounting for 16%), but they could meet the whole global needs, without the issues related to pollution and global warming. However, the present cost of renewable energies is not competitive without incentives, mainly due to the high costs of the related technologies, their discontinuous and non–uniform availability and the low generated power density per km^2. The use of hydroelectric power is not likely to increase substantially in the future, because most major sites are already being exploited or are unavailable for technological and/or environmental reasons. Biomass and geothermal power have to be managed carefully to avoid local depletion, so they are not able to meet a high percentage of the global consumption. Solar energy has been growing fast during the last years (35% average growth in the U.S. in the last few years, [38]), however it has high costs and requires large land occupation.

Focusing the attention on wind energy, in Section 1.2 it has been noted that there is enough potential in global wind power to sustain the world needs [6]. However, the technical and economical limitations to build larger turbines and to deploy wind towers in "good" sites, that are often difficult to reach, the low average power density per km^2 and the environmental impact of large wind farms hinder the potential of the actual technology to increase its share of global electric energy generation above the actual 1%. The expected technological improvements in the next decade are not enough to make the cost of wind energy competitive against that of fossil energy, without the need of incentives. As is is stated in [7], "There is no "big breakthrough" on the horizon for wind technology".
The major contribution of Part I of this dissertation is to demonstrate that a real revolution of wind energy can be achieved with the innovative HAWE technology. It will be showed that high–altitude wind power generation using controlled airfoils has the potential to overcome most of the main limits of the present wind energy technology, thus providing renewable energy, available in large quantities everywhere in the world, at lower costs with respect to fossil energy and without the need for ad–hoc policies and incentives. Moreover, it will be showed that such a breakthrough can be realized in a relatively short time, of the order of few years, with relatively small efforts in research and development. Indeed, the idea of harvesting high–altitude wind energy introduced in the early '80s (see [8]) can be fully developed nowadays thanks to recent advances in several engineering fields like aerodynamics, materials, mechatronics and control theory. In particular, the advanced control techniques investigated in Part II of this dissertation play a role of fundamental importance, since they allow to control and maximize the performance of complex systems like HAWE, while satisfying demanding operational constraints, at the relatively fast adopted sampling rate. In order to support these claims, the original results of the research activity performed in the last three years are organized in the next Chapters as follows.

I) Description of high–altitude wind technology using tethered airfoils and design of the related power generation cycles (Chapter 2). The concept and core components of HAWE are described, as well as the two possible configurations that have been studied and their respective operation cycles, originally designed in this research activity.

II) Modeling and control of high–altitude wind energy generators (Chapter 3). The dynamical model of HAWE described in Chapter 3 has been refined during the last three years and actually it includes also variable aerodynamic coefficients and cable drag and weight effects. Such a model is employed to simulate the system behavior and to evaluate the potential of HAWE to generate large quantities of wind energy. In order to stabilize the airfoil's flight and to maximize the generated energy, advanced Nonlinear Model Predictive Control (NMPC) techniques, together with an efficient implementation based on Set Membership (SM) theory, are employed. The

theoretical aspects of the employed control technique are investigated in Part II of this dissertation.

III) Optimization of HAWE (Chapter 4). The operation of the designed energy generation cycles involves several parameters that have to be set up according to the wind speed, the airfoil's characteristics, the number of employed airfoils, etc.. Simplified power equations and numerical optimization techniques are employed to design such parameters in order to maximize the energy output. The optimal parameters are then employed in the numerical simulations and the resulting average power is compared to its theoretical upper bound. Moreover, numerical optimization is employed to maximize the average energy generated by a kite wind farm (i.e. several HAWE generators working in the same location) while avoiding aerodynamical interference among the airfoils.

IV) Experimental activities (Chapter 5). On the basis also of the results of the numerical simulations presented in this dissertation, a small–scale HE–yoyo prototype has been built at Politecnico di Torino, in order to test the concept of HAWE. Such prototype is briefly described in this thesis and the data collected in the first tests are showed. The good matching between simulation and real measured data increases the confidence with the obtained numerical results also for medium–to–large scale generators.

V) Wind data, capacity factor and cost analyses (Chapter 6). Using the large amount of measured wind speed data contained in [27], the CF of HAWE in various locations around the world is estimated and compared to that of wind turbines. Moreover, on the basis of a comparison between actual wind farms and high–altitude wind farms, an estimate of the cost of energy obtained with HAWE is computed.

The various contributions given in this dissertation have been partly published in [9, 10, 11, 12, 13, 14]. Considering all of the research and development activities undergoing around the world and cited in Section 1.2.2, quite few research groups and companies are actually working on the innovative idea of high–altitude wind power. To the best of the author's knowledge, this is one of the first doctoral dissertations on wind energy generation using tethered airfoils which includes theoretical analyses, system design, control design, numerical simulations, capacity factor and economical analyses and experimental tests.

Chapter 2

HAWE: High–Altitude Wind Energy generation using tethered airfoils

This Chapter introduces the basic concepts, the possible configurations and the operational energy generation cycles of HAWE. Then, the role of control and optimization in HAWE is highlighted. Finally, the naval application of the concept, which is being studied in the project KiteNav, started in 2007, is also briefly described.

2.1 Basic concepts

The concept of HAWE is to use airfoils, linked to the ground by two cables, to extract energy from wind blowing at higher heights with respect to those of the actual wind technology. The flight of the airfoils is suitably driven by an automatic control unit, able to differentially pull the lines to influence the wing motion. Wind energy is collected at ground level by converting the traction forces acting on the airfoil lines into electrical power, using suitable rotating mechanisms and electric generators placed on the ground. The airfoils are able to exploit wind flows at higher altitudes than those of wind towers (up to 1000 m, using 1200–1500–m–long cables), where stronger and more constant wind can be found basically everywhere in the world.
The key idea of the HAWE is to harvest high–altitude wind energy with the minimal effort in terms of generator structure, cost and land occupation. In the actual wind towers, the outermost 20% of the blade surface contributes for 80% of the generated power. The main reason is that the blade tangential speed (and, consequently, the effective wind speed) is higher in the outer part, and wind power grows with the cube of the effective wind speed. Thus, the tower and the inner part of the blades do not directly contribute to energy generation. Yet, the structure of a wind tower determines most of its cost and imposes a limit to the elevation that can be reached (see Section 1.2.1). To understand the concept of HAWE, one can imagine to remove all the bulky structure of a wind tower and just keep

the outer part of the blades, which becomes a much lighter airfoil flying fast in crosswind conditions (see Figure 2.1), connected to the ground by only two cables. Thus, the rotor

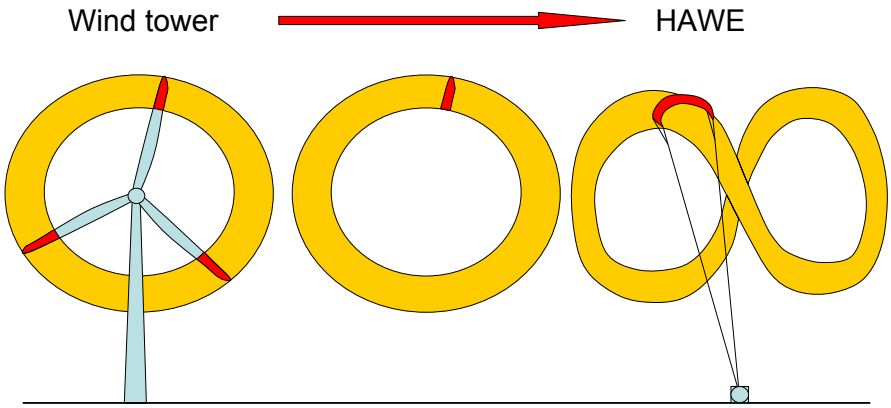

Figure 2.1. Basic concept of HAWE technology

and the tower of the present wind technology are replaced in HAWE technology by the airfoil and its cables, realizing a wind generator which is largely lighter and cheaper. For example, in a 2–MW wind turbine, the weight of the rotor and the tower is typically about 300 tons (see Table 1.7 in Section 1.2.1). As it will be showed in the next Chapters of this dissertation, a high–altitude generator of the same rated power can be obtained using a 500–m^2 airfoil and cables 1000–m long, with a total weight of about 2 tons only.

2.1.1 The airfoil

High efficiency, maneuverability, resistance to strain and lightness are the main characteristics that an airfoil should have to be employed for high–altitude wind energy production. Aerodynamic efficiency is defined as the ratio between the lift and drag coefficients of the wing, denoted as C_L and C_D respectively (see Section 3.1). Such coefficients are functions of the attack angle α, i.e. the angle between the airfoil's longitudinal axis and the effective wind flow (see Figure 2.2(a)). Assuming an infinite wingspan, functions $C_L(\alpha)$ and $C_D(\alpha)$ depends on the airfoil profile only. If a finite wingspan is considered, the effect of turbulence at the lateral edges of the wing reduces its aerodynamic efficiency. Such efficiency loss is higher with a lower aspect ratio, i.e. the ratio between the airfoil wingspan w_s and its chord c (Figure 2.2(b)). Since at first approximation the generated power increases with the square of aerodynamic efficiency, airfoils with high aspect ratios (i.e. high wingspan) should be employed. The maneuverability of the airfoil, in terms of minimal turning radius R_F during the flight, also depends on its wingspan, according to the approximate relationship $R_F \simeq 2.5\, w_s$. Since the optimal airfoil trajectory is a loop or a "figure eight" in the air (see Chapter 3), its wingspan should be contained in order

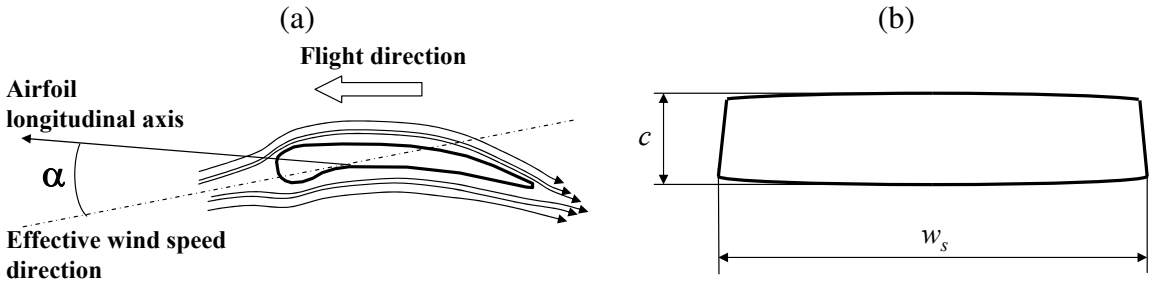

Figure 2.2. (a) Airfoil during flight and attack angle α. (b) Airfoil top view: wingspan w_s and chord c.

to obtain trajectories that are as strict as possible, thus allowing to employ more airfoils in a relatively small area. Thus, efficiency and maneuverability lead to opposite requirements on the wing geometry. As regards resistance and lightness, such characteristics depend mainly on the employed material and partly on the airfoil design. Flexible materials and air–inflated structures have been employed so far in the development of HAWE (see Chapter 5), since they are light and cheap and provide sufficient rigidity. In particular, commercially available power kites used for surfing or sailing have been employed, so that in the following the airfoil will be also referred to as "kite". Such power kites are not designed for generating energy and therefore their efficiency is relatively low. Indeed, rigid airfoils made of innovative composite materials and designed to maximize efficiency would provide a noticeable performance improvement.

2.1.2 The cables

The airfoil lift force is converted into mechanical power through the traction forces acting on the lines. Thus, the latter have to be strong enough to support high loads. At the same time, the cables have to be light and their diameter should be kept as small as possible, to limit their weight and aerodynamic drag. Lines realized in composite materials, with a traction resistance 8–10 times higher than that of steel cables of the same weight (see Figure 3.8 in Section 3.4), are being employed in HAWE. In order to extract energy from wind flows between 200–1000 m of elevation, 500–1500–m–long lines are needed. The HAWE prototype built at Politecnico di Torino is equipped with two 1000–m cables (see Chapter 5 for further details).

2.1.3 The Kite Steering Unit

At ground level, the airfoil cables are rolled around two drums, linked to two electric drives which are able to act either as generators or as motors. The kite flight is tracked using on–board wireless instrumentation (GPS, magnetic and inertial sensors) as well as

ground sensors, to measure the airfoil speed and position, the power output, the cable force and speed and the wind speed and direction. Such variables are employed for feedback by an electronic control system, able to influence the kite flight by differentially pulling the cables, via a suitable control of the electric drives (see Figure 2.3). The sys-

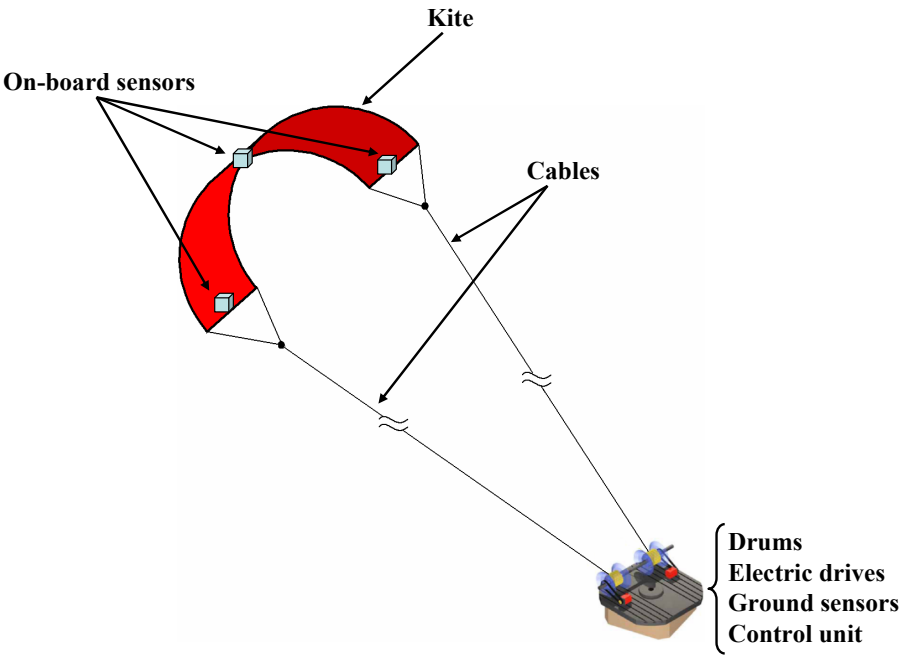

Figure 2.3. Sketch of a Kite Steering Unit (KSU)

tem composed by the electric drives, the drums, the on–board sensors and all the hardware needed to control a single kite is denoted as Kite Steering Unit (KSU) and it is the very core of the HAWE technology. The KSU can be employed in different ways to generate energy, depending on how the traction forces acting on the cables are converted into mechanical and electrical power. In particular, two different configurations have been investigated so far, namely the HE–yoyo and the HE–carousel configurations. In the HE–yoyo configuration, the KSU is fixed on the ground and wind power is captured by unrolling the kite lines, while in the HE–carousel configuration the KSU is put on a vehicle dragged by the line forces along a circular rail path, thus generating energy by means of additional electric generators linked to the wheels. Indeed, the described high–altitude wind energy generators are complex, open–loop unstable systems, affected by external disturbances (e.g. wind turbulence), with nonlinear dynamics and operational constraints. Thus, the use of an advanced automatic control technique, able to stabilize the kite flight while coping with disturbances and constraints, is the crucial feature of HAWE, since it is fundamental to achieve the best energy generation performance, as it will be highlighted in the next Section.

2.2 The role of control and optimization in HAWE

To generate energy in a reliable and effective way, in both the HE–yoyo and HE–carousel configurations the kite flight has to be stabilized and suitably controlled in order to continuously perform a cycle composed by two phases. In each of these working phases, the objective to be achieved (i.e. maximization of the generated energy) can be formulated as an optimization problem with its own cost function and with state and input constraints, in order to prevent the kite from crashing and to avoid line entangling and interference among more kites flying close in the same area. Then, a suitable control strategy has to be employed, able to achieve the required objective while avoiding constraint violation. To this end, Nonlinear Model Predictive Control (NMPC, see e.g. [39]) techniques are employed, since they are able to take into account state and input constraints and they can be applied to nonlinear systems in a quite straightforward way. However, in HAWE an efficient MPC implementation is needed for the real time control computations, which require the solution of a complex optimization problem at the employed sampling time (of the order of 0.2 s). Thus, a fast implementation technique of the obtained predictive controller is adopted (a deep analysis of the theoretical properties of such efficient MPC implementation is the main contribution of Part II of this dissertation). Note that, differently from what happens with control applications in many engineering fields, automatic control is the core of HAWE and advanced control techniques are fundamental to operate high–altitude power generators. As regards the measurement and/or estimation of the actual state value, needed to perform the control computation, the on–board sensors are employed together with advanced Set Membership (SM) filtering techniques (see e.g. [40, 41]).
As it will be showed in Chapter 3–4, the operation of the designed energy generation cycles also involves several parameters that have to be set up according to the wind speed, the airfoil's characteristics, the number of employed airfoils, etc.. In order to optimally design such parameters to maximize the energy output, numerical optimization techniques are employed (see Chapter 4). Indeed, optimization is also the instrument which the employed MPC techniques rely on. Thus, also numerical optimization theory plays a fundamental role in HAWE technology.

2.3 HAWE configurations and operating cycles

2.3.1 HE–yoyo configuration

In the HE–yoyo configuration, the KSU is fixed with respect to the ground. Energy is obtained by continuously performing a two-phase cycle (depicted in Figure 2.4): in the *traction phase* the kite exploits wind power to unroll the lines and the electric drives act as generators, driven by the rotation of the drums. When the maximum line length

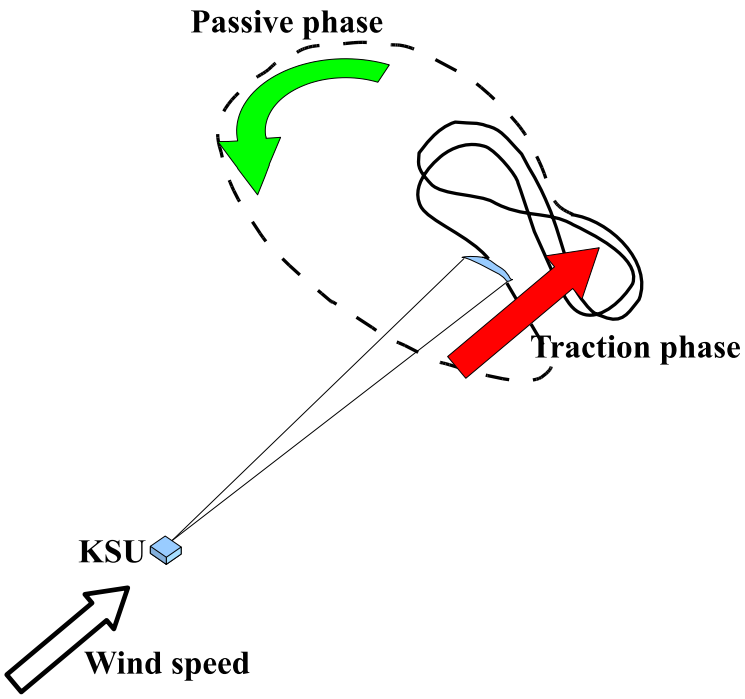

Figure 2.4. Sketch of a HE–yoyo cycle: traction (solid) and passive (dashed) phases.

is reached, the *passive phase* begins and the drives act as motors, spending a minimum amount of the previously generated energy, to recover the kite and to drive it in a position which is suitable to start another traction phase, i.e. when the kite is flying with wind advantage in a symmetric zone with respect to the nominal wind direction. The passive phase can be performed in two possible ways (see Figure 2.5):

I) "low power maneuver": the kite is driven to the borders of the "power zone" (see Figure 2.5), where its aerodynamic lift drops down and it can be therefore recovered with low energy expense;

II) "wing glide maneuver": a large length difference (approximately equal to the kite wingspan) is issued between the two cables by pulling them in subsequent order, thus making the kite lose its aerodynamic lift and allowing a fast winding back of the cables with low energy losses.

The wing glide maneuver has the advantage of occupying less aerial space than the low power maneuver, however it may lead to higher cable and airfoil wear. As anticipated, two different MPC controllers are designed to control the kite in the traction and passive phases. For the whole cycle to be generative, the total amount of energy produced in the traction phase has to be greater than the energy spent in the passive one. Therefore,

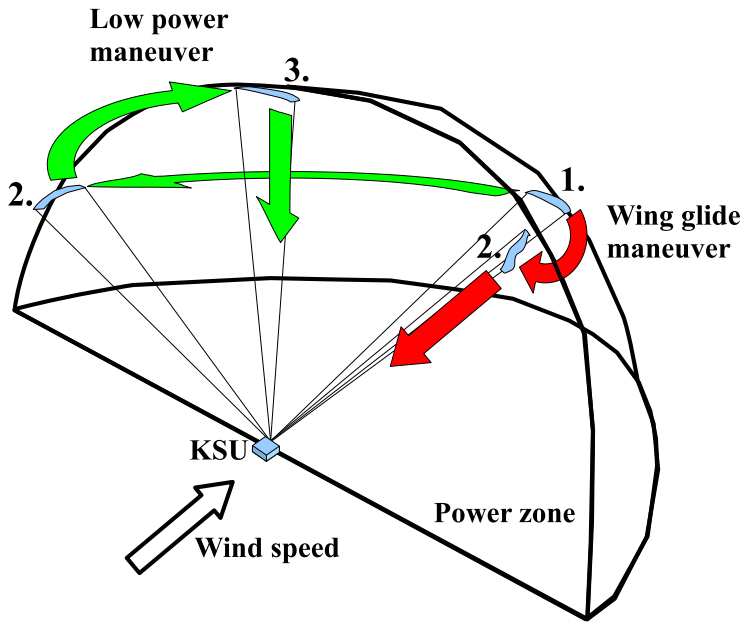

Figure 2.5. HE–yoyo passive phase: “low power” and “wing glide” maneuvers.

the controller employed in the traction phase must maximize the produced energy, while in the passive phase the objective is to maneuver the kite in a suitable position and to minimize, at the same time, the spent energy (see Chapter 3 for details). Other than in this dissertation and in the related published works [9, 10, 11, 12, 13, 14], the potential of the HE–yoyo configuration has also been investigated in [42] for the cases of one and two kites linked to a single cable: optimal kite periodic loops, which maximize the generated energy, have been computed considering as inputs the derivatives of the kite roll angle, lift coefficient and cable winding speed. Moreover, in [30] a real time nonlinear MPC scheme has been used to control a single kite and make it track pre–computed optimal reference orbits which are parameterized with respect to the nominal wind speed. In this paper, no pre–computed orbit is used and the designed nonlinear MPC controller directly maximizes the generated energy. Moreover, the sampling time of 0.2 s employed here is quite lower than the value used in [30] (equal to 1 s) and the kite lift coefficient is not considered as an input variable. The latter difference is due to the presence of a different kind of actuator: in the HE–yoyo prototype built at Politecnico di Torino, which this paper refers to, the kite is commanded just by differentially pulling its two lines, while in the prototype built at Delft University (see e.g. [43]), which [30] refers to, wireless–commanded linear actuators are put on the kite lateral extremes. This solution allow to also change the kite angle of attack (i.e. the aerodynamic characteristics), by changing the position of the line attach points on each side of the airfoil. Such a solution gives more control possibilities (since it allows to add an input channel to the system) but also seems

to be more susceptible to faults (e.g. wireless communication disturbances and failures).

2.3.2 HE–carousel configuration

The HE–carousel configuration is conceived for medium to large scale energy generators. In such a configuration, several airfoils are controlled by their KSUs placed on vehicles moving along a circular rail path (see Figure 2.6); the speeds of such vehicles are kept constant by electric generators/motors acting on the wheels. The potentials of the HE–

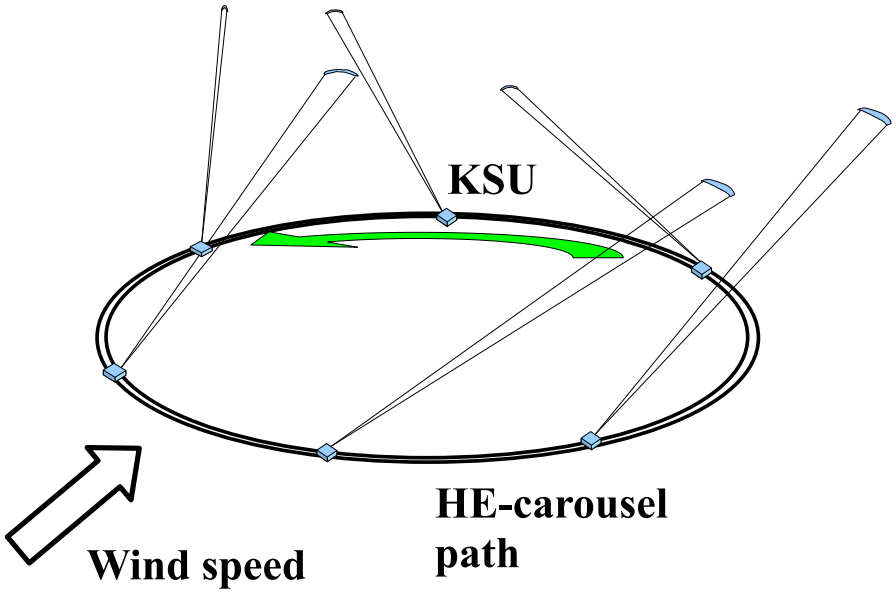

Figure 2.6. Sketch of a HE–carousel.

carousel configuration have been investigated using either variable line length or constant line length.

I) Constant line length. When fixed cable length is employed, energy is generated by continuously repeating a cycle composed of two phases, namely the *traction* and the *passive* phases. These phases are related to the angular position Θ of the control unit, with respect to the wind direction (see Figure 2.7). During the traction phase, which begins at $\Theta = \Theta_3$ in Figure 2.7, the MPC controller is designed in such a way that the kite pulls the vehicle, maximizing the generated power. This phase ends at $\Theta = \Theta_0$ and the passive phase begins: the kite is no more able to generate energy until angle Θ reaches the value Θ_3. In the passive phase, the MPC controller is designed to move the kite, with the minimal energy loss, in a suitable position to begin another traction phase, where once again the control is designed to maximize

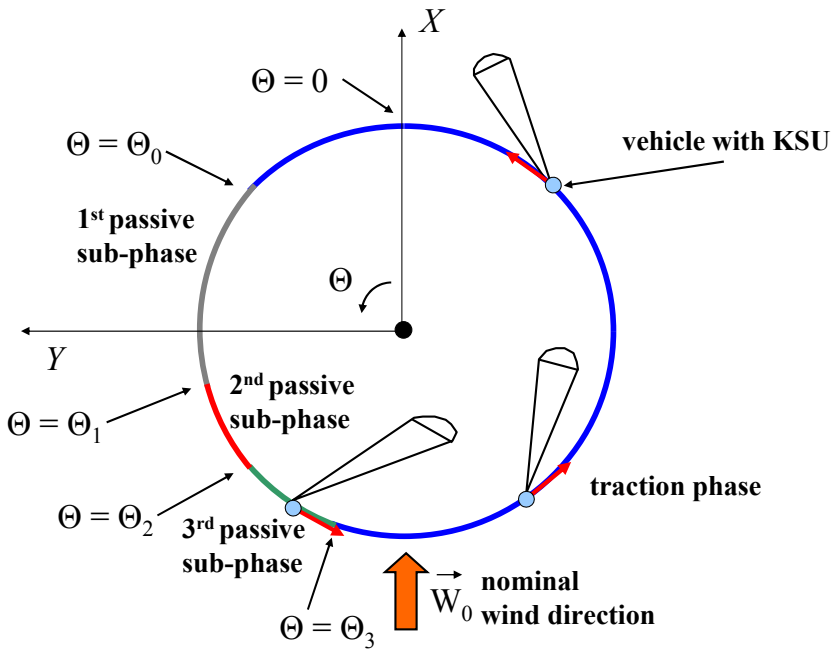

Figure 2.7. HE–carousel configuration phases with constant line length.

the generated power. In particular, the passive phase is divided into three sub–phases; the transitions between each two subsequent passive sub–phases are marked by suitable values of the vehicle angular position, Θ_1 and Θ_2 in Figure 2.7, which are chosen in order to minimize the total energy spent during the phase. The three passive sub–phases will be described in details in Section 3.3.2.

II) Variable line length. If line rolling/unrolling is suitably managed during the cycle, energy can be generated also when the rail vehicle is moving against the wind. In this case the operating phases of each KSU placed on the HE–carousel, namely the *traction* and the *unroll* phases, are depicted in Figure 2.8. The *unroll phase* approximately begins when the angular position Θ of the rail vehicle is such that the KSU is moving in the opposite direction with respect to the nominal wind: such situation is identified by angle Θ_0 in Figure 2.8. During the unroll phase, the electric drives linked to the rail vehicle wheels act as motors to drag the KSU against the wind. At the same time, the kite lines unroll, thus energy is generated as in the traction phase of the HE–yoyo configuration. The difference between the energy spent to drag the rail vehicle and the energy generated by unrolling the lines gives the net energy generated during this phase. When the KSU starts moving with wind advantage (i.e. its angular position is greater than Θ_1 in 2.8), the HE–carousel *traction phase* starts: the kite pulls the rail vehicle and the drives linked to the wheels act as generators. Meanwhile, the kite lines are rolled back

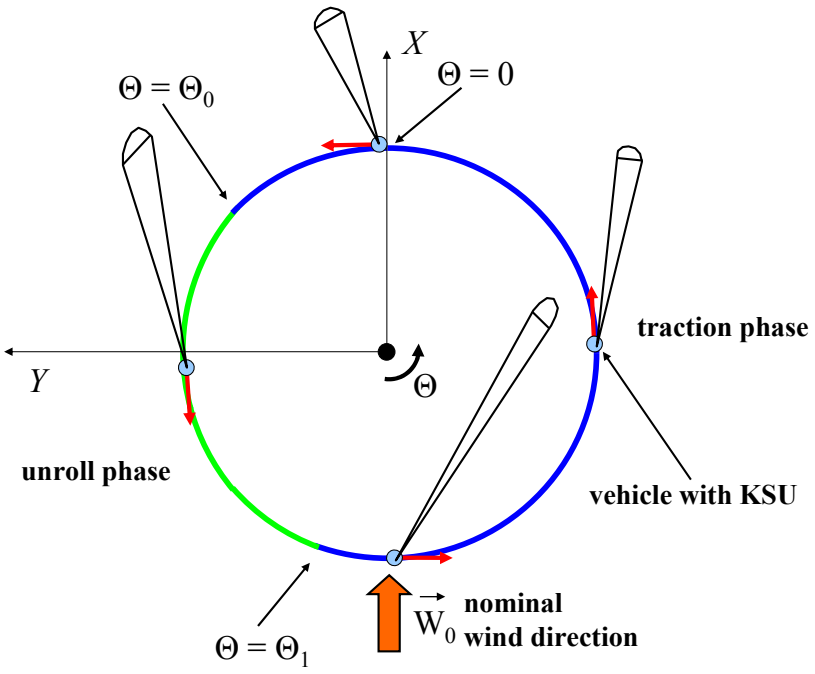

Figure 2.8. HE–carousel configuration phases with variable line length.

in order to always start the next unroll phase with the same line length. Thus, in the traction phase the net generated energy is given by the difference between the energy generated by pulling the rail vehicle and the energy spent to recover the lines. The MPC controllers employed in the HE–carousel with variable line length are therefore designed to maximize such a net generated energy.

The modeling of the HAWE generators and the design of the MPC controllers for each of the operational phases of the HE–yoyo and HE–carousel configurations are described in Chapter 3, together with the obtained numerical results.

2.4 Naval application of HAWE

Though this dissertation is focused on the application of the HAWE concept for electricity generation exploiting high–altitude wind flows, it is worth citing the project KiteNav, started at Politecnico di Torino, Italy, in 2007. The basic idea is to place a KSU on a boat (currently a small 10–m long boat is being considered in the project) and to employ the airfoil either to provide auxiliary propulsion by towing the boat (like the idea studied in [44] or the application being developed by [34]) or to generate electric energy that is then supplied to a stack of batteries. The latter provide energy to the boat's electric engines. Indeed, also in the naval application of HAWE advanced control and optimization play

an important role, since they are employed to control the kite and to devise the optimal operating conditions of both the kite and the boat. It is interesting to note that, according to the performed preliminary analysis, by generating energy through an operating cycle like the one of HE–yoyo and supplying it to the batteries, it is possible for the boat to travel in the opposite direction with respect to the wind (contrary to what happens with standard sailboats). To assess the potentials of this concept, experimental tests will be performed in 2009.

Chapter 3

Control of HAWE

This Chapter deals with the modeling, control and simulation of HAWE systems. At first, a dynamic model for the HE–yoyo and HE–carousel configurations is derived. Then, the Nonlinear Model Predictive Control (NMPC, see e.g. [45]) design is carried out and its approximation is computed using the "global" optimal Set Membership technique (see Section 11.1), in order to improve the on–line computational efficiency. Finally, numerical simulations are performed to evaluate the energy generation potentials of HAWE.

3.1 HAWE models

The kite model described in this dissertation is derived from the simpler one originally developed in [46]. More aspects are added in this study, like the computation of the airfoil attack angle (with consequent varying aerodynamical characteristics) and the model of the vehicle in the HE–carousel configuration.
A fixed Cartesian coordinate system (X,Y,Z) is considered (see Figure 3.1(b)), with X axis aligned with the nominal wind speed vector direction. Wind speed vector is represented as $\vec{W}_l = \vec{W}_0 + \vec{W}_t$, where $\vec{W}_0$ is the nominal wind, supposed to be known and expressed in (X,Y,Z) as:

$$\vec{W}_0 = \begin{pmatrix} W_x(Z) \\ 0 \\ 0 \end{pmatrix} \tag{3.1}$$

$W_x(Z)$ is a known function which gives the wind nominal speed at the altitude Z. The term $\vec{W}_t$ may have components in all directions and is not supposed to be known, accounting for wind unmeasured turbulence.
A second, possibly moving, Cartesian coordinate system (X',Y',Z') is considered, centered at the Kite Steering Unit (KSU) location. In this system, the kite position can be expressed as a function of its distance r from the origin and of the two angles θ and ϕ, as depicted in Figure 3.1(a), which also shows the three unit vectors e_θ, e_ϕ and e_r of a

local coordinate system centered at the kite center of gravity. Unit vectors (e_θ, e_ϕ, e_r) are expressed in the moving Cartesian system (X',Y',Z') by:

$$\begin{pmatrix} e_\theta & e_\phi & e_r \end{pmatrix} = \begin{pmatrix} \cos(\theta)\cos(\phi) & -\sin(\phi) & \sin(\theta)\cos(\phi) \\ \cos(\theta)\sin(\phi) & \cos(\phi) & \sin(\theta)\sin(\phi) \\ -\sin(\theta) & 0 & \cos(\theta) \end{pmatrix} \tag{3.2}$$

In the HE–carousel configuration, the KSU angular position Θ is defined by the direction

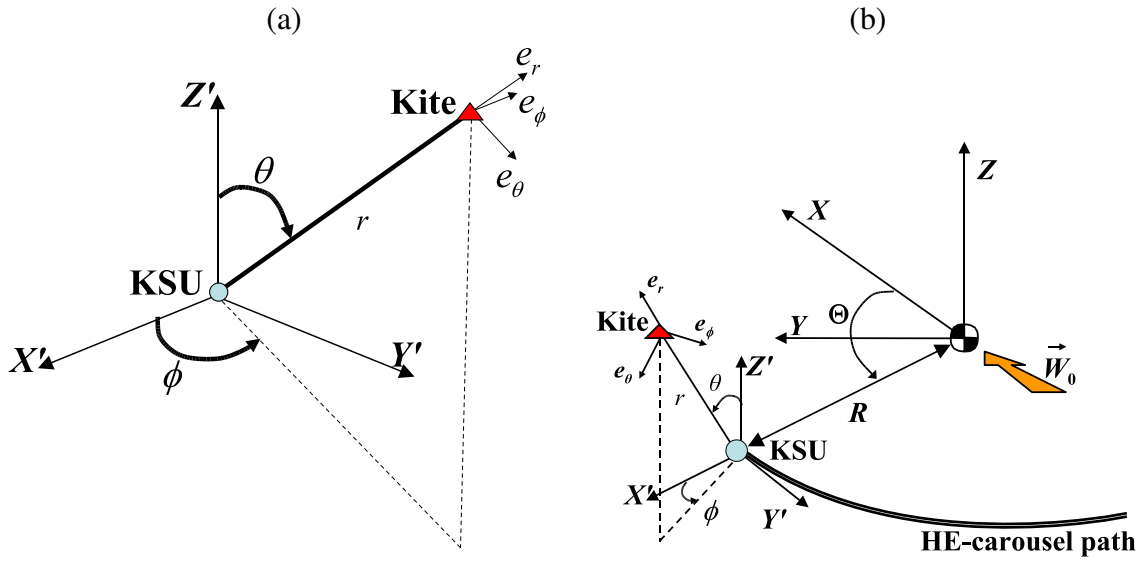

Figure 3.1. (a) Model diagram of a single KSU (b) Model diagram of a single KSU moving on a HE–carousel.

of axes X and X' (see Figure 3.1(b)).
Applying Newton's laws of motion to the kite in the local coordinate system (e_θ, e_ϕ, e_r), the following dynamic equations are obtained:

$$\begin{aligned} \ddot{\theta} &= \frac{F_\theta}{m\,r} \\ \ddot{\phi} &= \frac{F_\phi}{m\,r\sin\theta} \\ \ddot{r} &= \frac{F_r}{m} \end{aligned} \tag{3.3}$$

where m is the kite mass. Forces F_θ, F_ϕ and F_r include the contributions of gravity force $\vec{F}^{\text{grav}}$ of the kite and the lines, apparent force $\vec{F}^{\text{app}}$, kite aerodynamic force $\vec{F}^{\text{aer}}$, aerodynamic drag force $\vec{F}^{\text{c,aer}}$ of the lines and traction force $F^{\text{c,trc}}$ exerted by the lines on

the kite. Their relations, expressed in the local coordinates (e_θ, e_ϕ, e_r) are given by:

$$\begin{aligned} F_\theta &= F_\theta^{\text{grav}} + F_\theta^{\text{app}} + F_\theta^{\text{aer}} + F_\theta^{\text{c,aer}} \\ F_\phi &= F_\phi^{\text{grav}} + F_\phi^{\text{app}} + F_\phi^{\text{aer}} + F_\phi^{\text{c,aer}} \\ F_r &= F_r^{\text{grav}} + F_r^{\text{app}} + F_r^{\text{aer}} + F_r^{\text{c,aer}} - F^{\text{c,trc}} \end{aligned} \tag{3.4}$$

The following subsections describe how each force contribution is taken into account in the model.

3.1.1 Gravity forces

The magnitude of the overall gravity force applied to the kite center of gravity is the sum of the kite weight and the contribution $F^{\text{c,grav}}$ given by the weight of the lines. Assuming that the weight of each line is applied at half its length (i.e. $r/2$), $F^{\text{c,grav}}$ can be computed considering the rotation equilibrium equation around the point where the lines are attached to the KSU:

$$\frac{r\cos(\theta)}{2}\frac{2\,\rho_l\,\pi\,d_l^2\,r}{4}\,g = F^{\text{c,grav}} r\cos(\theta) \tag{3.5}$$

where g is the gravity acceleration, ρ_l is the line material density and d_l is the diameter of each line. Thus, the magnitude of the overall gravity force $\vec{F}^{\text{grav}}$ can be computed as:

$$|\vec{F}^{\text{grav}}| = m\,g + F^{\text{c,grav}} = \left(m + \frac{\rho_l\,\pi\,d_l^2\,r}{4}\right)\,g \tag{3.6}$$

Vector $\vec{F}^{\text{grav}}$ in the fixed coordinate system (X,Y,Z) is directed along the negative Z direction. Thus, using the rotation matrix (3.2) the following expression is obtained for the components of $\vec{F}^{\text{grav}}$ in the local coordinates (e_θ, e_ϕ, e_r):

$$\vec{F}^{\text{grav}} = \begin{pmatrix} F_\theta^{\text{grav}} \\ F_\phi^{\text{grav}} \\ F_r^{\text{grav}} \end{pmatrix} = \begin{pmatrix} \left(m + \frac{\rho_l\,\pi\,d_l^2\,r}{4}\right)\,g\,\sin(\theta) \\ 0 \\ -\left(m + \frac{\rho_l\,\pi\,d_l^2\,r}{4}\right)\,g\,\cos(\theta) \end{pmatrix} \tag{3.7}$$

3.1.2 Apparent forces

The components of vector $\vec{F}^{\text{app}}$ depend on the considered kite generator configuration: in particular, for the HE–yoyo configuration centrifugal inertial forces have to be considered:

$$\begin{aligned} F_\theta^{\text{app}} &= m(\dot{\phi}^2 r\sin\theta\cos\theta - 2\dot{r}\dot{\theta}) \\ F_\phi^{\text{app}} &= m(-2\dot{r}\dot{\phi}\sin\theta - 2\dot{\phi}\dot{\theta}r\cos\theta) \\ F_r^{\text{app}} &= m(r\dot{\theta}^2 + r\dot{\phi}^2\sin^2\theta) \end{aligned} \tag{3.8}$$

In the case of HE–carousel configuration, since each KSU moves along a circular trajectory with constant radius R (see Figure 3.1(b)), also the effects of the KSU angular position Θ and its derivatives have to be taken into account in apparent force calculation, therefore:

$$\begin{aligned} F_\theta^{\text{app}} &= m(\dot{\Theta}^2 R\cos\theta\cos\phi - \ddot{\Theta}R\cos\theta\sin\phi + (\dot{\Theta}+\dot{\phi})^2 r\sin\theta\cos\theta - 2\dot{r}\dot{\theta}) \\ F_\phi^{\text{app}} &= m(-(2\dot{r}\dot{\phi}+\ddot{\Theta}r)\sin\theta - 2(\dot{\Theta}+\dot{\phi})\dot{\theta}r\cos\theta - \ddot{\Theta}R\cos\phi - \dot{\Theta}^2 R\sin\phi) \\ F_r^{\text{app}} &= m(r\dot{\theta}^2 + r(\dot{\Theta}+\dot{\phi})^2\sin^2\theta - \ddot{\Theta}R\sin\theta\sin\phi + \dot{\Theta}^2 R\sin\theta\cos\phi) \end{aligned} \tag{3.9}$$

3.1.3 Kite aerodynamic forces

Aerodynamic force $\vec{F}^{\text{aer}}$ depends on the effective wind speed $\vec{W}_e$, which in the local system (e_θ, e_ϕ, e_r) is computed as:

$$\vec{W}_e = \vec{W}_l - \vec{W}_a \tag{3.10}$$

where $\vec{W}_a$ is the kite speed with respect to the ground. For the HE–yoyo configuration $\vec{W}_a$ can be expressed in the local coordinate system (e_θ, e_ϕ, e_r) as:

$$\vec{W}_a = \begin{pmatrix} \dot{\theta}\, r \\ \dot{\phi}\, r\sin\theta \\ \dot{r} \end{pmatrix} \tag{3.11}$$

while for the HE–carousel configuration:

$$\vec{W}_a = \begin{pmatrix} \dot{\theta}\, r + \dot{\Theta}\cos\theta\sin\phi R \\ (\dot{\phi}+\dot{\Theta})\, r\sin\theta + \dot{\Theta}\cos\phi R \\ \dot{r} + \dot{\Theta}\sin\theta\sin\phi R \end{pmatrix} \tag{3.12}$$

Let us consider now the kite wind coordinate system ($\vec{x}_{\text{w}}$,$\vec{y}_{\text{w}}$,$\vec{z}_{\text{w}}$) (Figure 3.2(a)–(b)), with the origin in the kite center of gravity, $\vec{x}_{\text{w}}$ basis vector aligned with the effective wind speed vector, pointing from the trailing edge to the leading edge of the kite, $\vec{z}_{\text{w}}$ basis vector contained in the kite symmetry plane and pointing from the top surface of the kite to the bottom and wind $\vec{y}_{\text{w}}$ basis vector completing the right handed system. Unit vector $\vec{x}_{\text{w}}$ can be expressed in the local coordinate system (e_θ, e_ϕ, e_r) as:

$$\vec{x}_{\text{w}} = -\frac{\vec{W}_e}{|\vec{W}_e|} \tag{3.13}$$

According to [46], vector $\vec{y}_{\text{w}}$ can be expressed in the local coordinate system (e_θ, e_ϕ, e_r) as:

$$\vec{y}_{\text{w}} = e_{\text{w}}(-\cos(\psi)\sin(\eta)) + (e_r \times e_{\text{w}})(\cos(\psi)\cos(\eta)) + e_r\sin(\psi) \tag{3.14}$$

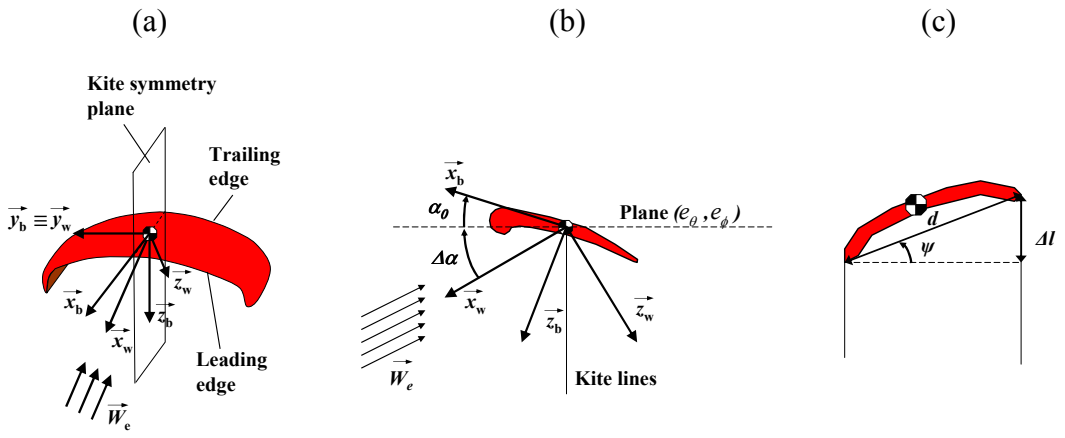

Figure 3.2. (a) Scheme of the kite wind coordinate system ($\vec{x}_\mathrm{w}$,$\vec{y}_\mathrm{w}$,$\vec{z}_\mathrm{w}$) and body coordinate system ($\vec{x}_\mathrm{b}$,$\vec{y}_\mathrm{b}$,$\vec{z}_\mathrm{b}$). (b) Wind axes ($\vec{x}_\mathrm{w}$, $\vec{z}_\mathrm{w}$), body axes ($\vec{x}_\mathrm{b}$, $\vec{z}_\mathrm{b}$) and angles α_0 and $\Delta\alpha$. (c) Command angle ψ

where:

$$e_\mathrm{w} = \frac{\vec{W}_e - e_r(e_r \cdot \vec{W}_e)}{|\vec{W}_e - e_r(e_r \cdot \vec{W}_e)|}\,, \quad \eta \doteq \arcsin\left(\frac{\vec{W}_e \cdot e_r}{|\vec{W}_e - e_r(e_r \cdot \vec{W}_e)|}\tan(\psi)\right) \tag{3.15}$$

Angle ψ is the control input, defined by

$$\psi = \arcsin\left(\frac{\Delta l}{d}\right) \tag{3.16}$$

with d being the distance between the two lines fixing points at the kite and Δl the length difference of the two lines (see Figure 3.2(c)). Δl is considered positive if, looking the kite from behind, the right line is longer than the left one. Equation (3.14) has been derived in [46] in order to satisfy the requirements that $\vec{y}_\mathrm{w}$ is perpendicular to $\vec{x}_\mathrm{w}$, that its projection on the unit vector e_r is $\vec{y}_\mathrm{w} \cdot e_r = \sin(\psi)$ and that the kite is always in the same orientation with respect to the lines. Angle ψ influences the kite motion by changing the direction of vector $\vec{F}^\mathrm{aer}$. Finally, the wind unit vector $\vec{z}_\mathrm{w}$ can be computed as:

$$\vec{z}_\mathrm{w} = \vec{x}_\mathrm{w} \times \vec{y}_\mathrm{w} \tag{3.17}$$

Then, the aerodynamic force $\vec{F}^\mathrm{aer}$ in the local coordinate system (e_θ, e_ϕ, e_r) is given by:

$$\vec{F}^\mathrm{aer} = \begin{pmatrix} F_\theta^\mathrm{aer} \\ F_\phi^\mathrm{aer} \\ F_r^\mathrm{aer} \end{pmatrix} = -\frac{1}{2}\,C_D\,A\,\rho\,|\vec{W}_e|^2\,\vec{x}_\mathrm{w} - \frac{1}{2}\,C_L\,A\,\rho\,|\vec{W}_e|^2\,\vec{z}_\mathrm{w} \tag{3.18}$$

where ρ is the air density, A is the kite characteristic area, C_L and C_D are the kite lift and drag coefficients. As a first approximation, the drag and lift coefficients are nonlinear

functions of the kite angle of attack α. To define angle α, the kite body coordinate system $(\vec{x}_\mathrm{b},\vec{y}_\mathrm{b},\vec{z}_\mathrm{b})$ needs to be introduced (Figure 3.2(a)–(b)), centered in the kite center of gravity with unit vector $\vec{x}_\mathrm{b}$ contained in the kite symmetry plane, pointing from the trailing edge to the leading edge of the kite, unit vector $\vec{z}_\mathrm{b}$ perpendicular to the kite surface and pointing down and unit vector $\vec{y}_\mathrm{b}$ completing a right–handed coordinate system. Such a system is fixed with respect to the kite. The attack angle α is then defined as the angle between the wind axis $\vec{x}_\mathrm{w}$ and the body axis $\vec{x}_\mathrm{b}$ (see Figure 3.2(b)). Note that in the employed model, it is supposed that the wind axis $\vec{x}_\mathrm{w}$ is always contained in the kite symmetry plane. Moreover, it is considered that by suitably regulating the attack points of the lines to the kite, it is possible to impose a desired *base* angle of attack α_0 to the kite: such an angle (depicted in Figure 3.2(b)) is defined as the angle between the kite body axis $\vec{x}_\mathrm{b}$ and the plane defined by local vectors e_θ and e_ϕ, i.e. the tangent plane to a sphere with radius r. Then, the actual kite angle of attack α can be computed as the sum of α_0 and the angle $\Delta\alpha$ between the effective wind $\vec{W}_e$ and the plane defined by (e_θ,e_ϕ):

$$\begin{aligned} \alpha &= \alpha_0 + \Delta\alpha \\ \Delta\alpha &= \arcsin\left(\frac{e_r \cdot \vec{W}_e}{|\vec{W}_e|}\right) \end{aligned} \tag{3.19}$$

An example of functions $C_L(\alpha)$ and $C_D(\alpha)$ is reported in Figure 3.3(a), while the related aerodynamic efficiency $E(\alpha) = C_L(\alpha)/C_D(\alpha)$ is reported in Figure 3.3(b). Such curves refer to a Clark–Y kite with aspect ratio (i.e. length of leading edge divided by kite width) equal to 3.19 (see Figure 3.4) and they have been obtained using CFD analysis with the STAR–CCM+® code (see [47]).

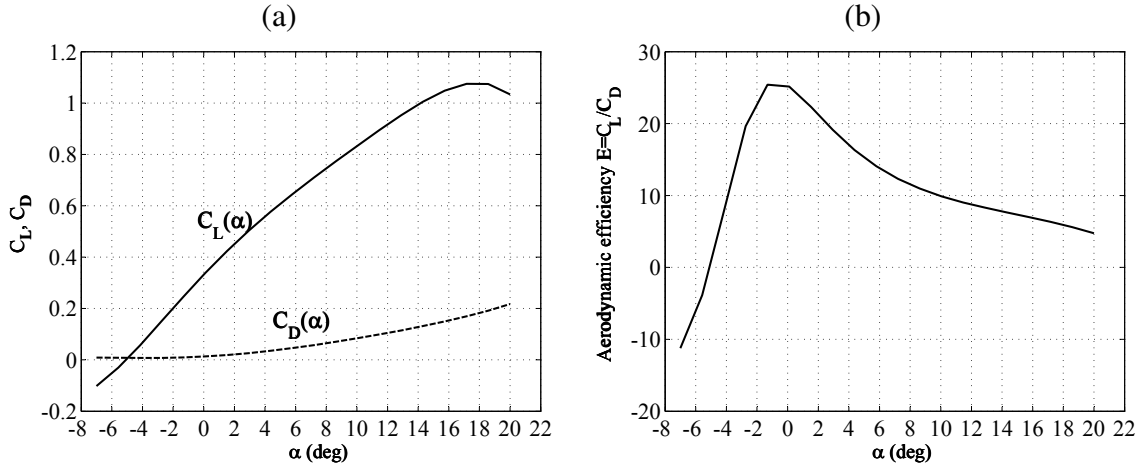

Figure 3.3. (a) Kite Lift coefficient C_L (solid) and drag coefficient C_D (dashed) as functions of the attack angle α. (b) Aerodynamic efficiency E as function of the attack angle α.

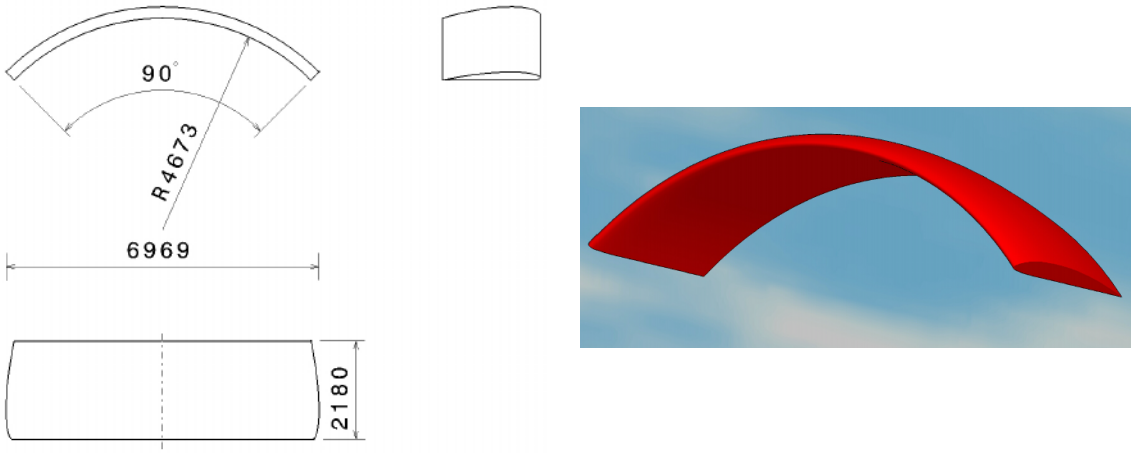

Figure 3.4. Geometrical characteristics of the Clark–Y kite considered for the CFD analysis to compute the aerodynamic lift and drag coefficients $C_L(\alpha)$ and $C_D(\alpha)$

3.1.4 Line forces

The lines influence the kite motion through their weight (see Section 3.1.1), their drag force $\vec{F}^{\text{c,aer}}$ and the traction force $F^{\text{c,trc}}$. An estimate of the drag of the lines has been considered in [42], where the overall angular momentum $\vec{M}_d = r\, e_r \times \vec{F}^{\text{c,aer}}$ exerted by the line drag force is computed by integrating, along the line length, the angular momentum given by the drag force acting on an infinitely small line segment:

$$\begin{aligned} \vec{M}_d &= \int_0^r \left(s\, e_r \times -\frac{\rho\, C_{D,l}\, d_l\, \cos(\Delta\alpha)}{2} \left(\frac{s\, |\vec{W}_e|}{r} \right)^2 \vec{x}_{\text{w}} \right) ds \\ &= r\, e_r \times -\frac{\rho\, C_{D,l}\, A_l\, \cos(\Delta\alpha)}{8} |\vec{W}_e|^2\, \vec{x}_{\text{w}} \end{aligned} \tag{3.20}$$

where $C_{D,l}$ is the line drag coefficient and $A_l \cos(\Delta\alpha) = r\, d_l \cos(\Delta\alpha)$ is the projection of the line front area on the plane perpendicular to the effective wind vector (see Figure 3.5). Note that in [42] the total front line area $A_l = r\, d_l$ is considered to compute M_d: such assumption is valid if the effective wind speed vector $\vec{W}_e$ is perpendicular to the kite lines, otherwise it leads to a conservative estimate of the line drag force. The line drag force is then computed as:

$$\vec{F}^{\text{c,aer}} = \begin{pmatrix} F_\theta^{\text{c,aer}} \\ F_\phi^{\text{c,aer}} \\ F_r^{\text{c,aer}} \end{pmatrix} = -\frac{\rho\, C_{D,l}\, A_l\, \cos(\Delta\alpha)}{8} |\vec{W}_e|^2\, \vec{x}_{\text{w}} \tag{3.21}$$

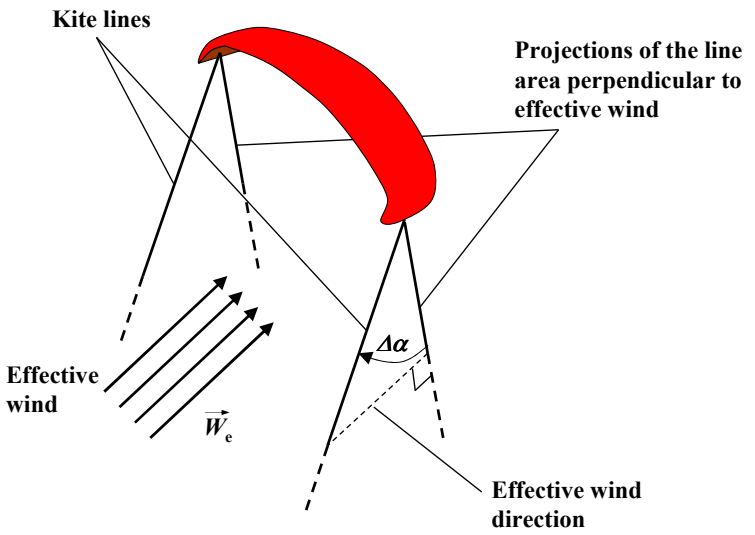

Figure 3.5. Detail of the kite lines and their projection on the plane perpendicular to the effective wind vector $\vec{W}_e$.

As regards the traction force $F^{\text{c,trc}}$, such a force is always directed along the local unit vector e_r and cannot be negative in equation (3.4), since the kite can only pull the lines. Moreover, $F^{\text{c,trc}}$ is measured by a force transducer on the KSU and, using a local controller of the electric drives, it is regulated in such a way that $\dot{r}(t) \approx \dot{r}_{\text{ref}}(t)$, where $\dot{r}_{\text{ref}}(t)$ is chosen to achieve a good compromise between high line traction force and high line winding speed. Basically, the stronger the wind, the higher the values of $\dot{r}_{\text{ref}}(t)$ that can be set obtaining high force values. It results that, in the case of HE–yoyo configuration, $F^{\text{c,trc}}(t) = F^{\text{c,trc}}(\theta,\phi,r,\dot{\theta},\dot{\phi},\dot{r},\dot{r}_{\text{ref}},\vec{W}_e)$, while for the HE–carousel configuration $F^{\text{c,trc}}(t) = F^{\text{c,trc}}(\theta,\phi,r,\Theta,\dot{\theta},\dot{\phi},\dot{r},\dot{\Theta},\dot{r}_{\text{ref}},\vec{W}_e)$.

3.1.5 Vehicle motion in HE–carousel configuration

In the case of HE–carousel configuration, the motion law of the KSU along the circular path of radius R has to be included too, with the following equation:

$$M\ddot{\Theta}R = F^{\text{c,trc}} \sin\theta \sin\phi - F^{\text{gen}} \tag{3.22}$$

where M is the total mass of the vehicle and the KSU and F^{gen} is the force given by the electric drives linked to the wheels. It is supposed that suitable kinematic constraints (e.g. rails) oppose to the centrifugal inertial force acting on the vehicle and to all the components of the line force, except for the one acting along the tangent to the vehicle path (i.e. $F^{\text{c,trc}} \sin\theta \sin\phi$). Note that any viscous term is neglected in equation (3.22), since the vehicle speed $\dot{\Theta}R$ is kept very low as it will be shown in Section 3.4. F^{gen} is positive when the kite is pulling the vehicle toward increasing Θ values, thus generating

energy, and it is negative when the electric drives are acting as a motors to drag the vehicle against the wind, when the kite is not able to generate a suitable pulling force. The force F^{gen} is calculated by a suitable local controller in order to keep the vehicle at constant angular speed $\dot{\Theta} = \dot{\Theta}_{\text{ref}}$.

3.1.6 Overall model equations and generated power

The model equations (3.3)–(3.22) describe the system dynamics in the form:

$$\dot{x}(t) = f(x(t),u(t),W_x(t),\dot{r}_{\text{ref}}(t),\dot{\Theta}_{\text{ref}}(t),\vec{W}_t(t)) \tag{3.23}$$

where $x(t) = [\theta(t)\ \phi(t)\ r(t)\ \Theta(t)\ \dot{\theta}(t)\ \dot{\phi}(t)\ \dot{r}(t)\ \dot{\Theta}(t)]^T$ are the model states and $u(t) = \psi(t)$ is the control input. Clearly, in the case of HE–yoyo configuration $\Theta = \dot{\Theta} = \dot{\Theta}_{\text{ref}} = 0$. All the model states are supposed to be measured or estimated, to be used for feedback control. The net mechanical power P generated (or spent) by the generator is the algebraic sum of the power generated (or spent) by unrolling/recovering the lines and by the vehicle movement:

$$P(t) = \dot{r}(t)F^{\text{c,trc}}(t) + \dot{\Theta}(t)\,R\,F^{\text{gen}}(t) \tag{3.24}$$

For the HE–yoyo configuration the term $\dot{\Theta}\,R\,F^{\text{gen}} = 0$ and generated mechanical power is only due to line unrolling.
Mechanical power is then converted into electric power by the drives linked to the drums of the KSU and (in the case of HE–carousel configuration) to the vehicle wheels. An overall efficiency $\eta_{\text{dtl}} < 1$ is considered to take into account the drive train losses, thus the generated electrical power can be computed as:

$$P_{\text{elt}}(t) = \eta_{\text{dtl}}\,P(t) \tag{3.25}$$

3.2 Wind speed model

The increase of wind speed with elevation is a key point in high–altitude wind power generation, since one of the main advantages of HAWE over wind turbines is that the kite flies at higher altitudes with respect to the 50–150 m of wind turbines (see Section 1.2.1), where stronger and more constant wind usually blows and, consequently, higher generated power values can be obtained. Thus, in numerical simulation studies it is important to consider a realistic nominal wind speed model $W_x(Z)$ (3.1), to increase the significance of the obtained results. Different functional forms for $W_x(Z)$ have been proposed in the literature (see [6] and the references therein): in this work, the following logarithmic wind shear model is considered:

$$W_x(Z) = W_0 \frac{\ln\left(\dfrac{Z}{Z_r}\right)}{\ln\left(\dfrac{Z_0}{Z_r}\right)} \tag{3.26}$$

where Z_0 is a reference elevation value and W_0 is the corresponding reference wind speed (i.e. $W_0 = W_x(Z_0)$), while Z_r is the roughness factor of the considered site. For a given site, parameters Z_0, W_0 and Z_r can be computed using a least square procedure applied to wind speed data collected at different altitudes using sounding stations. In particular, in this work the data measured at several locations between 1996 and 2006, retrieved from the database of the Earth System Research Laboratory of the National Oceanic & Atmospheric Administration [27] have been analyzed. The parameters of some of the computed wind shear models are resumed in Table 3.1. Figure 3.6 shows the wind shear model and the related measured data collected at De Bilt, in The Netherlands. It can be noted that the average wind speeds during winter months are higher than those measured in summer: this phenomenon occurs in every considered site. Such models will be

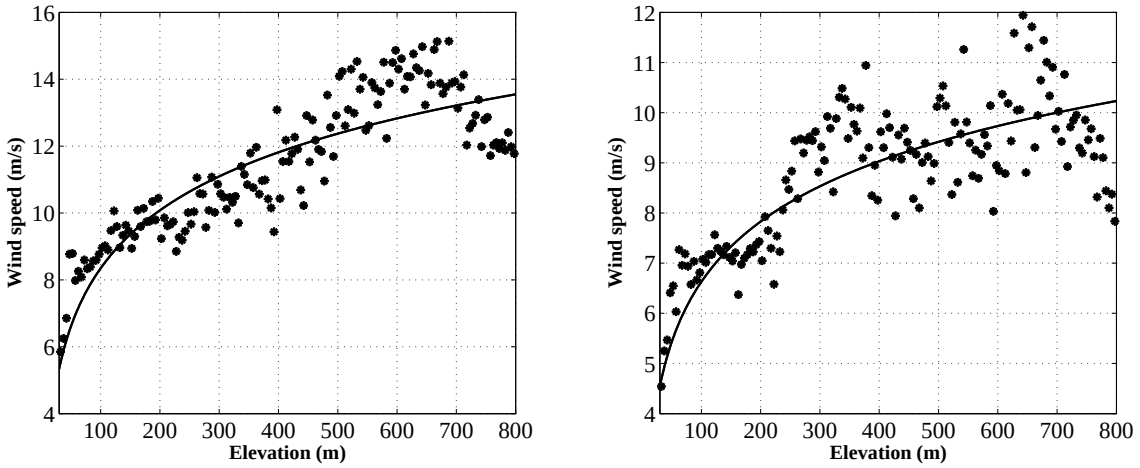

Figure 3.6. Wind shear model (solid line) and averaged experimental data (asterisks) related to the site of De Bilt, in The Netherlands, for winter (left) and summer (right) months

Table 3.1. Wind shear model parameters for some sites in Italy and The Netherlands

	Winter			**Summer**		
Site	Z_0 (m)	W_0 (m/s)	Z_r (m)	Z_0 (m)	W_0 (m/s)	Z_r (m)
Brindisi (Italy)	27.5	7.3	$7.0\,10^{-4}$	27.5	6.2	$5.0\,10^{-4}$
Cagliari (Italy)	27.5	6.7	$8.0\,10^{-4}$	32.5	6.6	$2.2\,10^{-6}$
Pratica di mare (Italy)	27.5	7.0	$7.0\,10^{-8}$	32.5	5.9	$7.0\,10^{-6}$
Trapani (Italy)	32.5	7.4	$6.0\,10^{-4}$	32.5	6.4	$3.2\,10^{-6}$
De Bilt (The Netherlands)	27.5	5.1	3.5	27.5	4.4	2.1

employed for the simulation studies of Section 3.4, regarding the power obtained by the HE–yoyo and HE–carousel generators, and for the Capacity Factor analyses of Chapter 6.

3.3 Nonlinear model predictive control application to HAWE

The control problem and related objectives are now described. As highlighted in Section 2.3, the main objective is to generate energy by a suitable control action on the kite. In order to accomplish this aim, a two–phase cycle has been designed for each generator configuration. A NMPC strategy is designed for each phase, according to its own cost function, state and input constraints and terminal conditions.
The control move computation is performed at discrete time instants defined on the basis of a suitably chosen sampling period Δ_t. At each sampling time $t_k = k\Delta_t$, $k \in \mathbb{N}$, the measured values of the state $x(t_k)$ and of the nominal wind speed $W_x(t_k)$ are used to compute the control move through the optimization of a performance index of the form:

$$J(U,t_k,T_p) = \int_{t_k}^{t_k+T_p} L(\tilde{x}(\tau),\tilde{u}(\tau),W_x(\tau),)d\tau \tag{3.27}$$

where $T_p = N_p\Delta_t$, $N_p \in \mathbb{N}$ is the prediction horizon, $\tilde{x}(\tau)$ is the state predicted inside the prediction horizon according to the state equation (3.23), using $\tilde{x}(t_k) = x(t_k)$ and the piecewise constant control input $\tilde{u}(t)$ belonging to the sequence $U = \{\tilde{u}(t)\}, t \in [t_k,t_{k+T_p}]$ defined as:

$$\tilde{u}(t) = \begin{cases} \bar{u}_i, \forall t \in [t_i,t_{i+1}], i = k,\ldots,k+T_c-1 \\ \bar{u}_{k+T_c-1}, \forall t \in [t_i,t_{i+1}], i = k+T_c,\ldots,k+T_p-1 \end{cases} \tag{3.28}$$

where $T_c = N_c\Delta_t$, $N_c \in \mathbb{N}$, $N_c \leq N_p$ is the control horizon.
The function $L(\cdot)$ in (3.27) is suitably defined on the basis of the performances to be achieved in the considered operating phase. Moreover, in order to take into account physical limitations on both the kite behaviour and the control input ψ in the different phases, constraints of the form $\tilde{x}(t) \in \mathbb{X}$, $\tilde{u}(t) \in \mathbb{U}$ have been included too.
Thus the predictive control law is computed using a receding horizon strategy:

1. At time instant t_k, get $x(t_k)$.
2. Solve the optimization problem:

$$\min_U \quad J(U,t_k,T_p) \tag{3.29a}$$
$$\text{subject to} \tag{3.29b}$$
$$\tilde{x}(t_k) = x(t_k) \tag{3.29c}$$
$$\dot{\tilde{x}}(t) = f(\tilde{x}(t),\tilde{u}(t),\dot{r}_{\text{ref}}(t),\dot{\Theta}_{\text{ref}}(t),W_x(t)) \ \forall t \in (t_k,t_{k+T_p}] \tag{3.29d}$$
$$\tilde{x}(t) \in \mathbb{X},\ \tilde{u}(t) \in \mathbb{U} \ \forall t \in [t_k,t_{k+T_p}] \tag{3.29e}$$

3. Apply the first element of the solution sequence U to the optimization problem as the actual control action $u(t_k) = \tilde{u}(t_k)$.

4. Repeat the whole procedure at the next sampling time t_{k+1}.

Therefore the predictive controller results to be a nonlinear static function of the system state x, the nominal measured wind speed W_x and the reference speed values $\dot{r}_{\text{ref}}$, $\dot{\Theta}_{\text{ref}}$ imposed to the local drive controllers of the KSU and of the vehicle in the HE–carousel (see Sections 3.1.4 and 3.1.5):

$$\psi(t_k) = \kappa(x(t_k),W_x(t_k),\dot{r}_{\text{ref}},\dot{\Theta}_{\text{ref}}(t_k)) = \kappa(w(t_k)) \tag{3.30}$$

As a matter of fact, an efficient NMPC implementation is required to ensure that the control move is computed within the employed sampling time, of the order of 0.2 s. This is obtained using the efficient implementation techniques based on Set Membership approximation theory (see Part II of this dissertation). Such techniques allow to compute off–line an approximated control law $\kappa^{\text{SM}}(w) \approx \kappa(w)$, with guaranteed performance and stabilizing properties, whose on–line computational load is lower than the one required to solve the optimization problem.
The cost functions and state and input constraints considered for the HE–yoyo and HE–carousel configurations are now presented.

3.3.1 HE–yoyo cost and constraint functions

In the HE–yoyo configuration, the traction phase starts when the following conditions are satisfied:

$$\begin{array}{l} \underline{\theta}_I \leq \theta(t) \leq \overline{\theta}_I \\ |\phi(t)| \leq \overline{\phi}_I \\ \underline{r}_I \leq r(t) \leq \overline{r}_I \end{array} \tag{3.31}$$

with

$$\begin{array}{l} 0 < \underline{\theta}_I < \overline{\theta}_I < \pi/2 \\ 0 < \overline{\phi}_I < \pi/2 \end{array} \tag{3.32}$$

Roughly speaking, the traction phase begins when the kite is flying in a symmetric zone with respect to the X axis, at an altitude Z_I such that $\underline{r}_I \cos\overline{\theta}_I \leq Z_I \leq \overline{r}_I \cos\underline{\theta}_I$.
When the traction phase starts, a positive value $\overline{\dot{r}}$ of $\dot{r}_{\text{ref}}$ is set so that the kite flies with increasing values of r while applying a traction force $F^{\text{c,trc}}$ on the lines, thus generating energy. The value $\overline{\dot{r}}$ is chosen to achieve high power values and depends on the wind speed: basically, the stronger the wind, the higher the values of $\overline{\dot{r}}$ that can be set obtaining high generated power values (see Chapter 4 for more details on the optimal value of $\dot{r}$).
As anticipated, control system objective in the traction phase is to maximize the energy generated in the interval $[t_k,t_k + T_P]$. Since the generated electrical power (3.25) at each instant is $P_{\text{elt}}(t) = \eta_{\text{dtl}}\dot{r}(t)F^{\text{c,trc}}(t)$, the following cost function is chosen to be minimized in MPC design (3.29):

$$J(t_k) = -\int_{t_k}^{t_k+T_p} (\eta_{\text{dtl}}\dot{r}(\tau)F^{\text{c,trc}}(\tau))d\tau \tag{3.33}$$

During the whole phase the following state constraint is considered to keep the kite sufficiently far from the ground:

$$\theta(t) \leq \overline{\theta} \tag{3.34}$$

with $\overline{\theta} < \pi/2$ rad. Actuator physical limitations give rise to the constraints:

$$\begin{array}{l} |\psi(t)| \leq \overline{\psi} \\ |\dot{\psi}(t)| \leq \overline{\dot{\psi}} \end{array} \tag{3.35}$$

As a matter of fact, other technical constraints are added to force the kite to go along "figure eight" trajectories rather than circular ones, in order to prevent the lines from wrapping one around the other. Such constraints force the kite ϕ angle to oscillate with double period with respect to θ angle, thus generating the proper kite trajectory.
To complete the traction phase description, ending conditions have to be introduced. Each kite line is initially rolled around a drum and unrolls while the kite gets farther. When r reaches a maximal value $\overline{r}$ it is needed to wrap the lines back, in order to make the HE–yoyo able to start a new cycle. Therefore, when the following condition is reached the traction phase ends and the passive phase can start:

$$r(t) \geq \overline{r} \tag{3.36}$$

As described in Section 2.3.1, two possible alternative maneuvers can be employed in the passive phase.

I) Low power maneuver. The low power maneuver has been divided into three sub–phases which allow to wrap back the lines using the least amount of energy, thus maximizing the net energy gain of the whole cycle.
In the first sub–phase, $\dot{r}_{\text{ref}}(t)$ is chosen to smoothly decrease towards zero from value $\overline{\dot{r}}$. The control objective is to move the kite in a zone with low values of θ and high values of $|\phi|$, where effective wind speed $\vec{W}_e$ and force $F^{\text{c,trc}}$ are low and the kite is ready to be recovered with low energy expense. Positive values $\overline{\theta}_{II}$ and $\underline{\phi}_{II} < \pi/2$ of θ and ϕ respectively are introduced to identify this zone. The following cost function is considered:

$$J(t_k) = \int_{t_k}^{t_k+T_p} \theta^2(\tau) + \left(|\phi(\tau)| - \pi/2\right)^2 d\tau \tag{3.37}$$

Once the following condition is reached:

$$\begin{array}{l} |\phi(t)| \geq \underline{\phi}_{II} \\ \theta(t) \leq \overline{\theta}_{II} \end{array} \tag{3.38}$$

the first sub–phase ends.
Then, $\dot{r}_{\text{ref}}(t)$ is chosen to smoothly decrease from zero to a negative constant value

$\underline{\dot{r}}$. Such a value is chosen to give a good compromise between high winding back speed and low $F^{\text{c,trc}}$ values. During this passive sub–phase, the control objective is to minimize the energy spent to wind back the lines, thus the following cost function is considered:

$$J(t_k) = \int_{t_k}^{t_k+T_p} |\dot{r}(\tau)| F^{\text{c,trc}}(\tau) d\tau \tag{3.39}$$

The second sub–phase ends when the following condition is satisfied:

$$\underline{r}_I \leq r(t) \leq \overline{r}_I \tag{3.40}$$

which means when the line length r is among the possible traction phase initial state values. Then, the third passive sub–phase begins and $\dot{r}_{\text{ref}}(t)$ is chosen to smoothly increase towards zero from the negative value $\underline{\dot{r}}$. Control objective is to move the kite in the traction phase starting zone, expressed by (3.31). Cost function $J(t_k)$ is set as follows:

$$J(t_k) = \int_{t_k}^{t_k+T_p} \left(|\theta(\tau) - \theta_1| + |\phi(\tau)|\right) d\tau \tag{3.41}$$

where $\theta_1 = (\underline{\theta}_I + \overline{\theta}_I)/2$.

II) Wing glide maneuver. The wing glide maneuver is divided into three sub–phases. In the first one, $\dot{r}_{\text{ref}}(t)$ is chosen to smoothly decrease towards zero from value $\overline{\dot{r}}$. The control objective is to move the kite in a zone with lower values of θ to prepare for the subsequent wing glide. A positive values $\overline{\theta}_{III}$ of θ is introduced to identify this zone. The following cost function is considered:

$$J(t_k) = \int_{t_k}^{t_k+T_p} \theta^2(\tau) d\tau \tag{3.42}$$

Once the following condition is reached:

$$\theta(t) \leq \overline{\theta}_{III} \tag{3.43}$$

the first sub–phase ends. In the second sub–phase, a preliminary maneuver is performed, during which a large length difference (approximately equal to the kite wingspan) is issued between the two cables by pulling them in subsequent order. This way, the airfoil's lift coefficient C_L drops to a (low) value $C_{L,WG}$ (while the drag coefficient increases to a value $C_{D,WG} > C_D$) and, consequently, also the traction force F_c is reduced, making it possible to wind back the lines with small energy expense. The duration of the described preliminary phase is quite short and the control system is only required to keep the airfoil stability and avoid constraint violation. Then, the reference winding speed $\dot{r}_{\text{ref}}(t)$ is chosen to smoothly decrease from zero to a negative constant value $\underline{\dot{r}}$. Such a value is chosen to give a good

compromise between high winding back speed and low $F^{\text{c,trc}}$ values. During this passive sub–phase, control objective is to minimize the energy spent to wind back the lines, thus the following cost function is considered:

$$J(t_k) = \int_{t_k}^{t_k+T_p} |\dot{r}(\tau)| F^{\text{c,trc}}(\tau) d\tau \tag{3.44}$$

The second sub–phase ends when the following condition is satisfied:

$$\underline{r}_I \leq r(t) \leq \overline{r}_I \tag{3.45}$$

which means when the line length r is among the possible traction phase initial state values. Then, the third passive sub–phase begins and $\dot{r}_{\text{ref}}(t)$ is chosen to smoothly increase towards zero from the negative value $\underline{\dot{r}}$. Control objective is to move the kite in the traction phase starting zone, expressed by (3.31). Cost function $J(t_k)$ is set as follows:

$$J(t_k) = \int_{t_k}^{t_k+T_p} \left(|\theta(\tau) - \theta_1| + |\phi(\tau)|\right) d\tau \tag{3.46}$$

where $\theta_1 = (\underline{\theta}_I + \overline{\theta}_I)/2$.

Independently on the employed recovery maneuver, the ending conditions for the whole passive phase coincide with the starting conditions of the traction phase. Moreover, during the whole passive phase the state constraint expressed by (3.34) and the input constraints (3.35) are considered in the MPC optimization problems.

3.3.2 HE–carousel cost and constraint functions

In the HE–carousel configuration, the force F^{gen} applied by the electric drives to the vehicle wheels is such that the vehicle moves at reference angular speed $\dot{\Theta}_{\text{ref}}$, which is kept constant and it is chosen in order to optimize the net energy generated in the cycle. Since the angular speed is constant, each kite placed on the HE–carousel can be controlled independently from the others, provided that their respective trajectories are such that their lines never collide. Thus, a single vehicle is considered in the following. The cost and constraint functions employed in the two different strategies described in Section 2.3.2 are now presented.

I) Constant line length. As described in Section 2.3.2, the operation of a HE–carousel with constant line length, equal to a chosen value r_{const}, is divided into two phases, denoted as the traction and the passive ones. In the traction phase, the aim is to obtain as much energy as possible from the wind stream. The traction phase begins when the vehicle angular position Θ with respect to the nominal wind vector $\vec{W}_0$ is

such that the kite can pull the vehicle (see Figure 2.7). Thus, the following traction phase initial condition is considered:

$$\Theta(t) \geq \Theta_3 \tag{3.47}$$

Control system objective adopted in the traction phase is to maximize the energy generated in the interval $[t_k,t_k + T_P]$, while satisfying constraints concerning state and input values. Power (3.25) generated at each instant is $P = \eta_{\text{dtl}}\dot{\Theta}\ T^{\text{gen}}$, since $\dot{r} = 0$ (i.e. constant line length is used), thus the following cost function is chosen to be minimized in MPC design (3.29):

$$J(t_k) = -\int_{t_k}^{t_k+T_p} \Big(\eta_{\text{dtl}}\dot{\Theta}(\tau)T^{\text{gen}}(\tau)\Big)d\tau \tag{3.48}$$

During the whole phase the following state constraint is considered to keep the kite sufficiently far from the ground:

$$\theta(t) \leq \overline{\theta} \tag{3.49}$$

with $\overline{\theta} < \pi/2$. Actuator physical limitations give rise to the constraints:

$$\begin{array}{l} |\psi(t)| \leq \overline{\psi} \\ |\dot{\psi}(t)| \leq \overline{\dot{\psi}} \end{array} \tag{3.50}$$

As a matter of fact, other technical constraints have been added to force the kite to go along "figure eight" trajectories rather than circular ones as they cause the winding of the lines. Such constraints force the kite ϕ angle to oscillate with double period with respect to θ angle, thus generating the proper kite trajectory. The traction phase ends when the vehicle angular position is such that the kite is no more able to pull the vehicle:

$$\Theta(t) \geq \Theta_0 \tag{3.51}$$

with $\Theta_0 \leq \pi/2$ according to Figure 2.7. When the condition (3.51) is reached the passive phase can start. During this phase, the electric generators act as motors to drag the vehicle between angles Θ_0 and Θ_3. Meanwhile, the kite is moved in a proper position in order to start another traction phase. The passive phase has been divided into three sub–phases. Transitions between each two subsequent drag sub–phases are marked by suitable values of the vehicle angular position, Θ_1 and Θ_2, which are chosen in order to minimize the total energy spent during the phase. In the first sub–phase, the control objective is to move the kite in a zone with low values of θ, where effective wind speed $\vec{W}_e$ and pulling force F^c component in plane (X,Y) (i.e. $F^c \sin\theta \sin\phi$) are much lower. A positive value θ_I of θ is introduced to identify this zone. The following cost function is considered:

$$J(t_k) = \int_{t_k}^{t_k+T_p} (\theta(\tau) - \theta_I)^2 d\tau \tag{3.52}$$

Once the following condition is reached:

$$\Theta \geq \Theta_1 \tag{3.53}$$

the first passive phase part ends. In the second drag sub–phase, control objective is to change the kite angular position ϕ toward values which are suitable to begin the traction phase. Thus, a value ϕ_I is introduced such that

$$\pi/2 < \phi_I < \pi \tag{3.54}$$

and the following cost function is considered:

$$J(t_k) = \int_{t_k}^{t_k+T_p} (\phi(\tau) - \phi_I)^2 d\tau \tag{3.55}$$

The second sub–phase ends when the following condition is satisfied:

$$\Theta \geq \Theta_2 \tag{3.56}$$

Then, the third drag sub–phase begins: control objective is to increase the kite angle θ toward a suitable value θ_{II} such that:

$$\pi/4 < \theta_{II} < \pi/2 \tag{3.57}$$

thus preparing the generator for the following traction phase. Cost function $J(t_k)$ is set as follows:

$$J(t_k) = \int_{t_k}^{t_k+T_p} (\theta(\tau) - \theta_{II})^2 d\tau \tag{3.58}$$

Ending conditions for the whole passive phase coincide with starting conditions for the traction phase (3.47). During the whole passive phase the state constraint expressed by (3.49) and the input constraints (3.50) are considered in the control optimization problems.

II) Variable line length. The HE–carousel operation with variable line length has been conceived to generate energy also when the vehicle is moving against the wind, by exploiting the line unrolling (see Section 2.3.2). The related operating phases are denoted as the traction and the unroll ones. The traction phase begins when the KSU angular position Θ is such that, with respect to the nominal wind vector $\vec{W}_0$, the kite can pull the vehicle (see Figure 2.7). Thus, the following traction phase initial condition is considered:

$$\Theta(t) \geq \Theta_1 \tag{3.59}$$

At the beginning of the traction phase, the line length is equal to a value r_1 resulting from the previous unroll phase (see Section 2.3.2). Thus, a value $\dot{r}_{\text{trc}} < 0$ for

reference speed $\dot{r}_{\text{ref}}$ is set during the traction phase in order to roll back the lines and begin the next unroll phase with a suitable line length value r_0. Recalling that electrical power (3.25) obtained at each instant is the sum of the effects given by line unrolling and vehicle movement, the following cost function is chosen to be minimized in MPC design (3.29):

$$J(t_k) = -\int_{t_k}^{t_k+T_p} \Big(\eta_{\text{dtl}}\dot{r}(\tau)F^{\text{c,trc}}(\tau) + \eta_{\text{dtl}}R\dot{\Theta}(\tau)F^{\text{gen}}(\tau)\Big)d\tau \tag{3.60}$$

The traction phase ends when the KSU angular position Θ is such that the kite is no more longer able to pull the vehicle:

$$\Theta(t) \geq \Theta_0 \tag{3.61}$$

with $\Theta_0 \leq \pi/2$ according to Figure 2.7.
When condition (3.61) is reached, the unroll phase starts and the electric drives linked to the vehicle wheels act as motors to drag the KSU between angles Θ_0 and Θ_1. Meanwhile, a suitable course of the reference $\dot{r}_{\text{ref}}$ is set to make the unrolling speed $\dot{r}$ smoothly reach the positive constant value $\dot{r}_{\text{c}}$, so that energy can be generated while the KSU moves against the nominal wind flow. During the unroll phase, the line length increases from the starting value r_0 to a final value $r_1 > r_0$. As regards the choice of $\dot{r}_{\text{c}}$, note that the mechanical power which opposes to the vehicle movement due to the line traction force is:

$$P_{\text{res}}(t) = |\eta_{\text{dtl}}R\dot{\Theta}(t)\, F^{\text{c,trc}}(t)\sin\theta(t)\sin\phi(t)| \leq |\eta_{\text{dtl}}R\dot{\Theta}(t)\, F^{\text{c,trc}}(t)| \tag{3.62}$$

The power generated by line unrolling is:

$$P_{\text{gen}}(t) = |\dot{r}(t)F^{\text{c,trc}}(t)| \tag{3.63}$$

thus if $\dot{r}(t) > R\dot{\Theta}(t)$ the net power $P_{\text{gen}}(t) - P_{\text{res}}(t)$ is positive and as a first approximation, without considering friction forces and with the same efficiency in electric power generation due to line unrolling and due to the vehicle movement, energy is generated. Therefore, a good choice for $\dot{r}_{\text{c}}$ would be:

$$\dot{r}_{\text{c}} > R\dot{\Theta}_{\text{ref}} \tag{3.64}$$

However, the reference unroll speed $\dot{r}_{\text{c}}$ should not be too high in order to keep the final line length r_1 below a reasonable value $\overline{r}$ (i.e. 1000–1200 m). Since $r_1 \simeq r_0 + \dot{r}_{\text{c}}R(\Theta_1 - \Theta_0)/(R\dot{\Theta}_{\text{ref}})$, the following choice is made:

$$\dot{r}_{\text{c}} \simeq \frac{\overline{r} - r_0}{(\Theta_1 - \Theta_0)}\dot{\Theta}_{\text{ref}} \tag{3.65}$$

The cost function considered in MPC design for the unroll phase is the same as for the traction phase (3.60), to maximize the net generated energy:

$$J(t_k) = -\int_{t_k}^{t_k+T_p} \Big(\dot{r}(\tau)F^{\text{c,trc}}(\tau) + R\dot{\Theta}(\tau)F^{\text{gen}}(\tau)\Big)d\tau \tag{3.66}$$

During the whole HE–carousel cycle with variable line length, the constraints (3.49)–(3.50) are considered, as well as other technical constraints to force the kite to go along "figure eight", as already described.

3.3.3 Fast model predictive control of HAWE

As already anticipated, an efficient implementation of MPC is needed in HAWE to perform the control computation within the chosen sampling interval. In particular, Set Membership approximation techniques, studied and developed in Part II of this dissertation, are employed to implement the designed predictive control laws for HAWE generators. The adopted approximation method is denoted as the "global" optimal SM technique and it is now briefly resumed (for complete analyses and details about the theoretical properties of this approach, see Section Part II of this thesis).
The main idea is to derive, using SM methodology, an approximating function κ^{SM} of the exact predictive control law $\psi(t_k) = \kappa(w(t_k))$ (3.30). Such approximating function guarantees a given degree of accuracy and its computation is faster than solving the constrained optimization problem (3.29) considered in MPC design.
To be more specific, consider a bounded region $W \subset \mathbb{R}^{11}$ where w can evolve (indeed, with the HE–yoyo configuration the subset $W \subset \mathbb{R}^8$, since variables Θ, $\dot{\Theta}$ and $\dot{\Theta}_{\text{ref}}$ are not present in the regressor w). A number ν of values of $\kappa(w)$ may be derived by performing off–line the MPC procedure starting from a set of values $W_\nu = \{\tilde{w}_k \in W,\ k = 1,\dots,\nu\}$, so that:

$$\tilde{\psi}_k = \kappa(\tilde{w}_k),\ k = 1,\dots,\nu \tag{3.67}$$

The aim is to derive, from these known values of $\tilde{\psi}_k$ and $\tilde{w}_k$ and from known properties of κ, an approximation κ^{SM} of κ and a measure of the approximation error. In order to achieve this goal, a Set Membership approach is employed. Basic to this approach is the observation that in order to derive a measure of the approximation error achieved by any method, the knowledge of $\kappa(\tilde{w}_k),\quad k = 1,\dots,\nu$ is not sufficient, but some additional information on κ is needed. In the case of HAWE control it is assumed that $\kappa \in \mathcal{F}_\gamma$, where $\mathcal{F}_\gamma$ is the set of all Lipschitz functions on W, with Lipschitz constant γ. An additional information to be used in the approximation is the input saturation condition giving $|\kappa(w)| \leq \bar{\psi}$. These information on function κ, combined with the knowledge of the value of the function at the points $\tilde{w}_k \in W,\ k = 1,\dots,\nu$, allows to conclude that $\kappa \in FFS$, where the set FFS (Feasible Functions Set), defined as:

$$FFS = \{\kappa \in \mathcal{F}_\gamma : |\kappa(w)| \leq \bar{\psi}; \kappa(\tilde{w}_k) = \tilde{\psi}_k,\ k = 1,\dots,\nu\} \tag{3.68}$$

summarizes the overall information on κ. Making use of such overall information, Set Membership theory allows to derive an optimal estimate of κ and its approximation error, in term of the $L_p(W)$ norm defined as $\|\kappa\|_p \doteq \left[\int_W |\kappa(w)|^p \, dw\right]^{\frac{1}{p}}$, $p \in [1,\infty)$ and $\|\kappa\|_\infty \doteq$ess-$\sup_{w\in W} |\kappa(w)|$. For given $\kappa^{\text{SM}} \approx \kappa$, the related L_p approximation error is $\|\kappa - \hat{\kappa}\|_p$. This error cannot be exactly computed, but its tightest bound is given by:

$$\left\|\kappa - \kappa^{\text{SM}}\right\|_p \leq \sup_{\tilde{\kappa}\in FFS} \left\|\tilde{\kappa} - \kappa^{\text{SM}}\right\|_p \doteq E(\kappa^{\text{SM}}) \tag{3.69}$$

where $E(\kappa^{\text{SM}})$ is called (guaranteed) *approximation error*.
A function κ^{OPT} is called an *optimal approximation* if:

$$E(\kappa^{\text{OPT}}) = \inf_{\hat{\kappa}} E(\kappa^{\text{SM}}) \doteq r_p$$

The quantity r_p, called *radius of information*, gives the minimal L_p approximation error that can be guaranteed.
Define:

$$\begin{aligned} \overline{\kappa}(w) &\doteq \min\left[\bar{\psi}, \min_{k=1,\ldots,\nu}\left(\tilde{\psi}_k + \gamma\|w - \tilde{w}_k\|\right)\right] \\ \underline{\kappa}(w) &\doteq \max\left[-\bar{\psi}, \max_{k=1,\ldots,\nu}\left(\tilde{\psi}_k - \gamma\|w - \tilde{w}_k\|\right)\right] \end{aligned} \tag{3.70}$$

It results that the function:

$$\kappa^{\text{OPT}}(w) = \frac{1}{2}[\overline{\kappa}(w) + \underline{\kappa}(w)] \tag{3.71}$$

is an optimal approximation for any $L_p(W)$ norm, with $p \in [1,\infty]$ (see Section 11.1). Moreover, the approximation error of κ^{OPT} is pointwise bounded as:

$$|\kappa(w) - \kappa^*(w)| \leq \frac{1}{2}|\overline{\kappa}(w) - \underline{\kappa}(w)|, \forall w \in W$$

and it is pointwise convergent to zero:

$$\lim_{\nu\to\infty} |\kappa(w) - \kappa^{\text{OPT}}(w)| = 0, \forall w \in W \tag{3.72}$$

Thus, evaluating $\sup_{w\in W} |\overline{\kappa}(w) - \underline{\kappa}(w)|$, it is possible to decide if the chosen ν is sufficient to achieve a desired accuracy in the estimation of κ or if ν has to be increased.
An estimate $\widehat{\gamma}$ of γ can be derived as follows:

$$\widehat{\gamma} = \inf_{\gamma:\overline{\kappa}(\tilde{w}_k)\geq\tilde{\psi}_k,\ k=1,\ldots,\nu} \gamma \tag{3.73}$$

Such estimate is convergent to γ:

$$\lim_{\nu\to\infty} \widehat{\gamma} = \gamma \tag{3.74}$$

Note that convergence results (3.72) and (3.74) hold if $\lim_{\nu\to\infty} d(W_\nu,W) = 0$, where $d(W_\nu,W)$ is the Hausdorff distance between sets W_ν and W (see Chapters 8–9). Such a condition is satisfied if, for example, W_ν is obtained by uniform gridding of W.
Thus, the approximated MPC control can be implemented on–line, by simply evaluating the function $\kappa^{\text{OPT}}(w_{t_k})$ at each sampling time:

$$\psi_{t_k} = \kappa^{\text{OPT}}(w_{t_k})$$

Indeed, as ν increases, the approximation error decreases at the cost of increased computation time and memory usage. Thus, a tradeoff between approximation accuracy, computational efficiency and memory requirements have to be issued. This can be also achieved, other than by changing the value of ν, by using one of the other techniques developed in this dissertation and described in Chapters 11–12.

3.4 Simulation results

This Section includes some of the simulation results obtained with the described HE–yoyo and HE–carousel models and the related control strategies (more results can be found in [9, 10, 11, 12, 13, 14]). In all of the presented simulation tests, the same kite and cable characteristics and nominal wind speed profile are used. In particular, Table 3.2 shows the numerical values of the model parameters: a 500–m^2 kite is considered. The functions employed to compute the aerodynamic lift and drag coefficients are showed in Figure 3.7. The cable diameter has been dimensioned, through trial–and–error procedures, in order to

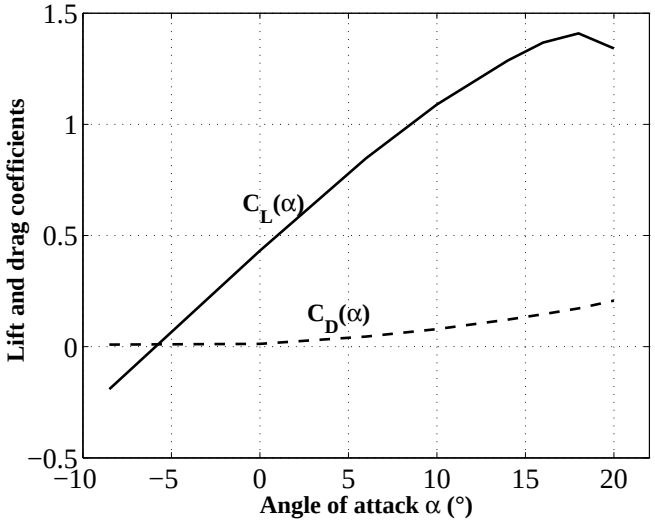

Figure 3.7. Lift and drag coefficients employed in the numerical simulations, as functions of the attack angle α.

support the traction forces generated by the considered kite, according to the breaking load characteristic of the polyethylene fiber composing the lines (see Section 5.2), reported in Figure 3.8. A safety coefficient of 1.2 has been considered in the dimensioning.

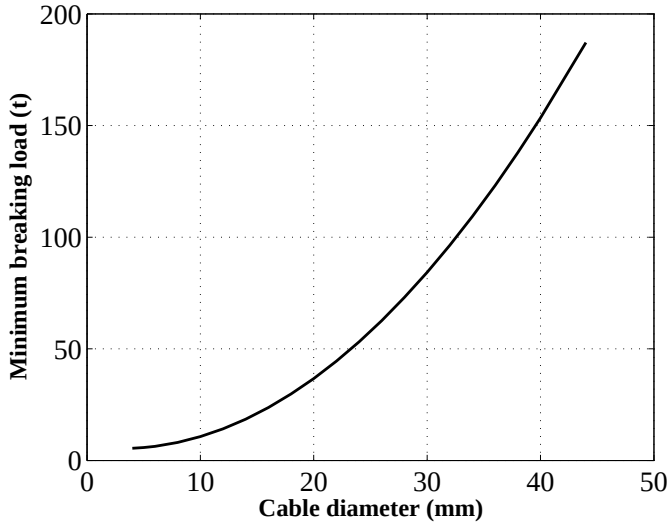

Figure 3.8. Minimum breaking load of the cable as a function of its diameter.

Table 3.2. Model parameters employed in the simulation tests of HAWE

m	300 HE	Kite mass
A	500 m^2	Characteristic area
d_l	0.03 m	Diameter of a single line
ρ_l	970 HE/m^3	Line density
$C_{L,WG}$	0.1	Kite lift coefficient during wing glide maneuver
$C_{D,WG}$	0.5	Kite drag coefficient during wing glide maneuver
$C_{D,l}$	1.2	Line drag coefficient
α_0	3.5°	Base angle of attack
ρ	1.2 HE/m^3	Air density
η_{dtl}	0.8	Drive train efficiency

As regards the nominal wind speed, the profile employed in the simulation is given by the wind shear model (3.26), computed in Section 3.2 considering the data collected at De Bilt airport during the summer months (i.e. with $Z_0 = 27.5\,\text{m}$, $Z_r = 2.1\,\text{m}$ and $W_0 = 4.38\,\text{m/s}$, see Table 3.1 and Figure 3.6). Moreover, uniformly distributed random wind turbulence $\vec{W}_t$ has also been introduced, with maximum absolute value along each direction equal to 3 m/s, i.e. about 33% of the nominal wind speed at 400 m of altitude.

3.4.1 HE–yoyo configuration

The HE–yoyo configuration has been tested in simulation using either the low power maneuver or the wing glide maneuver.

I) HE–yoyo with low power recovery maneuver. The results related to three complete cycles are reported. The numerical values of the parameters and constraints that define the operational cycle and the controller (introduced in Sections 2.3.1 and 3.3.1) are reported in Table 3.3. Figure 3.9(a) shows the obtained course of the line length,

Table 3.3. HE–yoyo configuration with low power maneuver: state and input constraints, cycle starting and ending conditions and control parameters.

θ_I	55°	Traction phase starting conditions
ϕ_I	45°	
$\underline{r}$	550 m	
$\overline{r}$	900 m	1st passive sub–phase starting conditions
$\underline{\phi}_{II}$	45°	2nd passive sub-phase starting conditions
$\overline{\theta}_{II}$	20°	
$\overline{\theta}$	75°	State constraint
$\overline{\psi}$	6°	Input constraints
$\overline{\dot{\psi}}$	20°/s	
$\overline{\dot{r}}$	1.8 m/s	Traction phase reference $\dot{r}_{\text{ref}}$
$\underline{\dot{r}}$	-2.0 m/s	Passive phase reference $\dot{r}_{\text{ref}}$
T_c	0.2 s	Sample time
N_c	1 steps	Control horizon
N_p	10 steps	Prediction horizon

which is kept between 550 m and 910 m. The kite trajectory during three complete HE–yoyo cycles is reported in Figure 3.9(b). The kite follows "figure eight" orbits during the traction phase, thus preventing line entangling. The kite elevation *Z* goes from 200 m to 400 m during the traction phase, corresponding to a mean value of $\theta(t)$ equal to 70°, while the lateral angle $\phi(t)$ oscillates between $\pm 20°$ with an average value of zero. Indeed, the kite flies fast in crosswind direction during the traction phase: as indicated in [8] and as it will be pointed out in Chapter 4, such a way of flying is the one that maximizes the traction forces on the cables. Note that the kite trajectory is not imposed a priori here, but it is a result of the choice of the cost function in the MPC control design, i.e. to maximize the generated energy. The power generated in the simulation is reported in Figure 3.10(a): the mean value is 1.45 MW. Note that the considered wind turbulence, though quite high does not cause system instability, showing the control system robustness. The course of the effective wind speed magnitude $|\vec{W}_e|$ is reported in Figure 3.10(b): mean values of

280 km/h during the traction phase and 95 km/h during the passive phase are obtained. Note that in a commercial 2–MW wind turbine with a 90–m diameter rotor, whose nominal rotor speed is 14.9 rpm (see [48]), the blade tip has an absolute tangential speed of about 70 m/s. Considering a wind flow of 12 m/s perpendicular to the rotor, the resulting effective wind speed on the outer part of the blade is equal to about 71 m/s, i.e. 255 km/h. Such a value is quite similar to that obtained by the kite in the performed simulation tests, according to the HAWE concept (see Figure 2.1 in Chapter 2) The courses of the kite attack angle and consequent lift and

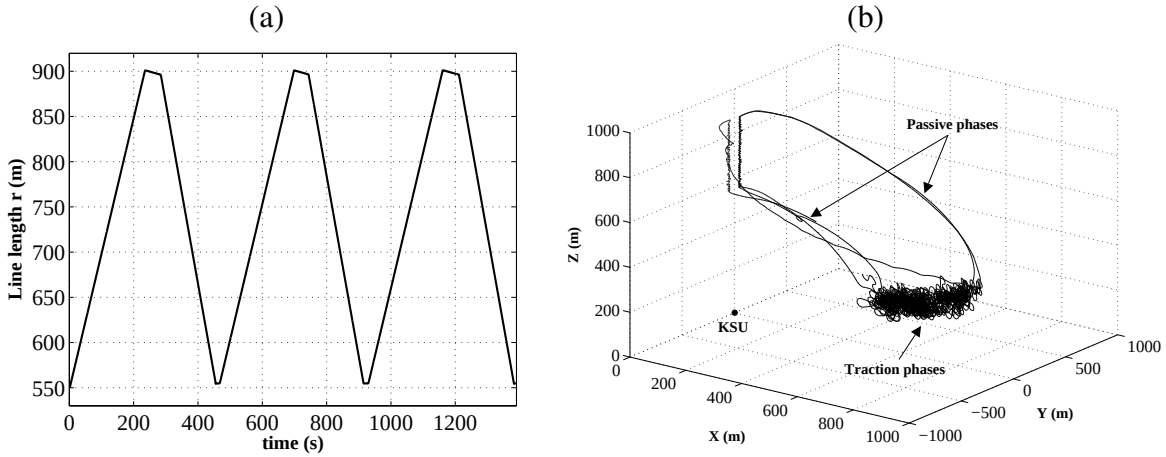

Figure 3.9. (a) Line length $r(t)$ and (b) kite trajectory during three complete HE–yoyo cycles with low power recovery maneuver and random wind disturbances.

drag coefficients are reported in Figure 3.11(a)–(b). The related kite aerodynamic efficiency is between 13 and 16 in the traction phases, with a mean value of 13.8.

II) HE–yoyo with wing glide recovery maneuver. The results related to three complete cycles are reported. The numerical values of the parameters and constraints that define the operational cycle and the controller (introduced in Sections 2.3.1 and 3.3.1) are reported in Table 3.4. The obtained line length and kite trajectory are reported in Figures 3.12(a) and 3.12(b) respectively. The line length is kept between 850 m and 910 m, making a single cycle much shorter than that obtained with the low power maneuver (also considering the higher winding back speed of -8 m/s, see Tables 3.3–3.4). As regards the kite trajectory, it can be seen that the kite follows "figure eight" orbits during the traction phase and that the kite elevation *Z* goes from about 350 m to 410 m during the traction phase, corresponding to a mean value of $\theta(t)$ equal to 63°, while the lateral angle $\phi(t)$ oscillates between $\pm 10°$ with zero in average. Also in this case the kite is flying fast in crosswind direction, maximizing the traction force on the cables. The kite trajectory during the whole cycle is confined in a polyhedral space region of about $(300 \times 300 \times 50)$ meters along the X,Y,Z axes

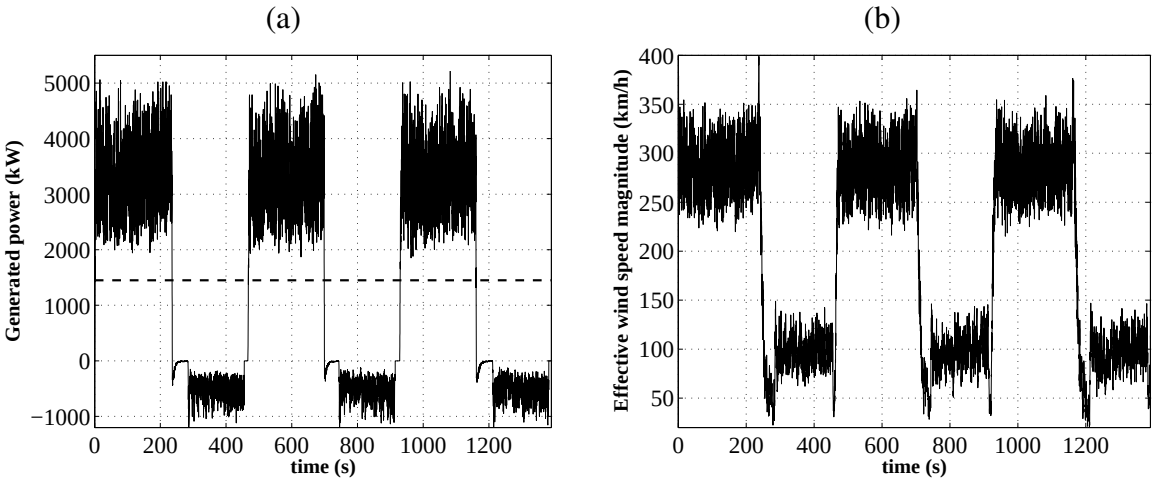

Figure 3.10. (a) Average (dashed) and actual (solid) generated power and (b) effective wind speed magnitude $|\vec{W}_e|$ during three complete HE–yoyo cycles with low power recovery maneuver and random wind disturbances.

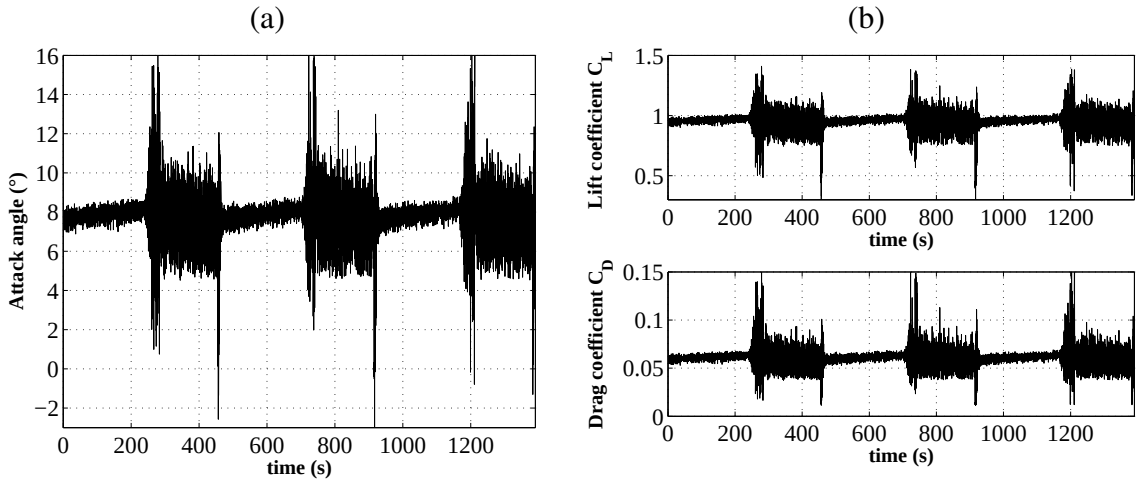

Figure 3.11. Kite (a) attack angle and (b) lift and drag coefficients during three HE–yoyo cycles with low power recovery maneuver and random wind disturbances.

respectively: this can be taken into account for the design of wind farms employing several HE–yoyo generators in the same area, to choose the position of the different KSUs in order to avoid interference between their respective kites (see Section 4.4). The power generated in the simulation is reported in Figure 3.13(a): the mean value is 2.16 MW. Such a value is much higher than that obtained with the low power passive phase, mainly due to the reduced duration of the recovery maneuver. Thus, the wing glide maneuver gives better energy generation performance

Table 3.4. HE–yoyo configuration with wing glide maneuver: state and input constraints, cycle starting and ending conditions, control parameters.

θ_I	55°	Traction phase starting conditions
ϕ_I	45°	
$\underline{r}$	850 m	
$\overline{r}$	900 m	Passive phase starting condition
$\overline{\theta}_{III}$	50°	Wing glide starting condition
$\overline{\theta}$	66°	State constraint
$\overline{\psi}$	6°	Input constraints
$\overline{\dot{\psi}}$	$20°/s$	
$\overline{\dot{r}}$	1.8 m/s	Traction phase reference $\dot{r}_{\text{ref}}$
$\underline{\dot{r}}$	-8.0 m/s	Passive phase reference $\dot{r}_{\text{ref}}$
T_c	0.2 s	Sample time
N_c	1 steps	Control horizon
N_p	10 steps	Prediction horizon

than the low power one. The considered wind turbulence does not cause system instability, showing again the control system robustness. The course of the wind effective speed magnitude $|\vec{W}_e|$ is reported in Figure 3.13(b): mean values of 220 km/h during the traction phase and 55 km/h during the passive phase are obtained. The courses of the kite attack angle and consequent lift and drag coefficients are reported in Figure 3.14(a)–(b). The related kite aerodynamic efficiency is between 12.8 and 15 in the traction phases, with a mean value of 13.5.

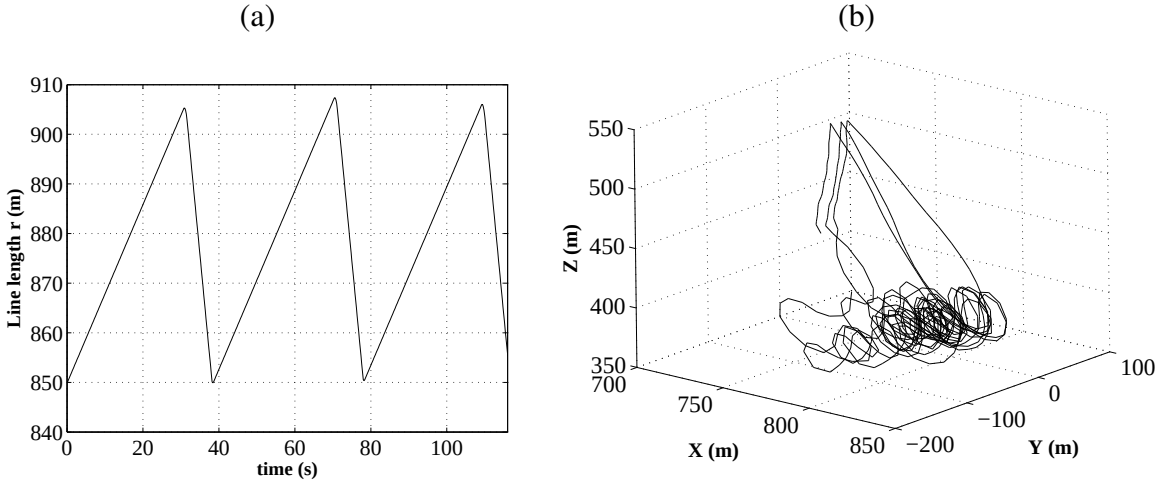

Figure 3.12. (a) Line length $r(t)$ and (b) kite trajectory during three complete HE–yoyo cycles with wing glide recovery maneuver and random wind disturbances.

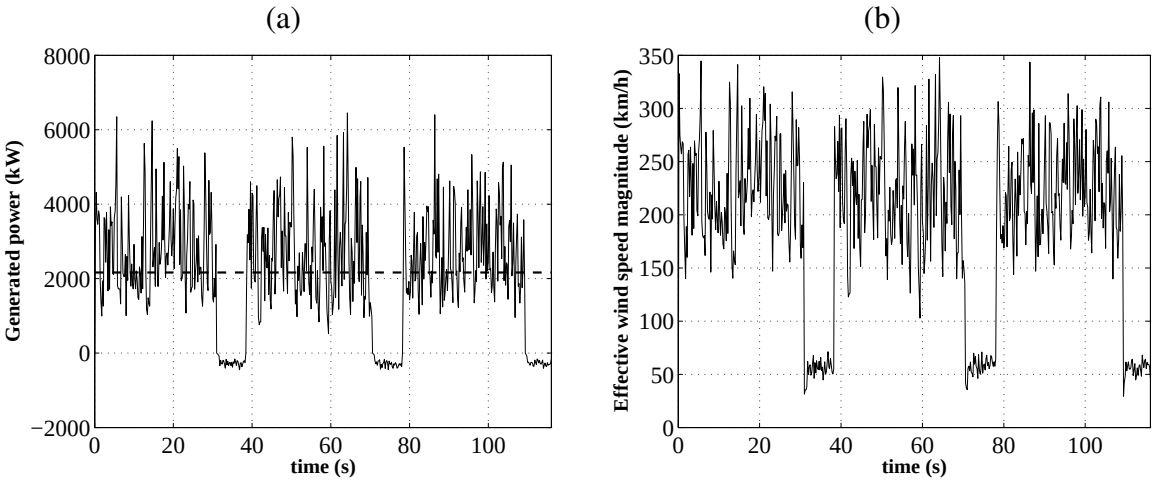

Figure 3.13. (a) Mean (dashed) and actual (solid) generated power and (b) effective wind speed magnitude $|\vec{W}_e|$ during three complete HE–yoyo cycles with wing glide recovery maneuver and random wind disturbances.

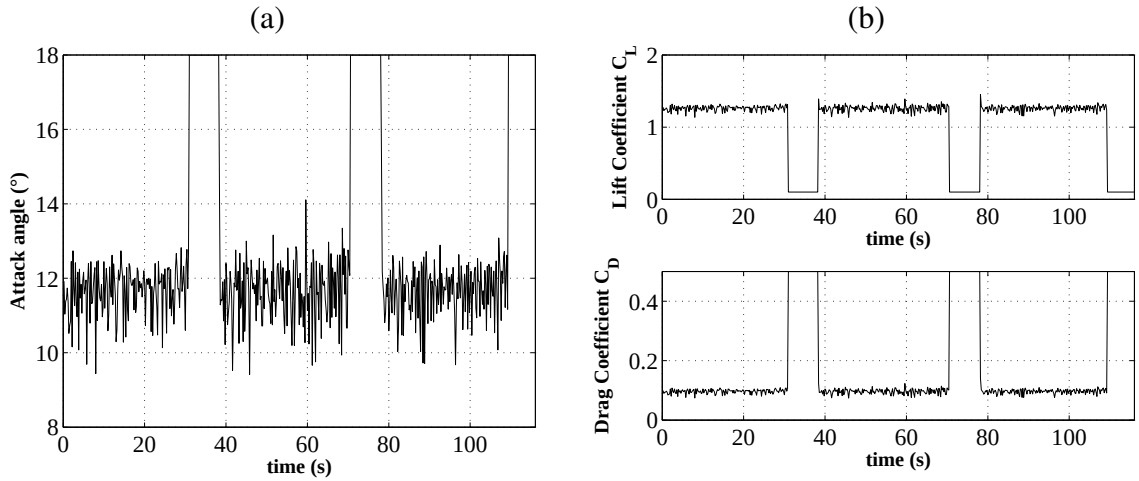

Figure 3.14. Kite (a) attack angle and (b) lift and drag coefficients during three HE–yoyo cycles with wing glide recovery maneuver and random wind disturbances.

3.4.2 HE–carousel configuration

The HE–carousel configuration has been simulated considering either the constant line length or the variable line length strategies, using the same kite and wind characteristics as those employed with the HE–yoyo configuration. In particular, the characteristics of the HE–carousel considered in the simulations are reported in Table 3.5. The functions employed to compute the aerodynamic lift and drag coefficients are showed in Figure 3.7.

Table 3.5. HE–carousel configuration: model parameters.

m	300 HE	Kite mass
A	500 m^2	Characteristic area
M	10000 HE	Vehicle mass
R	300 m	HE–carousel radius
d_l	0.03 m	Diameter of a single line
ρ_l	970 HE/m^3	Line density
$C_{D,l}$	1	Line drag coefficient
ρ	1.2 HE$/$m^3	Air density
α_0	3.5°	Base angle of attack

I) HE–carousel with constant line length The results related to three complete cycles are reported here. The considered control parameters and the values of the state and input constraints are given in Table 3.6, together with the starting and ending conditions for each phase (see Sections 2.3.2 and 3.3.2). Figure 3.15(a) shows the ob-

Table 3.6. HE–carousel with constant line length: cycle phases objectives and starting conditions, state and input constraints and control parameters.

r_{const}	900 m	Constant line length
$\dot{\Theta}_{\text{ref}}$	0.01 rad/s	Reference vehicle angular speed
Θ_0	45°	Passive phase starting condition
θ_I	10°	1$^{\text{st}}$ Passive sub-phase objective
Θ_1	135°	2$^{\text{nd}}$ Passive sub-phase starting condition
ϕ_I	160°	2$^{\text{nd}}$ Passive sub-phase objective
Θ_2	145°	3$^{\text{rd}}$ Passive sub-phase starting condition
θ_{II}	60°	3$^{\text{rd}}$ Passive sub-phase objective
Θ_3	165°	Traction phase starting condition
$\overline{\theta}$	75°	State constraint
$\overline{\psi}$	3°	Input constraints
$\overline{\dot{\psi}}$	20°/s	
T_c	0.2 s	Sample time
N_c	1 steps	Control horizon
N_p	12 steps	Prediction horizon

tained kite and vehicle trajectories during one complete cycle, while Figure 3.15(b) shows some "figure eight" kite trajectories. The power generated during the three cycles is reported in Figure 3.16(a): the mean value is 1.73 MW. Figure 3.16(b) depicts the obtained course of the wind effective speed magnitude $|\vec{W}_e|$: average

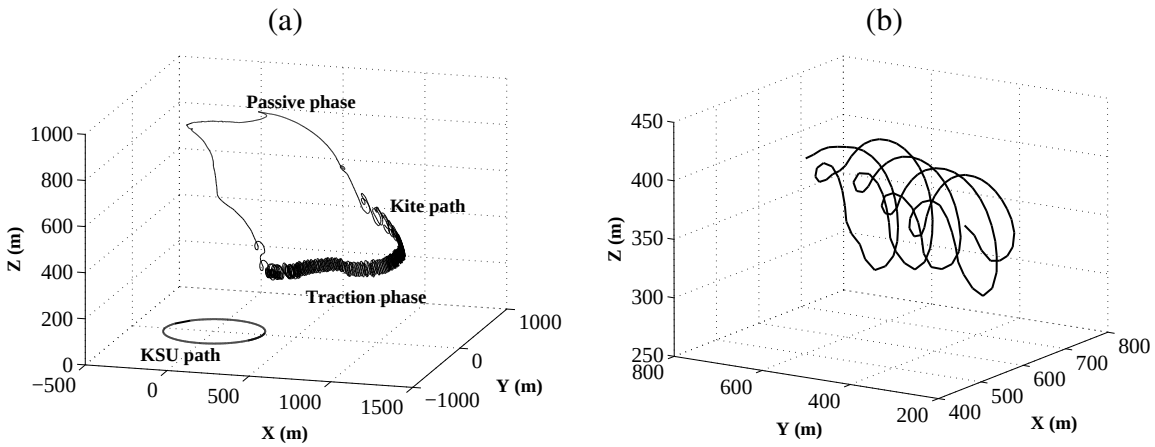

Figure 3.15. (a) Kite and vehicle trajectories during a single HE–carousel cycle with constant line length and random wind disturbances. (b) HE–carousel with constant line length: some "figure eight" kite trajectories during the traction phase.

values of 250 km/h and 50 km/h, during the traction and the passive phases respectively, are obtained. In particular, note that during the passive phase the effective speed is much reduced, thus allowing to minimize the energy loss. As regards the

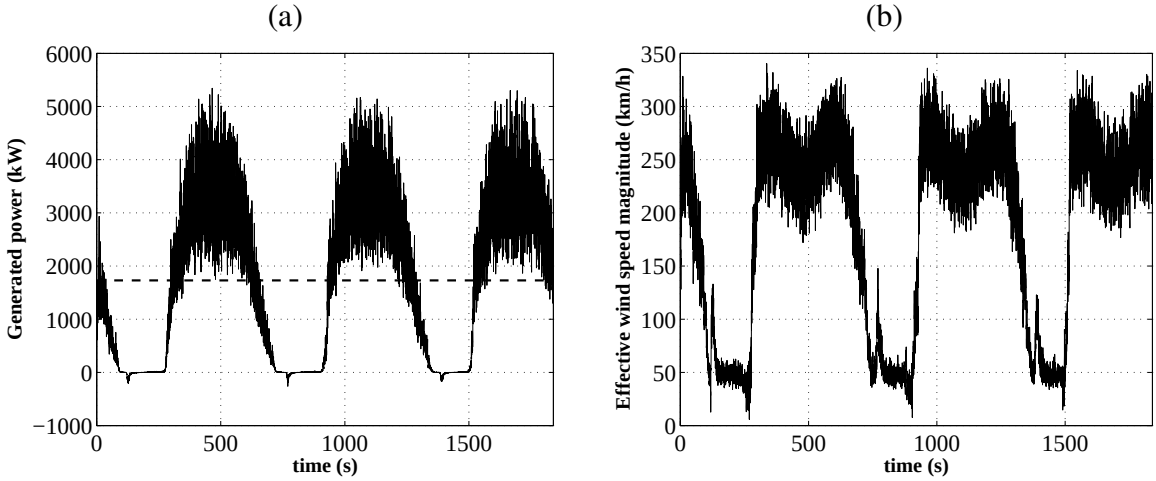

Figure 3.16. Simulation results of three complete cycles of a HE–carousel with constant line length and random wind disturbances. (a) Mean (dashed) and actual (solid) generated power and (b) effective wind speed magnitude $|\vec{W}_e|$.

obtained aerodynamic efficiency, during the traction phase an average value equal to 13.8 is obtained.

Note that since the fixed coordinate system (X,Y,Z) has been defined on the basis

of the nominal wind direction, a measurable change of the latter can be easily overcome by rotating the whole coordinate system (X,Y,Z), thus obtaining the same performances without changing neither the control system parameters nor the starting conditions of the various phases.

II) HE–carousel with variable line length The results related to three complete cycles are reported. The considered model and control parameters and the values of the state and input constraints are given in Table 3.7, together with the starting and ending conditions for each phase (see Sections 2.3.2 and 3.3.2). According to (3.65),

Table 3.7. HE–carousel configuration with variable line length: control and operational cycle parameters.

r_0	500 m	Minimal line length
$\overline{r}$	1000 m	Maximal line length
$\dot{r}_\mathrm{c}$	2.77 m/s	Reference line unrolling speed
$\dot{\Theta}_\mathrm{ref}$	0.0167 rad/s	Reference vehicle angular speed
Θ_0	5°	Unroll phase starting condition
Θ_1	165°	Traction phase starting condition
$\overline{\theta}$	75°	State constraint
$\overline{\psi}$	3°	Input constraints
$\overline{\dot{\psi}}$	$20°/s$	
T_c	0.2 s	Sample time
N_c	1 step	Control horizon
N_p	12 steps	Prediction horizon

the employed value of $\dot{r}_\mathrm{c}$ during the unroll phase is

$$\dot{r}_\mathrm{c} = 2.77 \simeq 2.98 = \frac{\overline{r} - r_0}{(\Theta_1 - \Theta_0)} \dot{\Theta}_\mathrm{ref}$$

The obtained course of $r(t)$ is reported in Figure 3.17(a). The line length is kept between 500 m and 1000 m and its mean value is equal to 747 m. Figure 3.17(b) shows the obtained kite and vehicle trajectories. The power generated during the two cycles is reported in Figure 3.18(a): the mean value is 1.62 MW. Figure 3.18(b) depicts the obtained course of the wind effective speed magnitude $|\vec{W}_e|$, with an average value of about 230 km/h. Note that in the case of variable line length, the effective wind speed is always quite high, since the kite continuously flies in crosswind conditions. The obtained average power is quite similar to that achieved by the HE–carousel with constant line length, but the use of variable line length makes it possible to achieve an overall power which is always positive, as expected. However, it has to be noted that while the total generated power is kept between

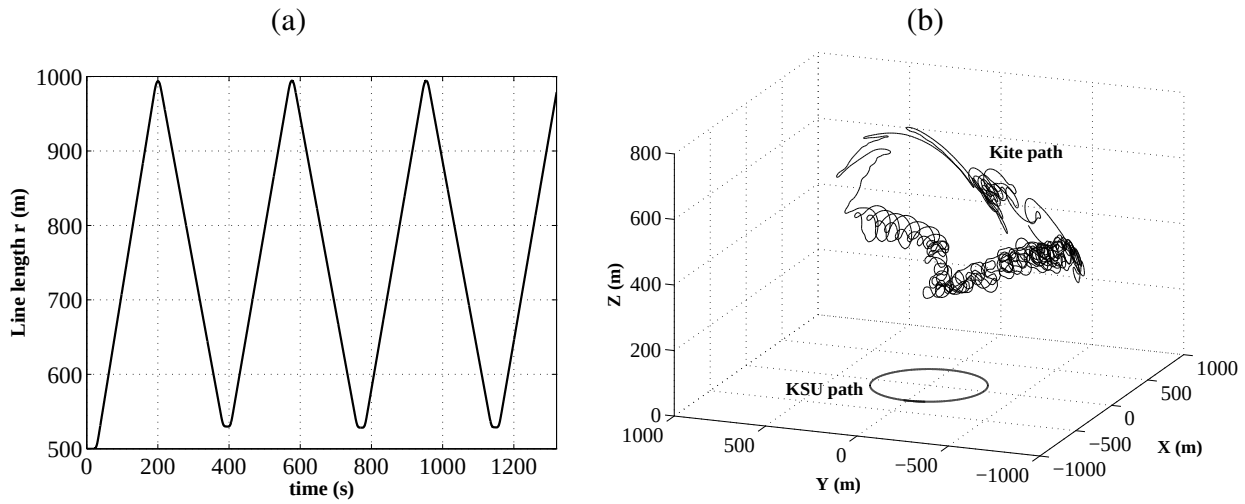

Figure 3.17. Simulation results of a HE–carousel with variable line length and random wind disturbances. (a) Line length $r(t)$ during three complete cycles. (b) Kite and vehicle trajectories during a single cycle.

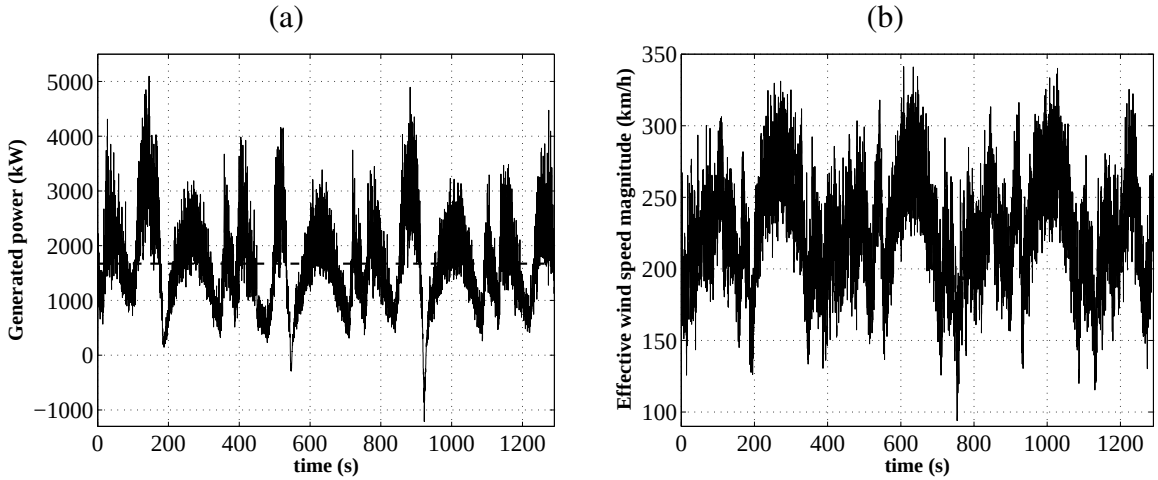

Figure 3.18. Simulation results of three complete cycles of a HE–carousel with variable line length and random wind disturbances. (a) Mean (dashed) and actual (solid) generated power and (b) effective wind speed magnitude $|\vec{W}_e|$.

about 0.2 MW and 5.0 MW, the contributions of either the vehicle motion or the line unrolling are much more variable. Figure 3.19(a)–(b) shows the power generated by line rolling/unrolling and by the vehicle motion. It can be noted that the average power given by the line unrolling is close to zero but the required rated power is about 10 MW, that have to be either generated from or supplied to the

machine. As regards the generators linked to the vehicle wheels, their average contribution is approximately equal to the overall average generated power, but their rated power has to be up to 15 MW (i.e. almost ten times higher than the average output power). This aspect represent a major drawback of the HE–carousel with variable line length, as it is discussed in Section 3.4.3.

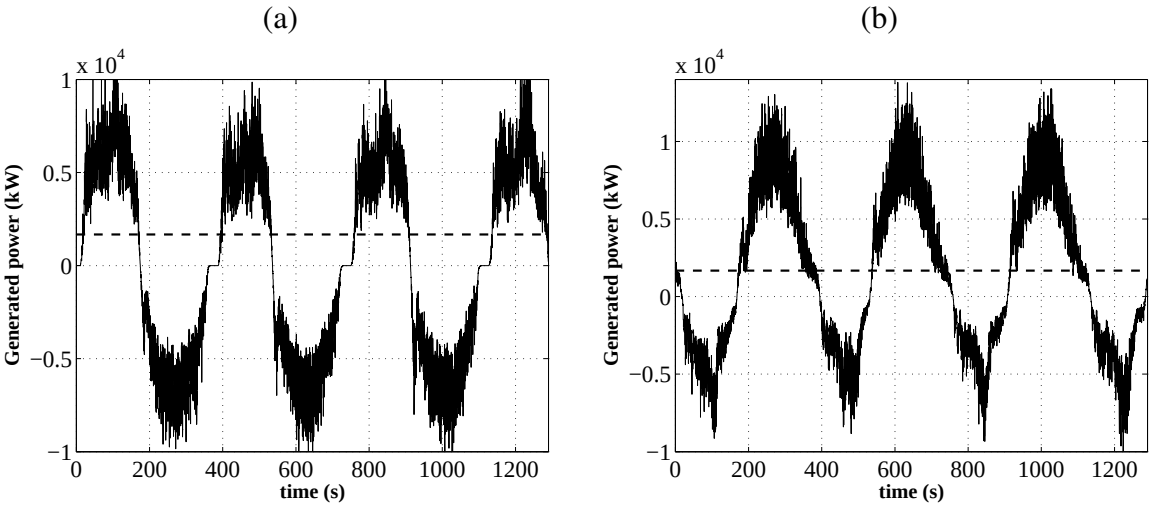

Figure 3.19. Simulation results of three complete cycles of a HE–carousel with variable line length and random wind disturbances. (a) Actual (solid) generated power by line rolling/unrolling and average total generated power (dashed). (b) Actual (solid) generated power by vehicle movement and average total generated power (dashed).

3.4.3 Comparison between HE–yoyo and HE–carousel configurations

On the basis of the simulation results presented in Sections 3.4.1 and 3.4.2, it is possible to make a first comparison between the proposed HAWE configurations. Table 3.8 shows some data about the energy generation performance obtained in the numerical simulations. The terms "KSU" and "vehicle" in the following refer to the power contributions given by the the line unrolling and by the vehicle movement respectively. The cycle efficiency in Table 3.8 has been computed according to the following equation:

$$\eta_{\text{cycle}} = \frac{\int_{t_0}^{t_{\text{end}}} (P(\tau))\, d\tau}{\int_{t_0}^{t_{\text{end}}} (P^{+}(\tau))\, d\tau} \tag{3.75}$$

Where t_0 and t_{end} are the starting and ending time instants for a single cycle and $P(t)$ is the net generated power (computed using (3.24)). $P^{+}(t)$ is the gross generated power, i.e.

Table 3.8. Simulation results for HAWE: average power, maximal power and cycle efficiency obtained with HE–yoyo and HE–carousel configurations

	Average power	**Maximum power**			**Cycle efficiency**		
		KSU	Vehicle	Overall	KSU	Vehicle	Total
HE–yoyo (low power)	1.45 MW	5.0 MW	–	5.0 MW	88%	–	88%
HE–yoyo (wing glide)	2.16 MW	5.5 MW	–	5.5 MW	97%	–	97%
HE–carousel (constant line)	1.73 MW	–	5.0 MW	5.0 MW	–	98%	98%
HE–carousel (variable line)	1.65 MW	10.0 MW	14.0 MW	5.0 MW	-23%	63%	99%

the power extracted from the wind without considering the power spent e.g. in the passive phases. Thus, η_{cycle} is a measure of the losses inherent in each operational cycle. In the HE–carousel configuration with variable line length, partial efficiencies have been also computed for the KSU and the vehicle contributions, by applying equation (3.75) to their respective power courses. On the basis of the reported data, it can be noted that quite high overall efficiencies are obtained by all the considered configurations and operational cycles, with the HE–carousel with variable line length reaching practically 100% efficiency. However, in this configuration such a good overall performance is achieved at the cost of quite bad partial performance of the KSU and vehicle energy balances (-23% and 63% respectively). On the other hand, the HE–yoyo with wind glide recovery phase and the HE–carousel with constant line length achieve high efficiencies, with only 2–3% losses due to their respective passive phases.
As regards the values of the maximal power reported in Table 3.8, they have been computed considering the absolute value of the generated power:

$$\max_t |P(t)|$$

This indicator has been evaluated also for the partial contributions of the KSU and of the vehicle in the case of HE–carousel with variable line length. Note that, in general, the maximal power is a "measure" of the resistance (i.e. the size) of all the mechanical and electrical components of the machine (i.e. the kite, the cables, the transmission gears, the mechanical structure, the electric generators etc.). Thus, the maximum power can be assumed to be proportional to the cost of the considered generator. In particular it can be noted that all the generators show similar maximal overall power values (about 5.0 MW): this aspect is confirmed by the theoretical analyses and optimization results performed in Chapter 4. Note that the gap between the overall maximal and average generated power

does not indicate that the energy generation performance are poor, since the obtained maximal power depends on the wind variability and not on the generator itself (see Chapter 6.2). However, in the HE–carousel with variable line length, the maximum power values related to line unrolling and vehicle movement are 10 MW and 14 MW respectively, while the overall maximal power is 5.0 MW only. Thus, the mechanical and electrical equipments of this configuration must be much more robust (i.e. expensive) than the other solutions. Since the increase of total efficiency achieved by the HE–configuration with variable line length is of few percent points (see Table 3.8), the related additional costs are not motivated by the obtained improvements, thus making this configuration not viable for further developments.
As a final remark, the performed simulations indicate that the HE–yoyo with low power recovery and that the HE–carousel with variable line length could be probably less effective in harnessing high–altitude wind energy. On the other hand, the HE–yoyo with wing glide passive phase and the HE–carousel with constant line length are more promising. Indeed, further investigations are needed to assess which HAWE configuration achieves the best overall performance, also considering the generated energy per km^2 achievable by using more HE–yoyo units in the same location (in a so–called HE–farm, see Section 4.4) and the use of more airfoils together on the same HE–carousel. Moreover, the operation of the generators presented so far involve several parameters, like the line unrolling speed in a HE–yoyo or the vehicle angular speed in a HE–carousel, that have to be chosen in a suitable way to obtain the maximal generated power. In Section 4.2, the HE–yoyo configuration with wing glide maneuver, which shows the most promising performance according to the presented simulation results, is further investigated and its operational cycle is designed using numerical optimization techniques, also considering its use in a large HE–farm.

Chapter 4

Optimization of HAWE

The operation of the described high–altitude wind energy generators involve several parameters, like the length and diameter of the lines, their rolling/unrolling speed, the angular speed of the vehicles in a HE–carousel, etc.. Such parameters have been tuned through physical insight and trial–and–error procedures in the simulation tests of Section 3.4. However, a more systematic procedure is needed to design the operation of the presented generators, in order to achieve the maximal output power for given wind characteristics (i.e. for a given location). Moreover, when more complex systems are considered, like large high–altitude wind farms composed of several HAWE generators working in the same area, suitable design tools have to be employed to maximize the generated power density per unit area while taking into account the possible interactions between the airfoils.
In this Chapter, numerical optimization techniques are applied to HAWE generators, in order to optimally choose their design and operational parameters. At first, simplified crosswind power equations are recalled. Such relations, already derived in the literature (see e.g. [8, 49, 50]), allow to compute the power obtained by an airfoil flying fast in crosswind conditions. Then, such power equations are employed to compare the potentials of the HE–yoyo and the HE–carousel configurations. Moreover, an optimal design of the operational cycle of a HE–yoyo generator, for a location with a given nominal wind profile, is carried out and the related numerical simulations are performed, in order to assess the control performance and the matching between the simplified power equations and the dynamical model described in Section 3.1. Then, numerical simulations and simplified equations are employed to assess the scalability of HAWE technology. Finally, numerical optimization is also employed to optimally design a kite wind farm, denoted as "HE–farm", composed of more HE–yoyo units in the same location.

4.1 Crosswind kite power equations

Consider an airfoil linked by a cable to a fixed point at ground level (i.e. the KSU). Indicate with r the cable length and with $\vec{e}_r$ a unit vector parallel to the cable and pointing towards increasing r values (see Figure 4.1). Moreover, indicate with $\vec{W}_e$ the effective wind speed, i.e. the vector sum of absolute wind speed and of the airfoil speed with respect to the ground, and with $\vec{W}_{e,p}$ the projection of $\vec{W}_e$ on the plane perpendicular to vector $\vec{e}_r$. The magnitudes of the airfoil lift and drag forces, $|\vec{F}_L|$ and $|\vec{F}_D|$ respectively,

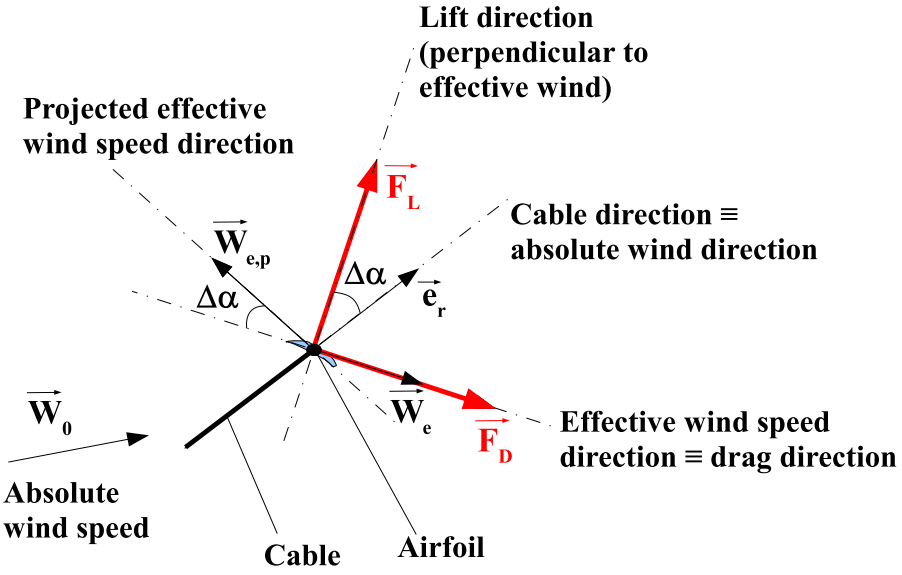

Figure 4.1. Sketch of an airfoil flying in crosswind conditions.

can be computed as:

$$\begin{aligned} |\vec{F}_L| &= \frac{1}{2}\rho A C_L |\vec{W}_e|^2 \\ |\vec{F}_D| &= \frac{1}{2}\rho A C_D |\vec{W}_e|^2 \end{aligned} \tag{4.1}$$

where ρ is the air density, C_L and C_D are the lift and drag aerodynamic coefficients and A is the airfoil projected area. Assume that:

- the the airfoil flies in crosswind conditions;
- the inertial and apparent forces are negligible with respect to the aerodynamic forces;
- the kite speed relative to the ground is constant;
- the kite aerodynamic lift force $\vec{F}_L$ approximately lies on the plane defined by vectors $\vec{W}_{e,p}$ and $\vec{e}_r$;

The drag force $\vec{F}_D$ is aligned with the effective wind speed vector $\vec{W}_e$, while the lift force $\vec{F}_L$ is perpendicular to $\vec{F}_D$ and, under the considered assumptions, it lies on the plane ($\vec{W}_{e,p}$,$\vec{e}_r$). Note that also vectors $\vec{e}_r$ and $\vec{W}_{e,p}$ are perpendicular, since by definition $\vec{W}_{e,p}$ is the projection of $\vec{W}_e$ on the plane perpendicular to $\vec{e}_r$. Thus, the angle $\Delta\alpha$ between $\vec{F}_D$ and $\vec{W}_{e,p}$ is the same as the angle between vectors $\vec{F}_L$ and $\vec{e}_r$ (see Figure 4.1). Since inertial and apparent forces are negligible, the following equilibrium condition on the plane perpendicular to vector $\vec{e}_r$ has to be satisfied:

$$|\vec{F}_L| \sin(\Delta\alpha) = |\vec{F}_D| \cos(\Delta\alpha) \tag{4.2}$$

thus it can be noted that:

$$\frac{|\vec{F}_D|}{|\vec{F}_L|} = \frac{\sin(\Delta\alpha)}{\cos(\Delta\alpha)} \tag{4.3}$$

and that, from (4.1),

$$\frac{\sin(\Delta\alpha)}{\cos(\Delta\alpha)} = \frac{C_D}{C_L} = \frac{1}{E} \tag{4.4}$$

Considering the trigonometrical relationship $\cos(\Delta\alpha)^2 + \sin(\Delta\alpha)^2 = 1$, equation (4.4) leads to:

$$\begin{aligned}
&\cos(\Delta\alpha)^2 = 1 - \sin(\Delta\alpha)^2 = 1 - \frac{\cos(\Delta\alpha)^2}{E^2} \\
&\cos(\Delta\alpha)^2 \left(1 + \frac{1}{E^2}\right) = 1 \\
&\cos(\Delta\alpha) = \sqrt{\frac{E^2}{(E^2+1)}} \\
&\sin(\Delta\alpha) = \sqrt{\frac{1}{(E^2+1)}}
\end{aligned} \tag{4.5}$$

Now, the traction force $F^{\text{c,trc}}\vec{e}_r$, $F^{\text{c,trc}} \geq 0$ acting on the cable, by which mechanical power can be generated, is the sum of the projections of vectors $\vec{F}_L$ and $\vec{F}_D$ on the cable direction $\vec{e}_r$:

$$F^{\text{c,trc}}\vec{e}_r = \vec{F}_L \cdot \vec{e}_r + \vec{F}_D \cdot \vec{e}_r \tag{4.6}$$

whose magnitude in the considered framework can be computed as (see Figure 4.1):

$$F^{\text{c,trc}} = |\vec{F}_L| \cos(\Delta\alpha) + |\vec{F}_D| \sin(\Delta\alpha) \tag{4.7}$$

Remark 1 *Note that equation (4.4) can be obtained also by computing the maximal value of $F^{c,trc}$ as a function of $\Delta\alpha$. This can be obtained by imposing the gradient $dF^{c,trc}/d\Delta\alpha = 0$:*

$$\frac{dF^{c,trc}}{d\Delta\alpha} = -|\vec{F}_L| \sin(\Delta\alpha) + |\vec{F}_D| \cos(\Delta\alpha) = 0 \tag{4.8}$$

this way, condition (4.4) is obtained once again:

$$\frac{|\vec{F}_D|}{|\vec{F}_L|} = \frac{\sin(\Delta\alpha)}{\cos(\Delta\alpha)}$$

Thus, considering equations (4.5) and (4.7), the following equation for the traction force is obtained:

$$F^{\text{c,trc}} = \frac{1}{2}\rho A C_L \sqrt{\frac{E^2}{(E^2+1)}}|\vec{W}_e|^2 + \frac{1}{2}\rho A \frac{C_L}{E}\sqrt{\frac{1}{(E^2+1)}}|\vec{W}_e|^2 \tag{4.9}$$

with straightforward manipulations, equation (4.9) leads to the following:

$$F^{\text{c,trc}} = \frac{1}{2}\rho A C_L \sqrt{\frac{E^2+1}{E^2}}|\vec{W}_e|^2 \tag{4.10}$$

Moreover, consider the projection $\vec{W}_{e,r} = \vec{W}_e \cdot \vec{e}_r$ of the effective wind speed on the cable direction. It can be noted that, by construction (see Figure 4.1) and due to equation (4.5), the following relationship holds :

$$|\vec{W}_e| = \frac{|\vec{W}_{e,r}|}{\sin(\Delta\alpha)} = |\vec{W}_{e,r}|\sqrt{\frac{(E^2+1)}{1}} \tag{4.11}$$

By substituting equation (4.11) in equation (4.10), the following result is obtained:

$$F^{\text{c,trc}} = \frac{1}{2}\rho A C_L \sqrt{\frac{E^2+1}{E^2}}\left(E^2+1\right)|\vec{W}_{e,r}|^2$$

$$F^{\text{c,trc}} = \frac{1}{2}\rho A C_L E^2 \left(1+\frac{1}{E^2}\right)^{\frac{3}{2}}|\vec{W}_{e,r}|^2 \tag{4.12}$$

Equation (4.12) gives the traction force on the cable as a function of the effective wind speed projected on the cable itself. In order to take into account also the cable drag force (computed as in Section 3.1.4), consider that:

$$\vec{F}_{D,tot} = \vec{F}_D + \vec{F}^{\text{c,aer}} = \frac{1}{2}\rho A C_D |\vec{W}_e|^2 \frac{\vec{W}_e}{|\vec{W}_e|} + \frac{1}{8}\rho\, C_{D,l}\, A_l\, |\vec{W}_e|^2 \frac{\vec{W}_e}{|\vec{W}_e|}$$

where $\vec{F}_{D,tot}$ is the total drag force, $\vec{F}^{\text{c,aer}}$ is the cable drag force, $C_{D,l}$ is the cable drag coefficient and A_l is the cable front area (see Section 3.1.4). Considering an airfoil with two cables of diameter d_l and length r each, the following relation is obtained:

$$\vec{F}_{D,tot} = \frac{1}{2}\rho A \underbrace{C_D\left(1+\frac{(2\,r\,d_l)\,C_{D,l}}{4\,A\,C_D}\right)}_{C_{D,\text{eq}}} \tag{4.13}$$

Defining:

$$E_{\text{eq}} = \frac{C_L}{C_{D,\text{eq}}} \tag{4.14}$$

The following equation is obtained for the traction force $F^{\text{c,trc}}$ (from equations (4.12) and (4.14)):

$$F^{\text{c,trc}} = \frac{1}{2}\rho A C_L E_{\text{eq}}^2 \left(1 + \frac{1}{E_{\text{eq}}^2}\right)^{\frac{3}{2}} |\vec{W}_{e,r}|^2 = C|\vec{W}_{e,r}|^2 \tag{4.15}$$

where

$$C = \frac{1}{2}\rho A C_L E_{\text{eq}}^2 \left(1 + \frac{1}{E_{\text{eq}}^2}\right)^{\frac{3}{2}} \tag{4.16}$$

Note that, as already pointed out in Remark 1, equation (4.15) gives the maximal traction force that can be generated by an airfoil, in accordance with the results obtained in [8]. Equation (4.15) can be employed to study the optimal operating conditions of the airfoil in order to achieve the maximal generated power. Indeed, the power extracted by the airfoil depends on how the force $F^{\text{c,trc}}$ is converted into mechanical and electrical power. In particular, in the following the HE–yoyo traction phase and the HE–carousel with variable line length are considered and compared. In the presented analyses, it is considered that the absolute wind speed $\vec{W}_0$ (introduced in Section 3.1) is independent on elevation and it is parallel with respect to the ground. Moreover, it is considered that the diameter of the two cables linking the airfoil to the KSU is fixed and that it is sufficiently high to make the cables able to support the generated traction forces.

4.1.1 HE–yoyo power equations

In the HE–yoyo configuration, power is generated by the line unrolling:

$$P_{\text{HE–yoyo}} = F^{\text{c,trc}}\dot{r} = C|\vec{W}_{e,r}|^2\dot{r}$$

For a given position of the kite, identified by angles θ and ϕ and by the line length r (see Section 3.1), the magnitude $|\vec{W}_{e,r}|$ of the effective wind speed along the unit vector $\vec{e}_r$ (i.e. the direction of the lines) can be computed as:

$$|\vec{W}_{e,r}| = \left||\vec{W}_0|\sin(\theta)\cos(\phi) - \dot{r}\right|$$

Where $\vec{W}_0$ is the nominal wind speed. Thus, the generated power on the basis of (4.15) is:

$$P_{\text{HE–yoyo}}(\theta,\phi,\dot{r}) = C|\vec{W}_{e,r}|^2\dot{r} = C\left(|\vec{W}_0|\sin(\theta)\cos(\phi) - \dot{r}\right)^2\dot{r} \tag{4.17}$$

If the nominal wind speed is constant with respect to the elevation and it is parallel with respect to the ground, it can be noted that the maximal value of $P_{\text{HE–yoyo}}$ is obtained when $\theta = \theta^* = \pi/2$, $\phi = \phi^* = 0$ and $\dot{r} = \dot{r}^*$ computed as:

$$\begin{gathered} \dot{r}^* = \arg\max_{\dot{r}} P_{\text{HE–yoyo}}(\theta^*,\phi^*,\dot{r}) \\ \text{s. t.} \\ \dot{r} \leq |\vec{W}_0| \end{gathered}$$

The constraint $\dot{r} \leq |\vec{W}_0|$ is included since, by physical intuition, the unrolling speed cannot exceed the absolute wind speed. By imposing:

$$\frac{dP_{\text{HE–yoyo}}}{d\dot{r}} = 3\dot{r}^2 - 4|\vec{W}_0|\dot{r} + |\vec{W}_0|^2 = 0$$

The following value is obtained:

$$\dot{r}^* = \frac{|\vec{W}_0|}{3}$$

and, consequently, the maximal power is

$$P^*_{\text{HE–yoyo}} = C\left(|\vec{W}_0| - \dot{r}^*\right)^2 \dot{r}^* = C\frac{4}{27}|\vec{W}_0|^3 \tag{4.18}$$

as already obtained e.g. in [8]. Indeed, the maximal power value $P^*_{\text{HE–yoyo}}$ (4.18) is a purely theoretical upper bound, since for example it does not take into account and change of wind speed with respect to elevation from the ground and it also does not consider the need to perform a passive phase to recover the airfoil when the line length has reached its maximum value. Such aspects are taken into account in Section 4.2, where more realistic settings are considered. Moreover, note that the fixed optimal airfoil position obtained on the basis of equation (4.15) cannot be achieved in practice, since the kite is moving in the air: for this reason, the optimal airfoil orbits are loops or "figure eight" trajectories, performed in the air in a zone that corresponds to the computed value of θ^* and ϕ^*.

4.1.2 HE–carousel power equation and theoretical equivalence with the HE–yoyo

In the HE–carousel with variable line length, power is generated in general by both the line unrolling and the vehicle movement (see Section 3.1.6). If the vehicle longitudinal acceleration is negligible (see equation (3.22) in Section 3.1.5), the following equation is obtained:

$$\begin{aligned} P_{\text{HE–carousel}} &= F^{\text{c,trc}}\dot{r} + \dot{\Theta}\, R\, F^{\text{gen}}(t) = F^{\text{c,trc}}\left(\dot{r} + R\,\dot{\Theta}\sin\theta\sin\phi\right) \\ P_{\text{HE–carousel}} &= C|\vec{W}_{e,r}|^2\left(\dot{r} + R\,\dot{\Theta}\sin\theta\sin\phi\right) \end{aligned}$$

Indeed, in the HE–carousel the magnitude of the effective wind speed $|\vec{W}_{e,r}|$ projected on the cable direction is a function of the vehicle position Θ, of the kite position (θ, ϕ) in the local coordinate system (see Figure 4.2 and Section 3.1), and of the vehicle tangential speed $R\,\dot{\Theta}$:

$$|\vec{W}_{e,r}| = \left|\sin(\theta)\left(|\vec{W}_0|\cos(\Theta+\phi) - R\,\dot{\Theta}\sin(\phi)\right) - \dot{r}\right| \tag{4.19}$$

Thus, the overall power generated by a HE–carousel (neglecting the mechanical and

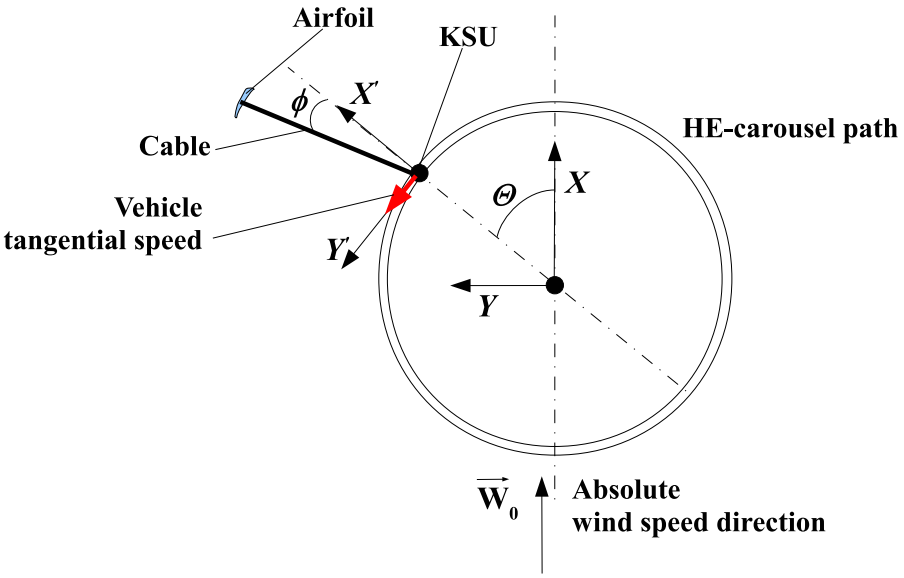

Figure 4.2. Sketch of HE–carousel (top view).

electrical efficiencies) can be computed as:

$$P_{\text{HE–carousel}} = C\left(\sin(\theta)\left(|\vec{W}_0|\cos(\Theta+\phi) - R\,\dot{\Theta}\sin(\phi)\right) - \dot{r}\right)^2\left(\dot{r} + R\,\dot{\Theta}\sin\theta\sin\phi\right) \tag{4.20}$$

For given values of angular position Θ and tangential speed $R\,\dot{\Theta}$, it is possible to compute the maximal overall power as follows:

$$\begin{gathered} P^*_{\text{HE–carousel}}(\Theta,\dot{\Theta}) = \max_{\theta,\phi,\dot{r}} P_{\text{HE–carousel}} \\ \text{s. t.} \\ \dot{r} \le \sin(\theta)\left(|\vec{W}_0|\cos(\Theta+\phi) - R\,\dot{\Theta}\sin(\phi)\right) \end{gathered} \tag{4.21}$$

The constraint on $\dot{r}$ has been included in order to find optimal conditions that are practically achievable. The optimizer $(\theta^*,\phi^*,\dot{r}^*)^T$ can be analytically computed as:

$$\begin{pmatrix} \theta^* \\ \phi^* \\ \dot{r}^* \end{pmatrix} = \begin{pmatrix} \frac{\pi}{2} \\ -\Theta \\ \frac{|\vec{W}_0|}{3} + R\,\dot{\Theta}\sin(\Theta) \end{pmatrix} \tag{4.22}$$

By replacing the optimal values (4.22) in equation (4.20) the following maximal power value is obtained:

$$P^*_{\text{HE–carousel}} = \frac{4}{27} C |\vec{W}_0|^3 \tag{4.23}$$

Thus, according to result (4.23), in any HE–carousel operating condition (in terms of Θ and $\dot{\Theta}$) the theoretical upper bound of the generated power can be achieved by suitably choosing ϕ and $\dot{r}$. Note that the optimal value of ϕ indicates that the airfoil must be always parallel to the absolute wind vector (see Figure 4.2), while the line unrolling/rolling speed $\dot{r}$ has to be equal to one third of the absolute wind speed magnitude plus the term $(R\,\dot{\Theta}\sin(\Theta))$, which balances the contribution of the vehicle motion to the effective wind speed. The analysis presented so far for the HE–carousel can be employed also in a more general framework, e.g. to investigate the potential of generating energy while onboard of a ship (as done in [44]). Now, a theoretically optimal HE–carousel operating cycle can be designed by choosing a suitable course of the vehicle angular speed $\dot{\Theta}$, such that a periodic course of all the involved variables is achieved. In particular, it is needed that the average value of $\dot{r}$ over a complete cycle equals zero:

$$\frac{1}{2\pi}\int_0^{2\pi} (\dot{r}(\Theta))\, d\Theta = 0 \tag{4.24}$$

By considering a periodical course of $R\,\dot{\Theta}$ of the form:

$$R\,\dot{\Theta} = R\,\overline{\dot{\Theta}}(1-\sin(\Theta)) \tag{4.25}$$

and imposing the optimal value $\dot{r}^*$ (4.22) of $\dot{r}$, the following result is obtained for $\overline{\dot{\Theta}}$:

$$\begin{aligned}
&\dot{r} = \tfrac{|\vec{W}_0|}{3} + R\,\overline{\dot{\Theta}}(1-\sin(\Theta))\sin(\Theta) \\
&\tfrac{1}{2\pi}\int_0^{2\pi} (\dot{r}(\Theta))\, d\Theta = \tfrac{1}{2\pi}\int_0^{2\pi} \left(\tfrac{|\vec{W}_0|}{3} + R\,\overline{\dot{\Theta}}(1-\sin(\Theta))\sin(\Theta)\right) d\Theta = \\
&= \tfrac{|\vec{W}_0|}{3} + \tfrac{1}{2\pi}\int_0^{2\pi} \left(R\,\overline{\dot{\Theta}}\sin(\Theta)\right) d\Theta - \tfrac{1}{2\pi}\int_0^{2\pi} \left(R\,\overline{\dot{\Theta}}\sin(\Theta)^2\right) d\Theta = \\
&= \tfrac{|\vec{W}_0|}{3} - R\,\overline{\dot{\Theta}}\tfrac{1}{2\pi}\int_0^{2\pi} \left(\sin(\Theta)^2\right) d\Theta = \tfrac{|\vec{W}_0|}{3} - \tfrac{1}{2}R\,\overline{\dot{\Theta}}
\end{aligned}$$

$$\Rightarrow R\,\overline{\dot{\Theta}} = \frac{2}{3}|\vec{W}_0| \tag{4.26}$$

From (4.25) and (4.26) the following course for the angular speed $\dot{\Theta}$ is obtained:

$$R\,\dot{\Theta} = \frac{2}{3}|\vec{W}_0|(1 - \sin(\Theta)) \tag{4.27}$$

The optimal courses of $\dot{\Theta}$, $\dot{r}$ and of the power P_{vehicle}, P_{line} generated by the vehicle motion and by the line unrolling respectively, as well as the overall optimal power $P^*_{\text{HE–carousel}}$, are reported in Figure 4.3(a)–(b) as functions of the vehicle angular position Θ. The considered HE–carousel characteristics are reported in Table 4.1. The overall power is constant

Table 4.1. Model parameters employed to compute an optimal HE–carousel cycle

A	500 m^2	Characteristic area
r	600 m	Mean line length
R	300 m	HE–carousel radius
C_L	1.2	Airfoil lift coefficient
E	13	Aerodynamic efficiency
d_l	0.02 m	Diameter of a single line
$C_{D,l}$	1	Line drag coefficient
ρ	1.2 HE/m^3	Air density
$\lvert\vec{W}_0\rvert$	6 m/s	Nominal wind speed magnitude

and equal to $\frac{4}{27}C|\vec{W}_0|^3 = 1.542\,\text{MW}$, i.e. the maximal power is continuously obtained. However, as already noticed in the simulation Section 3.4.2, the rated power of the generators equipped on the vehicle has to be about 6.5 MW (i.e. four times the obtained net power), while the KSU has to be able to provide about 5 MW to recover the airfoil when a negative value of $\dot{r}$ is issued (see Figure 4.3(a)–(b)). Such a drawback probably hinder the possibility to effectively design a HE–carousel with variable line length, due to the excessive costs for the electric equipments and the mechanical structure of the generator. Moreover, as it can be noted in Figure 4.3(a), the optimal cycle is such that $\dot{\Theta} = 0$ when $\Theta = \pi/2$, meaning that the vehicle should stop at such an angular position. This would prevent the HE–carousel from completing the cycle, however such issue could be easily solved by slightly modifying the optimal course of $\dot{\Theta}$ (at the expense of a little power loss with respect to the theoretical upper bound).

To conclude this Section, it has to be remarked that HE–yoyo and HE–carousel have the same power generation potentials, equal to Loyd's theoretical bound [8]. However, such potential cannot be completely exploited due to the need of performing a repeatable operational cycle. Thus, as already pointed out at the end of the Simulation section 3.4.3, both these HAWE configurations should be investigated in order to assess which one gives the best tradeoff between average generated energy, land occupation, investment and maintenance costs. In the following, the attention is focused on the HE–yoyo configuration

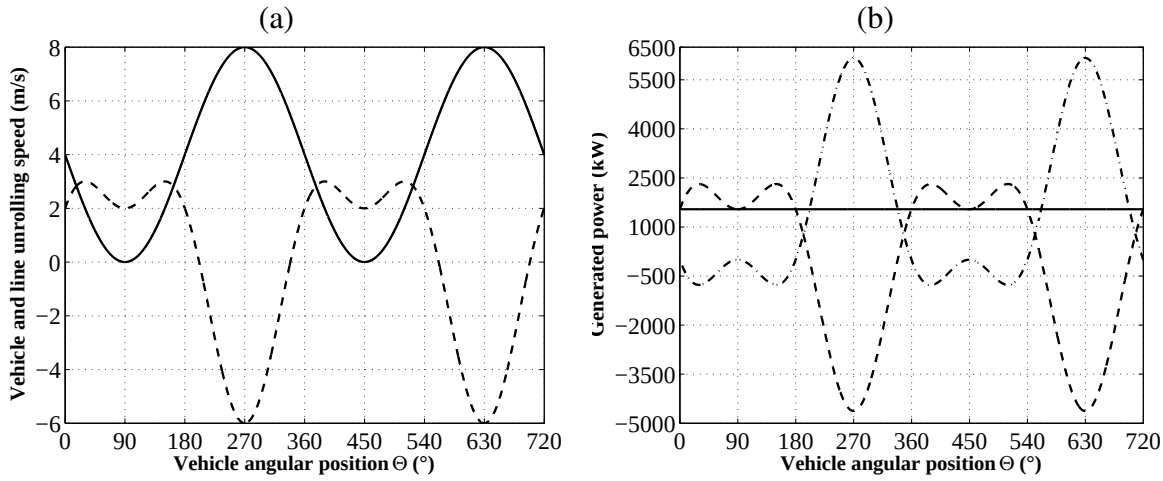

Figure 4.3. (a) Line speed $\dot{r}$ (dashed) and vehicle speed $R\dot{\Theta}$ (solid) during two complete optimal HE–carousel cycles as functions of Θ. (b) Power P_{vehicle} generated by the vehicle motion (dash–dot), power P_{line} given by the line unrolling (dashed) and overall optimal power $P^*_{\text{HE–carousel}}$ (solid).

with wing glide maneuver, since it proved to achieve the best overall performance in the simulation results of Section 3.4.

4.2 Optimization of a HE–yoyo operating cycle

The upper bound (4.23) is a theoretical limit of the power that can be obtained by an airfoil flying in crosswind conditions. As already highlighted in Sections 3.4 and 4.1.1, the need of performing a feasible operating cycle, which can be continuously repeated, leads to losses in the power generation performance. Moreover, other issues should be considered in the theoretical formulation, like the change of wind speed as a function of the elevation from the ground, the cable dimensioning in accordance with the generated power values and the maneuvering area required by the kite. In this Section, a HE–yoyo configuration with wing glide recovery maneuver is considered and its operating parameters are designed using numerical optimization methods, to take into account more realistic operational conditions and physical constraints. The designed generator is then simulated to assess the matching between the theoretical equations, which the optimization is based on, and the dynamical model described in Chapter 3.
As described in Sections 2.3.1 and 3.3.1, the operation of a HE–yoyo is divided into two phases, the traction and the passive ones. The operational parameters are the values θ_{trac} and θ_{pass} of angle θ during the traction and passive phase, the minimal cable length $\underline{r}$ during the cycle (as it will showed later, the cable maximal length variation Δr is fixed) and

the cable speed during the traction and the passive phase, $\dot{r}_{\text{trac}}$ and $\dot{r}_{\text{pass}}$ respectively. By indicating with $P_{\text{trac}}(t)$ and $P_{\text{pass}}(t)$ the power generated (or spent) in the traction and passive phases respectively, the average power $\overline{P}$ obtained in a cycle can be computed as:

$$\overline{P} = \frac{\int_{t_0}^{t_{\text{trac,end}}} P_{\text{trac}}(\tau)d\tau + \int_{t_{\text{trac,end}}}^{t_{\text{pass,end}}} P_{\text{pass}}(\tau)d\tau}{t_{\text{pass,end}} - t_0} \tag{4.28}$$

where t_0 and $t_{\text{trac,end}}$ are the starting and ending instants of the traction phase and $t_{\text{pass,end}}$ is the ending instant of the passive phase (in this analysis, it is assumed that the starting instant of the passive phase coincides with the ending instant of the traction one). Assume that:

- approximately constant angles θ_{trac} and θ_{pass} during the traction and passive phases are kept, as well as constant ϕ angle;
- constant cable unrolling speed $\dot{r}_{\text{trac}} > 0$ and winding back speed $\dot{r}_{\text{pass}} < 0$ are employed during the traction and passive phases respectively;
- the amplitude Δr of the variation of the cable length r during each cycle is imposed and it is relatively small (e.g. 50 m) with respect to the minimal cable length $\underline{r}$, which occurs at the beginning of each traction phase.

The third assumption makes it possible to consider, with little approximation error, a unique length value $\underline{r}$ for the cables during the whole operational cycle and consequently, together with the assumptions on constant line speed and angles θ and ϕ, unique values $F_{\text{trac}}^{\text{c,trc}}$ and $F_{\text{pass}}^{\text{c,trc}}$ of the cable forces generated in the traction and in the passive phases respectively. Then, on the basis of the considered assumptions, a simplified formulation for the average power $\overline{P}$ is obtained:

$$\overline{P} = \frac{\left(F_{\text{trac}}^{\text{c,trc}}\dot{r}_{\text{trac}}(t_{\text{trac,end}} - t_0)\right) + \left(F_{\text{pass}}^{\text{c,trc}}\dot{r}_{\text{pass}}(t_{\text{pass,end}} - t_{\text{trac,end}})\right)}{t_{\text{pass,end}} - t_0} \tag{4.29}$$

Note that also equation (4.28) could be employed in the following analyses, e.g. using numerical integration, however the increase of accuracy with respect to the simplified equation (4.29) would be negligible. Indeed, as it will be showed later on, the relation (4.29) gives a quite good estimate of the average power obtained in the numerical simulations. Now, by imposing a periodicity condition on the cable length r and considering the fixed cable length variation Δr, the time intervals $(t_{\text{trac,end}} - t_0)$ and $(t_{\text{pass,end}} - t_{\text{trac,end}})$ can be expressed as functions of $\dot{r}_{\text{trac}}$ and $\dot{r}_{\text{pass}}$ as follows (recalling that $\dot{r}_{\text{pass}} < 0$):

$$\begin{aligned}(t_{\text{trac,end}} - t_0) &= \frac{\Delta r}{\dot{r}_{\text{trac}}} \\ (t_{\text{pass,end}} - t_{\text{trac,end}}) &= \frac{-\Delta r}{\dot{r}_{\text{pass}}}\end{aligned} \tag{4.30}$$

On the basis of equations (4.29) and (4.30), through straightforward manipulations the following equation is obtained:

$$\overline{P} = \left(F_{\text{trac}}^{\text{c,trc}} - F_{\text{pass}}^{\text{c,trc}}\right) \frac{\dot{r}_{\text{trac}}\, \dot{r}_{\text{pass}}}{\dot{r}_{\text{pass}} - \dot{r}_{\text{trac}}} \tag{4.31}$$

Equation (4.31) can be used to optimally design the HE–yoyo operating parameters. Indeed, the values of the forces $F_{\text{trac}}^{\text{c,trc}}$ and $F_{\text{pass}}^{\text{c,trc}}$ depend on the parameters to be optimized, according to the theoretical equations (4.15)–(4.16) which assume a constant wind speed with respect to the elevation above the ground. If a wind profile is considered in equation (4.15) (e.g. the wind shear model introduced in Section 3.2), the optimal value of θ is in general lower than $\pi/2$, since a lower θ value means higher elevation and, consequently, stronger wind speed. Moreover, considering a variable wind speed, the generated power depends also on the line length r. In fact, the latter contributes to change the airfoil elevation Z:

$$Z = r\cos(\theta)$$

and, consequently, the nominal wind speed, according to the wind shear equation (3.26):

$$W_x(Z) = W_0 \frac{\ln\left(\dfrac{Z}{Z_r}\right)}{\ln\left(\dfrac{Z_0}{Z_r}\right)} = W_0 \frac{\ln\left(\dfrac{r\cos(\theta)}{Z_r}\right)}{\ln\left(\dfrac{Z_0}{Z_r}\right)}$$

where W_0, Z_0 and Z_r are the wind shear model parameters. Moreover, the coefficient C (4.16) also depends on r, due to its influence on line drag. Thus, in a more general case, the traction force on the cable is computed as:

$$F^{\text{c,trc}}(\theta,\phi,\dot{r},r) = C(r)\left(W_x(r\cos(\theta))\sin(\theta)\cos(\phi) - \dot{r}\right)^2$$

Again, it can be noted that the value of ϕ that gives the maximal traction force is $\phi^* = 0$, as it can be derived by intuition since $\phi = 0$ means that the airfoil is flying perfectly downwind. Thus in the operation of the HE–yoyo the value of ϕ is ideally zero during the traction phase. Note that in the passive phase a different value of ϕ would reduce the traction force on the cable, leading to lower energy expense. This phenomenon is exploited in the HE–yoyo operation with the low power recovery maneuver (see Sections 2.3.1 and 3.3.1). However, to change angle ϕ leads to a higher idle times between two subsequent traction and passive phases, since time is needed to move the airfoil at the requested position in terms of angle ϕ. Thus, in the HE–yoyo operation with wing glide maneuver the value $\phi = 0$ is chosen for the whole cycle, as it has been already done in the simulation tests of Section 3.4.1. With the chosen value of ϕ, the cable forces during the traction and passive phases can be computed as:

$$\begin{aligned} F_{\text{trac}}^{\text{c,trc}}(\theta_{\text{trac}},\dot{r}_{\text{trac}},\underline{r}) &= C_{\text{trac}}(r_{\text{trac}})\left(W_x(\underline{r}\cos(\theta_{\text{trac}}))\sin(\theta_{\text{trac}}) - \dot{r}_{\text{trac}}\right)^2 \\ F_{\text{pass}}^{\text{c,trc}}(\theta_{\text{pass}},\dot{r}_{\text{pass}},\underline{r}) &= C_{\text{pass}}(r_{\text{pass}})\left(W_x(\underline{r}\cos(\theta_{\text{pass}}))\sin(\theta_{\text{pass}}) - \dot{r}_{\text{pass}}\right)^2 \end{aligned} \tag{4.32}$$

where the values of C_{trac} and C_{pass} are computed according to (4.16), considering that different lift and drag coefficients have to be taken into account in the traction and in the passive phases, due to the wing glide maneuver (as explained in Sections 2.3.1 and 3.3.1). Therefore, the following optimization problem can be considered to design the operational parameters of the HE–yoyo:

$$\left(\theta^*_{\text{trac}},\dot{r}^*_{\text{trac}},\underline{r}^*,\theta^*_{\text{pass}},\dot{r}^*_{\text{pass}}\right) = \arg\max \overline{P}\left(\theta_{\text{trac}},\dot{r}_{\text{trac}},\underline{r},\theta_{\text{pass}},\dot{r}_{\text{pass}}\right)$$

Furthermore, operational constraints have to be taken into account in the optimization, in order to find out feasible operating conditions. In particular, the involved constraints regard the maximal and minimal cable unrolling/rewinding speed, the minimal elevation of the airfoil from the ground (considering also its maneuvering radius, see Section 2.1.1), the minimal angle θ during the cycle and the cable breaking force. The constraints on the line speed are the following:

$$\dot{r}_{\text{min}} \leq \dot{r} \leq \min(W_x(\underline{r}\cos(\theta))\sin(\theta),\dot{r}_{\text{max}})$$

where $\dot{r}_{\text{min}}, \dot{r}_{\text{max}}$ are either imposed by the limitations of the electric drives employed on the KSU or chosen in order to prevent excessive cable wear due to the high unrolling/rewinding speed. A minimal elevation $\underline{Z}$ can be imposed by requiring that (see Figure 4.4):

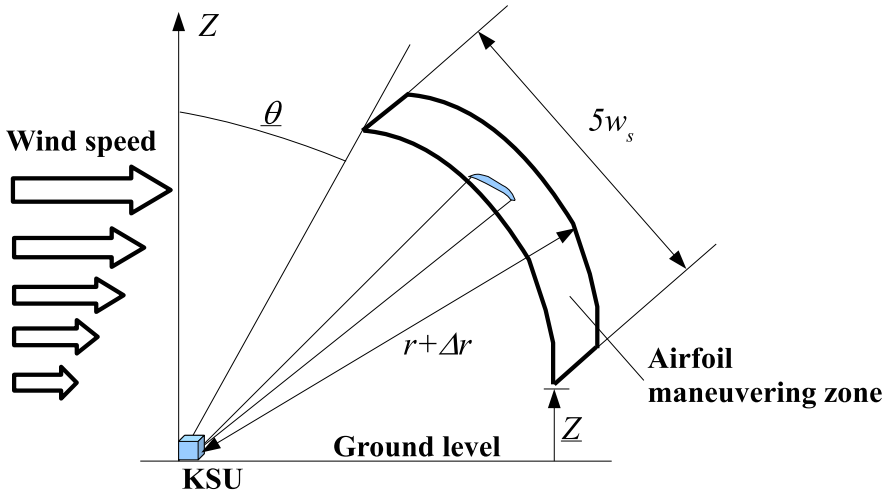

Figure 4.4. HE–yoyo operation: constraints on minimal elevation Z and on minimal angle θ.

$$\underline{r}\cos\left(\theta + \tfrac{5\,w_s}{2(\underline{r}+\Delta r)}\right) \geq \underline{Z}$$

where w_s is the airfoil wingspan (see Section 2.1.1). Indeed, the term $\frac{5\,w_s}{2(\underline{r}+\Delta r)}$ takes into account the variation of θ that may occur during the flight, due to the airfoil's minimal

maneuvering radius. A constraint on the minimal value of θ is also introduced, in order to keep the airfoil trajectory contained in a relatively small area and to obtain short idle time intervals between the traction and recovery phases:

$$\theta \geq \underline{\theta}$$

with $0 \leq \underline{\theta} \leq \pi/2$. Finally, the constraint related to the cable breaking load can be expressed, for two cables with a given cable diameter d_l, as:

$$\begin{aligned} F_{\text{trac}}^{\text{c,trc}} &\leq 2c_s\overline{F}(d_l) \\ F_{\text{pass}}^{\text{c,trc}} &\leq 2c_s\overline{F}(d_l) \end{aligned}$$

where $\overline{F}(\cdot)$ is the minimum breaking force of a single cable (see Figure 3.8 in Section 3.4) and c_s is a safety coefficient.
Considering all the described constraints, the optimization problem to be solved is given by:

$$\begin{gathered} \left(\theta^*_{\text{trac}},\dot{r}^*_{\text{trac}},\underline{r}^*,\theta^*_{\text{pass}},\dot{r}^*_{\text{pass}}\right) = \arg\max \overline{P}\left(\theta_{\text{trac}},\dot{r}_{\text{trac}},\underline{r},\theta_{\text{pass}},\dot{r}_{\text{pass}}\right) \\ \text{s. t.} \\ \dot{r}_{\text{min}} \leq \dot{r} \leq \min(W_x(\underline{r}\cos(\theta))\sin(\theta),\dot{r}_{\text{max}}) \\ \underline{r}\cos\left(\theta + \tfrac{5\,w_s}{2(\underline{r}+\Delta r)}\right) \geq \underline{Z} \\ \theta \geq \underline{\theta} \\ F_{\text{trac}}^{\text{c,trc}} \leq 2c_s\overline{F}(d_l) \\ F_{\text{pass}}^{\text{c,trc}} \leq 2c_s\overline{F}(d_l) \end{gathered} \tag{4.33}$$

Using the system data given in Table 4.2 and a wind shear profile with $Z_0 = 32.5\,\text{m}$, $W_0 = 7.4\,\text{m/s}$ and $Z_r = 6\,10^{-4}\,\text{m}$ (reported in Figure 4.5 and corresponding to the data collected at the site of Brindisi, Italy, during winter months, see Section 3.2), the solution of the optimization problem (4.33) is the following:

$$\begin{pmatrix} \theta^*_{\text{trac}} \\ \dot{r}^*_{\text{trac}} \\ \underline{r}^* \\ \theta^*_{\text{pass}} \\ \dot{r}^*_{\text{pass}} \end{pmatrix} = \begin{pmatrix} 68.4^\circ \\ 2.14\,\text{m/s} \\ 611\,\text{m} \\ 50^\circ \\ -6.0\,\text{m/s} \end{pmatrix} \tag{4.34}$$

The corresponding optimal average power value is equal to 2.10 MW. The optimal solution (4.34) has been employed to perform a numerical simulation of the HE–yoyo, in order to assess the control system performance and the matching between the theoretical equations and the dynamical model of the system. The model and control parameters employed in the simulation are showed in Table 4.3. The kite aerodynamical coefficients reported in Figure 3.7 have been employed in the traction phase. In order to better evaluate the matching between the theoretical equations and the numerical simulation, the latter has been performed with no wind disturbances. The results related to five complete cycles

Table 4.2. Optimization of a HE–yoyo operational cycle with wing glide maneuver: system parameters

A	500 m^2	Characteristic area
d_l	0.04 m	Diameter of a single line
$\overline{F}(d_l)$	1.50 10^6 N	Minimum breaking load of a single line
C_L	1.2	Average kite lift coefficient during the traction phase
E	13	Average kite efficiency during the traction phase
$C_{L,WG}$	0.1	Kite lift coefficient during wing glide maneuver
$C_{D,WG}$	0.5	Kite drag coefficient during wing glide maneuver
$C_{D,l}$	1.2	Line drag coefficient
ρ	1.2 HE/m^3	Air density
Δr	50 m	Maximum line variation during a cycle
$\dot{r}_{\text{min}}$	-6.0 m/s	Minimal line speed
$\dot{r}_{\text{max}}$	6 m/s	Maximal line speed
$\underline{Z}$	30 m	Minimal elevation from the ground
$\underline{\theta}$	50	Minimal angle θ
c_s	2	Safety coefficient
w_s	80 m	Airfoil wingspan

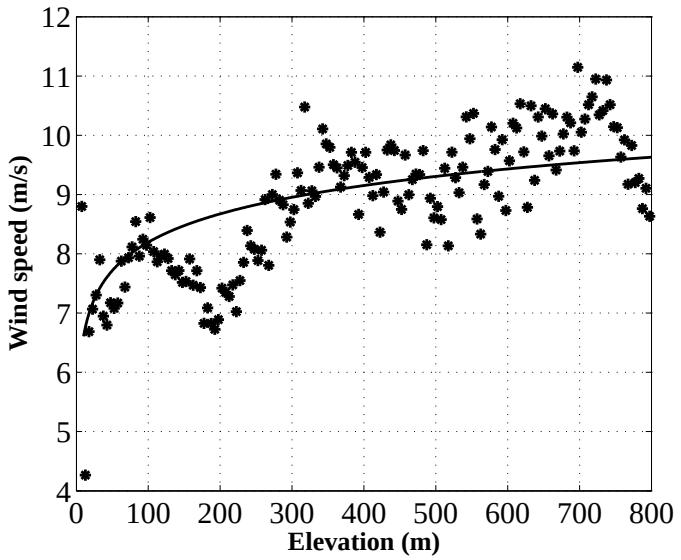

Figure 4.5. Wind shear model, related to the site of Brindisi (Italy) during winter months, employed in the simulation of the optimized HE–yoyo with wing glide recovery maneuver.

are reported. The obtained courses of the line length and kite trajectory are reported in Figures 4.6(a) and 4.6(b) respectively. The line length is kept between 610 and 660 m, as expected from the numerical optimization. As regards the kite trajectory, it can be noted

Table 4.3. Numerical simulation of a HE–yoyo with optimized operational cycle: system and control parameters.

m	300 HE	Kite mass
A	500 m^2	Characteristic area
d_l	0.04 m	Diameter of a single line
ρ_l	970 HE/m^3	Line density
$C_{L,WG}$	0.1	Kite lift coefficient during wing glide maneuver
$C_{D,WG}$	0.5	Kite drag coefficient during wing glide maneuver
$C_{D,l}$	1.2	Line drag coefficient
α_0	3.5°	Base angle of attack
ρ	1.2 HE$/$m^3	Air density
Δr	50 m	Maximum line variation during a cycle
θ_I	55°	Traction phase starting conditions
ϕ_I	45°	
$\underline{r}$	610 m	
$\overline{r}$	660 m	Passive phase starting condition
$\overline{\theta}_{III}$	50°	Wing glide starting condition
$\overline{\theta}$	70°	State constraint
$\overline{\psi}$	6°	Input constraints
$\overline{\dot{\psi}}$	20°$/$s	
$\overline{\dot{r}}$	3.69 m/s	Traction phase reference $\dot{r}_{\text{ref}}$
$\underline{\dot{r}}$	-6.0 m/s	Passive phase reference $\dot{r}_{\text{ref}}$
T_c	0.2 s	Sample time
N_c	1 steps	Control horizon
N_p	10 steps	Prediction horizon

that during the traction phase the kite follows "figure eight" orbits and that its elevation Z goes from about 214 m to 389 m, corresponding to a mean value of $\theta(t)$ equal to 68° (according to the optimized value), while the lateral angle $\phi(t)$ oscillates between $\pm 10°$ with zero in average. The power generated in the simulation is reported in Figure 4.7(a): the mean value is 1.96 MW, thus showing an error of only about 6% with respect to the optimal value, due to the presence of the inertial and apparent forces, the cable weight and the idle time between the traction and passive phases. In fact, such aspects are not taken into account in the theoretical equations. Figure 4.8 shows the comparison between the course of generated power obtained in the simulation, and the corresponding result of the theoretical equation (4.17), computed taking into account the nominal wind speed given by the employed wind shear model. It can be noted that a quite good matching exist, both in the traction and in the passive phases. The course of the traction force $F^{\text{c,trc}}$ acting on a single cable is showed in Figure 4.7(b): it can be noted that the obtained maximal value

of is about half the breaking load of $1.50\,10^6$, according to the safety coefficient $c_s = 2$ employed in the optimization procedure. In fact, at the optimal solution (4.34) of problem (4.33), the constraint on the cable break load results to be active, thus indicating again the good matching between theoretical equations and numerical simulations. Finally, the

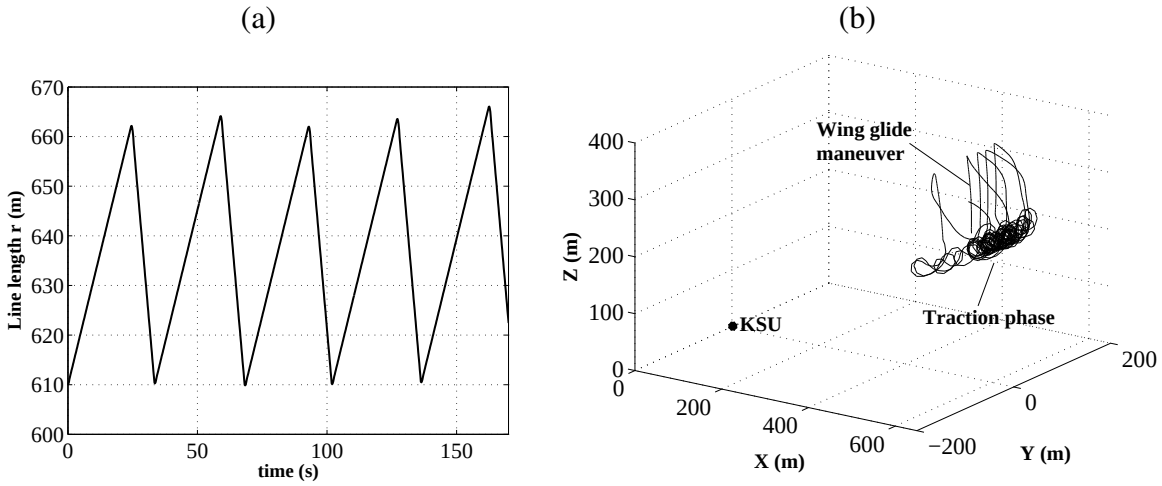

Figure 4.6. Optimized operation of a HE–yoyo with wing glide maneuver. (a) Line length $r(t)$ and (b) kite trajectory during five complete cycles.

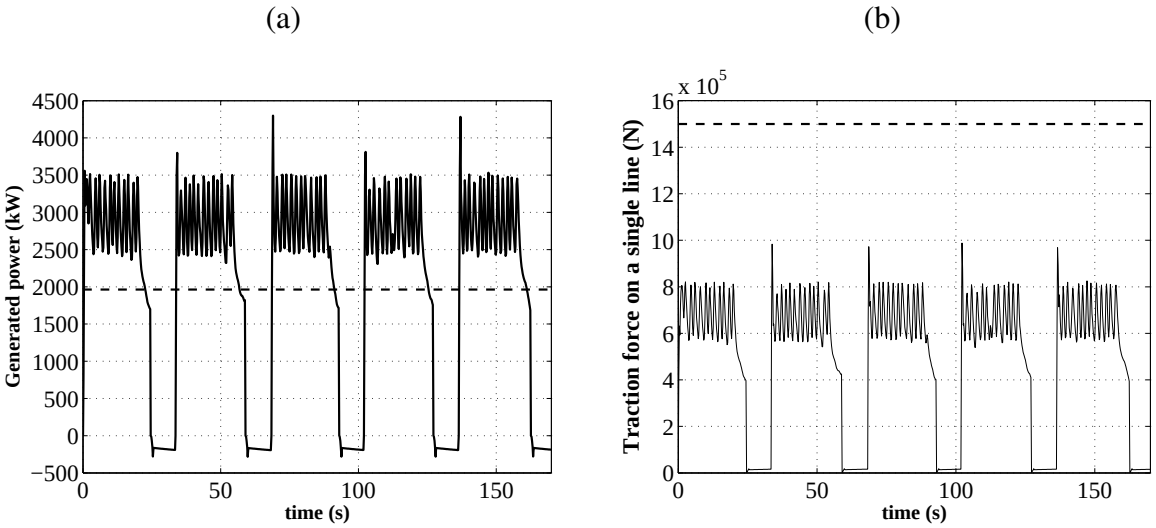

Figure 4.7. Optimized operation of a HE–yoyo with wing glide maneuver. (a) Mean (dashed) and actual (solid) generated power and (b) traction force on each cable $F^{\mathrm{c,trc}}$ (solid) and maximal breaking load (dashed) during five complete cycles.

courses of the kite efficiency and of the lift and drag coefficients are reported in Figure

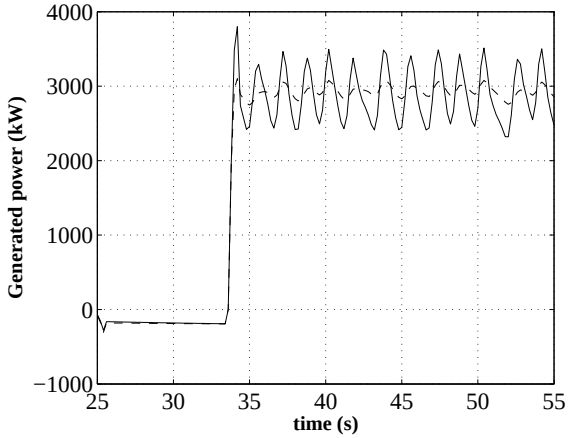

Figure 4.8. Optimized operation of a HE–yoyo with wing glide maneuver. Comparison between the power values obtained in the numerical simulation (solid) and using the theoretical equations (dashed).

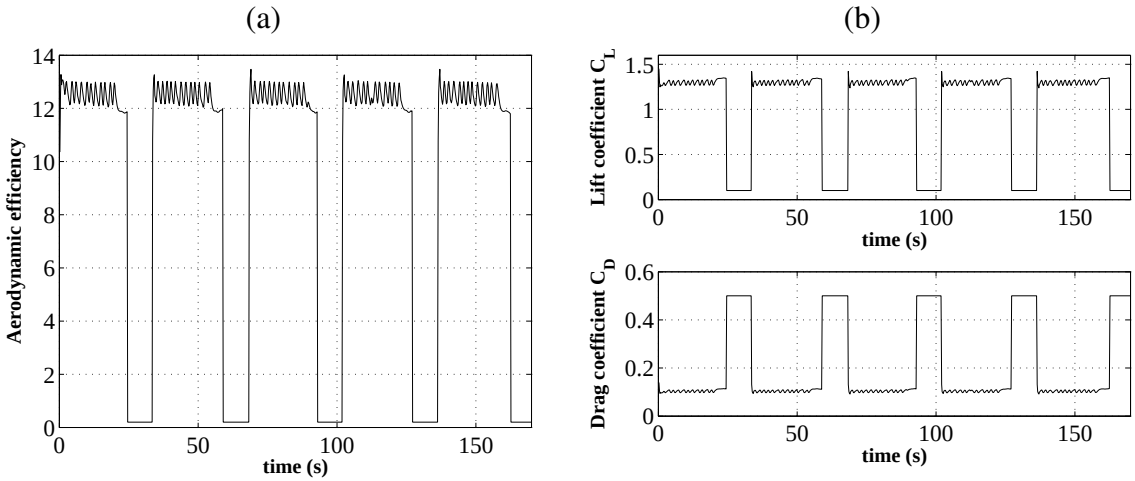

Figure 4.9. Optimized operation of a HE–yoyo with wing glide maneuver. Kite (a) aerodynamic efficiency and (b) lift and drag coefficients during five complete cycles.

4.9(a)–(b). The aerodynamic efficiency is between 12 and 13.1 in the traction phases, with a mean value of 12.5.

4.3 HAWE scalability

In this Section, the scalability of HAWE is studied using both numerical optimization and simulation tools, in order to understand the effects, on the power generation performance,

of different values of kite area and efficiency, cable length and wind speed. In the performed analyses, if not differently specified, a kite area of 500 m^2 has been considered, as well as the aerodynamic characteristics reported in Figure 3.7 (and, in the numerical optimization, average values of efficiency E and lift coefficient C_L of 13 and 1.2 respectively). For each considered combination of the involved parameters, the cable diameter has been dimensioned in accordance with the traction force exerted by the kite, which varies with the different considered parameter values. To this end, the breaking load characteristic reported in Figure 3.8 has been employed, considering a safety coefficient of 1.2 . The optimization procedure described in Section 4.2 has been used to compute the optimal average generated power with a fine grid of values of the considered parameters, while numerical simulations have been employed with a larger grid of values, to verify the good matching with the optimization results.

I) Kite area. The obtained average power as a function of the kite area is showed in Figure 4.10(a): a linear dependence can be observed, as expected from the aerodynamic laws. In these analyses, a fixed wind speed of 9 m/s has been imposed regardless of kite flight altitude.

II) Aerodynamic efficiency. The analyses have been realized by scaling the aerodynamic drag coefficient of the kite, so that different values of aerodynamic efficiency were obtained. A constant wind speed of 9 m/s has been considered regardless of kite flight altitude. Note that the traction force exerted by the kite on the cables grows with the square of kite aerodynamic efficiency. Thus if a fixed value of cable diameter were considered, the mean net power would increase with the square of kite aerodynamic efficiency. Figure 4.10(b) shows the generated power as a function of the kite aerodynamic efficiency, considering a cable diameter dimensioned to resist to the traction forces.

III) Cable length. The cable length can positively influence the generated power if the wind speed increases with the elevation with respect to the ground, depending on the rate of such increase. In Figure 4.10(c) the dependence of the mean net power on the cable length is reported for the wind shear models of Figure 3.6, related to the winter and summer months at De Bilt site, in the Netherlands. It can be observed that in both cases there is an optimal point (corresponding to about 1200 m and 1300 m for winter and summer wind, respectively) in which the positive effect of higher wind speed values, obtained with longer cables, is counter–balanced by the negative effect of higher cable weight and drag force. Beyond this point, an increase of cable length leads to lower mean generated power.

IV) Wind speed. The dependance of the mean generated power on wind speed is shown in Figure 4.10(d). It can be noted that, as expected, a cubic relationship exists between these two variables. In particular, note that the same 500–m^2 kite can

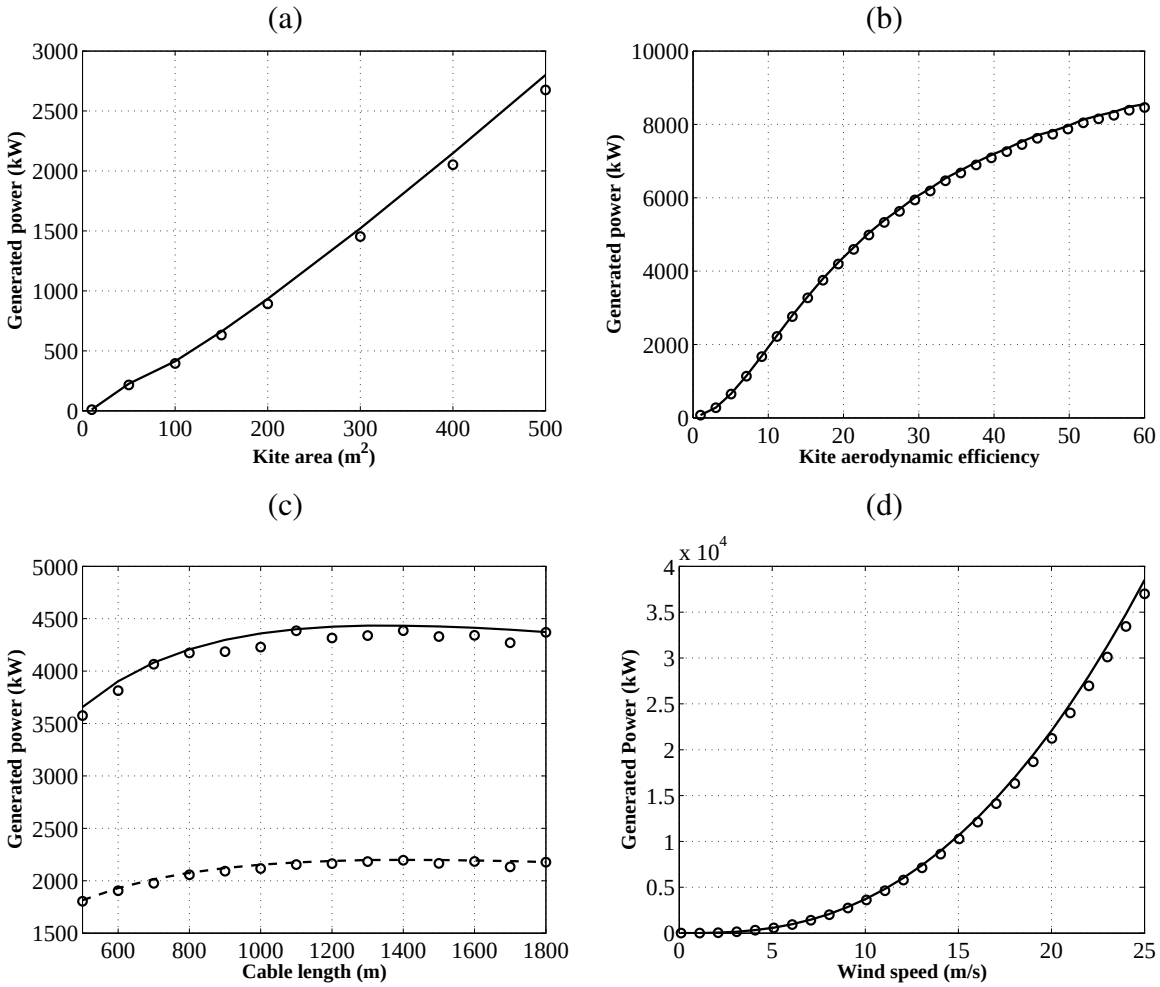

Figure 4.10. Generated net power as a function of (a) kite area, (b) aerodynamic efficiency, (c) cable length for winter (solid) and summer (dashed) periods at The Bilt, in the Netherlands, and (d) wind speed. Solid line: numerical optimization result. Circles: numerical simulation results.

be used to obtain either a HE–yoyo with 2–MW rated power, with 9–m/s wind speed, or a HE–yoyo with 10–MW rated power, with 15–m/s wind speed, without a significant cost increase, except for the electric equipments. Figure 4.11(a) shows the power curves obtained with two HE–yoyo units with 2–MW and 5–MW rated power. It can be noted that a quite high cut–out speed is achieved: this is due to the possibility of HAWE to make the traction forces decrease, in presence of very strong winds, by increasing the line unrolling speed and/or raising the airfoil to lower θ angles. Figure 4.11(b) shows a comparison between the power curves of a 2–MW, 500-m^2 area HE–yoyo and a 2–MW, 90–m diameter wind turbine [48]. Note that

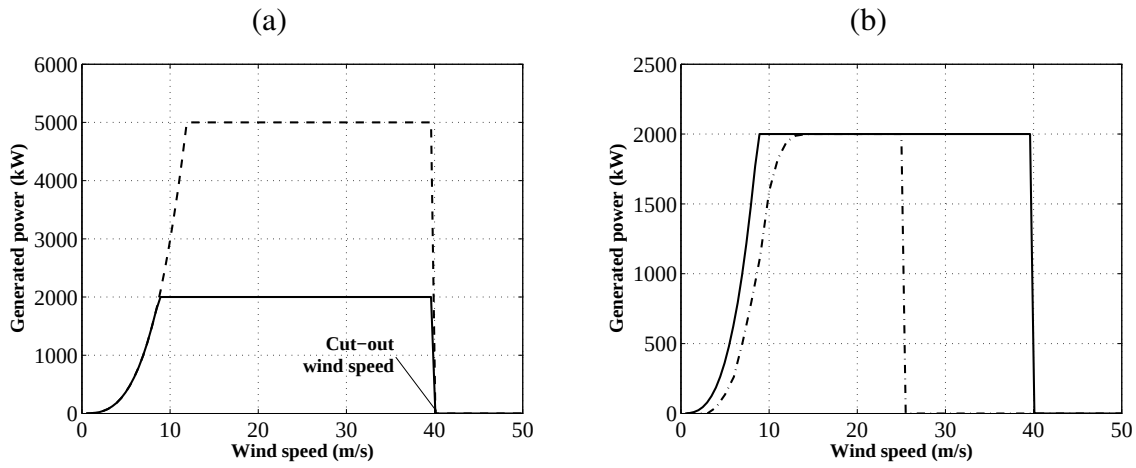

Figure 4.11. (a) Power curves of a 2–MW (solid) and of a 5–MW (dashed) rated power HE–yoyo. (b) Comparison between the power curves obtained by a 2–MW, 90–m diameter wind turbine (dashed) and a 2-MW, 500 m^2 HE–yoyo (solid).

the rated power is reached with 9 m/s wind speed by the HE–yoyo, while about 13 m/s are needed by the wind turbine. Moreover, the turbine cut–out speed is about 25 m/s, while about 40 m/s are obtained for the HE–yoyo. Such considerations are useful to perform a preliminary estimate of the energy production potential of a HAWE generator and of the related energy cost (see Chapter 6).

4.4 Optimization of a high–altitude wind farm

In this Section, the problem of suitably allocating and designing the operational cycles of several HE–yoyo generators on a given territory is considered, in order to maximize the average generated power per unit area while avoiding collision and aerodynamic interferences among the various kites. Indeed, in the present wind farms, in order to limit the aerodynamic interferences between wind turbines of a given diameter D, a distance of $7D$ in the prevalent wind direction and of $4D$ in the orthogonal one are typically used (see Section 1.2.1 and [25, 51]).
In a HE–farm, collision and aerodynamic interference avoidance are obtained if the space regions, in which the different kites fly, are kept separated. At the same time, to maximize the generated power density per km^2 of the HE–farm, it is important to keep the distance between the KSUs as short as possible. As already highlighted in the simulations of Section 3.4.1, the kite trajectory in a HE–yoyo generator with wing glide recovery maneuver is kept inside a space region which is limited by a polyhedron of given dimension $a \times a \times \Delta r$ (see Fig. 4.12). The value of a approximately depends on the kite wingspan,

which influences its minimal turning radius during the flight, while Δr is a design parameter which imposes the maximal range of cable length variation during the HE–yoyo cycle. A group of 4 HE–yoyo units, placed at the vertices of a square with sides of length

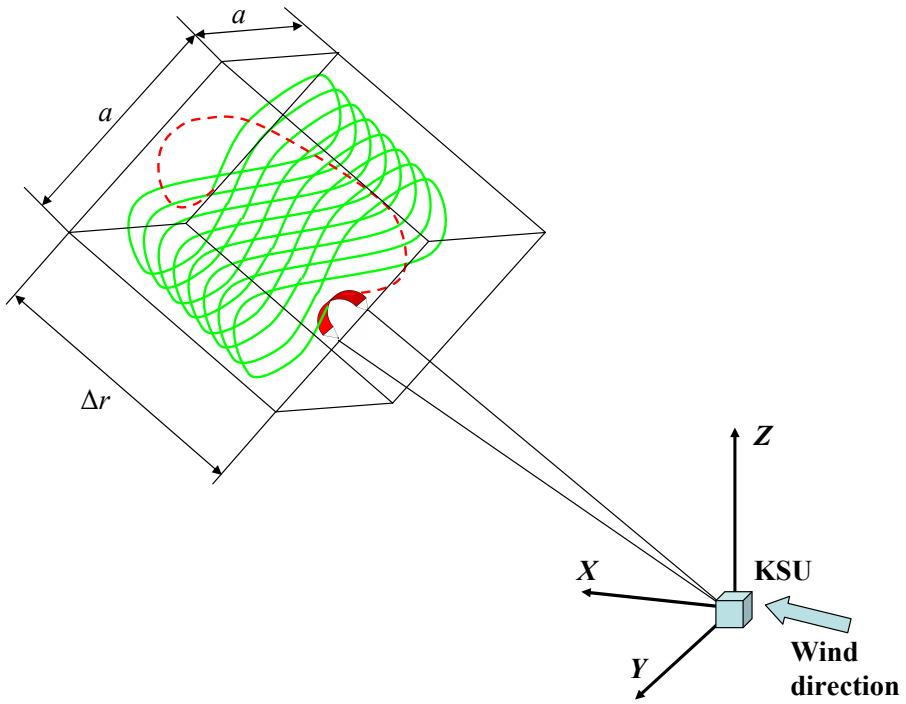

Figure 4.12. HE–yoyo cycle with wing glide maneuver: traction (solid) and passive (dashed) phases. The kite is kept inside a polyhedral space region whose dimensions are $(a \times a \times \Delta r)$ meters.

L, is now considered (see Fig. 4.13). The minimum cable length of the upwind kites is indicated with $\underline{r}_1$, while $\underline{r}_2$ is the minimum cable length of the downwind kites and Δr is the cable length variation of all the kites during the flight. Finally, θ_1 and θ_2 are the average inclinations of the upwind and downwind kites respectively, with respect to the vertical axis Z (see Fig. 4.13). For given characteristic of wind, kite, cables, etc., the values of $L, \underline{r}_1, \underline{r}_2, \theta_1$ and θ_2 can be computed to maximize the average net power per km^2 generated by the four HE–yoyo generators, subject to the constraints that the polyhedra limiting the kite flight regions do not intersect and that the maximum flight elevation of the downwind kites is lower than the minimum elevation of the upwind ones, so to avoid aerodynamic interferences. Moreover, the other operational parameters of each of the HE–yoyo units, i.e. the line rolling and unrolling speed values in the traction and passive phases, can be optimized as well. In particular, denote with $\overline{P}_1$ and $\overline{P}_2$ the average power obtained by the upwind and by the downwind generators respectively. As showed in Section 4.2, $\overline{P}_1$ and $\overline{P}_2$ are functions of $\theta_1, \dot{r}_{\text{trac},1}, \underline{r}_1, \dot{r}_{\text{pass},1}$ and of $\theta_2, \dot{r}_{\text{trac},2}, \underline{r}_2, \dot{r}_{\text{pass},2}$,

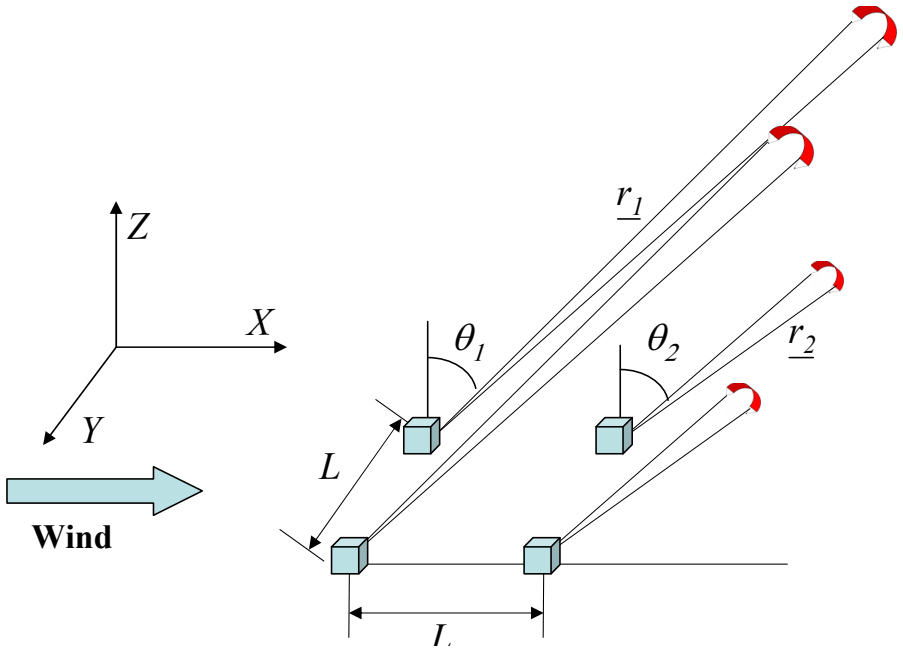

Figure 4.13. Group of 4 HE–yoyo placed on the vertices of a square land area.

where $\dot{r}_{\text{trac},1}, \dot{r}_{\text{pass},1}$ are the line unrolling and winding back speed values of the upwind HE–yoyo and $\dot{r}_{\text{trac},2}, \dot{r}_{\text{pass},2}$ are the line speed values of the downwind HE–yoyo. Note that, differently from the optimization of a single HE–yoyo performed in Section 4.2, a unique θ value is now considered for both the traction and the passive phases of the HE–yoyo. However, the analysis can be easily generalized to include different θ values for the two operational phases.
In a single group of 4 HE–yoyo units, considering as occupied land only the area in between the generators, the power density $\overline{P}_D$ per unit area can be computed as follows:

$$\overline{P}_D = \frac{2(\overline{P}_1 + \overline{P}_2)}{L^2} \tag{4.35}$$

If more basic groups are arranged together in a large square area, in such a way that along the wind direction any two subsequent HE–yoyo units gives different average power values and in the direction perpendicular to the wind any two subsequent HE–yoyo units give the same average power (i.e. $\overline{P}_1$ or $\overline{P}_2$, see Figure 4.14), the obtained power density is:

$$\overline{P}_D = \frac{N^2(\overline{P}_1 + \overline{P}_2)}{2(N-1)^2 L^2}$$

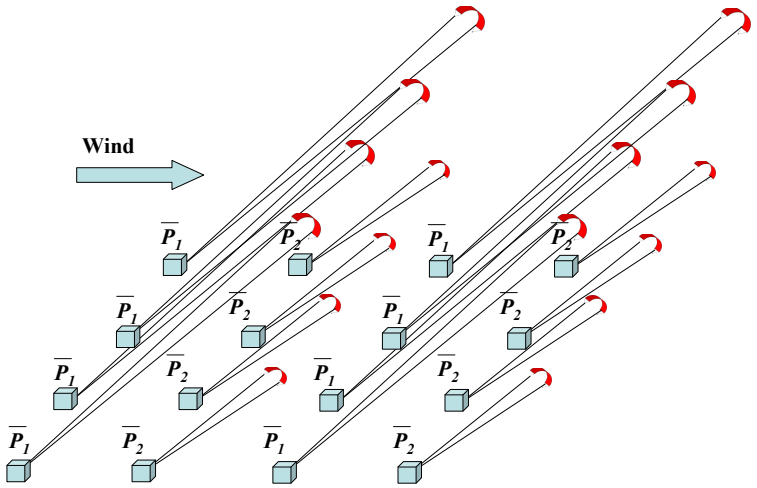

Figure 4.14. HE–farm composed of basic groups of 4 HE–yoyo units.

where N is the number of units on the side of the square. By letting $N \to \infty$, the following relation is obtained:

$$\overline{P}_D = \lim_{N\to\infty} \frac{N^2(\overline{P}_1 + \overline{P}_2)}{2(N-1)^2 L^2} = \frac{(\overline{P}_1 + \overline{P}_2)}{2} \frac{1}{L^2} \tag{4.36}$$

Thus, the average power density of the considered wind farm is given by the mean power of two subsequent units (along the wind direction) divided by the square of their distance. The value of $\overline{P}_D$ (4.36) clearly depends on the involved operational and design parameters $\theta_1, \dot{r}_{\text{trac},1}, \underline{r}_1, \dot{r}_{\text{pass},1}, \theta_2, \dot{r}_{\text{trac},2}, \underline{r}_2, \dot{r}_{\text{pass},2}, L$. Thus, the following numerical optimization

problem can be set up and solved to design the HE–farm configuration and operation:

$$
\begin{gathered}
\left(\theta_1^*, \dot{r}_{\text{trac},1}^*, \underline{r}_1^*, \dot{r}_{\text{pass},1}^*, \theta_2^*, \dot{r}_{\text{trac},2}^*, \underline{r}_2^*, \dot{r}_{\text{pass},2}^*, L^*\right) = \arg\max \overline{P}_D \\
\text{s. t.} \\
\dot{r}_{\min} \leq \dot{r}_1 \leq \min(W_x(\underline{r}_1 \cos(\theta_1))\sin(\theta_1), \dot{r}_{\max}) \\
\underline{r}_1 \cos(\theta_1 + \Delta\theta_1) \geq \underline{Z} \\
F_{\text{trac},1}^{\text{c,trc}} \leq 2c_s\overline{F}(d_l) \\
F_{\text{pass},1}^{\text{c,trc}} \leq 2c_s\overline{F}(d_l) \\
\dot{r}_{\min} \leq \dot{r} \leq \min(W_x(\underline{r}_2 \cos(\theta_2))\sin(\theta_2), \dot{r}_{\max}) \\
\underline{r}_2 \cos(\theta_2 + \Delta\theta_2) \geq \underline{Z} \\
F_{\text{trac},2}^{\text{c,trc}} \leq 2c_s\overline{F}(d_l) \\
F_{\text{pass},2}^{\text{c,trc}} \leq 2c_s\overline{F}(d_l) \\
(\underline{r}_2 + \Delta r)\cos(\theta_2 - \Delta\theta_2) - \underline{r}_1 \cos(\theta_1 + \Delta\theta_1) \leq 0 \\
\underline{r}_1 \sin(\Delta\theta_1) - \frac{L}{2} \leq 0 \\
\underline{r}_2 \sin(\Delta\theta_2) - \frac{L}{2} \leq 0 \\
((\underline{r}_2 + \Delta r)\sin(\theta_2 + \Delta\theta_2) - L)/\tan(\theta_1 - \Delta\theta_1) - (\underline{r}_2 + \Delta r)\cos(\theta_2 + \Delta\theta_2) \leq 0 \\
(\underline{r}_2 + \Delta r)\cos(\theta_2 - \Delta\theta_2) - (L + (\underline{r}_2 + \Delta r)\sin(\theta_2 - \Delta\theta_2))/\tan(\theta_1 + \Delta\theta_1) \leq 0 \\
\Delta\theta_1 - \theta_1 \leq 0 \\
\Delta\theta_2 - \theta_2 \leq 0
\end{gathered}
\tag{4.37}
$$

where $\Delta\theta_1 = \frac{5\,w_s}{2(\underline{r}_1+\Delta r)}$ and $\Delta\theta_2 = \frac{5\,w_s}{2(\underline{r}_2+\Delta r)}$. The constraints included in (4.37) prevent interference between the airfoil flying zones, both in the parallel and perpendicular directions with respect to the wind. Using the system data given in Table 4.4 and a wind shear profile with $Z_0 = 32.5\,\text{m}$, $W_0 = 7.4\,\text{m/s}$ and $Z_r = 6\,10^{-4}\,\text{m}$ (reported in Figure 4.5 and corresponding to the data collected at the site of Brindisi, Italy, during winter months, see Section 3.2), the solution of the optimization problem (4.37) is the following:

$$
\begin{pmatrix}
\theta_1^* \\
\dot{r}_{\text{trac},1}^* \\
\underline{r}_1^* \\
\dot{r}_{\text{pass},1}^* \\
\theta_2^* \\
\dot{r}_{\text{trac},2}^* \\
\underline{r}_2^* \\
\dot{r}_{\text{pass},2}^* \\
L
\end{pmatrix}
=
\begin{pmatrix}
46.5^\circ \\
2.3\,\text{m/s} \\
1100\,\text{m} \\
-6.0\,\text{m/s} \\
51.7^\circ \\
2.2\,\text{m/s} \\
232\,\text{m} \\
-6.0\,\text{m/s} \\
250\,\text{m}
\end{pmatrix}
\tag{4.38}
$$

With the obtained value of L, the distance between each pair of airfoils flying at the same elevation is about 500 m, thus limiting also aerodynamic interference. The obtained power density is 20 MW/km^2, with 16 HE–yoyo units per km^2. If electrical generators with 2–MW rated power are equipped on each HE–yoyo, a rated power of 32 MW/km^2 is achieved by the HE–farm. Note that an actual wind farm composed of 90–m diameter,

Table 4.4. Optimization of a HE-farm: system parameters

A	500 m^2	Characteristic area
d_l	0.04 m	Diameter of a single line
$\overline{F}(d_l)$	1.50 10^6 N	Minimum breaking load of a single line
C_L	1.2	Average kite lift coefficient during the traction phase
E	13	Average kite efficiency during the traction phase
$C_{L,WG}$	0.1	Kite lift coefficient during wing glide maneuver
$C_{D,WG}$	0.5	Kite drag coefficient during wing glide maneuver
$C_{D,l}$	1.2	Line drag coefficient
ρ	1.2 HE/m^3	Air density
Δr	50 m	Maximum line variation during a cycle
$\dot{r}_{\text{min}}$	-6.0 m/s	Minimal line speed
$\dot{r}_{\text{max}}$	6 m/s	Maximal line speed
$\underline{Z}$	30 m	Minimal elevation from the ground
$\underline{\theta}$	50	Minimal angle θ
c_s	2	Safety coefficient
w_s	50 m	Airfoil wingspan

2–MW turbines has a density of 4.4 turbines per km^2 and a corresponding rated power density of only about 9 MW. A more detailed comparison between a HE–farm and an actual wind farm is carried out in Chapter 6. Once the HE–farm configuration has been designed in "nominal" conditions (i.e. according to the nominal wind profile of the selected location), it is possible to derive its power curve using optimization and simulation tools. In particular, numerical optimization can be employed to compute the operational parameters with different values of wind speed. As it will be showed in Chapter 6, the power curve can then be used, together with the analysis of wind speed data related to the considered site, to estimate the capacity factor obtained by the HAWE technology. In order to compute the power curve of the designed HE–farm, the optimization problem (4.37) is solved assuming that the values of $\underline{r}_1, \underline{r}_2$ and L are not modified with respect to the values optimized in the nominal conditions. Thus, only the variables $\theta_1, \dot{r}_{\text{trac,1}}, \dot{r}_{\text{pass,1}}, \theta_2, \dot{r}_{\text{trac,2}}$ and $\dot{r}_{\text{pass,2}}$ have to be optimized again. Figure 4.15 shows the power curve obtained for the HE–farm with nominal parameters (4.38), considering a rated power of 2 MW for each HE–yoyo. It can be noted that, as it happens for a single HE–yoyo (Figure 4.11(a)), a much higher cut–out wind speed is achieved with respect to that of a wind turbine (see Figure 4.11(b)). Indeed, in HAWE the cut–out wind speed is related to the cable and/or kite breaking due to the excessive traction forces. By suitably changing the unrolling speed or the angle θ with respect to the vertical axis, it is possible to make the traction force decrease while still generating power. However, a lower cut–out speed is achieved in a HE–farm with respect to a single HE–yoyo (see Figures 4.11(a) and 4.15): this is due

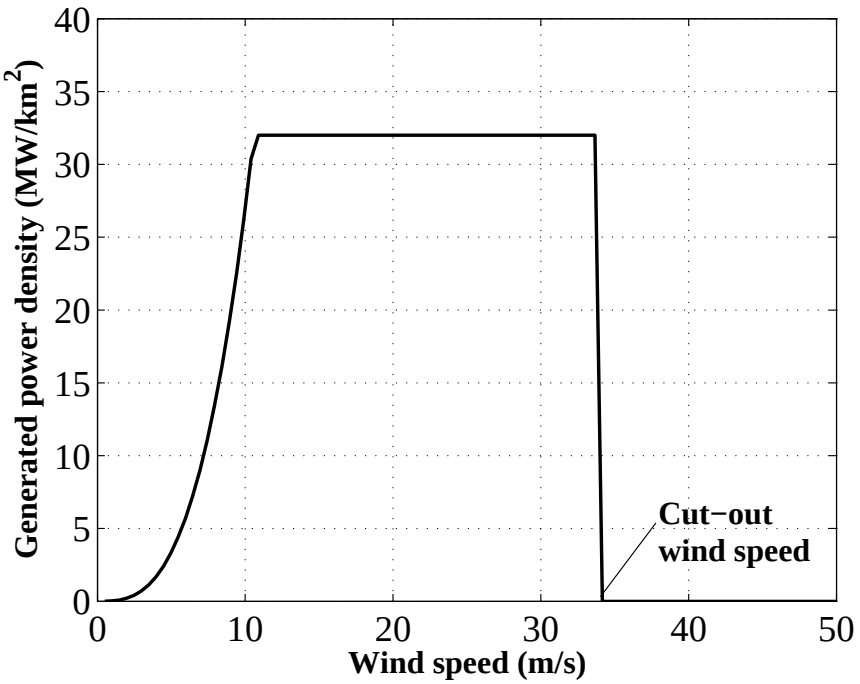

Figure 4.15. Power curve of a HE–farm composed of 2–MW, 500–m^2 HE–yoyo units.

to the fact that in the case of a wind farm such counteractions, particularly the increase of θ angle, are limited by the constraints imposed by the nearby kite flying zones. Such an aspect is highlighted in Figure 4.16, which shows the optimal operating conditions with two different absolute wind speed values. Thus, the presented results show that a HAWE system can have a much larger operating range than an actual wind turbine and that a HE–farm can achieve a much higher rated power density than a wind turbine farm.
In Chapter 6, the energy generation potential of HAWE is investigated further and an estimate of the cost of high–altitude wind energy is computed and compared with the cost of the present wind energy and of fossil energy.

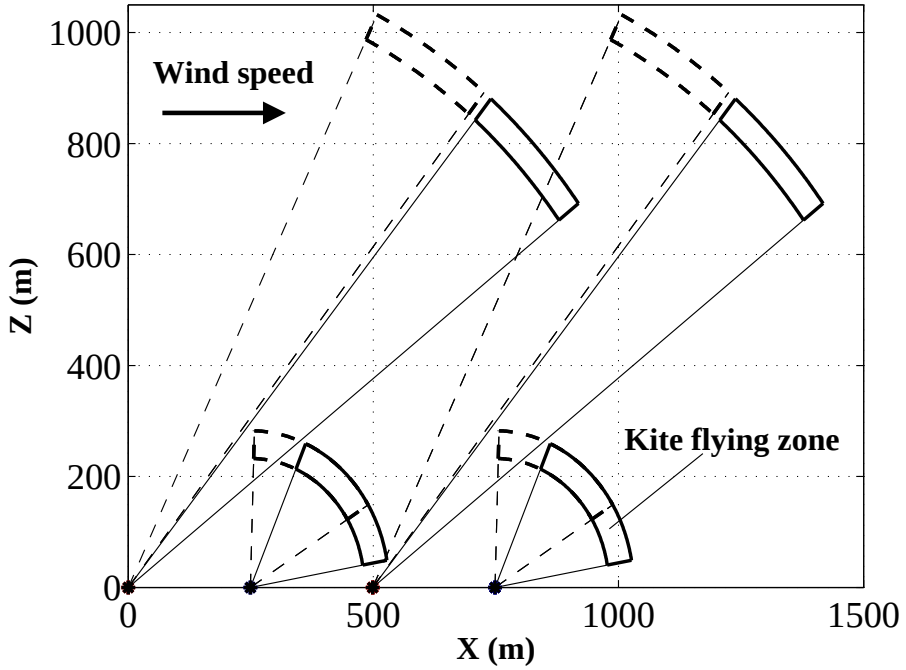

Figure 4.16. HE–farm operation with weaker wind speed (solid) and with stronger wind speed (dashed)

Chapter 5

Experimental activities

At Politecnico di Torino a small scale HE–yoyo prototype has been built, in order to experimentally verify the validity of the HAWE concept. The design of the prototype has been carried out in part on the basis of simulation results obtained with the model and control technique described in Chapter 3. In this Chapter, such simulation results are briefly recalled and the constructed prototype is described. Then, a comparison between the first collected experimental data and the results of the numerical simulations is performed.

5.1 Simulation of a small scale HE–yoyo

The numerical simulations presented in this Section have been employed in the design process of the HE–yoyo prototype. In particular, the simulated courses of the traction forces acting on the cables and of their direction have been used to dimension the mechanical structure and the transmission organs of the KSU. The low power passive phase has been considered. The model and control parameters are reported in Table 5.1. As regards the wind speed, in these simulations the following model has been considered:

$$W_x(Z) = \begin{cases} 0.02Z + 4 \text{ m/s} & \text{if } Z \leq 100\,\text{m}, \\ 0.0086(Z-100) + 6 \text{ m/s}, & \text{if } Z > 100\,\text{m}. \end{cases} \tag{5.1}$$

The nominal wind speed is 4 m/s at 0 m of altitude and grows to 6 m/s at 100 m altitude and to 7.7 m/s at 300 m altitude. Moreover, wind turbulence is introduced, with uniformly distributed random components along the inertial axes (X,Y,Z). The absolute value of each component of $\vec{W}_t$ ranges from 0 m/s to 3 m/s, which corresponds to 50% of the nominal wind speed at 100 m altitude.
Figure 5.1(a) shows the trajectory of the kite during three complete cycles, while the generated power is reported in Figure 5.1(b). The mean power is 5 kW. The magnitude of the traction force acting on the cable is showed in Figure 5.1(c). A maximal value of about 0.7 t for each cable is obtained. Finally, the course of cable length is kept between 400 m and 800 m (see Figure 5.1(d)).

Table 5.1. Model and control parameters employed in the simulation a small scale HE–yoyo generator

m	4 kg	Kite mass
A	10 m^2	Characteristic area
d_l	0.003 m	Diameter of a single line
ρ_l	970 kg/m^3	Line density
$C_{D,l}$	1.2	Line drag coefficient
α_0	3.5°	Base angle of attack
ρ	1.2 kg/m^3	Air density
$\overline{\dot{r}}$	2.2 m/s	Traction phase reference for $\dot{r}$
$\underline{\dot{r}}$	-5.5 m/s	passive phase reference for $\dot{r}$
θ_I	55°	Traction phase starting conditions
ϕ_I	45°	
$\underline{r}$	400 m	
$\overline{r}$	800 m	1st passive sub–phase starting conditions
$\underline{\phi}_{II}$	45°	2nd passive sub-phase starting conditions
$\overline{\theta}_{II}$	20°	
$\overline{\theta}$	75°	State constraint
$\overline{\psi}$	6°	Input constraints
$\overline{\dot{\psi}}$	20°/s	
T_c	0.2 s	Sample time
N_c	1 steps	Control horizon
N_p	10 steps	Prediction horizon

5.2 HAWE prototype

This Section briefly describes the small scale HE–yoyo prototype built at Politecnico di Torino, Italy. The prototype is fastened on a light truck, allowing to perform tests at different locations.

The airfoils. The employed airfoils are commercial power kites with an inflatable structure, normally used for kite surfing (see Figure 5.2). Kite with projected area ranging from 8 to 18 m^2 are used with the prototype. Note that these airfoils, though light, are not optimal for energy generation since they are usually designed to be less powerful, for safety reasons.

The cables. The two cables equipped on the prototype are 1000–m long, made of composite fibers (Dyneema®) with high traction resistance a density of about 0.970 kg/dm^3 (see Figure 5.3). The minimum breaking load of the employed cables as a function of the diameter is reported in Figure 3.8 of Section 3.4. The cables employed on the prototype have a diameter of 4 mm and a breaking load of 1.3 t, i.e. about twice the traction force

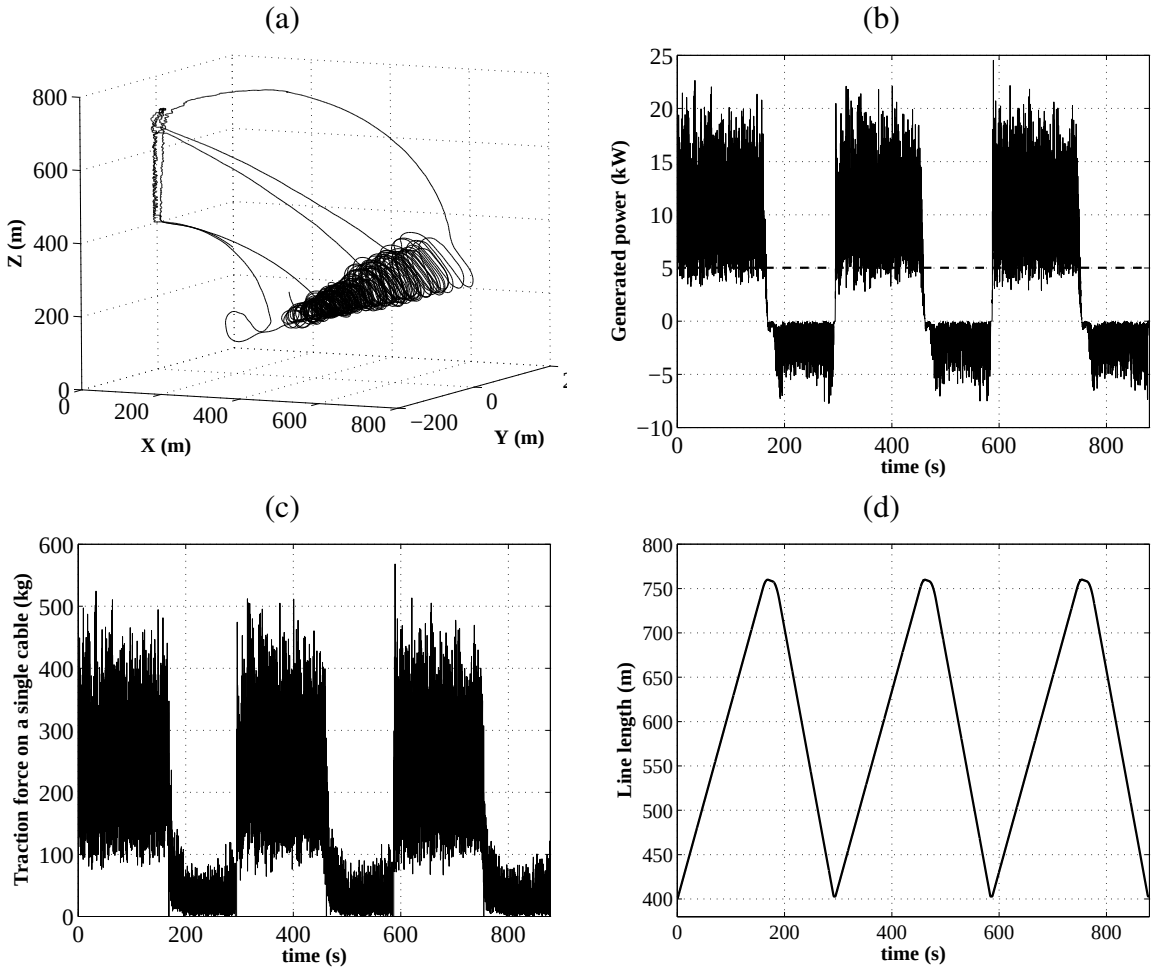

Figure 5.1. Simulation results of a small scale HE–yoyo unit. Obtained (a) kite trajectory and courses of (b) generated power, (c) traction force acting on a single cable and (d) line length.

values obtained in simulation. The cables are highly resistant to traction, however their fiber shows high wear if the operational temperature raises above 60–65°C.

Mechanical structure and electric drives. The mechanical and electrical components of the prototype are showed in Figure 5.4. The cables are winded around two steel drums of about 1–m length and 0.3–m diameter. A series of small winches allow to direct each cable in such a way that its direction is perpendicular to the rotational axis of the related drum. Two small electric drives, of 1 kW–power each, are employed to translate the position of the two cables with respect to their drums, while the cables are being unrolled/rewinded, in order to properly distribute the winded line along all of the drum length. Two electric drives with 20–kW peak power and 10–kW rated power are employed on the prototype to generate energy. The energy produced is accumulated in a

Figure 5.2. Power kites employed with the HAWE prototype.

Figure 5.3. Cables equipped on the HAWE prototype.

stack of batteries which have a total voltage of about 340 V. A steel structure bears the drives, the drums and the winches.

5.3 Comparison between numerical and experimental results

In this Section, experimental data obtained with the small-scale yo–yo prototype built at Politecnico di Torino are showed and compared to simulation results, in order to assess the matching between simulated and real generated energy. Such evaluation is useful to estimate the confidence level in the simulation results obtained in Sections 3.4 and 4.2. In particular, the measured generated power, line length and line speed related to two different experimental sessions are reported (see Figure 5.5(a)–(f)). In both cases, the kite

Figure 5.4. Small scale HE–yoyo prototype.

was controlled by a human operator. The collected measured values of line speed have been employed as reference speed to perform a simulation with the model described in Section 3.1. The first data are related to experimental tests performed in Sardinia, Italy, in September 2006, in presence of a quite good (although very disturbed) wind of about 4–5 m/s at ground level. The employed kite had an effective area of 5 m^2 and the maximum line length was 300 m. Figure 5.5(a) and 5.5(b) show the comparison between experimental and simulated line length r and line speed $\dot{r}$. The obtained courses of generated power are reported in Figure 5.5(c) and show that good correspondence between simulated and experimental data is achieved. The same analysis has been performed on the data collected in January, 2008, during experimental tests performed at the airport of Casale Monferrato near Torino, Italy (see Figure 5.6). A movie of the experimental tests performed near Torino is available on the web–site [52, 53]. The wind flow was quite weak (1–2 m/s at ground level and about 3–4 m/s at 500 m of height). The employed kite had an effective area of 10 m^2 and line length of 800 m. The courses of experimental and simulated line length and speed and power values are reported in Figure 5.5(d)–(f). Also in this case, a good matching between real measured and simulated data can be observed. Such correspondence allows to be quite confident about the power values obtained with the simulations of Sections 3.4 and 4.2.

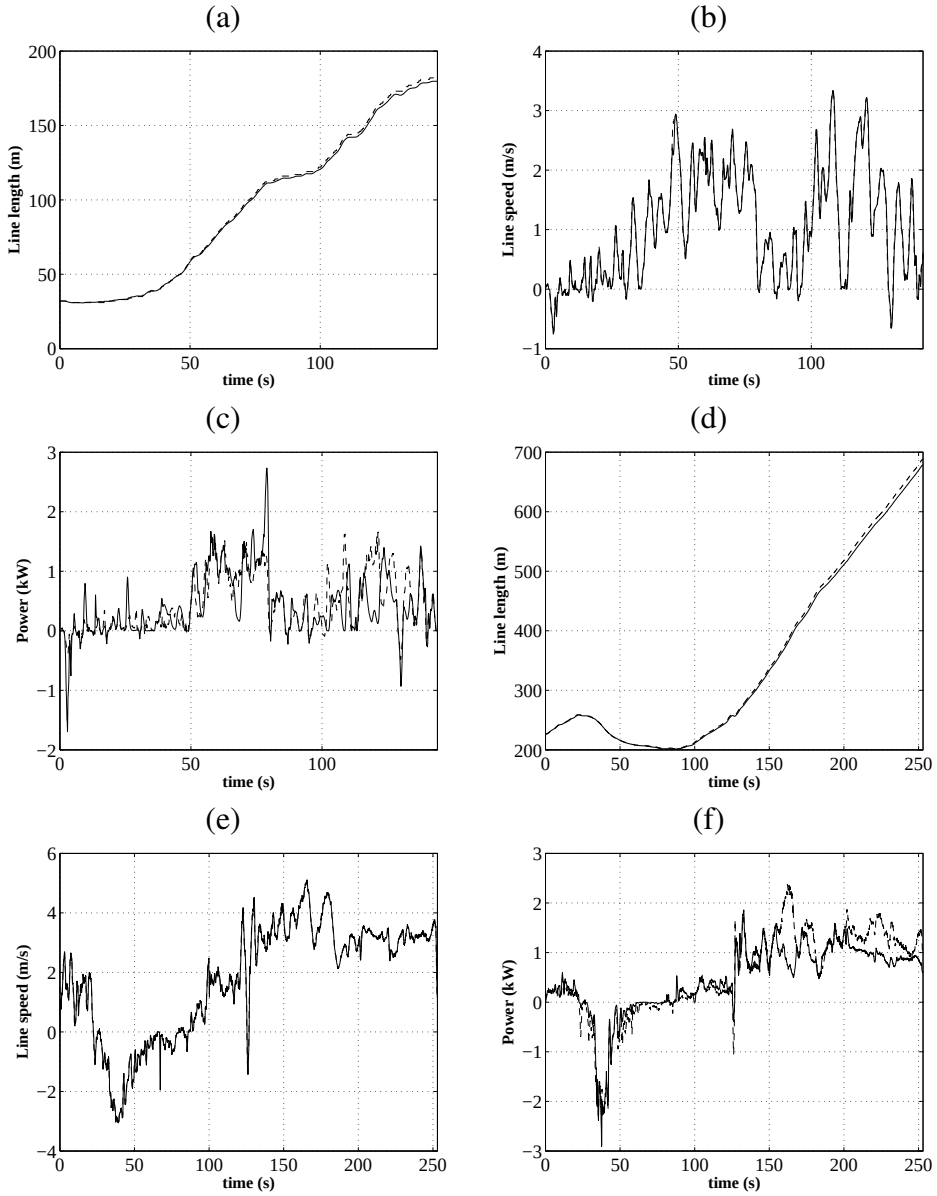

Figure 5.5. Measured (dashed) and simulated (solid) (a) line length r, (b) line speed $\dot{r}$ and (c) generated power P regarding experimental tests carried out in Sardegna, Italy, September 2006. Measured (dashed) and simulated (solid) (d) line length r, (e) line speed $\dot{r}$ and (f) generated power P regarding experimental tests carried out near Torino, Italy, January 2008.

Figure 5.6. A picture of the experimental tests performed at the airport of Casale Monferrato near Torino, Italy, in January, 2008.

Chapter 6

Wind speed, capacity factor and energy cost analyses

In Chapters 2–4 the HAWE technology has been described and studied using theoretical and numerical tools, based on well assessed physical and aerodynamical laws, in order to evaluate its energy generation potential and its scalability. Then, in Chapter 5, a comparison has been carried out between numerical results and experimental data, collected during the first tests performed with a small–scale prototype. The good matching between numerical simulations and real world measures increases the confidence level in the results obtained so far.
As already pointed out in the brief overview of the actual wind energy technology given in Section 1.2.1, the performance (and profit) of a wind energy generator depends on the strength and variability of the wind at the considered site. Now, in this Chapter, an analysis of wind data collected in several locations in Italy and around the world is carried out, in order to evaluate the average energy that can be extracted by a HAWE generator. Then, on the basis of the obtained results, the cost of high–altitude wind energy is estimated and compared with those of the actual wind and fossil energies.

6.1 Wind data analysis

In this Section, the measures of wind speed collected during eleven years (from 1996 to 2006) in several locations around the world are analyzed. In particular, the measurements have been performed daily using radiosondes at elevations ranging from 20 m to more than 4000 m above the ground. The collected data related to many locations all over the world are archived in the database [27] of the Earth System Research Laboratory of the National Oceanic & Atmospheric Administration.
The aim of the presented analysis is to evaluate the distribution of wind speed, for a given

site, at different elevations above the ground. In particular, the ranges 50–150 m and 200–800 m are of interests, since they correspond to the elevations at which wind turbines and HAWE generators operate respectively. The site of De Bilt, in The Netherlands, as well as five sites in Italy are considered. Figure 6.1 shows, for four of the considered locations, the histograms of wind speed at the considered altitudes. The computed distributions are

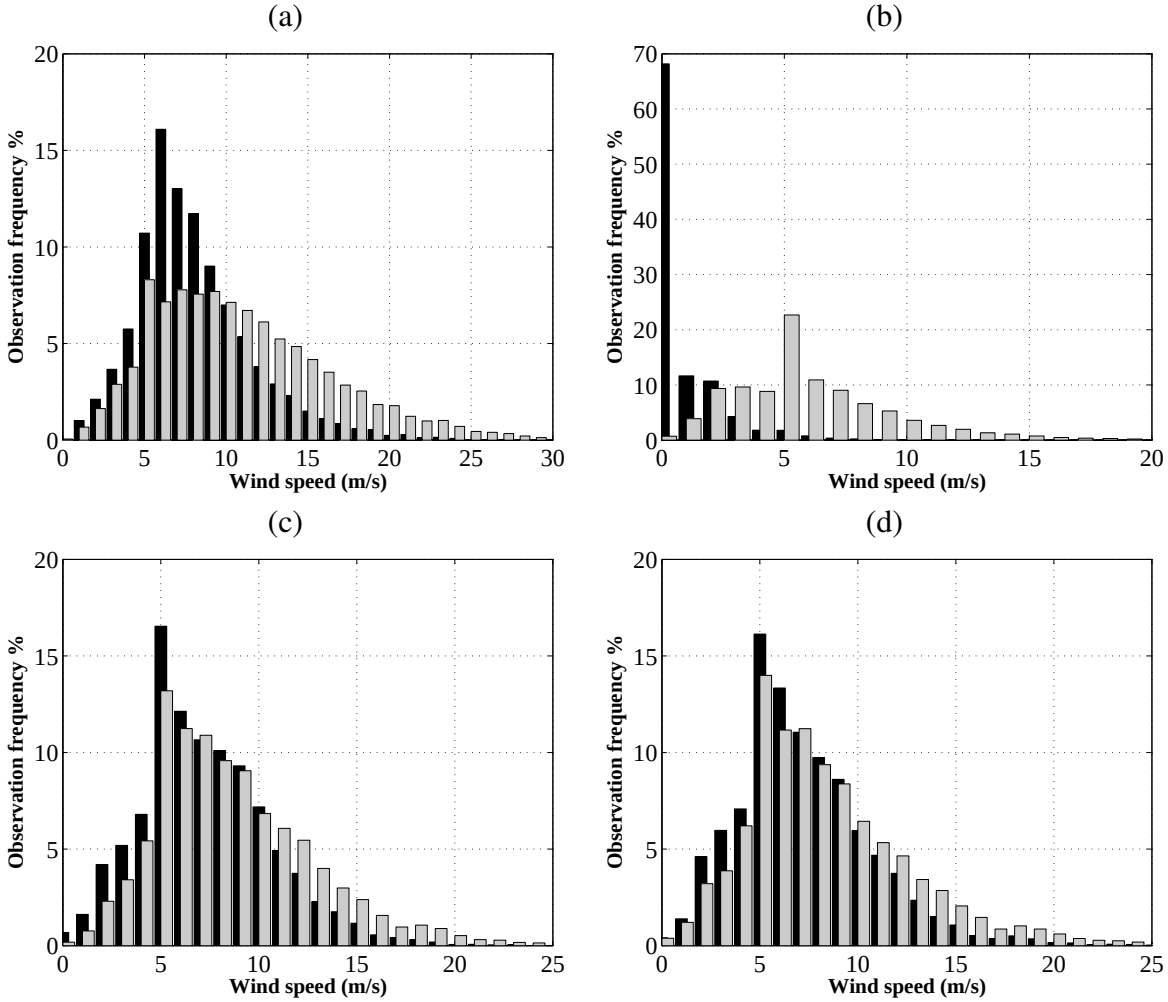

Figure 6.1. Histograms of wind speed between 50 and 150 meters above the ground (black) and between 200 and 800 meters above the ground (gray). Data collected at (a) De Bilt (NL), (b) Linate (IT), (c) Brindisi (IT), (d) Cagliari (IT). Source of data: database of the Earth System Research Laboratory, National Oceanic & Atmospheric Administration

fitted quite well by Weibull probability density distribution functions, as already known in the literature (see e.g. [54]). It can be noted that in all the considered sites the wind speed values between 200 m and 800 m are significantly higher than those observed between 50–150 m. Considering as an example the results obtained for De Bilt (Figure 6.1(a)), in the

elevation range 200–800 m the average wind speed is 10 m/s and wind speeds higher than 12 m/s (at which a 2–MW wind turbine approximately reaches its rated power, see [48]) can be found with a probability of 38%, while between 50 and 150 m above the ground the average wind speed is 7.9 m/s and speed values higher than 12 m/s occur only in the 8% of all the measurements. Similar results have been obtained with the data collected in the other considered sites. Moreover, the same analysis on the data related to Linate, Italy, leads to even more interesting results (see Figure 6.1(b)): in this case, between 50 and 150 meters above the ground the average wind speed is 0.7 m/s and speeds higher than 12 m/s practically never occur, thus making this location not profitable for the actual wind energy technology. On the other hand, in the operating range of HAWE an average speed of 6.9 m/s is obtained, with a probability of 7% to measure wind speed higher than 12 m/s. Thus, the wind speed distribution of a site like Linate, between 200 and 800 m above the ground, is comparable with that of a site like De Bilt at 50–150 m. Considering that the latter is a good site for the actual wind energy technology, the reported results indicate that locations like Linate may be profitable for high–altitude wind energy generation. This consideration is highlighted in the next Section, where the performed wind data analysis is linked to the energy generation potential of HAWE.

6.2 Capacity factor of wind energy generators

As recalled in Section 1.2.1, due to wind intermittency the average power produced by a wind generator over the year is only a fraction, often indicated as Capacity Factor (CF), of its rated power. For a given wind generator on a specific site, the CF can be evaluated on the basis of the probability density distribution function of wind speed and of the power curve of the generator. In Figure 6.2 the power curve of a commercial 2–MW, 90–m diameter wind turbine and that of a 2–MW, 500–m^2 area HE–yoyo (obtained in Section 4.3) are reported. Both generators have the same rated power, however the wind tower needs about 12–m/s wind speed to reach such a value, while the HE–yoyo generator achieves it already with 9–m/s wind speed, where the wind tower produces only 1 MW. Note that a 2–MW wind turbine with a power curve reaching the rated power at 9–m/s wind speed could be built, but it would require a rotor diameter of about 115 m, with consequent higher and heavier tower structure, leading to significant cost increases. Indeed, the actual wind turbines are probably close to their economical and technological limits (see Section 1.2.1). Moreover note that, as already pointed out in Section 4.3, the HAWE generator has a higher cut–out wind speed and a lower cut–in speed, which allow to capture wind energy in a larger range of operating conditions.
Using the power curves reported in Figure 6.2 and the wind speed distributions estimated from the available wind speed measures (showed in part in Figure 6.1), the CF of the two considered generators can be evaluated. Table 6.1 shows the obtained results, related to

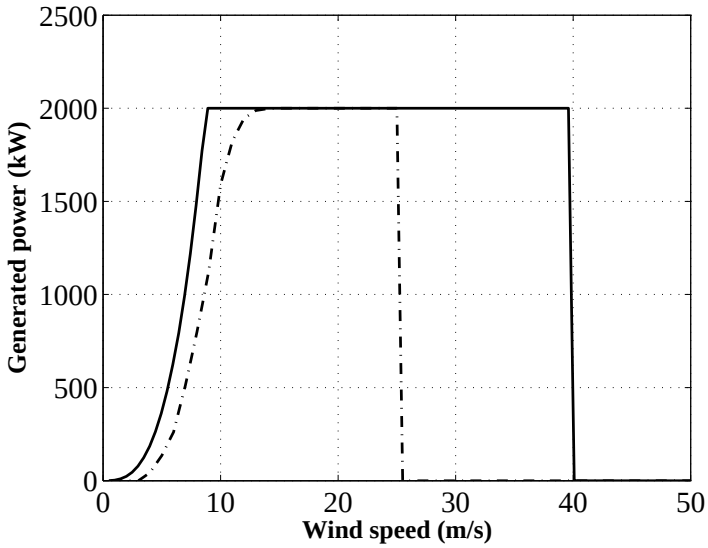

Figure 6.2. Power curves of a 2–MW, 90–m diameter wind turbine (dashed) and of a 2-MW, 500 m^2 HE–yoyo (solid).

the site of De Bilt in The Netherlands as well as the Italian sites of Linate, Cagliari, Brindisi, Trapani and Pratica di Mare. More results are reported in the Appendix C. Note that

Table 6.1. Capacity factor of a 2–MW, 90–m diameter wind tower and a 2–MW, 500–m^2 HE–yoyo for some sites in Italy and in The Netherlands, evaluated from daily wind measurements of radiosondes.

	2–MW Wind tower	**2–MW HE–yoyo**
De Bilt (NL)	0.36	0.71
Linate (IT)	0.006	0.33
Brindisi (IT)	0.31	0.60
Cagliari (IT)	0.31	0.56
Pratica di Mare (IT)	0.23	0.49
Trapani (IT)	0.30	0.56

in most of the considered sites, the CF of a 2–MW HE–yoyo is about two times greater than that of a 2–MW wind turbine. This means that in these sites the yearly generated energy given by the HE–yoyo is twice the energy extracted by the wind turbine, with consequent economical advantages. Moreover, in sites like Linate, where the actual wind energy technology has CF$\simeq$0 (i.e. almost no generated energy), the HE–yoyo achieves a CF of about 0.3–0.35, i.e. similar to the one obtained by the wind turbine in the good site of De Bilt.

If a HE–farm is considered, similar analyses can be made regarding the yearly generated

energy per unit area. On the basis of the power curve obtained using the optimization procedure presented in Section 4.4, considering the site of De Bilt, and reported in Figure 6.3, related to a HE–farm composed of 2–MW HE–yoyo units, a value of CF=0.6 is achieved. Note that the rated power of such a wind farm is 32 MW per km^2. Thus, an average yearly generated power of about 19 MW per km^2 is obtained. An actual wind farm composed by 2–MW, 90–m diameter wind turbines has a rated power density of about 9 MW per km^2 and, on the basis of the estimated CF reported in Table 6.1, an average yearly generated power density of about 3.2 MW per km^2. Thus, the energy per km^2 generated by the HE–farm would be about six times higher than that of an actual wind farm. Finally, it is interesting to also evaluate how the CF of HAWE changes with its

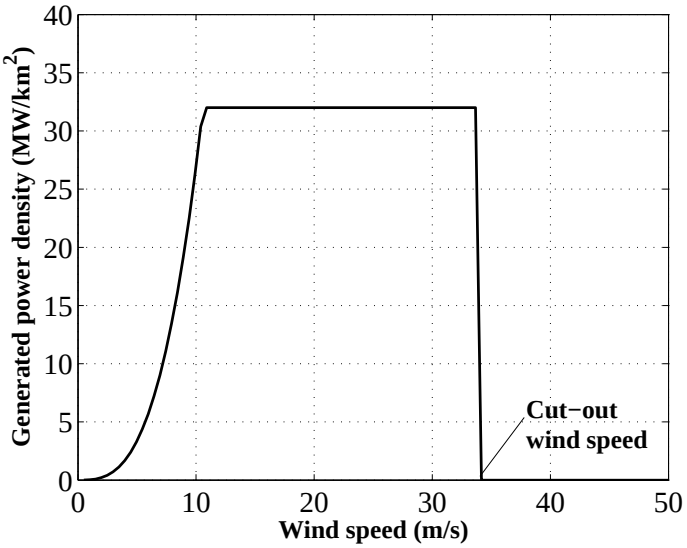

Figure 6.3. Power curve of a HE–farm composed of 2–MW, 500–m^2 HE–yoyo units.

rated power. Indeed, in general if a higher rated power is considered, the CF is expected to decrease, since stronger (and less frequent) wind speed values are needed to generate higher power values. Figure 6.4(a) and (b) show the dependance of the CF on the rated power at the sites of De Bilt and Linate, for a single 500–m^2 area HE–yoyo and for a HE–farm composed by several of such units. As expected, the CF decreases as the rated power increases. Note that at De Bilt site, a HE–farm composed of 5–MW HE–yoyo units (i.e. with a nominal rated power of 80 MW per km^2), has CF$\simeq$0.4 and, consequently, an average yearly generated power of about 32 MW per km^2, i.e. about ten times higher than the one achieved by a 2–MW wind turbine farm. In Section 6.3, such results are employed to perform an estimate of the cost of high–altitude wind energy produced with HAWE.
The curves reported in Figures 6.4(a)–(b) can be employed, considering also the cost increase due to the use of electric generators with higher rated power, to dimension a HAWE

generator/farm according to the characteristics of the wind at the considered site, in order to maximize the profit. Note that the cost of increasing the rated power of a HAWE generator is expected to be relatively low, since (differently from wind towers) the electric equipment are kept at ground level and structural problems are much less critical.

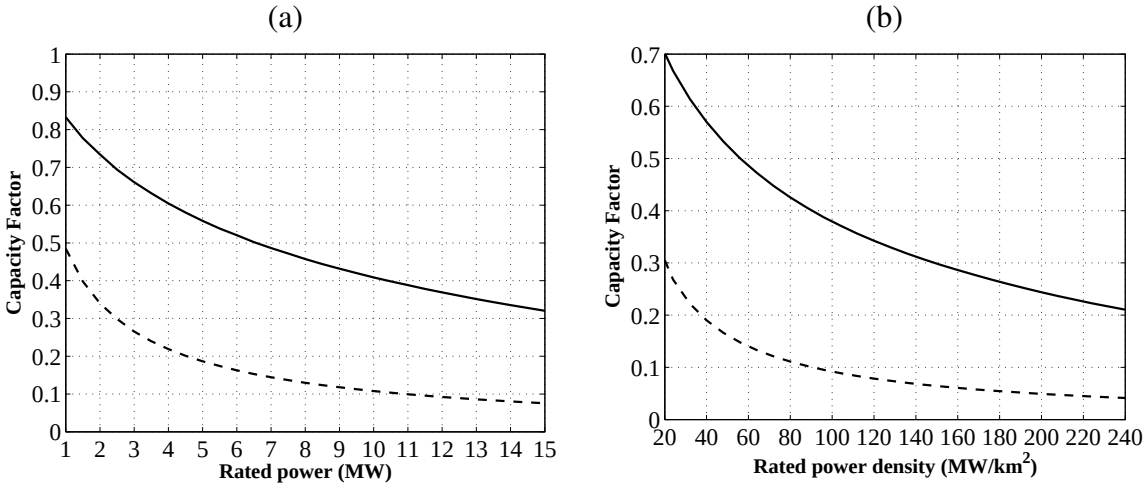

Figure 6.4. (a) Variation of the CF as a function of the rated power for a single 500–m^2 HE–yoyo generator, at the site of De Bilt (NL) (solid) and Linate (IT) (dashed). (b) Variation of the CF as a function of the rated power per km^2 for a HE–farm composed of 16 HE–yoyo units per km^2, at the site of De Bilt (NL) (solid) and Linate (IT) (dashed)

6.3 Estimate of energy cost of HAWE

On the basis of the results presented so far, a preliminary estimate of the costs of the energy produced with HAWE is now performed, considering the HE–yoyo configuration, and compared with the costs of the actual wind energy and of fossil energy. The production costs for HAWE and wind tower technologies are essentially due to the amortization of the costs of the related structures, foundations, electrical equipments to connect to the power grid, authorizations, site use, etc., while the maintenance costs are certainly marginal for both technologies, though possibly higher for HAWE. Thus, the main differences between the two technologies are related to their structures, foundations and required land, whose costs are significantly lower for HAWE. In fact, as explained in Chapter 2, the heavy tower and the rotor of a wind turbine are replaced by light composite fiber cables and airfoils in a HAWE. Given the same rated power, the foundations of a HE–yoyo have to resist to significantly lower strains and the required site dimension may be up to 10 times lower. A reliable estimate of the energy production costs of a HE–yoyo and of a HE–farm certainly requires more research and experimentations. However, for

all the aspects discussed so far, a very conservative estimate can be obtained, at least in relative terms with respect to the cost of the actual wind technology, by assuming that the cost of a HE–yoyo unit with 2–MW rated power is not greater than that of an actual wind tower with 2–MW rated power.
In a site with CF $\simeq$ 0.3, a wind farm composed of 2–MW towers with diameter D =90 m had energy production costs between 50 and 85 $/MWh in 2006 (see [7]). Due to the fluctuations of the energy market, it is difficult to obtain an accurate value of the actual cost of wind energy, however a reliable estimate is about 110$/MWh, also considering that the actual costs of energy production from fossil sources are in the range 60–90 $/MWh, depending on the kind of source (coal, oil, gas). As described in Sections 4.4 and 6.2, the considered wind turbine farm has a density of 4.5 towers per km^2 (applying the the "7D–4D rule", see Section 1.2.1 and [6, 25]). According to the presented analyses, in the same location a HE–farm composed of 2–MW HE–yoyo units, with the same overall rated power (i.e. the same number of generators) as the wind turbine farm, has CF$\simeq$0.6 and therefore produces an average power 2 times higher than the one of the wind turbine farm. Then, a conservative energy cost estimate of about 55 $/MWh is obtained for HAWE. Note that the considered cost assumption is a very conservative one and that the HE–farm has also a density of 16 HE–yoyo per km^2, i.e. 3.6 times higher than the wind turbine farm. Higher density of HE–yoyo units leads to lower land occupation (i.e. lower costs) given the same rated power. Moreover, the study presented in Section 6.2 shows that with the only additional costs related to the replacement of the 2–MW electric equipments with 5–MW ones, the same HE–farm, i.e. with the same 500–m^2 kites, can reach a rated power 2.5 times higher and an average yearly power 3.75 times higher than those of the wind tower farm. Note that, in order to increase the rated and average generated power of an actual wind farm, much higher investments would be needed, since higher and bulkier towers with bigger rotors should be employed. Thus, scale factors positively affect the production costs of HAWE technology, leading to cost estimates lower than 30–35 $/MWh, hence lower than fossil energy. Moreover, the high–altitude wind energy technology can be applied in a much higher number of locations than the actual wind technology. This is made extremely evident from the results related to the site of Linate (IT) (see Section 6.2), where a negligible CF is obtained by an actual wind tower, while a HE–yoyo achieves a CF greater than 0.3 which, according to the actual level of the incentives for renewable energy generation, would make the use of high–altitude wind energy technology profitable.

Chapter 7

Conclusions and future developments

The first part of this dissertation aimed at evaluating the potential of the innovative high–altitude wind energy technology. In particular, a class of generators denoted as HAWE has been considered, which exploits the aerodynamical forces generated by tethered airfoils to produce electric energy. Numerical simulations, theoretical studies and optimization, prototype experiments and wind data analyses have been employed to achieve the results presented in this work. Indeed, such results show that **the HAWE technology, capturing the wind energy at significantly higher altitude over the ground than the actual wind towers, has the potential of generating renewable energy available in large quantities almost everywhere, with a cost even lower than the one of fossil energy**. The key points that support this claim and that have been originally developed throughout this dissertation are now briefly resumed.

I) Description of the HAWE configurations and design of their operational cycles (Chapter 2). After having delineated the concept of HAWE technology and of the two considered configurations, the HE–yoyo and HE–carousel, the related operational cycles have been designed. In particular, two possible operation modes for each configuration have been evaluated, thus four different operational cycles have been defined in total.

II) Modeling, control design and numerical simulation analyses (Chapter 3). A model of the airfoil and of the Kite Steering Unit has been derived, on the basis of well assessed physical equations and of a simpler kite model already introduced in the literature. Then, a control strategy based on Nonlinear Model Predictive Control has been originally developed in order to perform the designed operational cycles for all of the considered HAWE configurations. Advanced implementation techniques, which are further investigated in Part II of this dissertation, have been employed to achieve an efficient control implementation. Finally, numerical simulations have been performed to study the system behaviour and the obtained energy generation performance. From a first comparison of the obtained results, two of the

four possible HAWE configurations have been indicated as more promising, i.e. the HE–yoyo with wing glide recovery maneuver and the HE–carousel with constant line length.

III) Optimization of HAWE operation (Chapter 4). The operation of the designed energy generation cycles has been optimized using mathematical programming tools. In particular, theoretical crosswind power equations, already developed in the literature, have been recalled and integrated in the formulation of suitable optimization problems, aimed at computing the values of the operational parameters of a HE–yoyo in order to achieve the maximal energy production. Operational constraints have been also considered, in order to achieve practically realizable operating cycles. The optimized parameters have employed to perform numerical simulations and the good matching between theoretical and numerical results has been assessed. Numerical simulation and theoretical equations have been also employed to assess the scalability of the system.
Finally, the design of a HE–farm, composed of several HE–yoyo units working in the same location, has been carried out and its operation has been optimized too.

IV) Experimental activities (Chapter 5). The results of numerical simulations related to a small scale HE–yoyo generator have been employed to design a prototype to be used for experimental activities. The first collected experimental data have been compared with the results of the simulations, verifying the good matching between numerical results and real world measures. Such a good correspondence increases the confidence with the obtained numerical and theoretical results also for medium–to–large scale generators.

V) Wind data, capacity factor and cost analyses (Chapter 6). The capacity factor achievable by HAWE generators has been estimated considering several sites in Italy and one site in The Netherlands. Then, on the basis of the obtained results and of all the previously performed analyses, an estimate of the cost of energy obtained with HAWE has been made. Such estimate is about one half of the cost of fossil energies. Moreover, the capacity factor analysis indicate that high–altitude wind energy can be produced with good profit also in sites where the actual wind energy technology is not viable, thus allowing to enlarge the list of energy–producing countries.

Thus, high–altitude wind energy could bring a significant contribution to resolve the actual problems related to global energy production and distribution and to excessive greenhouse gases emissions.
The idea of exploiting tethered airfoils to generate energy is not new, however it is practicable today thanks to recent advancements in several science and engineering fields like materials, aerodynamics, mechatronics and control theory. In particular, the latter is of

basic importance in HAWE technology and the theoretical aspects of the employed control strategy are deeply investigated in Part II of this dissertation.
Therefore, with an adequate support, the development and industrialization of the presented high–altitude wind energy technology can be carried out in a few years time, since no more basic research or technological innovations are needed, but only the fusion of the advanced competencies already available in various engineering fields.
The developments that should be carried out in the immediate future regards at first experimental activities aimed at collecting more data on the system behaviour, in order to build more accurate system models and to provide information to carry out a more specific design of all the components of a HAWE generator. In particular, ad–hoc airfoil shapes and materials, cables, transmission organs and electric equipments should be designed to maximize the system performance. A medium–to–large scale prototype should then be built to definitively assess the validity of the concept and of the studies performed so far.

Part II

Efficient nonlinear model predictive control via function approximation: the Set Membership approach

Chapter 8

Introduction

In nonlinear model predictive control (NMPC, see e.g. [39]) the control action is computed by means of a receding horizon (RH) strategy, which requires at each sampling time the solution of a constrained optimal control problem, where the systems state x (and, possibly, other measured parameters and reference variables) is a parameter in the optimization. For time invariant systems, the solution of such parametric optimization problem defines a static nonlinear function $\kappa^0(x)$, denoted here as the "nominal" control law. Starting from the late 1970s, the application of predictive techniques has received an increasing attention in industrial world (see e.g. [55]), due to its capability of treating different kinds of control problems in a quite general framework, in the presence of both linear and nonlinear system models, and its efficiency in handling constraints on the input, state and output variables. However, the RH strategy can be effectively applied only if the sampling time, employed in the considered application, is sufficiently large to allow the solution of the optimal control problem. For this reason, NMPC is widely employed for the control of slow and complex industrial processes (e.g. in petrochemical and power industries, see [55]), with sampling times of the order of tens of minutes. Indeed, the potential of NMPC makes this technique interesting also for systems with "fast" dynamics, which require small sampling periods that do not allow to solve the optimization problem in real–time. In order to allow the use of MPC also for this kind of applications, a significant research effort has been devoted in recent years to the problem of developing techniques for the efficient implementation of model predictive control laws. Moreover, in many applications (e.g. automotive) the capability to obtain good control performance with low–cost hardware is a point of great importance and a key for economical success: this aspect further motivates the research studies proposed in the literature to improve the efficiency of NMPC and to enable its application also on processors with limited computational performance. A concise overview of the existing approaches for efficient NMPC is given in Section 8.2. These contributions can be roughly categorized into two lines of research: the first one aims at improving the computational efficiency of the numerical techniques employed for the on–line optimization, while the second one investigates the

use of an approximated NMPC law $\hat{\kappa} \approx \kappa^0$, which is computed off–line and then evaluated on–line instead of solving the numerical optimization problem.
In the latter research direction, a common point to any approximation approach for efficient NMPC is the fact that the control law $\hat{\kappa}$ is derived on the basis of the off–line computation of a finite number ν of exact control moves. In general, the approximation accuracy improves as ν is increased, usually at the cost of higher memory usage, on–line computation complexity (which may even result to be higher than that of on–line optimization) and off–line computation. Thus, a tradeoff between accuracy and complexity has to be chosen in the approximation of a given NMPC law. Moreover, a crucial issue, arising when the approximated function $\hat{\kappa}$ is employed for feedback control, regards the properties of the resulting closed loop system, in terms of stability, state and input constraint satisfaction and degradation of the performance with respect to those of the closed loop system obtained with the nominal control law κ^0. It is quite intuitive that the better is the approximation accuracy, the closer are the performance obtained with $\hat{\kappa}$ to those obtained with κ^0. Therefore, the already mentioned tradeoff between accuracy and complexity should also take into account the closed loop system properties. Needless to say that, in order to obtain such a tradeoff, the employed approximation technique must be such that a finite bound on the approximation error $\Delta_{\hat{\kappa}} = \kappa^0 - \hat{\kappa}$ exists and can be computed or estimated as a function of ν.
In the described context, the theoretical results given in this second part of the thesis investigate the properties of approximated NMPC laws, in terms of guaranteed accuracy, closed loop performance, computational efficiency and memory usage and introduce techniques to compute approximated control laws able to reach different tradeoffs between all these aspects.
The presented theoretical studies have been mainly developed in the framework of Set Membership (SM) function identification theory and they have been published in [56, 57, 58, 59, 60]. Moreover, several control applications have been studied, like semi-active suspensions [61], vehicle yaw control [62] and control of power kites for energy generation (see Part I of this thesis and [9, 10, 11, 12, 13]). The methodological contributions given in [56]–[60] are collected, organized and thoroughly presented in this dissertation.
This Chapter is organized as follows. Section 8.1 contains a standard formulation of NMPC, to introduce the mathematical notation as well as the considered prior assumptions on the nominal control law κ^0, while Section 8.2 gives a brief overview of the existing approaches for efficient NMPC implementation. Finally, the problem formulation and the contributions given in the next Chapter of this dissertation are reported in Section 8.3.

8.1 Nonlinear Model Predictive Control

Consider the following nonlinear state space model:

$$x_{t+1} = f(x_t,u_t) \tag{8.1}$$

where $x_t \in \mathbb{R}^n$ and $u_t \in \mathbb{R}^m$ are the system state and control input respectively. In this thesis, it is assumed that function f in (8.1) is continuous over $\mathbb{R}^n \times \mathbb{R}^m$. Assume that the control objective is to regulate the system state to the origin under some input and state constraints represented by a compact set $\mathbb{U} \subseteq \mathbb{R}^m$ and a convex set $\mathbb{X} \subseteq \mathbb{R}^n$ respectively, both containing the origin in their interiors. Denoting by $N_p \in \mathbb{N}$ and $N_c \leq N_p, N_c \in \mathbb{N}$ the prediction horizon and the control horizon respectively, the following objective function J can be defined:

$$J(U,x_{t|t}) = \Phi(x_{t+N_p|t}) + \textstyle\sum_{j=0}^{N_p-1} L(x_{t+j|t},u_{t+j|t})$$

where $x_{t+j|t}$ denotes j step ahead state prediction using the model (8.1), given the input sequence $u_{t|t},\ldots,u_{t+j-1|t}$ and the "initial" state $x_{t|t} = x_t$. $U = \left[u_{t|t}^T,\ldots,u_{t+N_c-1|t}^T\right]^T$ is the vector of the control moves to be optimized. The remaining predicted control moves $[u_{t+N_c|t},\ldots,u_{t+N_p-1|t}]$ can be computed with different strategies, e.g. by setting $u_{t+j|t} = u_{N_c-1|t}$ or $u_{t+j|t} = K\,x_{t+j|t}, \forall j \in [N_c,N_p-1]$, where K is a suitable matrix. The per–stage cost function $L(\cdot)$ and the terminal state cost $F(\cdot)$ are chosen according to the desired performance and are continuous in their arguments (see e.g. [45] and [63] for details).
The NMPC control law is then obtained applying the following RH strategy [45, 63]:

1. At time instant t, get x_t.
2. Solve the optimization problem:

$$\min_U \quad J(U,x_{t|t}) \tag{8.2a}$$

s. t.

$$x_{t+j|t} \in \mathbb{X},\ j = 1,\ldots,N_p \tag{8.2b}$$

$$u_{t+j|t} \in \mathbb{U},\ j = 0,\ldots,N_p \tag{8.2c}$$

3. Apply the first element of the solution sequence U of the optimization problem as the actual control action, i.e. $u_t = u_{t|t}$.
4. Repeat from step 1. at time $t+1$.

Indeed, additional constraints (e.g. state contraction, terminal set) may be included in (8.2) in order to ensure stability of the controlled system. Note that the problem (8.2) is a parametric optimization problem in which the parameter is the system state x. It is

assumed that the problem (8.2) is feasible over a set $\mathcal{F} \subseteq \mathbb{R}^n$, which will be referred to as the "feasibility set". The application of the RH procedure gives rise to the following nonlinear state feedback configuration:

$$x_{t+1} = f(x_t,\kappa^0(x_t)) = F^0(x_t) \tag{8.3}$$

where the nominal control law κ^0 results to be a time invariant static function of the state:

$$u_t = [u_{t,1} \dots u_{t,m}]^T = [\kappa_1^0(x_t) \dots \kappa_m^0(x_t)]^T = \kappa^0(x_t)$$
$$\kappa^0 : \mathcal{F} \to \mathbb{U}$$

Thus, function κ^0 is implicitly defined by the solution of the parametric optimization problem (8.2). In this work, it is assumed that the nominal NMPC law is suitably designed so that the nonlinear autonomous system (8.3) is uniformly asymptotically stable at the origin for any initial state value $x_0 \in \mathcal{F}$, i.e. it is stable and

$$\forall \epsilon > 0,\ \forall \delta > 0\ \exists T \in \mathbb{N} \text{ such that}$$
$$\|\phi^0(t+T,x_0)\|_2 < \epsilon, \forall t \geq 0,\ \forall x_0 \in \mathcal{F} :\ \|x_0\|_2 \leq \delta$$

where $\phi^0(t,x_0) = \underbrace{F^0(F^0(\dots F^0}_{t \text{ times}}(x_0)\dots))$ is the solution of (8.3) at time instant t with initial condition x_0. Note that, according to (8.2b), for any $x_0 \in \mathcal{F}$ the state constraints are always satisfied after the first time step, i.e.:

$$\phi^0(t,x_0) \in \mathbb{X}, \forall x_0 \in \mathcal{F}, \forall t \geq 1 \tag{8.4}$$

Thus, the set $\mathbb{X} \cap \mathcal{F}$ is positively invariant with respect to system (8.3):

$$\phi^0(t,x_0) \in \mathbb{X}, \forall x_0 \in \mathbb{X} \cap \mathcal{F}, \forall t \geq 0 \tag{8.5}$$

Moreover, due to (8.2c) the input constraints are satisfied for any $x \in \mathcal{F}$:

$$\kappa^0(x) \in \mathbb{U}, \forall x \in \mathcal{F} \tag{8.6}$$

As a further assumption, it is supposed that the nominal control law κ^0 is continuous over the set $\mathcal{X} \subseteq \mathcal{F}$, considered for the approximation (see Section 8.3 for more details on the set $\mathcal{X}$). Such property depends on the characteristics of the optimization problem (8.2): results on this aspect can be found e.g. in [64, 65] and in [66] and the references therein. Note that stronger regularity assumptions (e.g. differentiability) cannot be made, since even in the particular case of linear dynamics, linear constraints and quadratic objective function, κ^0 is a piece-wise linear continuous function (see Section 8.2.2). Moreover, note that there exist cases in which the nominal NMPC law is for sure *not* continuous (see e.g. [65]). However, among the existing techniques for NMPC approximation (see Section 8.2.3), to the best of the author's knowledge the only approaches that are able to deliver

both an approximated controller and guaranteed accuracy bounds and stability properties rely on the convexity of the optimal cost function $J^*(x) = \min_U J(U,x)$ over the set $\mathcal{X}$. As it is showed in some of the numerical examples of Section 13.1, there exist cases in which the optimal cost is not convex, while the optimal control law is continuous. Thus, in these cases the approaches presented in this thesis can be systematically employed, while other approaches based on the convexity of $J^*(x)$ cannot be used or they can be applied only with ad–hoc modifications (see Section 8.2.3 for further details).
As a final remark, note that different control problems (e.g. reference tracking) can be treated by considering that, if the system is time invariant, the nominal control law κ^0 is a static function of the system state and of the other involved variables, like references $x_{\text{ref}} \in \mathbb{R}^n$ and parameters $\theta \in \mathbb{R}^q$, which can be considered together as a general regressor variable:

$$w = \begin{bmatrix} x \\ x_{\text{ref}} \\ \theta \end{bmatrix} \in \mathbb{R}^{n+n+q} \tag{8.7}$$

Then, the control law $u = \kappa^0(w)$ is defined on the feasibility set $\mathcal{F}^w \subseteq \mathbb{R}^{n+n+q}$ and it can be approximated on a set $\mathcal{X}^w \subseteq \mathcal{F}^w$, provided that the considered stability and continuity assumptions hold. For the sake of simplicity and without any loss of generality, in this work the case $w = x$ will be considered.

8.2 Approaches for efficient MPC

In this Section, a brief overview of existing techniques for efficient MPC implementation is given. As already anticipated, such approaches rely either on more efficient on–line optimization (Section 8.2.1), or on the off–line computation of an approximation of the nominal control law (Section 8.2.3). Moreover, for the particular case of linear systems with quadratic cost and linear constraints, an exact formulation of the nominal control law can be computed off–line and stored for on–line evaluation (Section 8.2.2).

8.2.1 On–line computational improvements

The computational efficiency of MPC depends strongly on the complexity of the underlying optimization problem, on its formulation and on the algorithms employed for its solution. Thus, the approaches proposed in the literature to improve the on–line efficiency aim either at exploiting the structure of the mathematical programming problem to be solved, or at employing solution techniques with higher efficiency and/or lower complexity, even at the cost of obtaining suboptimal solutions. To provide an in–depth survey of the existing approaches for on–line MPC computation is outside the scope of this thesis, however for the sake of completeness a brief overview of some existing works

(to which the interested reader is referred to for further deepening and for a more complete bibliography) is now given. In the case of linear system with linear constraints and quadratic cost, a recent work aimed at improving the on–line computational efficiency of MPC, exploiting the particular structure of the optimization problem as well as a series of other techniques, like warm–start and early–termination, is described in [67]. For the case of NMPC, efficient multiple shooting methods with exploitation of the problem structure have been proposed (see e.g. [68]), as well as real–time optimization schemes [69], in which the optimization and the control are carried out simultaneously. Other existing approaches rely on continuation methods (see [70]), in which the control input is updated by a differential equation which traces the solution of the RH optimal control problem (8.2). All these approaches aim to solve efficiently the RH optimization problem in its original formulation, i.e. using as optimization variables the predicted control inputs (and, eventually, also the predicted state values, as done in multiple shooting approaches). A different kind of approach, which in principle could be employed together with the previous ones, is proposed e.g. in [71], where the control input is parameterized using a suitable functional form and then the optimization is carried out in the parameter space. Depending on the choice of the parametrization, the original control problem can be simplified and efficiently solved.
As a final comment, efficient on–line optimization is probably the only practically feasible NMPC implementation method for systems in which the nominal control law depends on more than 8–10 variables . In fact, as it will be put into evidence in the next Sections, the use of explicit or approximate NMPC laws leads to an exponential increment of the memory usage and off–line computational burden with the size of x. However, in the case of "small" state dimension and/or complex optimization problems, due to the presence of, for example, long prediction and control horizons or a high number of (possibly nonlinear) constraints, on–line optimization may result to be less efficient than the use of an approximate control law.

8.2.2 Exact and approximate formulations for linear quadratic MPC

In the particular case of MPC for linear systems, with quadratic cost function and linear constraints (which will be referred to as the "linear quadratic MPC" in the following), it has been showed [72, 73] that the exact nominal control law is a piecewise affine (PWA) continuous function of the system state x, defined over a finite number N^{Part} of polyhedral partitions of the feasibility set $\mathcal{F}$. In the literature such an exact MPC formulation is referred to as the "explicit" MPC, since an explicit solution of the parametric optimization problem (8.2) is computed for all the feasible values of the parameter x. The topic of explicit/approximate linear quadratic MPC has been quite deeply investigated in the last 5–8 years, considering also issues like robustness of the closed loop system (see e.g. [74]) and the presence of hybrid linear models [75]. Recent surveys on explicit linear quadratic MPC are given in [76] and [77]. For the sake of completeness, the main characteristics of

explicit MPC are now briefly recalled. For a given state value x, the exact control move can be computed as follows:

$$u = \kappa^0(x) = K^k\, x + Q^k,\; k : x \in X^k \tag{8.8}$$

where

$$X^k = \{x \in \mathbb{R}^n : F^k\, x - G^k \leq 0\}$$
$$\mathcal{F} = \bigcup_{j=1}^{N^{\text{Part}}} X^j$$

and F^k, G^k are suitable matrices defining the k–th polyhedral partition, X^k. Thus, it is possible to compute off–line and store the matrices $F^j, G^j, K^j\, Q^j,\; j = 1, \ldots, N^{\text{Part}}$ and implement on–line the *exact* MPC law κ^0 using a procedure like the following:

1. At time instant t, get x_t.
2. Find the partition X^k such that:
$$x_t \in X^k$$
3. Compute the actual control action as
$$u_t = K^k\, x + Q^k$$
4. Repeat from step 1. at time $t + 1$.

Note that in explicit MPC the on–line optimization (8.2) is replaced with the search for the "active" polyhedral region X^k, which the actual state value lies in. Indeed, the computational burden needed to compute the linear control law $u = K^k\, x + Q^k$ is negligible with respect to the time needed to perform such a search. Moreover, the memory usage of this approach is related to the number N^{Part} of regions and to the size of x and u. As it is pointed out in [72], N^{Part} increases significantly with the state dimension, with the length of the control and prediction horizons and with the number of constraints. As a consequence, severe limitations may occur in the on–line computation of the control move, due to the increase in the computational time needed to find the active region. To mitigate this issue, a technique to improve the efficiency of the search for the active region has been introduced in [78], through the construction of a binary search tree to evaluate the PWA control law, achieving logarithmic computational time in the number of regions. Other approaches to improve the efficiency of explicit MPC have been proposed in [79] and [80], deriving explicit suboptimal solutions with lower number of regions.
Note that the latter approaches do not provide the exact solution to the original optimization problem and they can be therefore regarded as techniques to find an approximation of the nominal controller κ^0. However, they have been included in this Section since they all refer to the problem of linear quadratic MPC. Thus, the techniques mentioned above

cannot be applied in the presence of nonlinear constraints (see e.g. Example 13.1.2 in Section 13.1) and/or nonlinear systems and non–quadratic cost functions. The next Section gives a brief survey of the existing approaches that can cope with this limitation, to compute off–line approximations of given MPC laws for nonlinear systems.

8.2.3 Approximate nonlinear model predictive control laws

A first contribution in the field of approximated nonlinear model predictive control has been given in [81], using a neural network approximation of κ^0. However, no guaranteed approximation error and constraint satisfaction properties were obtained. Moreover, the non convexity of the functional used in the "learning phase" of the neural network gives rise to possible deteriorations in the approximation, due to trapping in local minima.
In [82], a Set Membership (SM) approximation technique has been proposed in order to overcome such drawbacks. However, in both [81] and [82] no analysis has been carried out on the effects of the approximated control law on the performance of the closed loop system, which is one of the critical issues arising in the use of an approximated controller. Some results in this direction can be found in [83], where an off–line approximate multi–parametric programming algorithm is employed for the construction of a PWA approximation of the nominal predictive control law, defined over an hypercubic partition of the state region $\mathcal{X}$ where the approximation is carried out, and its implementation via a binary search tree. A similar technique, employing a simplicial partition of $\mathcal{X}$ and a PWA approximation, has been employed in [74]. In these cases, guaranteed accuracy can be obtained, in terms of a bound on the error between the nominal and the approximated cost functions (rather than on the control error, i.e. $\kappa^0 - \hat{\kappa}$). However, with these approaches the computational efficiency depends on the number of the state space partitions, which increases as the required error tolerance decreases. Moreover, the obtained accuracy, closed loop stability and constraint satisfaction properties rely on the assumption of convexity of the optimal cost function. If such assumption is not met, ad-hoc solutions have to be used.
A further approach for approximate NMPC has been proposed in [84], by approximating the nonlinear system model with a set of PWA systems over the state space and computing for each one the PWA exact solution of the related linear quadratic MPC controller [72, 73]. Then, a set of off–line solutions of such PWA control laws is considered and a polynomial interpolation technique is employed to compute an approximation of the overall control law. However, the approximation of a given nonlinear model with a set of PWA systems is not a trivial task and model approximation errors are introduced. Moreover, no guarantees are given on the stabilizing properties of the computed polynomial law.
Finally, approximation techniques based on SM theory have been further developed and studied in [56, 57, 58, 59, 60]. In the framework of SM function approximation theory, approximated NMPC laws with guaranteed accuracy (in terms of a bound on the error

$\kappa^0 - \hat{\kappa}$) and consequent performance and stability properties have been derived, with the only assumption of continuity of κ^0 over the compact set $\mathcal{X} \subseteq \mathcal{F}$ considered for the approximation.
Efficient NMPC via SM approximation techniques have been also applied to problems like control of semi-active suspension systems [61], vehicle yaw control using a rear active differential device [62] and control of tethered airfoils for high–altitude wind energy generation (see Part I, Chapter 3 of this thesis and [9, 10, 11, 12, 13]).
The next parts of the thesis present the main theoretical results regarding SM approximation of NMPC, together with several numerical examples and the application to a vehicle yaw control problem.

8.3 Problem formulation and contributions of this dissertation

In this Section, the problem settings and the objectives of the performed theoretical studies are briefly summarized, together with the obtained results. It is considered that the approximating function $\hat{\kappa} \approx \kappa^0$ is defined over a compact set $\mathcal{X}$, containing the origin in its interior, such that:

$$\hat{\kappa} : \mathcal{X} \to \mathbb{R},\ \mathcal{X} \subseteq \mathcal{F}$$

In practice, $\mathcal{X}$ is a set of interest for control purposes, i.e. it is the set where the system state usually evolves in the considered application. As already anticipated, function $\hat{\kappa}$ is computed on the basis of the knowledge of a finite number ν of exact control moves, i.e.:

$$\tilde{u}^k = \kappa^0(\tilde{x}^k), k = 1, \ldots, \nu \tag{8.9}$$

where the state values $\tilde{x}^k$ are suitably chosen and define the set:

$$\mathcal{X}_\nu = \{\tilde{x}^k, k = 1, \ldots, \nu\} \subseteq \mathcal{F}$$

It is assumed that $\mathcal{X}_\nu$ is chosen such that the following property holds:

$$\lim_{\nu \to \infty} d_H(\mathcal{X}, \mathcal{X}_\nu) = 0 \tag{8.10}$$

where $d_H(X, X_\nu)$ is defined as:

$$d_H(\mathcal{X}, \mathcal{X}_\nu) = \sup_{x \in \mathcal{X}} \inf_{\tilde{x} \in \mathcal{X}_\nu} (\|x - \tilde{x}\|_2) \tag{8.11}$$

Note that uniform gridding over $\mathcal{X}$ satisfies condition (8.10).

Remark 2 *For simplicity, all of the theoretical results presented in the following are obtained considering the Euclidean norm* $\|\tilde{x} - x\|_2 = \sqrt{(\tilde{x} - x)^T(\tilde{x} - x)}$ *to measure the distance between two generic points* $\tilde{x}$ *and* x*. Such a choice gives good results in the numerical examples of Section 13.1. However, in practical applications it is usually needed to scale the variable* x *to adapt to the properties of data. This is obtained using a weighted Euclidean norm:*

$$\|\tilde{x} - x\|_2^M = \sqrt{(\tilde{x} - x)^T M(\tilde{x} - x)} \tag{8.12}$$

where

$$M = diag(m_i), i = 1, \ldots, n \tag{8.13}$$

and $m_i \in (0,1) : \sum_{i=1}^{n} m_i = 1$ *are suitable scalar weights. An example of how to choose such weights is given in the yaw control application of Section 13.2.*

The use of $\hat{\kappa}(x)$ in place of $\kappa^0(x)$ leads to the autonomous system:

$$\hat{x}_{t+1} = \hat{F}(\hat{x}_t) = f(\hat{x}_t, \hat{\kappa}(\hat{x}_t)) \tag{8.14}$$

whose state trajectory at time instant t with initial condition x_0 is indicated as $\hat{\phi}(t,x_0) = \underbrace{\hat{F}(\hat{F}(\ldots \hat{F}}_{t \text{ times}}(x_0)\ldots))$.

A crucial issue, arising when the approximated function $\hat{\kappa}$ is employed for feedback control, regards the stability properties of the resulting closed loop system (8.14), given the properties of the controlled system (8.3). Moreover, it is interesting to study the link between the number and the choice of the off–line computed values $\tilde{u}^k, k = 1, \ldots, \nu$ and the properties of $\hat{\kappa}$ and of the closed loop system (8.14). Thus, the aims of the presented work are:

I) to study the worst–case accuracy obtained by a generic approximating function $\hat{\kappa} \approx \kappa^0$, in terms of a bound on the approximation error $\hat{\kappa} - \kappa^0$, and to link such a bound to the closed loop system behaviour, deriving sufficient conditions for $\hat{\kappa}$ to achieve guaranteed closed loop stability, constraint satisfaction and performance degradation, in terms of distance between the state trajectories $\phi^0(t,x_0)$ and $\hat{\phi}(t,x_0)$.

II) to derive techniques which can be systematically employed to obtain approximating functions with bounded error and guaranteed closed loop properties, and to study the optimality (i.e. the capability of achieving minimal worst–case error) of such approaches with respect to the considered prior information on κ^0. To obtain suitable tradeoffs between accuracy, on–line computational efficiency, memory usage and off–line computational burden.

In the described context, the contributions given by this dissertation are the following:

I) analysis of the properties of stability, constraint satisfaction and performance degradation of the closed loop system (8.14) (Chapter 9).
The main theoretical result states that if $\hat{\kappa}$ enjoys three *key properties*, then guaranteed closed loop stability and performance can be obtained. Namely, such properties are satisfaction of input constraints, boundedness of the pointwise approximation error $\Delta_{\hat{\kappa}}(x) = \kappa^0(x) - \hat{\kappa}(x)$ and its convergence to an arbitrary small value, as ν increases. The obtained guaranteed closed loop properties regard the boundedness and convergency of the controlled state trajectories, satisfaction of state constraints and a bound on the maximum distance between the state trajectories $\phi^0(t,x_0)$ and $\hat{\phi}(t,x_0)$.

II) Analysis of the guaranteed accuracy obtained by a generic approximating function $\hat{\kappa}$ (Chapter 10).
A general framework is considered, where $\hat{\kappa}$ is obtained with any technique (e.g. polynomial curve fitting, interpolation, neural networks, etc.), and sufficient conditions are derived for $\hat{\kappa}$ to satisfy the above–mentioned key properties.

III) Derivation of novel approaches to approximate a given NMPC law (Chapters 11–13).
Five different approaches are described, all of them satisfy the considered key properties and can be therefore employed to obtain approximating functions with guaranteed closed loop stability and performance. The first two approaches (treated in Chapter 11), namely the "global" [56, 59] and "local" [58] SM approximations, are optimal in the sense that they obtain the minimal worst–case error according to the considered prior information. The other three techniques (described in Chapter 12) are suboptimal (i.e. their worst–case accuracy is worse than that of the optimal approaches) but they are able to achieve different tradeoffs between accuracy, computational efficiency, memory usage and off-line computational effort (required to derive the approximating function). Such suboptimal techniques are the "nearest point" [57, 59], linear interpolation [60] and "SM neighborhood" [60] approximations. Several numerical examples are given in Chapter 13, together with an application example in the field of vehicle yaw control.

Chapter 9

Stability and performance properties of approximate NMPC laws

In this Chapter, starting from the assumptions and problem formulation given in Sections 8.1 and 8.3, sufficient conditions are derived for a generic approximated NMPC law $\hat{\kappa}$ to guarantee closed loop stability and convergence properties. Section 9.1 contains some preliminary analyses and problem settings, while the main theoretical results are given in Section 9.2.

9.1 Problem settings

It is considered that the approximated NMPC law $\hat{\kappa}$ enjoys the following *key properties*:

I) Input constraint satisfaction. For the sake of simplicity of presentation, it will be assumed that $\mathbb{U} = \{u \in \mathbb{R}^m : \underline{u}_i \leq u_i \leq \overline{u}_i, i = 1, \ldots, m\}$, where $\underline{u}_i, \overline{u}_i \in \mathbb{R}, i = 1, \ldots, m$. Thus, the considered property is the following:

$$\underline{u}_i \leq \hat{\kappa}_i(x) \leq \overline{u}_i, \; \forall i \in [1,m], \; \forall x \in \mathcal{X} \tag{9.1}$$

II) The pointwise approximation error $\Delta_{\hat{\kappa}}(x) \doteq \kappa^0(x) - \hat{\kappa}(x)$ is bounded:

$$\|\Delta_{\hat{\kappa}}(x)\| \leq \zeta, \; \forall x \in \mathcal{X} \tag{9.2}$$

where $\|\cdot\|$ is a suitable norm (the Euclidean norm will be considered in the following).

III) The bound $\zeta(\nu)$ converges to zero as the number ν of the off–line computed solutions increases:

$$\lim_{\nu \to \infty} \zeta(\nu) = 0 \tag{9.3}$$

Since $\mathcal{X}$ and the image set $\mathbb{U}$ of κ^0 are compact sets, continuity of κ^0 implies that its components $\kappa_i^0, i = 1,\ldots,m$ are Lipschitz continuous functions over $\mathcal{X}$, i.e. there exist finite constants $L_{\kappa^0,i}, i = 1,\ldots,m$ such that:

$$\forall x^1,x^2 \in \mathcal{X},\ \forall i \in [1,m], |\kappa_i^0(x^1) - \kappa_i^0(x^2)| \leq L_{\kappa^0,i}\|x^1 - x^2\|_2 \tag{9.4}$$

Thus, κ^0 is Lipschitz continuous over $\mathcal{X}$, i.e.:

$$\forall x^1,x^2 \in \mathcal{X}, \|\kappa^0(x^1) - \kappa^0(x^2)\|_2 \leq \|L_{\kappa^0}\|_2 \|x^1 - x^2\|_2 \tag{9.5}$$

where $L_{\kappa^0} = [L_{\kappa^0,1},\ldots,L_{\kappa^0,m}]^T$. Estimates $\hat{L}_{\kappa^0,i}, i = 1,\ldots,m$ of $L_{\kappa^0,i}$ can be derived as follows:

$$\hat{L}_{\kappa^0,i} = \inf\left(\tilde{L}_i : \tilde{u}_i^h + \tilde{L}_i\|\tilde{x}^h - \tilde{x}^k\|_2 \geq \tilde{u}_i^k,\ \forall k,h = 1,\ldots,\nu\right) \tag{9.6}$$

The next result proves convergence of $\hat{L}_{\kappa^0,i}$ to $L_{\kappa^0,i}, i = 1,\ldots,m$.

Theorem 1

$$\lim_{\nu\to\infty} \hat{L}_{\kappa^0,i} = L_{\kappa^0,i},\ \forall i = 1,\ldots,m$$

Proof.For any $x^1,x^2 \in \mathcal{X}$, consider two values $\tilde{x}^1,\tilde{x}^2 \in \mathcal{X}_\nu$ such that:

$$\|x^1 - \tilde{x}^1\|_2 \leq d_H(\mathcal{X},\mathcal{X}_\nu)$$
$$\|x^2 - \tilde{x}^2\|_2 \leq d_H(\mathcal{X},\mathcal{X}_\nu)$$

Property (8.10) leads to:

$$0 \leq \lim_{\nu\to\infty} \|x^1 - \tilde{x}^1\|_2 \leq \lim_{\nu\to\infty} d_H(\mathcal{X},\mathcal{X}_\nu) = 0;$$
$$0 \leq \lim_{\nu\to\infty} \|x^2 - \tilde{x}^2\|_2 \leq \lim_{\nu\to\infty} d_H(\mathcal{X},\mathcal{X}_\nu) = 0;$$

which implies that

$$\lim_{\nu\to\infty} \tilde{x}^1 = x^1,\ \forall x^1 \in \mathcal{X},\ \lim_{\nu\to\infty} \tilde{x}^2 = x^2,\ \forall x^2 \in \mathcal{X} \tag{9.7}$$

For any $i \in [1,m]$, the estimate $\hat{L}_{\kappa^0,i}$ (9.6) of $L_{\kappa^0,i}$ is such that:

$$\tilde{u}_i^h + \hat{L}_{\kappa^0,i}\|\tilde{x}^h - \tilde{x}^k\|_2 \geq \tilde{u}_i^k,\ \forall \tilde{x}^h,\tilde{x}^k \in \mathcal{X}_\nu$$

which implies that:

$$\begin{aligned}
&\forall \tilde{x}^h,\tilde{x}^k \in \mathcal{X}_\nu,\\
&\kappa_i^0(\tilde{x}^k) - \kappa_i^0(\tilde{x}^h) = \tilde{u}_i^k - \tilde{u}_i^h \leq \hat{L}_{\kappa^0,i}\|\tilde{x}^h - \tilde{x}^k\|_2\\
&\kappa_i^0(\tilde{x}^h) - \kappa_i^0(\tilde{x}^k) = \tilde{u}_i^h - \tilde{u}_i^k \leq \hat{L}_{\kappa^0,i}\|\tilde{x}^h - \tilde{x}^k\|_2\\
\Rightarrow\ &|\kappa_i^0(\tilde{x}^h) - \kappa_i^0(\tilde{x}^k)| \leq \hat{L}_{\kappa^0,i}\|\tilde{x}^h - \tilde{x}^k\|_2,\ \forall \tilde{x}^h,\tilde{x}^k \in \mathcal{X}_\nu
\end{aligned} \tag{9.8}$$

According to (9.7), as $\nu \to \infty$ inequality (9.8) holds for any $x^1,x^2 \in \mathcal{X}$, therefore $\hat{L}_{\kappa^0,i}$ tends to satisfy definition (9.4) and to approximate the Lipschitz constant $L_{\kappa^0,i}$ of κ_i^0 on $\mathcal{X}$ for any $i = 1,\ldots,m$. ■

Remark 3 *Note that in the case of linear quadratic MPC, functions κ_i^0 can be explicitly computed and are affine over a finite number N^{Part} of polyhedral subregions X^j, $j = 1,\ldots,N^{Part}$ of the state space [72]. Then, by denoting with $\partial\kappa_i^{0,j}/\partial x$ the gradient of κ_i^0 within region X^j, the values of $L_{\kappa^0,i}, i = 1,\ldots,m$ (9.4) can be also computed as:*

$$L_{\kappa^0,i} = \max_{j=1,\ldots,N^{Part}} \left\|\partial\kappa_i^{0,j}/\partial x\right\|_2 \tag{9.9}$$

Moreover, continuity of f over $\mathbb{R}^n \times \mathbb{R}^m$ implies that also f is Lipschitz continuous over $\mathcal{X} \times \mathbb{U}$ with Lipschitz constant L_f, i.e.:

$$\|f(w^1) - f(w^2)\|_2 \leq L_f\|w^1 - w^2\|_2,\ \forall w^1,w^2 \in \mathcal{X} \times \mathbb{U} \tag{9.10}$$

where $w = (x^T,u^T)^T$. Since f is known, L_f can be numerically or analytically computed. Due to the Lipschitz properties (9.5) and (9.10), function $F^0(x)$ defined in (8.3) is Lipschitz continuous too over $\mathcal{X}$, with Lipschitz constant L_F:

$$L_F = L_f\sqrt{1 + \|L_{\kappa^0}\|_2^2} \tag{9.11}$$

Remark 4 *In the case of linear time invariant systems, function $f(x,u) = A\,x + B\,u$. Thus, it can be easily showed that:*

$$L_F = \|A\| + \|L_{\kappa^0}\|_2\,\|B\| \tag{9.12}$$

Consider now the one-step state trajectory perturbation induced by the use of control function $\hat{\kappa}$ instead of κ^0. Such a perturbation can be expressed as:

$$\hat{x}_{t+1} - x_{t+1} = f(x_t,\hat{\kappa}(x_t)) - f(x_t,\kappa^0(x_t)) = \Omega(x_t),\ \forall x_t \in \mathcal{X} \tag{9.13}$$

Therefore, the following state equation is obtained:

$$\hat{x}_{t+1} = F^0(\hat{x}_t) + e(\hat{x}_t) \tag{9.14}$$

Since in general $\kappa^0(x)$ is not known, $\Omega(x)$ cannot be explicitly computed, but a bound μ on its Euclidean norm can be derived from (9.2) and (9.13):

$$\begin{aligned}&\|\Omega(x)\|_2^2 = \|f(x,\hat{\kappa}(x)) - f(x,\kappa^0(x))\|_2^2 \leq L_f^2\,\|(x^T,\hat{\kappa}(x)^T)^T - (x^T,\kappa^0(x)^T)^T\|_2^2 = \\ &= L_f^2\,(\|(x_0 - x_0\|_2^2 + \|\hat{\kappa}(x) - \kappa^0(x))\|_2^2) = L_f^2\,(\|\Delta_{\hat{\kappa}}(x))\|_2^2) \leq L_f^2\,\zeta(\nu)^2,\ \forall x \in \mathcal{X}\end{aligned}$$

$$\Rightarrow \|\Omega(x)\|_2 \leq L_f\,\zeta(\nu) = \mu(\nu) \tag{9.15}$$

Remark 5 *In the case of linear time invariant systems, function* $f(x,u) = A\,x + B\,u$. *Thus, it can be easily showed that:*

$$\mu(\nu) = \|B\|\,\zeta(\nu)$$

The value of $\mu(\nu)$ depends on the number ν of exact solutions of (8.2) considered for the approximation of κ^0. On the basis of property (9.3) it can be noted that:

$$\lim_{\nu\to\infty} \mu(\nu) = 0 \tag{9.16}$$

Thus it is always possible to choose a suitable value of ν which guarantees a given upper bound $\mu(\nu)$ on the one–step perturbation Ω.
Given these preliminary considerations, the attention will be focused on the following points:

I) to find sufficient conditions on μ (and, consequently, on ν) which guarantee that the state trajectory $\hat{\phi}(t,x_0)$ is kept inside the compact set $\mathcal{X}$ and converge to an arbitrarily small neighborhood of the origin, for any $t \geq 0$ and any $x_0 \in \mathcal{G} \subset \mathcal{X}$, where $\mathcal{G}$ is a positively invariant set for the closed loop system (8.3):

$$\mathcal{G} \subset \mathcal{X} : \phi^0(t,x_0) \in \mathcal{G}, \forall x_0 \in \mathcal{G}, \forall t \geq 0 \tag{9.17}$$

Note that, due to property (8.5), if the state constraint set $\mathbb{X}$ is bounded and the feasibility set $\mathcal{F}$ is such that $\mathbb{X} \subset \mathcal{F}$, any set $\mathcal{G}$ such that $\mathbb{X} \subseteq \mathcal{G} \subset \mathcal{F}$ is positively invariant with respect to system (8.3). Moreover, note that $\{0\} \in \mathcal{G}$, since the origin is a stable fixed point for the nominal system (8.3).

II) To evaluate the constraints satisfaction properties of $\hat{\kappa}$:

$$\hat{F}(x) \in \mathbb{X}$$
$$\hat{\kappa}(x) \in \mathbb{U}$$

If $\hat{\kappa}$ has property (9.1), only the state constraints have to be addressed.

III) To estimate an upper bound $\Delta(\nu)$ of the distance $d(t,x_0) = \|\hat{\phi}(t,x_0) - \phi^0(t,x_0)\|_2$ between the nominal and FMPC controlled state trajectories:

$$d(t,x_0) \leq \Delta(\nu),\ \forall x_0 \in \mathcal{G},\ \forall t \geq 0$$

such that

$$\lim_{\nu\to\infty} \Delta(\nu) = 0$$

The bound Δ will be regarded as a measure of performance degradation of system (8.14) with respect to system (8.3).

The results given in the next Section address all of the presented issues.

9.2 Stability results

In order to derive the stability properties of system (8.14), the following candidate Lyapunov function $V : \mathcal{X} \to \mathbb{R}^+$ will be considered:

$$V(x) = \sum_{j=0}^{\hat{T}-1} \|\phi^0(j,x)\|_2 \tag{9.18}$$

where:

$$\hat{T} \geq T$$
$$T = \inf_{x \in \mathcal{X}} (T \in \mathbb{N} : \|\phi^0(t+T,x)\|_2 < \|x\|_2, \, \forall t \geq 0)$$

The following inequalities hold:

$$\|x\|_2 \leq V(x) = \frac{V(x)}{\|x\|_2}\|x\|_2 \leq b\,\|x\|_2, \forall x \in \mathcal{X} \tag{9.19}$$

where

$$b = \sup_{x \in \mathcal{X}} \frac{V(x)}{\|x\|_2}$$

and

$$V(F^0(x)) - V(x) = \Delta V(x) = -\frac{\|x\|_2 - \|\phi^0(\hat{T},x)\|_2}{\|x\|_2}\|x\|_2 \leq -K\|x\|_2, \forall x \in \mathcal{X} \tag{9.20}$$

with

$$K = \inf_{x \in \mathcal{X}} \frac{\|x\|_2 - \|\phi^0(\hat{T},x)\|_2}{\|x\|_2}, \; 0 < K < 1$$

Thus $V(x)$ is a Lyapunov function for system (8.3) over $\mathcal{X}$. Moreover, it can be easily showed that $V(x)$ is Lipschitz continuous, with Lipschitz constant $\tilde{L}_V$:

$$|V(x^1) - V(x^2)| \leq \tilde{L}_V \|x^1 - x^2\|_2, \forall x^1, x^2 \in \mathcal{X} \tag{9.21}$$

with

$$\tilde{L}_V = \sum_{j=0}^{\hat{T}-1} (L_F)^j \tag{9.22}$$

thus the following inequality holds:

$$\begin{aligned} &\forall x \in \mathcal{X}, \, \forall e : (F^0(x) + e) \in \mathcal{X} \\ &V(F^0(x) + e) \leq V(F^0(x)) + \tilde{L}_V \mu \end{aligned} \tag{9.23}$$

Note that constant $\tilde{L}_V$ as defined in (9.22) is not in general the one with the lowest value such that (9.21) holds. From a practical point of view, a less conservative estimate $\hat{L}_V$ of the "best" constant L_V can be computed as:

$$\hat{L}_V = \inf(\tilde{L}_V : V(\tilde{x}^h) + \tilde{L}_V \|\tilde{x}^h - x^k\| \geq V(x^k),\, \forall x^k, x^h \in \mathcal{X}_\nu) \tag{9.24}$$

Similarly to Theorem 1, it can be shown that $\lim_{\nu \to \infty} \hat{L}_V = L_V$. In the following, the $\|\cdot\|_2$–ball set centered in x is denoted as:

$$\mathbb{B}(x,r) = \{\hat{x} \in \mathbb{R}^n \,:\, \|\hat{x} - x\|_2 \leq r,\}$$

and notation $\mathbb{B}(\mathcal{A},r)$, $\mathcal{A} \subseteq \mathbb{R}^n$ is used to indicate the set:

$$\mathbb{B}(\mathcal{A},r) = \bigcup_{x \in \mathcal{A}} \mathbb{B}(x,r)$$

Theorem 2 *Let $\hat{\kappa}$ be an approximation of the nominal NMPC law κ^0, computed using a number ν of exact off–line solutions, such that (9.1)–(9.3) hold. Let $\mathcal{G} \subset \mathcal{X}$ be a set such that (9.17) holds. Then, it is always possible to find a suitable value of ν such that there exists a finite value $\Delta \in \mathbb{R}^+$ with the following properties:*

I) *the trajectory distance $d(t,x_0) = \hat{\phi}(t,x_0) - \phi^0(t,x_0)$ is bounded by Δ:*

$$d(t,x_0) \leq \Delta, \forall x_0 \in \mathcal{G}, \forall t \geq 0 \tag{9.25}$$

II) *Δ can be explicitly computed as:*

$$\Delta = \sup_{t \geq 0} \min(\Delta_1(t,\mu), \Delta_2(t,\mu)) \tag{9.26}$$

where:

$$\Delta_1(t,\mu) = \sum_{k=0}^{t-1} (L_F)^k \mu \tag{9.27}$$

$$\Delta_2(t,\mu) = 2\,\eta^t \sup_{x_0 \in \mathcal{G}} V(x_0) + \frac{b}{K}\, L_V\, \mu \tag{9.28}$$

with $\eta = \left(1 - \dfrac{K}{b}\right), 0 < \eta < 1.$

III) *$\Delta(\nu)$ converges to 0:*

$$\lim_{\nu \to \infty} \Delta(\nu) = 0 \tag{9.29}$$

IV) *the state trajectory of system (8.14) is kept inside the set* $\mathbb{B}(\mathcal{G},\Delta)$ *for any* $x_0 \in \mathcal{G}$*:*

$$\hat{\phi}(t,x_0) \in \mathbb{B}(\mathcal{G},\Delta), \forall x_0 \in \mathcal{G}, \forall t \geq 0 \tag{9.30}$$

V) *the set* $\mathbb{B}(\mathcal{G},\Delta)$ *is contained in* $\mathcal{X}$

$$\mathbb{B}(\mathcal{G},\Delta) \subseteq \mathcal{X}$$

VI) *the state trajectories of system (8.14) asymptotically converge to the set* $\mathbb{B}(0,q)$*:*

$$\lim_{t\to\infty} \|\hat{\phi}(t,x_0)\|_2 \leq q, \, \forall x_0 \in \mathcal{G}$$

with

$$q = \frac{b}{K} L_V \, \mu \leq \Delta \tag{9.31}$$

Proof.

I)–III) Choose any $x_0 \in \mathcal{G}$ as initial condition for system (8.14). On the basis of (9.11), (9.14) and (9.15) it can be noted that:

$$\begin{aligned}
&d(1,x_0) = \|\hat{\phi}(1,x_0) - \phi^0(1,x_0)\|_2 = \|F^0(x_0) + e(x_0) - F^0(x_0)\|_2 = \|e(x_0)\|_2 \leq \mu \\
&d(2,x_0) = \|\hat{\phi}(2,x_0) - \phi^0(2,x_0)\|_2 = \|F^0(\hat{\phi}(1,x_0)) + e(\hat{\phi}(1,x_0)) - F^0(\phi^0(1,x_0))\|_2 \leq \\
&\leq \|e(\hat{\phi}(1,x_0))\|_2 + \|F^0(\hat{\phi}(1,x_0)) - F^0(\phi^0(1,x_0))\|_2 \leq \\
&\leq \mu + L_F \|\hat{\phi}(1,x_0) - \phi^0(1,x_0)\|_2 \leq \mu + L_F \mu \\
&\dots \\
&d(t,x_0) = \|\hat{\phi}(t,x_0) - \phi^0(t,x_0)\|_2 \leq \sum_{k=0}^{t-1} (L_F)^k \mu
\end{aligned}$$

Thus, the following upper bound of the distance between trajectories $\hat{\phi}(t,x_0)$ and $\phi^0(t,x_0)$ is obtained:

$$d(t,x_0) \leq \sum_{k=0}^{t-1} (L_F)^k \mu = \Delta_1(t,\mu) \, , \, \forall x_0 \in \mathcal{G} \, , \, \forall t \geq 1 \tag{9.32}$$

As $t \to \infty$ the bound Δ_1 may converge, if $L_F < 1$, or diverge, if $L_F \geq 1$. Assuming that $L_F \geq 1$ (see Remark 6 below for the other case), it cannot be proved, on the basis of inequality (9.32) alone, that the trajectory distance $d(t,x_0)$ is bounded. On the other hand, by using the properties of Lyapunov function (9.18) it is possible to compute another upper bound $\Delta_2(t,\mu)$ of $d(t,x_0)$. First of all, through equations (9.20) and (9.23) the following inequality is obtained:

$$\begin{aligned}
&\forall x \in \mathcal{X}, \, \forall e : (F^0(x) + e) \in \mathcal{X} \\
&V(F^0(x) + e) \leq V(x) - K\|x\|_2 + L_V \mu
\end{aligned} \tag{9.33}$$

On the basis of (9.19) and (9.33), the state trajectory $\hat{\phi}(t,x_0)$ is such that:

$$\begin{aligned}
&\|\hat{\phi}(t,x_0)\|_2 \leq V(\hat{\phi}(t,x_0)) \leq \\
&V(\hat{\phi}(t-1,x_0)) - K\|\hat{\phi}(t-1,x_0)\|_2 + L_V\mu \leq \\
&\leq V(\hat{\phi}(t-1,x_0)) - \frac{K}{b}V(\hat{\phi}(t-1,x_0)) + L_V\mu \leq \\
&\leq \eta V(\hat{\phi}(t-1,x_0)) + L_V\mu \leq \\
&\ldots \leq \eta^t V(x_0) + \sum_{j=0}^{t-1}\eta^j\, L_V\mu \leq \eta^t V(x_0) + \frac{1}{1-\eta}L_V\mu
\end{aligned}$$

with $\eta = \left(1 - \frac{K}{b}\right) < 1$. Thus, the following result is obtained:

$$\begin{aligned}
&\|\hat{\phi}(t,x_0)\|_2 \leq \eta^t V(x_0) + \frac{b}{K}\, L_V\, \mu \\
&\|\phi^0(t,x_0)\|_2 \leq \eta^t V(x_0)
\end{aligned} \tag{9.34}$$

Inequalities (9.34) can be used to obtain the upper bound $\Delta_2(t,\mu)$ of the distance between nominal and perturbed state trajectories:

$$\begin{aligned}
&d(t,x_0) = \|\hat{\phi}(t,x_0) - \phi^0(t,x_0)\|_2 \leq \\
&\leq \|\hat{\phi}(t,x_0)\|_2 + \|\phi^0(t,x_0)\|_2 \leq 2\,\eta^t V(x_0) + \frac{b}{K}\, L_V\, \mu \leq \\
&\leq 2\,\eta^t \sup_{x_0\in\mathcal{G}} V(x_0) + \frac{b}{K}\, L_V\, \mu = \Delta_2(t,\mu)\,,\ \forall x_0 \in \mathcal{X}\,,\ \forall t \geq 0
\end{aligned}$$

Note that, since $\mu < \infty$ and $\mathcal{X}$ is compact:

$$\begin{aligned}
&\Delta_2(t,\mu) < \infty,\ \forall t \geq 0 \\
&\lim_{t\to\infty} \Delta_2(t,\mu) = \frac{b}{K}\, L_V\, \mu = q \\
&q < \Delta_2(t,\mu) < \infty,\ \forall t \geq 0
\end{aligned}$$

Thus, as t increases towards ∞, the bound $\Delta_2(t,\mu)$ (9.28) decreases monotonically from a finite positive value, equal to $2 \sup_{x_0\in\mathcal{G}} V(x_0) + \frac{b}{K}\, L_V\, \mu$, towards a finite positive value $q = \frac{b}{K}\, L_V\, \mu$, while the bound $\Delta_1(t,\mu)$ (9.27) increases monotonically from 0 to ∞. Therefore, for a fixed value of μ there exists a finite discrete time instant $\widehat{t} > 0$ such that $\Delta_1(\widehat{t},\mu) > \Delta_2(\widehat{t},\mu)$. As a consequence, by considering the lowest bound between $\Delta_1(t,\mu)$ and $\Delta_2(t,\mu)$ for any $t \geq 0$, the following bound $\Delta(\mu)$ of $d(t,x)$, which depends only on μ, is obtained:

$$\Delta(\mu) = \sup_{t\geq 0} \min(\Delta_1(t,\mu),\Delta_2(t,\mu))$$

$$q \leq \Delta(\mu) < \infty$$

$$\|\hat{\phi}(t,x_0) - \phi^0(t,x_0)\|_2 \leq \Delta(\mu),\ \forall x_0 \in \mathcal{G},\forall t \geq 0$$

Since for any fixed positive value $\tilde{t}$ of t both $\Delta_1(\tilde{t},\mu)$ and $\Delta_2(\tilde{t},\mu)$ increase linearly with $\mu(\nu)$, on the basis of (9.16) $\Delta(\nu)$ is such that

$$\lim_{\nu\to\infty} \Delta(\nu) = 0 \tag{9.35}$$

IV)–V) On the basis of (9.35), it is possible to tune ν such that, for any initial condition $x_0 \in \mathcal{G} \subset \mathcal{X}$, $\Delta(\mu)$ is as small as needed. Indeed, it is needed that $\hat{\phi}(t,x_0) \in \mathcal{X}$ for all $t \geq 0$ for all the considered assumptions to hold. Since by hypothesis the set $\mathcal{G}$ (9.17) is positively invariant for the nominal state trajectories, for a given value of $\Delta(\mu)$ the perturbed state trajectories are such that $\hat{\phi}(t,x_0) \in \mathbb{B}(\mathcal{G},\Delta(\mu)), \forall x_0 \in \mathcal{G}, \forall t \geq 0$. Thus, it is sufficient to choose ν such that $\mathbb{B}(\mathcal{G},\Delta(\mu)) \subseteq \mathcal{X}$. Such a choice is always possible in the considered context.

VI) On the basis of (9.34) and (9.19) it can be noted that:

$$\begin{aligned}\lim_{t\to\infty} \|\hat{\phi}(t,x_0)\|_2 &\leq \lim_{t\to\infty} \eta^t b \|x_0\|_2 + \frac{b}{K} L_V \mu \\ &= \frac{b}{K} L_V \mu = q,\ \forall x_0 \in \mathcal{G}\end{aligned}$$

■

Remark 6 *If $L_F < 1$ (i.e. F^0 is a contraction operator), a simplified formulation for bound Δ is obtained. In fact, Lyapunov function (9.18) can be chosen as $V(x) = \|x\|_2$, with $b = 1$ in (9.19) and $K = (1 - L_F)$ in (9.20), leading to $L_V = 1$. Thus the bound $\Delta_2(t,\mu)$ in (9.28) is computed as:*

$$\Delta_2(t,\mu) = 2(L_F)^t \sup_{x_0\in\mathcal{G}} \|x_0\|_2 + \frac{1}{1 - L_F}\mu$$

and q in (9.31) is $q = \dfrac{1}{1 - L_F}\,\mu$. On the other hand the bound $\Delta_1(t,\mu)$ in (9.27) is such that:

$$\Delta_1(t,\mu) \leq \frac{1}{1 - L_F}\mu,\ \forall t \geq 0$$

therefore a simpler formulation for Δ is obtained:

$$\Delta = \sup_{t\geq 0} \min(\Delta_1(t,\mu),\Delta_2(t,\mu)) = \frac{1}{1 - L_F}\mu$$

Remark 7 *A simplified formulation for bound $\Delta_2(t,\mu)$ is obtained if the MPC problem (8.2) includes a state contraction constraint (see e.g. [85]):*

$$\|\phi^0(t,x_0)\|_2 \leq \sigma \|\phi^0(t-1,x_0)\|_2,\ 0 < \sigma < 1$$

In this case, Lyapunov function (9.18) can be chosen as $V(x) = \|x\|_2$*, with* $b = 1$ *in (9.19) and* $K = (1-\sigma)$ *in (9.20), leading to* $L_V = 1$*. Thus the bound* $\Delta_2(t,\mu)$ *in (9.28) is computed as:*

$$\Delta_2(t,\mu) = 2\sigma^t \sup_{x_0 \in \mathcal{G}} \|x_0\|_2 + \frac{1}{1-\sigma}\mu$$

and q *in (9.31) is* $q = \dfrac{1}{1-\sigma}\,\mu$*.*

The main consequence of Theorem 2 is that, with the proper value of ν, for any initial condition $x_0 \in \mathcal{G}$ it is guaranteed that the state trajectory is kept inside the set $\mathcal{X}$ and converges to the set $\mathbb{B}(0,q)$, which can be arbitrarily small since q linearly depends on μ, i.e. $:\lim_{\nu\to\infty} q = \left(\frac{b}{K} L_V \lim_{\nu\to\infty} \mu(\nu)\right) = 0$. Moreover, on the basis of (9.25) and (9.29) it can be noted that for any $\epsilon > 0$ it is always possible to find a suitable value of ν such that $d(t,x_0) < \epsilon$, $\forall x_0 \in \mathcal{G}$, $\forall t \geq 0$. Therefore, for any given required regulation precision $\overline{q}$, using (9.31) it is possible to compute a priori a sufficient one step perturbation bound $\overline{\mu}$ to guarantee the desired accuracy. Similarly, on the basis of (9.25)–(9.28) a bound $\overline{\mu}$ can be computed a priori, such that the trajectory distance is lower than any required maximum value $\overline{\Delta}$. Then, the approximating function $\hat{\kappa}$ can be computed with increasing values of ν, until the corresponding obtained value of μ is such that $\mu \leq \overline{\mu}$, thus guaranteeing the desired performances (i.e. $q \leq \overline{q}$ and/or $\Delta \leq \overline{\Delta}$). Indeed, as $\nu \to \infty$ (i.e. the performances of control system $\hat{F}$ match with those of F^0), the computation time of $\hat{\kappa}(x)$ increases in general, as well as memory usage. Thus, the value of ν can be chosen in order to set a tradeoff between system performances, computation times and memory requirements.
Theorem 2 does not address explicitly the problem of state constraint satisfaction for the controlled system (8.14), i.e.:

$$\hat{\phi}(t,x) \in \mathbb{X}, \forall x \in \mathcal{G}, \forall t \geq 1$$

However, in consequence of Theorem 2, it is possible to choose ν such that there exists a finite number $\overline{T}$ of time steps after which the state trajectory $\hat{\phi}$ is kept inside the constraint set $\mathbb{X}$, for any initial condition $x_0 \in \mathcal{G}$. Moreover the value of $\overline{T}$ decreases as ν increases. In fact, using (9.25) it follows that

$$\begin{array}{l} \forall x_0 \in \mathcal{G},\ \forall t \geq 0 \\ \|\hat{\phi}(t,x_0)\|_2 \leq \|\phi^0(t,x_0)\|_2 + \Delta(\nu) \end{array} \tag{9.36}$$

Then, considering a value of ν such that:

$$\mathbb{B}(0,\epsilon + \Delta(\nu)) \subset \mathbb{X} \tag{9.37}$$

with $\epsilon > 0$ "small" enough, on the basis of the uniform asymptotic stability assumption (8.4), it is always possible to find $\overline{T} < \infty$ such that:

$$\|\phi^0(t + \overline{T},x_0)\|_2 < \epsilon,\ \forall x_0 \in \mathcal{G},\ \forall t \geq 0$$

Using (9.36) it can be noted that:

$$\begin{aligned} \|\hat{\phi}(t + \overline{T},x_0)\|_2 \leq \|\phi^0(t + \overline{T},x_0)\|_2 + \Delta(\nu) < \\ < \epsilon + \Delta(\nu),\ \forall x_0 \in \mathcal{G},\ \forall t \geq 0 \\ \Rightarrow \hat{\phi}(t + \overline{T},x_0) \in \mathbb{B}(0,\epsilon + \Delta(\nu)),\ \forall x_0 \in \mathcal{G},\ \forall t \geq 0 \end{aligned}$$

and, on the basis of (9.37):

$$\hat{\phi}(t + \overline{T},x_0) \in \mathbb{X},\ \forall x_0 \in \mathcal{G},\ \forall t \geq 0$$

thus after a finite number $\overline{T}$ of time steps there is the guarantee that state constraints are satisfied. Note that in general the higher is ϵ in (9.37), the lower is $\overline{T}$. Since the maximum value of ϵ such that (9.37) holds is higher as $\Delta(\nu)$ decreases, $\overline{T}$ in general decreases as $\Delta(\nu)$ does, i.e. as ν increases.
The stability results presented so far assume that $\hat{\kappa}$ satisfies the key properties (9.1)–(9.3), which are related to the approximation accuracy of $\hat{\kappa}$. In the next Chapter, such properties are further investigated.

Chapter 10

Accuracy properties of approximate NMPC laws

In this Chapter the accuracy properties of a generic approximating function

$$\hat{\kappa} = [\hat{\kappa}_1, \ldots, \hat{\kappa}_m]^T$$

derived with any approximation method (e.g. interpolation, neural networks, etc.), are investigated. In particular, the aim is to provide sufficient conditions for $\hat{\kappa}$ to satisfy properties (9.1)–(9.3), i.e. to be able to guarantee the closed loop stabilizing performance considered by Theorem 2. In the following, it is implicitly meant that any i is considered and notation "$\forall i : i = 1, \ldots, m$" is omitted for simplicity of reading.
The available information on κ_i^0 defines the following function set:

$$\kappa_i^0 \in FFS_{L_{\kappa^0,i}} = \{\kappa_i : \mathcal{X} \to [\underline{u}_i, \overline{u}_i] : \kappa_i \in \mathcal{A}_{L_{\kappa^0,i}};\ \kappa_i(\tilde{x}) = \tilde{u}_i,\ \forall \tilde{x} \in \mathcal{X}_\nu\} \tag{10.1}$$

where:

$$\mathcal{A}_{L_{\kappa^0,i}} = \{\kappa_i : |\kappa_i(x^1) - \kappa_i(x^2)| \leq L_{\kappa^0,i}\|x^1 - x^2\|_2,\ \forall x \in \mathcal{X}\} \tag{10.2}$$

The following Lemma, developed from the results presented in [86], is instrumental to prove the theoretical results presented in this Chapter.

Lemma 1 *Let $h : \mathcal{X} \to \mathbb{R}$ be an unknown function defined over a compact domain $\mathcal{X} \in \mathbb{R}^n$. Let the prior information available on h be described by:*

$$h \in FFS_{L_h} = \{\tilde{h} \in \mathcal{A}_{L_h} : \tilde{h}(\tilde{x}) = \tilde{g},\ \forall \tilde{x} \in \mathcal{X}_\nu,\ \underline{g}(x) \leq h(x) \leq \overline{g}(x),\ \forall x \in \mathcal{X}\}$$

where $\mathcal{A}_{L_h}$ is the set of Lipschitz continuous functions with Lipschitz constant L_h. $\mathcal{X}_\nu \in \mathcal{X}$ is a set containing a finite number ν of values $\tilde{x}$ for which the corresponding values $\tilde{g} = h(\tilde{x})$ are known:

$$\mathcal{X}_\nu = \{\tilde{x}^k \in \mathcal{X} : h(\tilde{x}^k) = \tilde{g}^k, k = \ldots, \nu\}$$

and $\underline{g}, \overline{g} : \mathcal{X} \to \mathbb{R}$ are Lipschitz continuous functions with Lipschitz constant L_g. Define the functions:

$$\begin{aligned} \overline{h}\,(x) &\doteq \min[\overline{g}(x), \min_{\tilde{x}\in\mathcal{X}_\nu} (h(\tilde{x}) + L_h\|x-\tilde{x}\|_2)] \\ \underline{h}\,(x) &\doteq \max[\underline{g}(x), \max_{\tilde{x}\in\mathcal{X}_\nu} (h(\tilde{x}) - L_h\|x-\tilde{x}\|_2)] \end{aligned} \tag{10.3}$$

Then:

I)

$$\begin{aligned} \overline{h}\,(x) &\geq \sup_{\tilde{h}\in FFS_{L_h}} \tilde{h}\,(x) \\ \underline{h}\,(x) &\leq \inf_{\tilde{h}\in FFS_{L_h}} \tilde{h}\,(x) \end{aligned}$$

II) *if $L_g \leq L_h$, then the bounds $\overline{h}, \underline{h} \in FFS_{L_h}$ and they are tight:*

$$\begin{aligned} \overline{h}\,(x) &= \max_{\tilde{h}\in FFS_{L_h}} \tilde{h}\,(x) \\ \underline{h}\,(x) &= \min_{\tilde{h}\in FFS_{L_h}} \tilde{h}\,(x) \end{aligned}$$

Proof.

I) The proof is by contradiction. Suppose that a function $h^a \in FFS_{L_h}$ exists such that, for a certain $x^1 \in \mathcal{X}$,

$$h^a(x^1) > \min[\overline{g}(x^1), \min_{\tilde{x}\in\mathcal{X}_\nu} \big(h(\tilde{x}) + L_h\|x^1-\tilde{x}\|_2\big)] = \overline{h}(x^1) \tag{10.4}$$

Denote by $\tilde{x}^b$ a value of $\tilde{x} \in \mathcal{X}_\nu$ such that:

$$h(\tilde{x}^b) + L_h\|x^1-\tilde{x}^b\|_2 = \min_{\tilde{x}\in\mathcal{X}_\nu} \big(h(\tilde{x}) + L_h\|x^1-\tilde{x}\|_2\big)$$

If $h(\tilde{x}^b) + L_h\|x^1-\tilde{x}^b\|_2 \geq \overline{g}(x^1)$, it means that

$$h^a(x^1) > \overline{g}(x^1) \Rightarrow h^a \notin FFS_{L_h}$$

Otherwise, if $h(\tilde{x}^b) + L_h\|x^1-\tilde{x}^b\|_2 < \overline{g}(x^1)$, it can be noted that

$$h^a(x^1) > h(\tilde{x}^b) + L_h\|x^1-\tilde{x}^b\|_2$$

since it was assumed that $h^a \in FFS_{L_h} \Rightarrow h^a(\tilde{x}^b) = h(\tilde{x}^b)$ thus:

$$h^a(x^1) - h(\tilde{x}^b) = h^a(x^1) - h^a(\tilde{x}^b) > L_h\|x^1-\tilde{x}^b\|_2$$

Moreover since $h^a(x^1) > h(\tilde{x}^b) + L_h\|x^1-\tilde{x}^b\|_2 \Rightarrow h^a(x^1) > h(\tilde{x}^b) \Rightarrow h^a(x^1) - h(\tilde{x}^b) > 0$ then:

$$\begin{aligned} &h^a(x^1) - h^a(\tilde{x}^b) = |h^a(x^1) - h^a(\tilde{x}^b)| > L_h\|x^1-\tilde{x}^b\|_2 \\ &\Rightarrow h^a \notin FFS_{L_h} \end{aligned}$$

Therefore, there is no function $h^a \in FFS_{L_h}$ with the characteristics specified in (10.4), i.e. $\overline{h}(x) \geq h(x)$, $\forall x \in \mathcal{X}$, $\forall h \in FFS_{L_h}$. A similar proof holds for the lower bound $\underline{h}$.

II) Consider the function $\overline{h}$. It will be now shown that $\overline{h}$ belongs to FFS_{L_h}. Conditions $\overline{h}(x) \leq \overline{g}(x), \forall x \in \mathcal{X}$, and $\overline{h}(\tilde{x}) = \tilde{g}, \forall \tilde{x} \in \mathcal{X}_\nu$, are satisfied by definition. Condition $\overline{h}(x) \geq \underline{g}(x)$ is also satisfied, since $L_g \leq L_h$ and $\overline{h}(x) = \min[\overline{g}(x), \min_{\tilde{x} \in \mathcal{X}_\nu} (h(\tilde{x}) + L_h \|x - \tilde{x}\|_2)] \geq \min[\overline{g}(x), \min_{\tilde{x} \in \mathcal{X}_\nu} (\underline{g}(\tilde{x}) + L_g \|x - \tilde{x}\|_2)] \geq \underline{g}(x), \forall x \in \mathcal{X}$. About the Lipschitz continuity of $\overline{h}$, for any $x^1 \in \mathcal{X}$ consider a value $\tilde{x}^b \in \mathcal{X}_\nu$ such that:

$$h(\tilde{x}^b) + L_h \|x^1 - \tilde{x}^b\|_2 = \min_{\tilde{x} \in \mathcal{X}_\nu} \left(h(\tilde{x}) + L_h \|x^1 - \tilde{x}\|_2 \right)$$

If $h(\tilde{x}^b) + L_h \|x^1 - \tilde{x}^b\|_2 \geq \overline{g}(x^1)$, it means that $\overline{h}(x^1) = \overline{g}(x^1)$, thus for any $x^2 \in \mathcal{X}$, since $\overline{h}(x^2) \leq \overline{g}(x^2)$, the following holds:

$$\overline{h}(x^2) - \overline{h}(x^1) \leq \overline{g}(x^2) - \overline{g}(x^1) \leq L_g \|x^2 - x^1\|_2 \leq L_h \|x^2 - x^1\|_2$$

otherwise, if $h(\tilde{x}^b) + L_h \|x^1 - \tilde{x}^b\|_2 < \overline{g}(x^1)$, it means that $\overline{h}(x^1) = h(\tilde{x}^b) + L_h \|x^1 - \tilde{x}^b\|_2$ and, for any $x^2 \in \mathcal{X}$, it can be noted that

$$\begin{aligned} &\overline{h}(x^2) = \min[\overline{g}(x^2), \min_{\tilde{x} \in \mathcal{X}_\nu} (h(\tilde{x}) + L_h \|x^2 - \tilde{x}\|_2)] \leq h(\tilde{x}^b) + L_h \|x^2 - \tilde{x}^b\|_2 \leq \\ &h(\tilde{x}^b) + L_h \|x^2 - x^1\|_2 + L_h \|x^1 - \tilde{x}^b\|_2 = \overline{h}(x^1) + L_h \|x^2 - x^1\|_2 \\ &\Rightarrow \overline{h}(x^2) - \overline{h}(x^1) \leq L_h \|x^2 - x^1\|_2 \end{aligned}$$

In a similar way, by considering a value $\tilde{x}^c \in \mathcal{X}_\nu$ such that $h(\tilde{x}^c) + L_h \|x^2 - \tilde{x}^c\|_2 = \min_{\tilde{x} \in \mathcal{X}_\nu} (h(\tilde{x}) + L_h \|x^2 - \tilde{x}\|_2)$ it can be shown that:

$$\overline{h}(x^2) - \overline{h}(x^1) \geq -L_h \|x^2 - x^1\|_2$$

Therefore, since $\overline{h}(x^2) - \overline{h}(x^1) \leq L_h \|x^2 - x^1\|_2$ and $\overline{h}(x^2) - \overline{h}(x^1) \geq -L_h \|x^2 - x^1\|_2$:

$$\begin{aligned} &|\overline{h}(x^2) - \overline{h}(x^1)| \leq L_h \|x^2 - x^1\|_2, \, \forall x^1, x^2 \in \mathcal{X} \\ &\Rightarrow h \in \mathcal{A}_{L_h} \end{aligned}$$

Thus, if $L_g \leq L_h$ function $\overline{h}$ defined in (10.3) is Lipschitz continuous with constant L_h, belongs to FFS_{L_h} and is a tight upper bound for $\tilde{h}(x), \forall x \in \mathcal{X}, \forall \tilde{h} \in FFS_{L_h}$. A similar proof holds for the tight lower bound $\underline{h}$. ■

As a first step, sufficient conditions are derived for any approximating function $\hat{\kappa}_i$ to obtain a bound ζ_i on the pointwise approximation error norm $|\Delta_{\hat{\kappa},i}(x)| = |\kappa_i^0(x) - \hat{\kappa}_i(x)|$ and, consequently, for $\|\Delta_{\hat{\kappa}}(x)\|_2 = \sqrt{\sum_{i=1}^{m} \Delta_{\hat{\kappa},i}^2(x)}$ to be bounded (i.e. property (9.2)). From the knowledge of the ν exact control moves computed off–line (8.9), the exact values of $\Delta_{\hat{\kappa},i}(\tilde{x})$ are known:

$$\Delta_{\hat{\kappa},i}(\tilde{x}) = \tilde{u}_i - \hat{\kappa}_i(\tilde{x}), \, \forall \tilde{x} \in \mathcal{X}_\nu$$

The following Theorem shows how to compute a bound on $|\Delta_{\hat{\kappa},i}(x)|$ on the basis of the knowledge of $\Delta_{\hat{\kappa},i}(\tilde{x})$.

Theorem 3 *Suppose that $\kappa_i^0 \in FFS_{L_{\kappa^0,i}}$ and $\hat{\kappa}_i$ is Lipschitz continuous with Lipschitz constant $L_{\hat{\kappa},i}$ and satisfies property (9.1), then:*

I) *the approximation error $\Delta_{\hat{\kappa},i}$ is a Lipschitz continuous function over $\mathcal{X}$, with Lipschitz constant $L_{\Delta_{\hat{\kappa},i}}$ bounded as:*

$$L_{\Delta_{\hat{\kappa},i}} \leq L_{\hat{\kappa},i} + L_{\kappa^0,i} \tag{10.5}$$

II) *$|\Delta_{\hat{\kappa},i}(x)|$ is bounded:*

$$|\Delta_{\hat{\kappa},i}(x)| \leq \zeta_i,\ \forall x \in \mathcal{X}$$

III) *A bound ζ_i can be computed as:*

$$\zeta_i = \sup_{x\in\mathcal{X}} \max\left(\overline{\Delta}_{\hat{\kappa},i}(x), -\underline{\Delta}_{\hat{\kappa},i}(x)\right) \tag{10.6}$$

where

$$\begin{aligned}
\overline{\Delta}_{\hat{\kappa},i}(x) &\doteq \min[\overline{u}_i - \hat{\kappa}_i(x), \min_{\tilde{x}\in\mathcal{X}_\nu} \left(\Delta_{\hat{\kappa},i}(\tilde{x}) + L_{\Delta_{\hat{\kappa},i}}\|x-\tilde{x}\|_2\right)] \\
\underline{\Delta}_{\hat{\kappa},i}(x) &\doteq \max[\underline{u}_i - \hat{\kappa}_i(x), \max_{\tilde{x}\in\mathcal{X}_\nu} \left(\Delta_{\hat{\kappa},i}(\tilde{x}) - L_{\Delta_{\hat{\kappa},i}}\|x-\tilde{x}\|_2\right)]
\end{aligned} \tag{10.7}$$

IV) *if $L_{\hat{\kappa},i} \leq L_{\Delta_{\hat{\kappa},i}}$, the bound ζ_i (10.6) is the tightest one according to the available information on κ_i^0*

Proof.

I) Application of Lipschitz continuity properties of κ_i^0 and $\hat{\kappa}_i$:

$$\begin{aligned}
&\forall x^1, x^2 \in \mathcal{X},\ |\Delta_{\hat{\kappa},i}(x^1) - \Delta_{\hat{\kappa},i}(x^2)| = |\kappa_i^0(x^1) - \hat{\kappa}_i(x^1) - \kappa_i^0(x^2) + \hat{\kappa}_i(x^2)| \leq \\
&|\kappa_i^0(x^1) - \kappa_i^0(x^2)| + |\hat{\kappa}_i(x^2) - \hat{\kappa}_i(x^1)| \leq L_{\kappa^0,i}\|x^1 - x^2\|_2 + L_{\hat{\kappa},i}\|x^1 - x^2\|_2 \\
&\Rightarrow |\Delta_{\hat{\kappa},i}(x^1) - \Delta_{\hat{\kappa},i}(x^2)| \leq \underbrace{(L_{\kappa^0,i} + L_{\hat{\kappa},i})}_{L_{\Delta_{\hat{\kappa},i}}} \|x^1 - x^2\|_2
\end{aligned}$$

Thus, function $\Delta_{\hat{\kappa},i}$ belongs to the following set:

$$\mathcal{A}_{L_{\Delta_{\hat{\kappa},i}}} = \left\{\Delta_i : \mathcal{X} \to \mathbb{R}, |\Delta_i(x^1) - \Delta_i(x^2)| \leq L_{\Delta_{\hat{\kappa},i}} \|x^1 - x^2\|_2,\ \forall x^1, x^2 \in \mathcal{X}\right\} \tag{10.8}$$

II)–III) Note that the pointwise value of $\Delta_{\hat{\kappa},i}$ is bounded:

$$\begin{aligned}
&\forall x \in \mathcal{X},\ \underline{u}_i \leq \kappa_i^0(x) \leq \overline{u}_i \\
&\Rightarrow \underline{u}_i - \hat{\kappa}_i(x) \leq \kappa_i^0(x) - \hat{\kappa}_i(x) = \Delta_{\hat{\kappa},i}(x) \leq \overline{u}_i - \hat{\kappa}_i(x)
\end{aligned}$$

and that the bounds $\underline{u}_i - \hat{\kappa}_i, \overline{u}_i - \hat{\kappa}_i : \mathcal{X} \to \mathbb{R}$ are Lipschitz continuous functions with Lipschitz constant $L_{\hat{\kappa},i}$. Thus, the prior information on $\Delta_{\hat{\kappa},i}$ is summarized by:

$$\begin{aligned}
&\Delta_{\hat{\kappa},i} \in \mathcal{D}_i = \{\Delta_i \in \mathcal{A}_{L_{\Delta_{\hat{\kappa},i}}} : \Delta_i(\tilde{x}) = \tilde{u}_i - \hat{\kappa}_i(\tilde{x}) = \Delta_{\hat{\kappa},i}(\tilde{x}),\ \forall \tilde{x} \in \mathcal{X}_\nu, \\
&\underline{u}_i - \hat{\kappa}_i(x) \leq \Delta_i(x) \leq \overline{u}_i - \hat{\kappa}_i(x),\ \forall x \in \mathcal{X}\}
\end{aligned} \tag{10.9}$$

where $\mathcal{A}_{L_{\Delta_{\hat{\kappa},i}}}$ is defined in (11.16). Thus, Lemma 1 can be used to compute the bounds of $\mathcal{D}_i$, given by (10.7):

$$\overline{\Delta}_{\hat{\kappa},i}(x) \doteq \min[\overline{u}_i - \hat{\kappa}_i(x), \min_{\tilde{x}\in\mathcal{X}_\nu} \left(\Delta_{\hat{\kappa},i}(\tilde{x}) + L_{\Delta_{\hat{\kappa},i}}\|x-\tilde{x}\|_2\right)]$$
$$\underline{\Delta}_{\hat{\kappa},i}(x) \doteq \max[\underline{u}_i - \hat{\kappa}_i(x), \max_{\tilde{x}\in\mathcal{X}_\nu} \left(\Delta_{\hat{\kappa},i}(\tilde{x}) - L_{\Delta_{\hat{\kappa},i}}\|x-\tilde{x}\|_2\right)]$$

On the basis of these bounds, it can be noted that:

$$\Delta_{\hat{\kappa},i}(x) \leq \overline{\Delta}_{\hat{\kappa},i}(x) \leq \max\left(\overline{\Delta}_{\hat{\kappa},i}(x), -\underline{\Delta}_{\hat{\kappa},i}(x)\right)$$
$$-\Delta_{\hat{\kappa},i}(x) \leq -\underline{\Delta}_{\hat{\kappa},i}(x) \leq \max\left(\overline{\Delta}_{\hat{\kappa},i}(x), -\underline{\Delta}_{\hat{\kappa},i}(x)\right)$$
$$|\Delta_{\hat{\kappa},i}(x)| \leq \max\left(\overline{\Delta}_{\hat{\kappa},i}(x), -\underline{\Delta}_{\hat{\kappa},i}(x)\right)$$

Thus,

$$\forall x \in \mathcal{X},\ |\Delta_{\hat{\kappa},i}(x)| \leq \sup_{x\in\mathcal{X}} \max\left(\overline{\Delta}_{\hat{\kappa},i}(x), -\underline{\Delta}_{\hat{\kappa},i}(x)\right) = \zeta_i(\nu)$$

IV) If $L_{\hat{\kappa},i} \leq L_{\Delta_{\hat{\kappa},i}}$, due to Lemma 1 the bound $\zeta_i(\nu)$ (10.6) is the tightest on the basis of the available prior information on κ_i^0, since it is computed on the basis of functions $\overline{\Delta}_{\hat{\kappa},i}, \underline{\Delta}_{\hat{\kappa},i}$ which tightly bound the set $\mathcal{D}_i$. ■

Remark 8 *Note that if the approximation method employed to derive $\hat{\kappa}_i$ does not guarantee input constraint satisfaction, condition (9.1) can be imposed by modifying $\hat{\kappa}_i$ as follows:*

$$\hat{\kappa}_{i,S}(x) = \begin{cases} \hat{\kappa}_i(x) \ \textit{if}\ \underline{u}_i \leq \hat{\kappa}_i(x) \leq \overline{u}_i \\ \underline{u}_i \ \textit{if}\ \hat{\kappa}_i(x) < \underline{u}_i \\ \overline{u}_i \ \textit{if}\ \hat{\kappa}_i(x) > \overline{u}_i \end{cases}$$

Remark 9 *Depending on the properties of $\hat{\kappa}_i$, the Lipschitz constant $L_{\hat{\kappa},i}$ can be computed analytically or numerically or using a procedure similar to (9.6).*

Remark 10 *Note that the bound (10.5) on the Lipschitz constant of the approximation error $\Delta_{\hat{\kappa},i}(x)$ may be conservative. Alternatively, an estimate $\hat{L}_{\Delta_{\hat{\kappa},i}}$ of $L_{\Delta_{\hat{\kappa},i}}$ can be computed using a procedure similar to (9.6).*

According to Theorem 3, a bound $\zeta_i(\nu)$ on the approximation error can be computed for any continuous approximated control law $\hat{\kappa}_i$ and any value of ν, thus satisfying property (9.2) with:

$$\zeta = \sqrt{\sum_{i=1}^{m} \zeta_i^2} \tag{10.10}$$

The next Theorem gives the additional condition needed to satisfy also property (9.3), i.e. the capability of guaranteeing an arbitrary small approximation error.

Theorem 4 *Let $\mathcal{X}_\nu$ be chosen such that (8.10) holds. Let $\kappa_i^0 \in FFS_{L_{\kappa^0,i}}$. If $\hat{\kappa}_i$ satisfies the assumptions of Theorem 3 and moreover it satisfies the following property (data interpolation):*

$$\hat{\kappa}_i(\tilde{x}) = \kappa_i^0(\tilde{x}) = \tilde{u}_i,\ \forall \tilde{x} \in \mathcal{X}_\nu \tag{10.11}$$

then, in addition to the results I)–II) of Theorem 3, the following results hold:

I) *the bound ζ_i on the approximation error can be computed as:*

$$\zeta_i = \sup_{x\in\mathcal{X}} \min\left[\max\left(\overline{u}_i - \hat{\kappa}_i(x), -\underline{u}_i + \hat{\kappa}_i(x)\right), \chi_i(x)\right] \tag{10.12}$$

where

$$\chi_i(x) = \min_{\tilde{x}\in\mathcal{X}_\nu} \left(L_{\Delta_{\hat{\kappa},i}} \|x - \tilde{x}\|_2\right)$$

II) *$\zeta_i(\nu)$ converges to zero:*

$$\lim_{\nu\to\infty} \zeta_i(\nu) = 0$$

Proof.

I) Due to property (10.11), it can be noted that:

$$\Delta_{\hat{\kappa},i}(\tilde{x}) = \kappa_i^0(\tilde{x}) - \hat{\kappa}_i(\tilde{x}) = \tilde{u}_i - \tilde{u}_i = 0,\ \forall \tilde{x} \in \mathcal{X}_\nu$$

then, substituting $\Delta_{\hat{\kappa},i}(\tilde{x}) = 0$ and $\chi_i(x) = \min_{\tilde{x}\in\mathcal{X}_\nu} \left(L_{\Delta_{\hat{\kappa},i}} \|x - \tilde{x}\|_2\right)]$ in the computation of ζ_i given in (10.6):

$$\begin{aligned}
&\zeta_i = \sup_{x\in\mathcal{X}} \max[\overline{\Delta}_{\hat{\kappa},i}(x), -\underline{\Delta}_{\hat{\kappa},i}(x)] = \\
&\sup_{x\in\mathcal{X}} \max[\min(\overline{u}_i - \hat{\kappa}_i(x), \chi_i(x)), -\max(\underline{u}_i - \hat{\kappa}_i(x), \max_{\tilde{x}\in\mathcal{X}_\nu} \left(-L_{\Delta_{\hat{\kappa},i}} \|x - \tilde{x}\|_2\right))] = \\
&\sup_{x\in\mathcal{X}} \max[\min(\overline{u}_i - \hat{\kappa}_i(x), \chi_i(x)), \min(\hat{\kappa}_i(x) - \underline{u}, \chi_i(x))] = \\
&\sup_{x\in\mathcal{X}} \min[\max(\overline{u}_i - \hat{\kappa}_i(x), \hat{\kappa}_i(x) - \underline{u}_i), \chi_i(x)]
\end{aligned}$$

II) Note that:

$$\chi_i(x) = \min_{\tilde{x}\in\mathcal{X}_\nu} \left(L_{\Delta_{\hat{\kappa},i}} \|x - \tilde{x}\|_2\right) = L_{\Delta_{\hat{\kappa},i}} \min_{\tilde{x}\in\mathcal{X}_\nu} \left(\|x - \tilde{x}\|_2\right) \leq L_{\Delta_{\hat{\kappa},i}}\, d_H(\mathcal{X}, \mathcal{X}_\nu)$$

moreover, due to its formulation, $\chi_i(x)$ is such that:

$$\chi_i(x) \geq 0$$

then, due to property (8.10):

$$\begin{aligned}
&0 \leq \lim_{\nu\to\infty} \chi_i(x) \leq \lim_{\nu\to\infty} L_{\Delta_{\hat{\kappa},i}}\, d_H(\mathcal{X}, \mathcal{X}_\nu) = 0 \\
&\Rightarrow \lim_{\nu\to\infty} \chi_i(x) = 0
\end{aligned}$$

Moreover, note that $\overline{u}_i - \hat{\kappa}_i(x) \geq 0$ and $\hat{\kappa}_i(x) - \underline{u}_i \geq 0$, because $\hat{\kappa}_i$ satisfies the input saturation constraints by assumption. Thus, the value of ζ_i (10.12) is such that:

$$\zeta_i = \sup_{x \in \mathcal{X}} \min \left[\max \left(\overline{u}_i - \hat{\kappa}_i(x), - \underline{u}_i + \hat{\kappa}_i(x) \right), \chi_i(x) \right] \geq 0$$

then, it can be noted that

$$\begin{aligned} & 0 \leq \lim_{\nu \to \infty} \zeta_i = \lim_{\nu \to \infty} \sup_{x \in \mathcal{X}} \min \left(\max \left(\overline{u}_i - \hat{\kappa}_i(x), - \underline{u}_i + \hat{\kappa}_i(x) \right), \chi_i(x) \right) = \\ & \sup_{x \in \mathcal{X}} \min \left(\max \left(\overline{u}_i - \hat{\kappa}_i(x), - \underline{u}_i + \hat{\kappa}_i(x) \right), \lim_{\nu \to \infty} \chi_i(x) \right) = 0 \\ & \Rightarrow \lim_{\nu \to \infty} \zeta_i = 0 \end{aligned}$$

■

Theorem 4 can be used to compute an upper bound ζ (10.10) on the error obtained using any approximated control law $\hat{\kappa}$, which satisfies the assumptions for Theorem 3 to hold and interpolates the off–line computed data, and to "tune" ν to guarantee a given desired accuracy. This is sufficient to guarantee closed–loop stability and performance properties according to Theorem 2.

Remark 11 *Theorems 3 and 4 provide only sufficient conditions for a generic function $\hat{\kappa}$ to satisfy properties (9.1)–(9.3). As it will be shown in Chapter 12, there exist approximating functions, enjoying (9.1)–(9.3), which do not satisfy the assumptions for Theorem 4 to hold. In particular, such functions are obtained with the Nearest Point or the SM Neighborhood approaches (see Sections 12.1) and 12.3) respectively).*

In the next Chapters, the attention will be focused on deriving techniques which can be systematically applied to approximate a given NMPC law, satisfying the key properties (9.1)–(9.3).

Chapter 11

Optimal set membership approximations of NMPC

In this Chapter, the problem of deriving approximating functions $\hat{\kappa}_i$ fulfilling the hypotheses of Theorem 4 is studied. As it has been done in Chapter 10, in the following it is implicitly meant that any i is considered and notation "$\forall i : i = 1, \ldots, m$" is omitted for simplicity of reading. Indeed, standard methods, e.g. based on expansions in term of suitable basis functions (polynomials, sigmoids, wavelets, etc.) could be used to satisfy the assumptions of Theorem 4. However, it is well known that in general, as the number of basis functions is increased in order to achieve the interpolation condition (10.11), the approximation error $\|\kappa^0 - \hat{\kappa}\|_p$, in terms of $L_p(\mathcal{X})$ norm, $p \in [1,\infty]$, defined as $\|\kappa_i\|_p \doteq \left[\int_{\mathcal{X}} |\kappa_i(x)|^p dx\right]^{\frac{1}{p}}$, $p \in [1,\infty)$ and $\|\kappa_i\|_\infty \doteq \text{ess–}\sup_{x\in\mathcal{X}} |\kappa_i(x)|$, may become very large. Thus, it is interesting is to find, among all functions $\hat{\kappa}_i$ fulfilling the conditions of Theorem 4, an "optimal" approximation of κ_i^0, in the sense that it gives low (possibly minimal) approximation error with respect to the considered prior assumptions. Let us define more precisely the optimization problem to be investigated. The function κ_i^0 to be approximated is assumed to belong to the Feasible Function Set defined as:

$$FFS_i = \{\kappa_i : \mathcal{X} \to [\underline{u}_i, \overline{u}_i] : \kappa_i \in \mathcal{A}_i;\ \kappa_i(\tilde{x}) = \tilde{u}_i,\ \forall \tilde{x} \in \mathcal{X}_\nu\} \tag{11.1}$$

where $\mathcal{A}_i$ is a given subset of continuous functions. For given $\hat{\kappa}_i \approx \kappa_i^0$, the related L_p approximation error is $\|\kappa_i^0 - \hat{\kappa}_i\|_p$. This error cannot be exactly computed, but its tightest bound is given by:

$$\|\kappa_i^0 - \hat{\kappa}_i\|_p \leq \sup_{\tilde{\kappa}_i \in FSS_i} \|\tilde{\kappa}_i - \hat{\kappa}_i\|_p \doteq E(\hat{\kappa}_i) \tag{11.2}$$

where $E(\hat{\kappa}_i)$ is called *guaranteed* approximation error.
A function κ_i^{SM} is called an *optimal approximation* if:

$$E(\kappa_i^{\text{SM}}) = \inf_{\hat{\kappa}_i} E(\hat{\kappa}_i) \doteq r_{p,i} \tag{11.3}$$

The quantity $r_{p,i}$, called *radius of information*, gives the minimal L_p approximation error that can be guaranteed. Note that such a κ_i^{SM}, if found, satisfies the conditions required by Theorem 4 and has the minimal guaranteed approximation error $E(\kappa_i^0,\kappa_i^{\mathrm{SM}})$ achievable from the considered information on κ_i^0, summarized in the FFS_i, which in turn depends on the known values (8.9) and on other (possibly qualitative) information described by $\mathcal{A}_i$. The next Sections present two possible techniques to derive an optimal approximation $\kappa_i^{\mathrm{SM}} \approx \kappa_i^0$, which differ depending on the considered prior assumptions on the set κ_i^0.

11.1 Global optimal approximation

The SM global optimal approximation (OPT), which was originally introduced in [82] on the basis of the results of [86], is computed on the basis of the prior information (10.1)–(10.2) on κ_i^0, recalled here for simplicity of reading:

$$\kappa_i^0 \in FFS_{L_{\kappa^0,i}} = \{\kappa_i : \mathcal{X} \to [\underline{u}_i,\overline{u}_i] : \kappa_i \in \mathcal{A}_{L_{\kappa^0,i}};\ \kappa_i(\tilde{x}) = \tilde{u}_i,\, \forall \tilde{x} \in \mathcal{X}_\nu\}$$

where:

$$\mathcal{A}_{L_{\kappa^0,i}} = \{\kappa_i : |\kappa_i(x^1) - \kappa_i(x^2)| \leq L_{\kappa^0,i}\|x^1 - x^2\|_2,\, \forall x \in \mathcal{X}\}$$

Note that the property $\kappa_i \in \mathcal{A}_{L_{\kappa^0,i}}$ is "global" in the sense that a unique Lipschitz constant $L_{\kappa^0,i}$ is considered for the whole set $\mathcal{X}$.
The prior information (10.1)–(10.2) satisfies the assumptions for results I)–II) of Lemma 1 to hold, since the bounding functions $\overline{g}(x) = \overline{u})$ and $\underline{g}(x) = \underline{u})$ are constant, i.e. $L_g = 0 < L_{\kappa^0,i}$. Thus, by applying Lemma 1 the following optimal bounds can be computed:

$$\begin{aligned}
\overline{\kappa}_i &\doteq \sup_{\tilde{\kappa}_i \in FFS_{L_{\kappa^0,i}}} \tilde{\kappa}_i(x) = \min\left[\overline{u}_i, \min_{k=1,\ldots,\nu}\left(\tilde{u}_i^k + L_{\kappa^0,i}\|x - \tilde{x}^k\|_2\right)\right] \in FFS_{L_{\kappa^0,i}} \\
\underline{\kappa}_i &\doteq \inf_{\tilde{\kappa}_i \in FFS_{L_{\kappa^0,i}}} \tilde{\kappa}_i(x) = \max\left[\underline{u}_i, \max_{k=1,\ldots,\nu}\left(\tilde{u}_i^k - L_{\kappa^0,i}\|x - \tilde{x}^k\|_2\right)\right] \in FFS_{L_{\kappa^0,i}}
\end{aligned} \tag{11.4}$$

Finding the optimal bounds is instrumental to solve the optimal approximation problem, as shown in the next result.

Theorem 5 *Consider the function:*

$$\kappa_i^{OPT}(x) = \tfrac{1}{2}[\overline{\kappa}_i(x) + \underline{\kappa}_i(x)] \in FFS_{L_{\kappa^0,i}} \tag{11.5}$$

I) *Function $\kappa_i^{OPT}(x)$ is an optimal approximation of $\kappa_i^0(x)$ for any $L_p(\mathcal{X})$ norm, with $p \in [1,\infty]$*

II) *The radius of information is given by:*

$$r_{p,i} = \frac{1}{2}\|\overline{\kappa}_i - \underline{\kappa}_i\|_p, \forall p \in [1,\infty] \tag{11.6}$$

III) *For given ν, it results:*

$$\|\kappa_i^0 - \kappa_i^{OPT}\|_p \leq r_{p,i}, \forall p \in [1,\infty] \tag{11.7}$$

IV) *The radius of information $r_{\infty,i}$ is bounded:*

$$r_{\infty,i} \leq L_{\kappa^0,i} d_H(\mathcal{X},\mathcal{X}_\nu) \tag{11.8}$$

Proof.

I)-II) Consider the diameter $d_{p,i}$ of $FFS_{L_{\kappa^0,i}}$:

$$d_{p,i} = \sup_{\hat{\kappa}_i,\tilde{\kappa}_i \in FFS_{L_{\kappa^0,i}}} \|\hat{\kappa}_i - \tilde{\kappa}_i\|_p$$

In the considered case, it is possible to show that $d_{p,i} = \|\overline{\kappa}_i - \underline{\kappa}_i\|_p$. For any $\hat{\kappa}_i,\tilde{\kappa}_i \in FFS_{L_{\kappa^0,i}}$ note that:

$$\begin{aligned}
&\hat{\kappa}_i(x) - \tilde{\kappa}_i(x) \leq \overline{\kappa}_i(x) - \underline{\kappa}_i(x), \forall x \in \mathcal{X} \\
&\hat{\kappa}_i(x) - \tilde{\kappa}_i(x) \geq -(\overline{\kappa}_i(x) - \underline{\kappa}_i(x)), \forall x \in \mathcal{X} \\
&\Rightarrow |\hat{\kappa}_i(x) - \tilde{\kappa}_i(x)| \leq |\overline{\kappa}_i(x) - \underline{\kappa}_i(x)|, \forall x \in \mathcal{X}
\end{aligned}$$

Thus the following inequality holds:

$$\|\hat{\kappa}_i - \tilde{\kappa}_i\|_p \leq \|\overline{\kappa}_i - \underline{\kappa}_i\|_p, \forall \hat{\kappa}_i,\tilde{\kappa}_i \in FFS_{L_{\kappa^0,i}}$$

and it can be concluded that:

$$d_{p,i} = \sup_{\hat{\kappa}_i,\tilde{\kappa}_i \in FFS_{L_{\kappa^0,i}}} \|\hat{\kappa}_i - \tilde{\kappa}_i\|_p = \|\overline{\kappa}_i - \underline{\kappa}_i\|_p$$

Therefore the radius of information $r_{p,i}$ of $FFS_{L_{\kappa^0,i}}$ is bounded by [87]:

$$r_{p,i} \geq \frac{1}{2} d_{p,i} = \frac{1}{2}\|\overline{\kappa}_i - \underline{\kappa}_i\|_p \tag{11.9}$$

Consider now the function $\kappa_i^{\text{OPT}} = \frac{1}{2}(\overline{\kappa}_i + \underline{\kappa}_i)$. For any $\tilde{\kappa}_i \in FFS_{L_{\kappa^0,i}}$ it can be noted that:

$$\begin{aligned}
&\forall x \in \mathcal{X}, \\
&\tilde{\kappa}_i(x) - \kappa_i^{\text{OPT}}(x) \leq \overline{\kappa}_i(x) - \kappa_i^{\text{OPT}}(x) = \frac{1}{2}(\overline{\kappa}_i(x) - \underline{\kappa}_i(x)) \\
&\tilde{\kappa}_i(x) - \kappa_i^{\text{OPT}}(x) \geq \underline{\kappa}_i(x) - \kappa_i^{\text{OPT}}(x) = -\frac{1}{2}(\overline{\kappa}_i(x) - \underline{\kappa}_i(x)) \\
&\Rightarrow |\tilde{\kappa}_i(x) - \kappa_i^{\text{OPT}}(x)| \leq \frac{1}{2}|\overline{\kappa}_i(x) - \underline{\kappa}_i(x)|, \forall x \in \mathcal{X}
\end{aligned}$$

which means that, for any $p \in [1,\infty]$,

$$\|\tilde{\kappa}_i - \kappa_i^{\text{OPT}}\|_p \leq \frac{1}{2}\|\overline{\kappa}_i - \underline{\kappa}_i\|_p,\ \forall \tilde{\kappa}_i \in FFS_{L_{\kappa^0,i}}$$

As a consequence, the approximation error $E(\kappa_i^{\text{OPT}})$ defined in (11.2) is

$$E(\kappa_i^{\text{OPT}}) = \sup_{\tilde{\kappa}_i \in FFS_{L_{\kappa^0,i}}} \|\tilde{\kappa}_i - \kappa_i^{\text{OPT}}\|_p = \frac{1}{2}\|\overline{\kappa}_i - \underline{\kappa}_i\|_p \tag{11.10}$$

Since the radius of information $r_{p,i}$ is a lower bound of the approximation error that can be obtained on the basis of the given prior information, the following inequality holds:

$$r_{p,i} \leq E(\kappa_i^{\text{OPT}}) = \frac{1}{2}\|\overline{\kappa}_i - \underline{\kappa}_i\|_p \tag{11.11}$$

Combining inequalities (11.9) and (11.11) leads to

$$E(\kappa_i^{\text{OPT}}) = r_{p,i} = \frac{1}{2}\|\overline{\kappa}_i - \underline{\kappa}_i\|_p,\ \forall p \in [1,\infty]$$

which means that function κ_i^{OPT} is an optimal approximation for any $L_p(\mathcal{X})$ norm, with $p \in [1,\infty]$. Note that $\kappa_i^{\text{OPT}} \in FFS_{L_{\kappa^0,i}}$, since $\overline{\kappa}_i, \underline{\kappa}_i \in FFS_{L_{\kappa^0,i}}$.

III) Consequence of (11.6) and (11.10)

IV) For any $x \in \mathcal{X}$, consider a value $\tilde{x}^b$ of $\tilde{x}^k, k = 1,\ldots,\nu$ such that:

$$\|x - \tilde{x}^b\|_2 \leq d_H(\mathcal{X},\mathcal{X}_\nu)$$

Consider now functions $\overline{\kappa}_i(x)$ and $\underline{\kappa}_i(x)$. The Lipschitz continuity property leads to:

$$\overline{\kappa}_i(x) \leq \overline{\kappa}_i(\tilde{x}^b) + \gamma_i\|x - \tilde{x}^b\|_2, \underline{\kappa}_i(x) \geq \underline{\kappa}_i(\tilde{x}^b) - \gamma_i\|x - \tilde{x}^b\|_2$$

which implies, since $\overline{\kappa}_i(\tilde{x}^b) = \underline{\kappa}_i(\tilde{x}^b) = \tilde{u}_i^b$:

$$\overline{\kappa}_i(x) \leq \tilde{u}_i^b + \gamma_i\, d_H(\mathcal{X},\mathcal{X}_\nu),\ \underline{\kappa}_i(x) \geq \tilde{u}_i^b - \gamma_i\, d_H(\mathcal{X},\mathcal{X}_\nu)$$

As a consequence, for any $x \in \mathcal{X}$ the value $|\overline{\kappa}_i(x) - \underline{\kappa}_i(x)|$ is bounded by:

$$|\overline{\kappa}_i(x) - \underline{\kappa}_i(x)| = \overline{\kappa}_i(x) - \underline{\kappa}_i(x) \leq 2\,\gamma_i\, d_H(\mathcal{X},\mathcal{X}_\nu)$$

thus the radius of information $r_{p,i}$ (11.6) is bounded:

$$\begin{aligned}
&r_{p,i} = \frac{1}{2}\|\overline{\kappa}_i(x) - \underline{\kappa}_i(x)\|_p = \frac{1}{2}\left[\int_{\mathcal{X}} |\overline{\kappa}_i(x) - \underline{\kappa}_i(x)|^p dx\right]^{\frac{1}{p}} \leq \\
&\leq \gamma_i\, d_H(\mathcal{X},\mathcal{X}_\nu)\mu_L(\mathcal{X})^{\frac{1}{p}}, \forall p \in [1,\infty) \\
&r_{\infty,i} = \frac{1}{2}\|\overline{\kappa}_i(x) - \underline{\kappa}_i(x)\|_\infty = \\
&= \frac{1}{2}\text{ess}\sup_{x\in\mathcal{X}} |\overline{\kappa}_i(x) - \underline{\kappa}_i(x)| \leq \gamma_i\, d_H(\mathcal{X},\mathcal{X}_\nu)
\end{aligned}$$

where $\mu_L(\mathcal{X}) = \left[\int_{\mathcal{X}} dx\right] < \infty$ since $\mathcal{X}$ is compact. ■

Since function $\kappa_i^{\text{OPT}} \in FFS_{L_{\kappa^0,i}}$, it satisfies all the assumptions of Theorem 4. The following approximation error bound is obtained:

$$|\kappa_i^0(x) - \hat{\kappa}_i(x)| \leq \zeta_i^{\text{OPT}} = r_{\infty,i},\ \forall x \in \mathcal{X} \tag{11.12}$$

Define the function:

$$\kappa^{\text{OPT}} \doteq [\kappa_1^{\text{OPT}}, \ldots, \kappa_m^{\text{OPT}}]^T$$

On the basis of (11.12) it can be noted that:

$$\|\kappa^0(x) - \kappa^{\text{OPT}}(x)\|_2 \leq \|r_\infty\|_2 = \|\zeta^{\text{OPT}}\|_2 = \zeta^{\text{OPT}}, \forall x \in \mathcal{X} \tag{11.13}$$

with $r_\infty = [r_{\infty,1}, \ldots, r_{\infty,m}]$ and $\zeta^{\text{OPT}} = [\zeta_1^{\text{OPT}}, \ldots, \zeta_m^{\text{OPT}}]$. Moreover, since from Theorem 4 $\lim_{t\to\infty} \zeta_i^{\text{OPT}} = 0$, it can be noted that $\lim_{t\to\infty} \zeta^{\text{OPT}} = 0$. Thus, properties (9.1)–(9.3) are satisfied and the stability Theorem 2 can be applied. Moreover, κ_i^{OPT} gives the minimal worst–case approximation error on the basis of the prior information (10.1)–(10.2).
Finally, note that, as a consequence of (11.8), the following inequality holds:

$$\zeta^{\text{OPT}} = \|r_\infty\|_2 \leq \|L_{\kappa^0}\|_2\, d_H(\mathcal{X}, \mathcal{X}_\nu) \tag{11.14}$$

Remark 12 *Functions $\kappa_i^{OPT}, i = 1, \ldots, m$ (11.5) belong to $FFS_{L_{\kappa^0,i}}, i = 1, \ldots, m$, thus they are Lipschitz continuous functions with Lipschitz constants $L_{\kappa^0,i}, i = 1, \ldots, m$ defined in (9.4). Thus the closed loop system $F^{OPT}(x) = f(x, \kappa^{OPT}(x))$ results to be Lipschitz continuous with Lipschitz constant L_F (9.11). Then if $L_F < 1$, system F^{OPT} results to be a contraction operator and its stability analysis is straightforward, since it is known that exponential asymptotic stability in the origin is guaranteed for such systems (see e.g. [88]).*

Remark 13 *As regards the computation of $r_{\infty,i}, i = 1, \ldots, m$, numerical approaches like the one presented in [89] can be employed.*

11.2 Local optimal approximation

As already pointed out, the OPT approximation is based on a global assumption on the Lipschitz constant $L_{\kappa^0,i}$, and the obtained pointwise approximation error bound depends on such a Lipschitz constant. It is clear that the more detailed information on κ_i^0 is used, the lower is the guaranteed approximation error $E(\kappa_i^0, \kappa_i^{\text{OPT}})$. For example, the set $\mathcal{X}$ can be subdivided in a finite number of subsets $X^j, j = 1, \ldots, N^{\text{part}}$ over which κ_i^0 has Lipschitz constants $L_{\kappa^0,i}^j \leq L_{\kappa^0,i}$. Using the corresponding $\kappa_i^{\text{OPT},j}$ derived as in (11.5) as approximating function of κ_i^0 on each subset $\mathcal{X}^j$ could lead to significant reductions of

the guaranteed approximation error, especially in the subregions where $L^j_{\kappa^0,i} << L_{\kappa^0,i}$. As the number of subdivisions grows, this approach allows to use information on the "local" Lipschitz constants of κ^0_i. However, the computational complexity of such approach would grow with the number of partitions.
A simpler approach is now presented, allowing to use such "local" information to systematically derive an approximation satisfying the conditions of Theorem 4, starting from a preliminary approximating function $\hat{\kappa}$ which satisfies conditions for Theorem 3 only. Moreover, the local SM technique (LOC) proposed here can be applied to improve the accuracy of function $\hat{\kappa}$, in terms of the bound ζ_i, $i = 1 \dots ,m$ (10.12), and, depending on the characteristics of $\hat{\kappa}$, it also allows to compute an optimal approximation of κ^0, in the sense of (11.3).
For a given preliminary approximating function $\hat{\kappa}$, satisfying the assumptions of Theorem 3, consider the related residue function $\Delta_{\hat{\kappa},i} = \kappa^0_i - \hat{\kappa}_i$ which, on the basis of Theorem 3, is Lipschitz continuous over $\mathcal{X}$, with Lipschitz constant $L_{\Delta_{\hat{\kappa},i}}$. Then, the information available on κ^0_i can be summarized by the following set $FFS_{\Delta,i}$:

$$FFS_{\Delta,i} = \{\kappa_i : \mathcal{X} \to [\underline{u}_i,\overline{u}_i],\ (\kappa_i - \hat{\kappa}_i) \in \mathcal{A}_{L_{\Delta_{\hat{\kappa},i}}},\ \kappa_i(\tilde{x}) = \tilde{u}_i,\ \forall \tilde{x} \in \mathcal{X}_\nu\} \tag{11.15}$$

where

$$\mathcal{A}_{L_{\Delta_{\hat{\kappa},i}}} = \left\{\Delta_i : \mathcal{X} \to \mathbb{R}, |\Delta_i(x^1) - \Delta_i(x^2)| \leq\ L_{\Delta_{\hat{\kappa},i}} \|x^1 - x^2\|_2,\ \forall x^1,x^2 \in \mathcal{X}\right\} \tag{11.16}$$

Define the following functions:

$$\Delta^{\text{OPT}}_{\hat{\kappa},i}(x) \doteq \frac{1}{2}[\overline{\Delta}_{\hat{\kappa},i}(x) + \underline{\Delta}_{\hat{\kappa},i}(x)] \tag{11.17}$$

$$\kappa^{\text{LOC}}_i \doteq \hat{\kappa}_i + \Delta^{\text{OPT}}_{\hat{\kappa},i} \tag{11.18}$$

where $\overline{\Delta}_{\hat{\kappa},i}(x)$ and $\underline{\Delta}_{\hat{\kappa},i}(x)$ are defined in (10.7). The next theorem states the properties of the SM local optimal approximation κ^{LOC}_i.

Theorem 6 *For any given function $\hat{\kappa}_i$ satisfying the conditions of Theorem 3, the corresponding function κ^{LOC}_i (11.18) enjoys the following properties:*

I) *Function κ^{LOC}_i interpolates the off–line computed data:*

$$\kappa^{LOC}_i(\tilde{x}) = \tilde{u}_i,\ \forall \tilde{x} \in \mathcal{X}_\nu$$

II) *The quantity*

$$\zeta^{LOC}_i \doteq \sup_{x \in \mathcal{X}} \frac{1}{2}\left(\overline{\Delta}_{\hat{\kappa},i}(x) - \underline{\Delta}_{\hat{\kappa},i}(x)\right)$$

ia a bound on the approximation error $|\kappa^0_i(x) - \kappa^{LOC}_i(x)|$:

$$|\kappa^0_i(x) - \kappa^{LOC}_i(x)| \leq \zeta^{LOC}_i,\ \forall x \in \mathcal{X} \tag{11.19}$$

III) *The bound ζ_i^{LOC} is lower than the bound ζ_i related to the preliminary approximating function $\hat{\kappa}$, computed using Theorem 3 (see (10.6)):*

$$\zeta_i^{LOC} \leq \zeta_i$$

Moreover, if $L_{\hat{\kappa},i} \leq L_{\Delta_{\hat{\kappa},i}}$ the function κ_i^{LOC} enjoys also the following properties:

IV) $\kappa_i^{LOC} \in FFS_{\Delta,i}$

V) *κ_i^{LOC} is an optimal approximation of κ_i^0 with respect to the information $\kappa_i^0 \in FFS_{\Delta,i}$:*

$$\sup_{\kappa_i^0 \in FFS_{\Delta,i}} e(\kappa_i^0, \kappa_i^{LOC}) = \inf_{\tilde{\kappa}_i \in FFS_{\Delta,i}} \sup_{\kappa_i^0 \in FFS_{\Delta,i}} e(\kappa_i^0, \tilde{\kappa}_i) = r_{\Delta,\infty,i}$$

where $r_{\Delta,\infty,i}$ is the ∞-norm radius of information of $FFS_{\Delta,i}$ [87].

Proof.

I) For any $\tilde{x}^h \in \mathcal{X}_\nu$, note that, due to the Lipschitz continuity (11.16) of $\Delta_{\hat{\kappa},i}$ with constant $L_{\Delta_{\hat{\kappa},i}}$:

$$\begin{aligned}
&\min_{\tilde{x} \in \mathcal{X}} (\Delta_{\hat{\kappa},i}(\tilde{x}) + L_{\Delta_{\hat{\kappa},i}} \|\tilde{x}^h - \tilde{x}\|_2) = \Delta_{\hat{\kappa},i}(\tilde{x}^h) \\
&\max_{\tilde{x} \in \mathcal{X}} (\Delta_{\hat{\kappa},i}(\tilde{x}) - L_{\Delta_{\hat{\kappa},i}} \|\tilde{x}^h - \tilde{x}\|_2) = \Delta_{\hat{\kappa},i}(\tilde{x}^h)
\end{aligned}$$

Moreover, since by assumption (9.1) $\hat{\kappa}_i$ satisfies the input constraints, it can be noted that:

$$\begin{aligned}
\Delta_{\hat{\kappa},i}(\tilde{x}^h) &= \kappa_i^0(\tilde{x}^h) - \hat{\kappa}_i(\tilde{x}^h) \leq \overline{u}_i - \hat{\kappa}_i(\tilde{x}^h) \\
\Delta_{\hat{\kappa},i}(\tilde{x}^h) &= \kappa_i^0(\tilde{x}^h) - \hat{\kappa}_i(\tilde{x}^h) \geq \underline{u}_i - \hat{\kappa}_i(\tilde{x}^h)
\end{aligned}$$

Thus, the following result is obtained:

$$\begin{aligned}
\overline{\Delta}_{\hat{\kappa},i}(\tilde{x}^h) &= \min[\overline{u}_i - \hat{\kappa}_i(\tilde{x}^h), \min_{\tilde{x} \in \mathcal{X}_\nu} (\Delta_{\hat{\kappa},i}(\tilde{x}) + L_{\Delta_{\hat{\kappa},i}} \|\tilde{x}^h - \tilde{x}\|_2)] = \Delta_{\hat{\kappa},i}(\tilde{x}^h) \\
\underline{\Delta}_{\hat{\kappa},i}(\tilde{x}^h) &= \max[\underline{u}_i - \hat{\kappa}_i(\tilde{x}^h), \max_{\tilde{x} \in \mathcal{X}_\nu} (\Delta_{\hat{\kappa},i}(\tilde{x}) - L_{\Delta_{\hat{\kappa},i}} \|\tilde{x}^h - \tilde{x}\|_2)] = \Delta_{\hat{\kappa},i}(\tilde{x}^h)
\end{aligned}$$

and, as a consequence:

$$\Delta_{\hat{\kappa},i}^{\text{OPT}}(\tilde{x}^h) = \frac{1}{2}(\overline{\Delta}_{\hat{\kappa},i}(\tilde{x}^h) + \underline{\Delta}_{\hat{\kappa},i}(\tilde{x}^h)) = \Delta_{\hat{\kappa},i}(\tilde{x}^h), \, \forall \tilde{x}^h \in \mathcal{X}_\nu \tag{11.20}$$

Therefore, it can be noted that:

$$\begin{aligned}
&\kappa_i^{\text{LOC}}(\tilde{x}) = \hat{\kappa}_i(\tilde{x}) + \Delta_{\hat{\kappa},i}^{\text{OPT}}(\tilde{x}) = \hat{\kappa}_i(\tilde{x}) + \Delta_{\hat{\kappa},i}(\tilde{x}) = \\
&= \kappa_i^0(\tilde{x}) - \hat{\kappa}_i(\tilde{x}) + \hat{\kappa}_i(\tilde{x}) = \kappa_i^0(\tilde{x}) = \tilde{u}, \, \forall \tilde{x} \in \mathcal{X}_\nu
\end{aligned}$$

II) As it has been shown in the proof of Theorem 3, the prior information on the approximation error $\Delta_{\hat{\kappa},i}$ is summarized by (10.9):

$$\Delta_{\hat{\kappa},i} \in \mathcal{D}_i = \{\Delta_i \in \mathcal{A}_{L_{\Delta_{\hat{\kappa},i}}} : \Delta_i(\tilde{x}) = \tilde{u}_i - \hat{\kappa}_i(\tilde{x}) = \Delta_{\hat{\kappa},i}(\tilde{x}),\, \forall \tilde{x} \in \mathcal{X}_\nu$$
$$\underline{u}_i - \hat{\kappa}_i(x) \leq \Delta_i(x) \leq \overline{u}_i - \hat{\kappa}_i(x),\, \forall x \in \mathcal{X}\}$$

where the bounds $\underline{u}_i - \hat{\kappa}_i, \overline{u}_i - \hat{\kappa}_i : \mathcal{X} \to \mathbb{R}$ are Lipschitz continuous functions with Lipschitz constant $L_{\hat{\kappa},i}$. Thus, according to Lemma 1:

$$\Delta_{\hat{\kappa},i}(x) \leq \sup_{\Delta_i \in \mathcal{D}_i} \Delta_i(x) \leq \overline{\Delta}_{\hat{\kappa},i}(x)$$
$$\Delta_{\hat{\kappa},i}(x) \geq \inf_{\Delta_i \in \mathcal{D}_i} \Delta_i(x) \geq \underline{\Delta}_{\hat{\kappa},i}(x)$$

Therefore, it can be noted that, for any $x \in \mathcal{X}$:

$$\kappa_i^0(x) - \kappa_i^{\mathrm{LOC}}(x) = \kappa_i^0(x) - \hat{\kappa}_i(x) - \frac{1}{2}(\overline{\Delta}_{\hat{\kappa},i}(x) + \underline{\Delta}_{\hat{\kappa},i}(x)) =$$
$$= \Delta_{\hat{\kappa},i}(x) - \frac{1}{2}(\overline{\Delta}_{\hat{\kappa},i}(x) + \underline{\Delta}_{\hat{\kappa},i}(x)) \leq \overline{\Delta}_{\hat{\kappa},i}(x) - \frac{1}{2}(\overline{\Delta}_{\hat{\kappa},i}(x) + \underline{\Delta}_{\hat{\kappa},i}(x)) =$$
$$= \frac{1}{2}(\overline{\Delta}_{\hat{\kappa},i}(x) - \underline{\Delta}_{\hat{\kappa},i}(x))$$
$$-\kappa_i^0(x) + \kappa_i^{\mathrm{LOC}}(x) = -\kappa_i^0(x) + \hat{\kappa}_i(x) + \frac{1}{2}(\overline{\Delta}_{\hat{\kappa},i}(x) + \underline{\Delta}_{\hat{\kappa},i}(x)) =$$
$$= -\Delta_{\hat{\kappa},i}(x) + \frac{1}{2}(\overline{\Delta}_{\hat{\kappa},i}(x) + \underline{\Delta}_{\hat{\kappa},i}(x)) \leq -\underline{\Delta}_{\hat{\kappa},i}(x) + \frac{1}{2}(\overline{\Delta}_{\hat{\kappa},i}(x) + \underline{\Delta}_{\hat{\kappa},i}(x)) =$$
$$= \frac{1}{2}(\overline{\Delta}_{\hat{\kappa},i}(x) - \underline{\Delta}_{\hat{\kappa},i}(x))$$

Thus:

$$|\kappa_i^0(x) - \kappa_i^{\mathrm{LOC}}(x)| \leq \frac{1}{2}(\overline{\Delta}_{\hat{\kappa},i}(x) - \underline{\Delta}_{\hat{\kappa},i}(x),\, \forall x \in \mathcal{X}$$
$$\Rightarrow |\kappa_i^0(x) - \kappa_i^{\mathrm{LOC}}(x)| \leq \sup_{x \in \mathcal{X}} \frac{1}{2}(\overline{\Delta}_{\hat{\kappa},i}(x) - \underline{\Delta}_{\hat{\kappa},i}(x)) = \zeta_i^{\mathrm{LOC}},\, \forall x \in \mathcal{X}$$

III) Due to Theorem 3, the approximation error $\Delta_{\hat{\kappa},i}$ is bounded by (10.6):

$$\zeta_i = \sup_{x \in \mathcal{X}} \max\left(\overline{\Delta}_{\hat{\kappa},i}(x), -\underline{\Delta}_{\hat{\kappa},i}(x)\right)$$

It can be noted that:

$$\frac{1}{2}(\overline{\Delta}_{\hat{\kappa},i}(x) - \underline{\Delta}_{\hat{\kappa},i}(x)) \leq \max\left(\overline{\Delta}_{\hat{\kappa},i}(x), -\underline{\Delta}_{\hat{\kappa},i}(x)\right),\, \forall x \in \mathcal{X}$$

thus:

$$\zeta_i^{\mathrm{LOC}} = \sup_{x \in \mathcal{X}} \frac{1}{2}(\overline{\Delta}_{\hat{\kappa},i}(x) - \underline{\Delta}_{\hat{\kappa},i}(x)) \leq \sup_{x \in \mathcal{X}} \max\left(\overline{\Delta}_{\hat{\kappa},i}(x), -\underline{\Delta}_{\hat{\kappa},i}(x)\right) = \zeta_i$$

IV)–V) The considered prior information on κ_i^0 is given by (11.15):

$$FFS_{\Delta,i} = \{\kappa_i : \mathcal{X} \to [\underline{u}_i,\overline{u}_i],\ (\kappa_i - \hat{\kappa}_i) \in \mathcal{A}_{L_{\Delta_{\hat{\kappa},i}}},\ \kappa_i(\tilde{x}) = \tilde{u}_i,\ \forall \tilde{x} \in \mathcal{X}_\nu\}$$

For any generic function $\tilde{\kappa}_i$, consider the corresponding error function $\tilde{\Delta}_i = \tilde{\kappa}_i - \hat{\kappa}_i$. From (11.15) it can be noted that:

$$\begin{aligned}
&\tilde{\kappa}_i \in FFS_{\Delta,i} \Rightarrow \tilde{\Delta}_i \in \mathcal{A}_{L_{\Delta_{\hat{\kappa},i}}} \\
&\tilde{\kappa}_i \in FFS_{\Delta,i} \Rightarrow \tilde{\Delta}_i(\tilde{x}) = \tilde{u}_i - \hat{\kappa}_i(\tilde{x}),\ \forall \tilde{x}_i \in \mathcal{X}_\nu \\
&\tilde{\kappa}_i \in FFS_{\Delta,i} \Rightarrow \underline{u}_i - \hat{\kappa}_i(x) \leq \tilde{\Delta}_i(x) \leq \overline{u}_i - \hat{\kappa}_i(x),\ \forall x \in \mathcal{X}
\end{aligned}$$

thus, the following necessary condition is obtained:

$$\tilde{\kappa}_i \in FFS_{\Delta,i} \Rightarrow \tilde{\Delta}_i \in \mathcal{D}_i$$

On the other hand, if $\tilde{\Delta}_i \in \mathcal{D}_i$ then:

$$\begin{aligned}
&\underline{u}_i - \hat{\kappa}_i(x) \leq \tilde{\Delta}_i(x) \leq \overline{u}_i - \hat{\kappa}_i(x) \\
&\underline{u}_i \leq \tilde{\Delta}_i(x) + \hat{\kappa}_i(x) \leq \overline{u}_i \\
&\underline{u}_i \leq \tilde{\kappa}_i(x) \leq \overline{u}_i
\end{aligned}$$

moreover,

$$\tilde{\Delta}_i \in \mathcal{D}_i \Rightarrow \tilde{\kappa}_i(\tilde{x}) = \hat{\kappa}_i(\tilde{x}) + \tilde{\Delta}_i(\tilde{x}) = \hat{\kappa}_i(\tilde{x}) + \tilde{u}_i - \hat{\kappa}_i(\tilde{x}) = \tilde{u}_i,\ \forall \tilde{x} \in \mathcal{X}_\nu$$

and, due to (10.9):

$$\tilde{\Delta}_i \in \mathcal{D}_i \Rightarrow \tilde{\kappa}_i - \hat{\kappa}_i = \tilde{\Delta}_i \in \mathcal{A}_{L_{\Delta_{\hat{\kappa},i}}}$$

Thus the following sufficient condition is also obtained:

$$\tilde{\kappa}_i \in FFS_{\Delta,i} \Leftarrow \tilde{\Delta}_i \in \mathcal{D}_i$$

Therefore,

$$\tilde{\kappa}_i \in FFS_{\Delta,i} \iff \tilde{\Delta}_i \in \mathcal{D}_i \tag{11.21}$$

Moreover, note that:

$$\begin{aligned}
&e(\kappa_i^0,\tilde{\kappa}_i) = \|\kappa_i^0 - \hat{\kappa}_i - \tilde{\Delta}_i\|_\infty = \|\Delta_{\hat{\kappa},i} - \tilde{\Delta}_i\|_\infty = e(\Delta_{\hat{\kappa},i},\tilde{\Delta}_i) \\
&E(\kappa_i^0,\tilde{\kappa}_i) = \sup_{\kappa_i^0 \in FFS_{\Delta,i}} e(\kappa_i^0,\tilde{\kappa}_i) = \sup_{\Delta_{\hat{\kappa},i} \in \mathcal{D}_i} e(\Delta_{\hat{\kappa},i},\tilde{\Delta}_i) = E(\Delta_{\hat{\kappa},i},\tilde{\Delta}_i)
\end{aligned} \tag{11.22}$$

Therefore, due to (11.21) and (11.22), finding an optimal approximation $\kappa_i^{\text{LOC}} = \hat{\kappa}_i + \Delta_{\hat{\kappa},i}^{\text{OPT}} \approx \kappa_i^0$ such that $\kappa_i^{\text{LOC}} \in FFS_{\Delta,i}$, considering the information $\kappa_i^0 \in FFS_{\Delta,i}$, is equivalent to finding an optimal approximation $\Delta_{\hat{\kappa},i}^{\text{OPT}} \approx \Delta_{\hat{\kappa},i}$ such that $\Delta_{\hat{\kappa},i}^{\text{OPT}} \in \mathcal{D}_i$, considering the information $\Delta_{\hat{\kappa},i} \in \mathcal{D}_i$:

$$E(\kappa_i^0,\kappa_i^{\text{LOC}}) = \inf_{\tilde{\kappa}_i \in FFS_{\Delta,i}} E(\kappa_i^0,\tilde{\kappa}_i) = \inf_{\tilde{\Delta}_i \in \mathcal{D}_i} E(\Delta_{\hat{\kappa},i},\tilde{\Delta}_i) = E(\Delta_{\hat{\kappa},i},\Delta_{\hat{\kappa},i}^{\text{OPT}}) = r_{\Delta,\infty,i}$$

Thus, the aim is to show that $\Delta^{\text{OPT}}_{\hat{\kappa},i} = 1/2\,(\overline{\Delta}_{\hat{\kappa},i} + \underline{\Delta}_{\hat{\kappa},i})$ (11.17) belongs to $\mathcal{D}_i$ and is an optimal approximation of $\Delta_{\hat{\kappa},i}$. Since both $\overline{\Delta}_{\hat{\kappa},i}$,$\underline{\Delta}_{\hat{\kappa},i} \in \mathcal{D}_i$ (see Lemma 1), it can be noted that:

$$\begin{aligned}&\forall x \in \mathcal{X},\\ &\Delta^{\text{OPT}}_{\hat{\kappa},i}(x) = 1/2\,(\overline{\Delta}_{\hat{\kappa},i}(x) + \underline{\Delta}_{\hat{\kappa},i}(x)) \leq \overline{\Delta}_{\hat{\kappa},i}(x) \leq \overline{u}_i - \hat{\kappa}_i(x)\\ &\Delta^{\text{OPT}}_{\hat{\kappa},i}(x) = 1/2\,(\overline{\Delta}_{\hat{\kappa},i}(x) + \underline{\Delta}_{\hat{\kappa},i}(x)) \geq \underline{\Delta}_{\hat{\kappa},i}(x) \geq \underline{u}_i - \hat{\kappa}_i(x)\end{aligned}$$

moreover, $\Delta^{\text{OPT}}_{\hat{\kappa},i} \in \mathcal{A}_{L_{\Delta_{\hat{\kappa},i}}}$:

$$\|\Delta^{\text{OPT}}_{\hat{\kappa},i}(x^1) - \Delta^{\text{OPT}}_{\hat{\kappa},i}(x^2)\|_2 \leq 1/2(\|\overline{\Delta}_{\hat{\kappa},i}(x^1) - \overline{\Delta}_{\hat{\kappa},i}(x^2)\|_2 + \|\underline{\Delta}_{\hat{\kappa},i}(x^1) - \underline{\Delta}_{\hat{\kappa},i}(x^2)\|_2) \leq L_{\Delta_{\hat{\kappa},i}}\|x^1 - x^2\|_2,\ \forall x^1,x^2 \in \mathcal{X}$$

Finally, $\Delta^{\text{OPT}}_{\hat{\kappa},i}$ interpolates the available data, as shown in (11.20).
Thus, $\Delta^{\text{OPT}}_{\hat{\kappa},i} \in \mathcal{D}_i$.
The problem of showing that $\Delta^{\text{OPT}}_{\hat{\kappa},i}$ is an optimal approximation of $\Delta_{\hat{\kappa},i}$, i.e. $E(\Delta_{\hat{\kappa},i},\Delta^{\text{OPT}}_{\hat{\kappa},i}) = \inf_{\tilde{\Delta}_i \in \mathcal{D}_i} E(\Delta_{\hat{\kappa},i},\tilde{\Delta}_i) = r_{\Delta,\infty,i}$ is analogous to that of showing that the OPT approximation κ^{OPT} is an optimal approximation of κ^0 (see the Proof of Theorem 5). Thus, this part of the proof is omitted for brevity. ■

According to Theorem 6, SM theory can be employed to improve the performance of a given approximating function $\hat{\kappa}_i$. In fact, result III) of Theorem 6 shows that the error bound ζ^{LOC}_i of the approximated NMPC law κ^{LOC}_i is lower than that of $\hat{\kappa}_i$. Moreover, from result II) κ^{LOC}_i satisfies the data interpolation condition (10.11) for Theorem 4 to hold, even if $\hat{\kappa}_i$ does not satisfy it. The error bound (9.2) related to function $\kappa^{\text{LOC}} = [\kappa^{\text{LOC}}_1, \ldots, \kappa^{\text{LOC}}_m]^T$ is computed as:

$$\zeta^{\text{LOC}} = \sqrt{\sum_{i=1}^{m} (\zeta^{\text{LOC}}_i)^2}$$

Moreover, if condition $L_{\hat{\kappa},i} \leq L_{\Delta_{\hat{\kappa},i}}$ holds, the worst–case approximation error is minimal in front of the considered prior information (11.15).

Remark 14 *Theorem 6 also applies if the preliminary approximation $\hat{\kappa}$ already satisfies the assumptions of Theorem 4: also in this case, the error bound ζ^{LOC}_i (11.19) is lower than the bound ζ_i, computed using (10.12).*

Remark 15 *Note that the OPT approach is a particular case of the results presented in this paper, i.e. using $\hat{\kappa}_i = 0$. An important point is to find a condition under which the use of $\hat{\kappa}_i \neq 0$ improves the worst–case accuracy, giving lower guaranteed approximation errors. Indeed, it can be noted that if:*

$$\zeta^{LOC} \leq \zeta^{OPT}$$

then the guaranteed accuracy obtained with κ^{LOC} is higher than the one given by κ^{OPT}. As a consequence, a lower number ν of off–line computed values are sufficient for κ^{LOC} to achieve given guaranteed stability and performance properties according to Theorem 2. Lower ν numbers may lead to lower function evaluation times, depending on the computational burden of $\hat{\kappa}_i$.

Remark 16 *Note that condition $L_{\hat{\kappa},i} \leq L_{\Delta_{\hat{\kappa},i}}$ can be checked by computing or estimating (e.g. using (9.6)) the Lipschitz constants $L_{\hat{\kappa},i}$ and $L_{\Delta_{\hat{\kappa},i}}$. Moreover, such assumption can be always satisfied using a preliminary approximating function $\hat{\kappa}_i$ whose complexity is not too high with respect to κ_i^0, with the extreme case of $\hat{\kappa} = 0$, i.e. $L_{\hat{\kappa}} = 0$. For example, if $\hat{\kappa}_i$ is computed as an expansion of basis functions, it is possible to improve the obtained accuracy by gradually increasing the number of basis functions: in this case the value of $L_{\hat{\kappa},i}$ may grow and condition $L_{\hat{\kappa},i} \leq L_{\Delta_{\hat{\kappa},i}}$ can be used as a stopping criterium, avoiding also data over–fitting. Then, the optimal SM approximation $\Delta_{\hat{\kappa},i}^{OPT} \approx \Delta_{\hat{\kappa},i}$ can be designed to further improve the performance of $\hat{\kappa}_i$.*

Chapter 12

Suboptimal approximations of NMPC: the tradeoff between complexity and accuracy

The optimal approaches presented so far achieve the minimal guaranteed error, however their evaluation (which involves the evaluation of the upper and lower bounds (10.7)) requires that all of the ν off–line computed values are considered at each sampling instant. Thus, the obtained computational time grows linearly with ν and it may result too high for the considered application. Thus, in this Chapter other kinds of approximating functions, which satisfy conditions (9.1)–(9.3), are sought–after, whose approximation error is not the optimal one, but whose computational effort is lower and, possibly, does not grow linearly with ν. As already pointed out, these control laws are indicated here as "suboptimal approximations" of NMPC.

A further issue, in addition to accuracy and computational efficiency, is related to the memory requirements of the approximated control law. In the case of the optimal approximation, the memory usage is that of the raw data only, $\tilde{x}^k, \tilde{u}^k, k = 1, \ldots, \nu$. As it is showed in this Chapter, the suboptimal approximations may require that also some data structures and additional information are stored (e.g. partitions of the set $\mathcal{X}$, coefficients of piecewise linear interpolating functions, etc.), resulting in higher memory usage.

Finally, techniques with worse accuracy usually need higher ν values to achieve a given accuracy level, causing a growth of off–line computational time.

Thus, the approximating technique has to be chosen and employed taking into account all of these aspects, in order to achieve a tradeoff between accuracy, on–line computational efficiency, memory usage and off–line computational burden which is suitable for the considered application. To this end, no one of the presented approaches is better than the others under all points of view.

As it has been done in the previous Chapters 9–10, in the following the notation κ_i implicitly means that any i is considered and notation "$\forall i : i = 1, \ldots, m$" is omitted for

simplicity of reading.

12.1 Nearest point approach

The "Nearest Point" (NP) approximation is probably the simplest example of suboptimal approximating technique. For a given value of ν, the NP approximation leads in general to an higher approximation error bound ζ^{NP} than OPT approximation, but to lower on–line computation times, whose growth as a function of ν is much slower than that of OPT approximation (see the numerical examples in Section 13.1). Thus, the NP approximation required to guarantee given stability and performance properties may need much lower on–line computation times with respect to OPT approximation, at the cost of higher off–line computation time and memory usage.
The NP technique is now presented. For any $x \in \mathcal{X}$, denote with $\tilde{x}^{\text{NP}}$ a state value such that:

$$\tilde{x}^{\text{NP}} \in \mathcal{X}_\nu : \|\tilde{x}^{\text{NP}} - x\|_2 = \min_{\tilde{x} \in \mathcal{X}_\nu} \|\tilde{x} - x\|_2 \tag{12.1}$$

Then, the NP approximation $\kappa_i^{\text{NP}}(x)$ is computed as:

$$\begin{array}{l} \kappa_i^{\text{NP}}(x) = \kappa_i^0(\tilde{x}^{\text{NP}}) \\ \kappa^{\text{NP}}(x) = [\kappa_1^0(\tilde{x}^{\text{NP}}), \ldots, \kappa_m^0(\tilde{x}^{\text{NP}})]^T \end{array} \tag{12.2}$$

Such approximation trivially satisfies condition (9.1). The next Theorem 7 shows that NP approximation (12.2) satisfies also properties (9.2) and (9.3), needed for Theorem 2 to hold.

Theorem 7 I) *The pointwise approximation error $\|\kappa^0(x) - \kappa^{NP}(x)\|_2$ is bounded:*

$$\begin{array}{l} \|\kappa_i^0(x) - \kappa_i^{NP}(x)\|_2 \leq \zeta_i^{NP} \doteq L_{\kappa^0,i}\, d_H(\mathcal{X},\mathcal{X}_\nu),\ \forall x \in \mathcal{X} \\ \|\kappa^0(x) - \kappa^{NP}(x)\|_2 \leq \zeta^{NP} \doteq \|L_{\kappa^0}\|_2\, d_H(\mathcal{X},\mathcal{X}_\nu),\ \forall x \in \mathcal{X} \end{array} \tag{12.3}$$

II) *The bound ζ^{NP} converges to zero:*

$$\begin{array}{l} \lim\limits_{\nu \to \infty} \zeta_i^{NP} = 0 \\ \lim\limits_{\nu \to \infty} \zeta^{NP} = 0 \end{array} \tag{12.4}$$

Proof.

I) For any $x \in \mathcal{X}$ consider the NP approximation κ_i^{NP} (12.2). Due to the Lipschitz property (9.4) it can be noted that:

$$|\kappa_i^0(x) - \kappa_i^{\text{NP}}(x)| = |\kappa_i^0(x) - \kappa_i^0(\tilde{x}^{\text{NP}})| \leq L_{\kappa^0,i} \|x - \tilde{x}^{\text{NP}}\|_2$$

The state value $\tilde{x}^{\text{NP}}$ (12.1) is such that:

$$\|x - \tilde{x}^{\text{NP}}\|_2 = \min_{\tilde{x} \in \mathcal{X}_\nu} \|x - \tilde{x}\|_2 \leq d_H(\mathcal{X},\mathcal{X}_\nu)$$

thus,

$$|\kappa_i^0(x) - \kappa_i^{\text{NP}}(x)| \leq L_{\kappa^0,i}\, d_H(\mathcal{X},\mathcal{X}_\nu) = \zeta_i^{\text{NP}}$$

And, as a consequence:

$$\|\kappa^0(x) - \kappa^{\text{NP}}(x)\|_2 \leq \|L_{\kappa^0}\|_2\, d_H(\mathcal{X},\mathcal{X}_\nu) = \zeta^{\text{NP}}$$

II) The result follows directly from property (8.10):

$$\lim_{\nu\to\infty} \zeta_i^{\text{NP}} = \lim_{\nu\to\infty} L_{\kappa^0,i}\, d_H(\mathcal{X},\mathcal{X}_\nu) = 0$$
$$\lim_{\nu\to\infty} \zeta^{\text{NP}} = \lim_{\nu\to\infty} \|L_{\kappa^0}\|_2\, d_H(\mathcal{X},\mathcal{X}_\nu) = 0$$

■

Remark 17 *The NP approximation (12.2) satisfies the properties (9.1)–(9.3), with* $\zeta^{NP} = \|L_{\kappa^0}\|_2\, d_H(\mathcal{X},\mathcal{X}_\nu)$*. Note that the error bound of the OPT approximation is* $\zeta^{OPT} = \|r_\infty\|_2$ *(11.13). Since* $\|r_\infty\|_2 \leq \|L_{\kappa^0}\|_2\, d_H(\mathcal{X},\mathcal{X}_\nu)$ *(see (11.14)), it can be noted that:*

$$\zeta^{OPT}(\nu) \leq \zeta^{NP}(\nu)$$

Thus for a given value of ν *the guaranteed accuracy obtained using OPT approximation is better than the one obtained with NP approximation. However, with NP approximation it is possible to obtain the same accuracy bound using a higher number of off–line evaluations of the MPC control law, i.e. there exist a finite value* $\nu' > \nu$ *such that:* $\zeta^{NP}(\nu') \leq \zeta^{OPT}(\nu)$*. Due to the simplicity of* κ^{NP}*, the on–line computational times needed to evaluate the NP approximation based on* ν' *off–line computed values may be much lower than the one needed to evaluate the OPT approximation based on* ν *off–line computations. Indeed, for the same reasons the NP approach requires a higher memory usage and higher off–line computational time than OPT, given the same guaranteed accuracy.*

12.2 Linear interpolation

Let $X^1,X^2,...,X^q$ be a triangulation defined by the set of points $\mathcal{X}_\nu$. Such a triangulation is a collection of sets $X^1,X^2,...,X^q$ such that

$$\bigcup_{j=1}^{q} X^j = \text{chull}(\mathcal{X}_\nu),$$
$$\text{int}(X^h) \cap \text{int}(X^j) = 0 \text{ for } h \neq j,$$
all X^j's are simplices (triangles for $n = 2$),
the vertices of the simplices are points of $\mathcal{X}_\nu$,
all points of $\mathcal{X}_\nu$ are vertices of the simplices.

Here int$(\cdot)$ denotes the interior of a set and chull$(\cdot)$ denotes the convex hull of a set. A triangulation partitions the convex hull of $\mathcal{X}_\nu$ into a set of simplices, which will be also referred to as "triangles" in the following. For each triangle X^j, consider the set of points

$$\{\tilde{x}^{j,k}, k = 1, \ldots, n+1 : \tilde{x}^{j,k} \text{ is a vertex of } X^j\}$$

Since a triangle has $n+1$ vertices, such a set contains $n+1$ points in $\mathbb{R}^n$. Let $K_i^j x + Q_i^j$ be the hyperplane interpolating the corresponding exact control moves $\tilde{u}^{j,k} = \kappa_i^0(\tilde{x}^{j,k})$. The coefficients $K_i^j \in \mathbb{R}^n$, $Q_i^j \in \mathbb{R}$ can be trivially obtained as

$$\begin{bmatrix} K_i^{jT} \\ Q_i^j \end{bmatrix} = \begin{bmatrix} (\tilde{x}^{j,1})^T & 1 \\ \vdots & \vdots \\ (\tilde{x}^{j,n+1})^T & 1 \end{bmatrix}^{-1} \begin{bmatrix} \tilde{u}_i^{j,1} \\ \vdots \\ \tilde{u}_i^{j,n+1} \end{bmatrix} \tag{12.5}$$

Assume that $\mathcal{X} \subseteq$chull$(\mathcal{X}_\nu)$ and define the piecewise linear approximation (LIN)

$$\kappa_i^{\text{LIN}}(x) \doteq K_i^{\hat{j}} x + Q_i^{\hat{j}} \tag{12.6}$$

where $\hat{j} \in \arg\min_{j=1,\ldots,q} d_S(x, X^j)$ and $d_S(x, X^J) \doteq \inf_{\xi \in X^J} (\|x - \xi\|_2)$ is the distance between the point x and the set X^j. Clearly, for given $x \in \mathcal{X}$, $X^{\hat{j}}$ is a triangle which contains x. If $x \in \text{int}(X^{\hat{j}})$, this triangle is unique. According to the above definition, κ_i^{LIN} is a continuous piecewise linear function, which can be used to approximate κ_i^0. Define the approximation error:

$$\Delta_{\kappa^{\text{LIN},i}}(x) \doteq \kappa_i^0(x) - \kappa_i^{\text{LIN}}(x) \tag{12.7}$$

The next result shows that $\kappa_i^{\text{LIN}}(x)$ satisfies input constraints and that $\Delta_{\kappa^{\text{LIN},i}}(x)$ is bounded and converges to 0 as $\nu \to \infty$, for any $x \in \mathcal{X}$.

Theorem 8 *The following properties hold:*

I) $\kappa_i^{LIN}(x) \in [\underline{u}_i, \overline{u}_i], \forall x \in \mathcal{X}$.

II) *The pointwise approximation error* $\Delta_{\kappa^{LIN},i}(x)$ *of* κ_i^{LIN} *is bounded as*

$$\begin{aligned} &\forall x \in \mathcal{X},\ |\Delta_{\kappa^{LIN},i}(x)| \le e_i^{LIN}(x) = \\ &= |\kappa_i^{OPT}(x) - \kappa_i^{LIN}(x)| + \frac{1}{2}(\overline{\kappa}_i(x) - \underline{\kappa}_i(x)) \ge \frac{1}{2}(\overline{\kappa}_i(x) - \underline{\kappa}_i(x)) \\ &\forall x \in \mathcal{X},\ e_i^{LIN}(x) \le \zeta_i^{LIN} = \sup_{x \in \mathcal{X}} e_i^{LIN}(x) \ge \zeta_i^{OPT} \end{aligned} \tag{12.8}$$

III) $\lim_{\nu \to \infty} \zeta_i^{LIN}(\nu) = 0$

Proof.

I) For any $x \in \mathcal{X}$, consider the the vertices $\tilde{x}^l, l = 1,\dots,n+1$ of the partition $X^{\hat{j}} : \hat{j} \in \arg\min_{j=1,\dots,q} d_S(x,X^j)$, and the corresponding exact control moves $\tilde{u}_i^l = \kappa_i^0(\tilde{x}^l)$. Note that $\tilde{u}_i^l = \kappa_i^{\text{LIN}}(\tilde{x}^l)$ by definition (12.5). The point x can be expressed as:

$$x = \sum_{l=1}^{n+1} w_l\, \tilde{x}^l,\ w_l > 0\, \forall l \in [1,n+1],\ \sum_{l=1}^{n+1} w_l = 1$$

and the approximated control move $\kappa_i^{\text{LIN}}(x)$ can be therefore computed as:

$$\kappa_i^{\text{LIN}}(x) = \sum_{l=1}^{n+1} w_l\, (K_i^j \tilde{x}^l + Q_i^j) =$$
$$= \sum_{l=1}^{n+1} w_l\, \kappa_i^{\text{LIN}}(\tilde{x}^l) = \sum_{l=1}^{n+1} w_l\, \tilde{u}_i^l$$

thus it can be noted that:

$$\kappa_i^{\text{LIN}}(x) \leq \max_{l=1,\dots,n+1}(\tilde{u}_i^l) \sum_{l=1}^{n+1} w_l = \max_{l=1,\dots,n+1}(\tilde{u}_i^l) \leq \overline{u}_i$$
$$\kappa_i^{\text{LIN}}(x) \geq \min_{l=1,\dots,n+1}(\tilde{u}_i^l) \sum_{l=1}^{n+1} w_l = \min_{l=1,\dots,n+1}(\tilde{u}_i^l) \geq \underline{u}_i$$
$$\Rightarrow \kappa_i^{\text{LIN}}(x) \in [\underline{u}_i, \overline{u}_i]$$

II) Due to the properties of the optimal bounds $\overline{\kappa}_i(x), \underline{\kappa}_i(x)$ (11.4), already showed in the proof od Theorem 5, it can be noted that:

$$|\Delta_{\kappa^{\text{LIN},i}}(x)| = |\kappa_i^0(x) - \kappa_i^{\text{LIN}}(x)| = |\kappa_i^0 - \kappa_i^{\text{OPT}}(x) + \kappa^{\text{OPT}},i(x) - \kappa_i^{\text{LIN}}(x)| \leq$$
$$\leq |\kappa_i^{\text{OPT}}(x) - \kappa_i^{\text{LIN}}(x)| + |\kappa_i^0(x) - \kappa_i^{\text{OPT}}(x)| \leq$$
$$\leq |\kappa_i^{\text{OPT}}(x) - \kappa_i^{\text{LIN}}(x)| + \frac{1}{2}(\overline{\kappa}_i(x) - \underline{\kappa}_i(x)) = e_i^{\text{LIN}}(x) \geq \frac{1}{2}(\overline{\kappa}_i(x) - \underline{\kappa}_i(x))$$

$$e_i^{\text{LIN}}(x) \leq \sup_{x\in\mathcal{X}} e_i^{\text{LIN}}(x) = \zeta_i^{\text{LIN}} \geq \sup_{x\in\mathcal{X}} |\kappa_i^0(x) - \kappa_i^{\text{OPT}}(x)| = \zeta_i^{\text{OPT}}$$

III) Considering that $\lim_{\nu\to\infty} \frac{1}{2}(\overline{\kappa}_i(x) - \underline{\kappa}_i(x)) = 0, \forall x \in \mathcal{X}$ (i.e. $\lim_{\nu\to\infty} \kappa^{\text{OPT}}(x) = \kappa^0(x)$) and that, since κ_i^0 is Lipschitz continuous, $\lim_{\nu\to\infty} \kappa_i^{\text{LIN}}(x) = \kappa_i^0(x), \forall x \in \mathcal{X}$, it can be noted that:

$$\forall x \in \mathcal{X},\ \lim_{\nu\to\infty} e_i^{\text{LIN}}(x) = \lim_{\nu\to\infty} |\kappa_i^{\text{OPT}}(x) - \kappa_i^{\text{LIN}}(x)| + \lim_{\nu\to\infty} \frac{1}{2}(\overline{\kappa}_i(x) - \underline{\kappa}_i(x)) =$$
$$= |\kappa_i^0(x) - \kappa_i^0(x)| + 0 = 0$$

thus

$$\lim_{\nu\to\infty} \zeta_i^{\text{LIN}}(\nu) = \lim_{\nu\to\infty} \sup_{x\in\mathcal{X}} e_i^{\text{LIN}}(x,\nu) = 0$$

■

Define the following approximating function:

$$\kappa^{\text{LIN}}(x) = [\kappa_1^{\text{LIN}}(x), \ldots, \kappa_m^{\text{LIN}}(x)]^T \tag{12.9}$$

According to Theorem 8, function $\kappa^{\text{LIN}}(x)$ satisfies properties (9.1)–(9.3), with $\zeta^{\text{LIN}} = \sqrt{\sum_{i=1}^{m} (\zeta_i^{\text{LIN}})^2} \geq \zeta^{\text{OPT}}$ (11.13). Thus, given the same value of ν the guaranteed approximation error obtained with LIN technique is higher than that of the OPT approach. Note that in general the bound ζ^{LIN} may be higher than that of NP approach too, depending on how the off–line computed data are chosen. However, from a practical point of view, the LIN technique gives very good accuracy with low ν values. This is due to the fact that all the results presented in this dissertation refer to worst–case error bounds only.

12.3 SM Neighborhood approach

Let X^1,X^2,...,X^q be a collection of sets such that

$$\mathcal{X} \subseteq \bigcup_{j=1}^{q} X^j. \tag{12.10}$$

For any $x \in \mathcal{X}$, let $\hat{j} \in \arg\min_{j=1,\ldots,q} d_S(x,X^j)$, so that $X^{\hat{j}}$ contains x. Define the sets of indices

$$P^j \doteq \left\{k : \tilde{x}^k \in X^j \cup \{\tilde{x}^{\text{NP}}\}\right\},\ j = 1,\ldots,q \tag{12.11}$$

The SM neighborhood (NB) approximation of κ_i^0 is given by:

$$\kappa_i^{\text{NB}}(x) \doteq \frac{1}{2}[\overline{\kappa}_i^{\text{NB}}(x) + \underline{\kappa}_i^{\text{NB}}(x)] \tag{12.12}$$

with

$$\begin{aligned} \overline{\kappa}_i^{\text{NB}}(x) &\doteq \min\left[\overline{u}_i, \min_{k\in P^{\hat{j}}} \left(\tilde{u}_i^k + L_{\kappa^0,i}\|x - \tilde{x}^k\|_2\right)\right] \\ \underline{\kappa}_i^{\text{NB}}(x) &\doteq \max\left[\underline{u}_i, \max_{k\in P^{\hat{j}}} \left(\tilde{u}_i^k - L_{\kappa^0,i}\|x - \tilde{x}^k\|_2\right)\right] \end{aligned} \tag{12.13}$$

Note that the function κ_i^{NB} is defined similarly to κ_i^{OPT}, except that only a subset of points of $\mathcal{X}_\nu$ is used to compute the (suboptimal) bounds $\overline{\kappa}_i^{\text{NB}}(x)$ and $\underline{\kappa}_i^{\text{NB}}(x)$. In order to investigate the properties of κ_i^{NB}, let us define the indices

$$\begin{aligned}
\overline{k}_i &\doteq \arg\min_{k=1,\dots,\nu} (\tilde{u}_i^k + L_{\kappa^0,i}\|x - \tilde{x}^k\|_2) \\
\underline{k}_i &\doteq \arg\max_{k=1,\dots,\nu} (\tilde{u}_i^k - L_{\kappa^0,i}\|x - \tilde{x}^k\|_2) \\
\overline{j}_i &\doteq \arg\min_{k\in P^{\hat{j}}} \left(\tilde{u}^k + L_{\kappa^0,i}\|x - \tilde{x}^k\|_2\right) \\
\underline{j}_i &\doteq \arg\max_{k\in P^{\hat{j}}} \left(\tilde{u}_i^k - L_{\kappa^0,i}\|x - \tilde{x}^k\|_2\right)
\end{aligned}$$

Moreover, define the following scalar quantities:

$$\delta_i(x) = L_{\kappa^0,i}(\|\tilde{x}^{\overline{k}_i} - \tilde{x}^{\overline{j}_i}\|_2 + \|\tilde{x}^{\underline{k}_i} - \tilde{x}^{\underline{j}_i}\|_2) \tag{12.14}$$

$$\Delta_{\kappa^{\text{NB}},i}(x) \doteq \kappa_i^0(x) - \kappa_i^{\text{NB}}(x)$$

Theorem 9 *The following properties hold:*

I) $\kappa_i^{NB}(x) \in [\underline{u}_i, \overline{u}_i], \forall x \in \mathcal{X}$

II) *The pointwise approximation error* $\Delta_{\kappa^{NB},i}(x)$ *of* κ_i^{NB} *is bounded as*

$$\begin{aligned}
&\forall x \in \mathcal{X}, |\Delta_{\kappa^{NB},i}(x)| \le e_i^{NB}(x) \doteq \min(L_{\kappa^0,i} d_H(\mathcal{X},\mathcal{X}_\nu), \delta_i(x) + \frac{1}{2}(\overline{\kappa}_i(x) - \underline{\kappa}_i(x))) \\
&\forall x \in \mathcal{X}, e_i^{NB}(x) \le \zeta_i^{NB} = \sup_{x\in\mathcal{X}} e_i^{NB} \le L_{\kappa^0,i} d_H(\mathcal{X},\mathcal{X}_\nu) = \zeta_i^{NP}
\end{aligned}$$

where ζ_i^{NP} *is the guaranteed accuracy obtained by the NP approximation (12.3)*

III) *The following convergence property holds:*

$$\lim_{\nu\to\infty} \zeta_i^{NB}(\nu) = 0. \tag{12.15}$$

IV) *If* $\overline{k}_i = \overline{j}_i$ *and* $\underline{k}_i = \underline{j}_i$ *then*

$$\kappa_i^{NB}(x) = \kappa_i^{OPT}(x). \tag{12.16}$$

Proof.

I) From (12.12)–(12.13) it can be noted that, for any $x \in \mathcal{X}$:

$$\begin{aligned}
\kappa_i^{\text{NB}}(x) = \frac{1}{2}(\overline{\kappa}_i^{\text{NB}} + \underline{\kappa}_i^{\text{NB}}) \le \overline{\kappa}_i^{\text{NB}} \le \overline{u}_i \\
\kappa_i^{\text{NB}}(x) = \frac{1}{2}(\overline{\kappa}_i^{\text{NB}} + \underline{\kappa}_i^{\text{NB}}) \ge \underline{\kappa}_i^{\text{NB}} \ge \underline{u}_i \\
\Rightarrow \kappa_i^{\text{NB}}(x) \in [\underline{u}_i, \overline{u}_i]
\end{aligned}$$

II) For any $x \in \mathcal{X}$, note that (from (11.4) and (12.13)):

$$\begin{array}{l}\underline{\kappa}_i^{\text{NB}}(x) \leq \underline{\kappa}_i(x) \leq \kappa_i^0(x) \leq \overline{\kappa}_i(x) \leq \overline{\kappa}_i^{\text{NB}}(x) \\ \underline{\kappa}_i^{\text{NB}}(x) - \kappa_i^{\text{NB}}(x) \leq \kappa_i^0(x) - \kappa^{\text{NB}}(_i x) \leq \overline{\kappa}_i^{\text{NB}}(x) - \kappa_i^{\text{NB}}(x) \\ -\frac{1}{2}(\overline{\kappa}_i^{\text{NB}}(x) - \underline{\kappa}_i^{\text{NB}}(x)) \leq \kappa_i^0(x) - \kappa_i^{\text{NB}}(x) \leq \frac{1}{2}(\overline{\kappa}_i^{\text{NB}}(x) - \underline{\kappa}_i^{\text{NB}}(x))\end{array}$$

$$\Rightarrow |\kappa_i^0(x) - \kappa_i^{\text{NB}}(x)| \leq \frac{1}{2}(\overline{\kappa}_i^{\text{NB}}(x) - \underline{\kappa}_i^{\text{NB}}(x)) \tag{12.17}$$

Consider now the distance between the optimal upper bound $\overline{\kappa}_i(x)$ (11.4) and the suboptimal upper bound $\overline{\kappa}_i^{\text{NB}}(x)$ (12.13). Since by definition $\overline{\kappa}_i(x) \leq \overline{\kappa}_i^{\text{NB}}(x) \leq \overline{u}_i$, if $\overline{\kappa}_i(x) = \overline{u}_i$ then $\overline{\kappa}_i^{\text{NB}}(x) - \overline{\kappa}_i^{\text{OPT}}(x) = \overline{u}_i - \overline{u}_i = 0$. Otherwise note that:

$$\begin{array}{l}0 < \overline{\kappa}_i^{\text{NB}}(x) - \overline{\kappa}_i(x) \leq \tilde{u}_i^{\bar{j}_i} + L_{\kappa^0,i}\|x - \tilde{x}^{\bar{j}_i}\|_2 - \tilde{u}_i^{\bar{k}_i} - L_{\kappa^0,i}\|x - \tilde{x}^{\bar{k}_i}\|_2 \leq \\ \leq L_{\kappa^0,i}\|\tilde{x}^{\bar{j}_i} - \tilde{x}^{\bar{k}_i}\|_2 + L_{\kappa^0,i}\|x - \tilde{x}^{\bar{j}_i} - x + \tilde{x}^{\bar{k}_i}\|_2 = 2L_{\kappa^0,i}\|\tilde{x}^{\bar{j}_i} - \tilde{x}^{\bar{k}_i}\|_2\end{array}$$

Similarly,it can be obtained that:

$$\begin{array}{l}0 < \underline{\kappa}_i(x) - \underline{\kappa}_i^{\text{NB}}(x) \leq \tilde{u}_i^{\underline{k}_i} - L_{\kappa^0,i}\|x - \tilde{x}^{\underline{k}_i}\|_2 - \tilde{u}_i^{\underline{j}_i} + L_{\kappa^0,i}\|x - \tilde{x}^{\underline{j}_i}\|_2 \leq \\ \leq L_{\kappa^0,i}\|\tilde{x}^{\underline{j}_i} - \tilde{x}^{\underline{k}_i}\|_2 + L_{\kappa^0,i}\|x - \tilde{x}^{\underline{j}_i} - x + \tilde{x}^{\underline{k}_i}\|_2 = 2L_{\kappa^0,i}\|\tilde{x}^{\underline{j}_i} - \tilde{x}^{\underline{k}_i}\|_2\end{array}$$

thus, the distance between the OPT and NB approximations is bounded:

$$\begin{array}{l}|\kappa_i^{\text{OPT}}(x) - \kappa_i^{\text{NB}}(x)| = \\ = \frac{1}{2}|\overline{\kappa}_i(x) + \underline{\kappa}_i(x) - \overline{\kappa}_i^{\text{NB}}(x) - \underline{\kappa}_i^{\text{NB}}(x)| \leq \\ \leq \frac{1}{2}(|\overline{\kappa}_i(x) - \overline{\kappa}_i^{\text{NB}}(x)| + |\underline{\kappa}_i(x) - \underline{\kappa}_i^{\text{NB}}(x)|) \leq \\ \leq L_{\kappa^0,i}(\|\tilde{x}^{\bar{j}_i} - \tilde{x}^{\bar{k}_i}\|_2 + \|\tilde{x}^{\underline{j}_i} - \tilde{x}^{\underline{k}_i}\|_2) = \delta_i(x)\end{array} \tag{12.18}$$

Consequently, note that:

$$\begin{array}{l}|\Delta_{\kappa^{\text{NB}},i}(x)| = |\kappa_i^0(x) - \kappa_i^{\text{NB}}(x)| \leq \\ \leq |\kappa_i^0(x) - \kappa_i^{\text{OPT}}(x) + (\kappa_i^{\text{OPT}}(x) - \kappa_i^{\text{NB}}(x))| \leq \\ \leq \delta_i(x) + \frac{1}{2}(\overline{\kappa}_i(x) - \underline{\kappa}_i(x)),\ \forall x \in \mathcal{X}\end{array} \tag{12.19}$$

At the same time, since by construction (12.11) for any $x \in \mathcal{X}$ the set of points $\{\tilde{x}^j : j \in \hat{P^j}\}$ contains the nearest neighbor $\tilde{x}^{\text{NP}}$ of x, it can be noted that (from (12.13)):

$$\begin{array}{l}\overline{\kappa}_i^{\text{NB}} \leq \tilde{u}_i^{\text{NP}} + L_{\kappa^0,i}\|x - \tilde{x}^{\text{NP}}\|_2 \\ \underline{\kappa}_i^{\text{NB}} \geq \tilde{u}_i^{\text{NP}} - L_{\kappa^0,i}\|x - \tilde{x}^{\text{NP}}\|_2\end{array}$$

Thus, from (12.17):

$$\begin{array}{l}|\Delta_{\kappa^{\text{NB}},i}(x)| = |\kappa_i^0(x) - \kappa_i^{\text{NB}}(x)| \leq \\ \frac{1}{2}(\overline{\kappa}_i^{\text{NB}}(x) - \underline{\kappa}_i^{\text{NB}}(x)) \leq \\ \leq \frac{1}{2}(\tilde{u}_i^{\text{NP}} + L_{\kappa^0,i}\|x - \tilde{x}^{\text{NP}}\|_2 - \tilde{u}_i^{\text{NP}} + L_{\kappa^0,i}\|x - \tilde{x}^{\text{NP}}\|_2) = \\ = L_{\kappa^0,i}\|x - \tilde{x}^{\text{NP}}\|_2\end{array} \tag{12.20}$$

By considering the tightest bound between (12.19) and (12.20) and taking into account the formulation of the error bound of NP approximation (12.3), it can be obtained that:

$$
\begin{array}{l}
|\Delta_{\kappa^{\text{NB}},i}(x)| \leq \min(L_{\kappa^0,i}\|x-\tilde{x}^{\text{NP}}\|_2, \dfrac{1}{2}(\overline{\kappa}_i(x)-\underline{\kappa}_i(x))+\delta(x)) = e_i^{\text{NB}}(x) \leq \\
\leq L_{\kappa^0,i}\|x-\tilde{x}^{\text{NP}}\|_2,\ \forall x \in \mathcal{X} \\
\zeta_i^{\text{NB}} = \sup\limits_{x\in\mathcal{X}} e_i^{\text{NB}} \leq L_{\kappa^0,i} d_H(\mathcal{X},\mathcal{X}_\nu) = \zeta_i^{\text{NP}}
\end{array}
$$

III) Trivially follows from (12.20) and the property (12.4) of the NP approximation

IV) Trivially follows from (12.18) by using $\overline{k}_i = \overline{j}_i$ and $\underline{k}_i = \underline{j}_i$

■

Define the following approximating function:

$$\kappa^{\text{NB}}(x) = [\kappa_1^{\text{NB}}(x),\ldots,\kappa_m^{\text{NB}}(x)]^T \tag{12.21}$$

According to Theorem 9, function $\kappa^{\text{NB}}(x)$ satisfies properties (9.1)–(9.3), with $\zeta^{\text{NB}} = \sqrt{\sum\limits_{i=1}^{m}(\zeta_i^{\text{NB}})^2}$. Moreover, the following inequalities hold:

$$\zeta^{\text{OPT}} \leq \zeta^{\text{NB}} \leq \zeta^{\text{NP}}$$

Thus, the guaranteed accuracy obtained with NB technique, which clearly depends on the performed partition (12.10), is between those of NP and OPT approaches.

Remark 18 *For given number of data ν, under suitable choices of the sets X^1,X^2,...,X^q and using efficient search algorithms, the NB approximation leads to a significantly better on–line computational efficiency than the OPT approximation, at the expense of higher memory usage and some degradation of the worst case approximation error. However note that, as already pointed out for the linear interpolation, in practical applications such a degradation does not necessarily imply that the performance of the suboptimal techniques are worse than those of the optimal one. These aspects will be highlighted in the numerical examples of Section 13.1.*

Chapter 13

Examples

This Chapter presents a series of numerical examples to practically show the effectiveness and the characteristics of the presented approximation approaches. Moreover, in Section 13.2 the application of NP technique to a vehicle yaw control problem is described. Indeed, the presented examples aim to illustrate the applicability of the NMPC approximations and to compare the computational efficiency of the various methods in relative terms only.

13.1 Numerical examples

13.1.1 Example 1: double integrator

Consider the double integrator system:

$$x_{t+1} = \begin{bmatrix} 1 & 1 \\ 0 & 1 \end{bmatrix} x_t + \begin{bmatrix} 0.5 \\ 1 \end{bmatrix} u_t$$

A predictive controller is designed using a quadratic cost function J:

$$J(U,x_{t|t}) = x_{t+N|t}^T P x_{t+N|t} + \sum_{k=0}^{N-1} \{x_{t+k|t}^T Q x_{t+k|t} + u_{t+k|t}^T R u_{t+k|t}\} \tag{13.1}$$

where $P \succ 0$, $Q = Q^T \succ 0$ and $R = R^T \succ 0$ are positive definite matrices. The following choice has been made in the considered example:

$$Q = \begin{bmatrix} 4 & 0 \\ 0 & 1 \end{bmatrix},\ R = 1,\ P = \begin{bmatrix} 0 & 0 \\ 0 & 0 \end{bmatrix},\ N = 5$$

Input and output constraints are defined by:

$$\mathbb{X} = \{x \in \mathbb{R}^2 : \|x\|_\infty \leq 1\},\ \mathbb{U} = \{u \in \mathbb{R} : |u| \leq 1\}$$

The MATLAB® Multi–Parametric Toolbox [90] has been used to compute the explicit MPC solution [72]. The obtained feasibility set $\mathcal{F}$ is reported in Fig. 13.1. The number of regions (after the merging of regions with the same control law) over which the nominal control law κ^0 is affine is equal to 5. The computed values of the Lipschitz constants

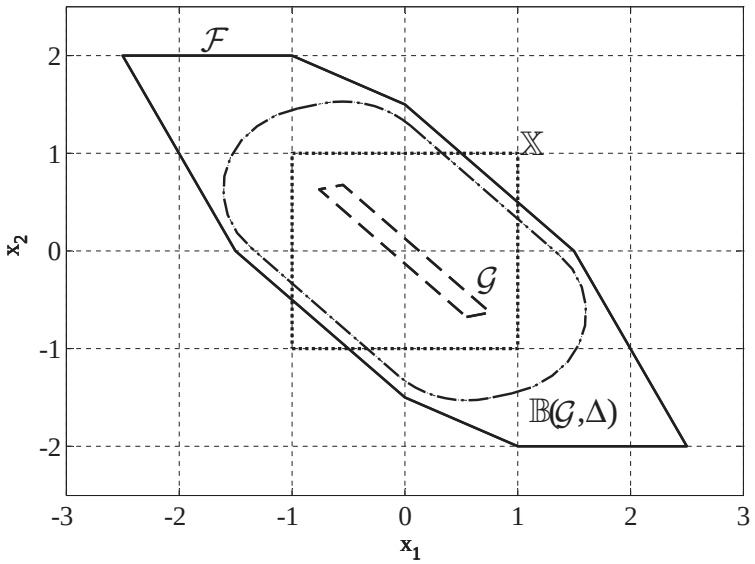

Figure 13.1. Example 1: sets $\mathcal{F} = \mathcal{X}$ (solid line), $\mathcal{G}$ (dashed line), $\mathbb{B}(\mathcal{G},\Delta)$ (dash–dotted line) and $\mathbb{X}$ (dotted line). Sets $\mathcal{G}$ and $\mathbb{B}(\mathcal{G},\Delta)$ obtained using OPT approximation with $\nu \simeq 1.6\ 10^6$.

(9.6) and (9.12) are $L_{\kappa^0} = 1.4$ and $L_F = 3.19$ respectively. The set $\mathcal{X} = \mathcal{F}$ has been considered for the approximation of κ^0 and Lyapunov function (9.18) has been computed with $\widehat{T} = 7$: the resulting values of b and K in (9.19) and (9.20) are $b = 3.15$, $K = 0.99$, while $\hat{L}_V$ of (9.24) is $\hat{L}_V = 8.1$.
Assume that the required regulation precision is $\|x_t\|_2 \leq \overline{q} = 5\,10^{-2}$ for $t \to \infty$. According to (9.31), the corresponding sufficient value of μ is equal to $\overline{\mu} = (\overline{q}\,K)/(b\,L_V) = 1.9\,10^{-3}$. By performing OPT approximation κ^{OPT} of κ^0 with $\nu \simeq 1.6\ 10^6$, a value of $\mu = 1.4\,10^{-3} < \overline{\mu}$ is obtained, which leads to $q = 3.7\ 10^{-2} < \overline{q}$. The corresponding upper bound Δ (9.25) on distance trajectories can be computed using (9.26), via the computation of the bounds $\Delta_1(t)$ (9.27) and $\Delta_2(t)$ (9.28): the obtained value is $\Delta = 0.849$. A graphical interpretation of the computation of Δ_1, Δ_2 and Δ is reported in Fig. 13.2. The obtained set $\mathcal{G}$ and the corresponding set $\mathbb{B}(\mathcal{G},\Delta) \subseteq \mathcal{F}$ (9.30) are reported in Fig. 13.1. Fig. 13.3 shows the distance between the state trajectories, obtained with the nominal and the approximated controllers, during a simulation performed considering the initial state $x_0 = [0.54,\ -0.67]^T$: it can be noted that such a distance is practically zero. As a matter of fact, the obtained properties of the system regulated using the approximated controller are quite good despite the computed theoretical values of Δ and q. This fact

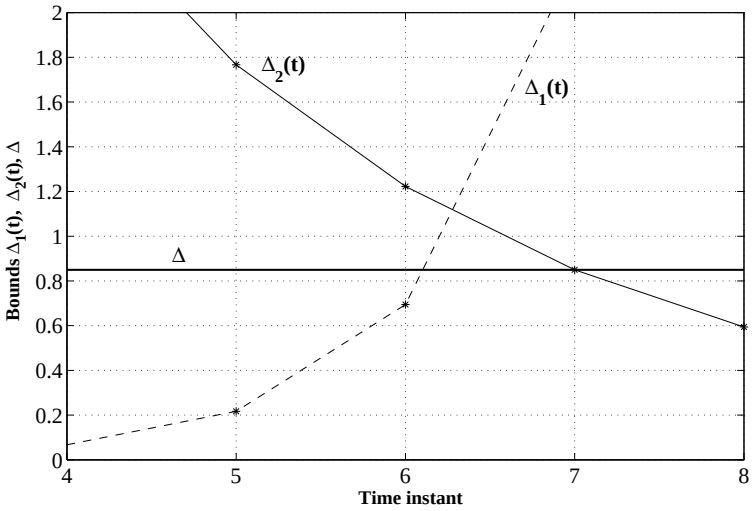

Figure 13.2. Example 1: bounds $\Delta_1(t)$ (dashed line), $\Delta_2(t)$ (thin solid line) and Δ (solid line) obtained with OPT approximation and $\nu \simeq 1.6\ 10^6$.

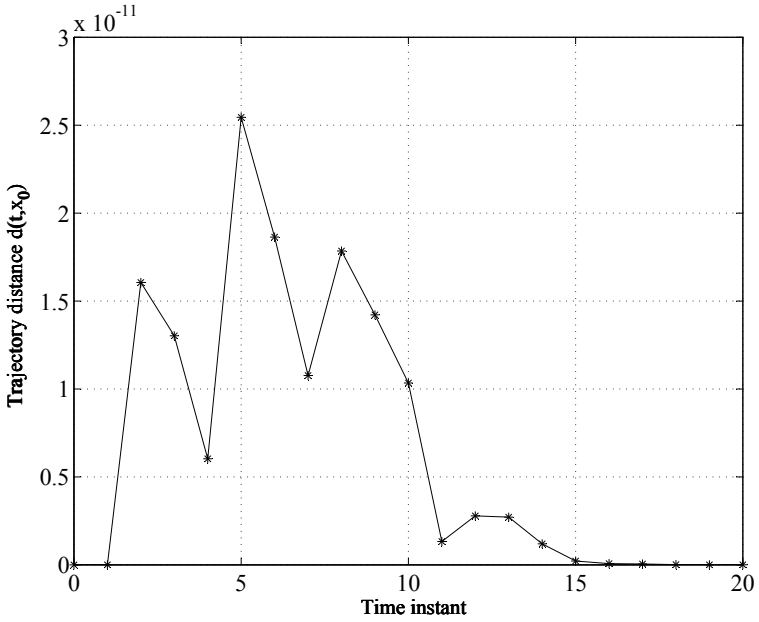

Figure 13.3. Example 1: distance $d(t,x_0)$ between the state trajectories obtained with the nominal and the approximated controllers, with initial state $x_0 = [0.54, -0.67]^T$. Approximation carried out with OPT approach and $\nu \simeq 1.6\ 10^6$.

highlights that the stability and performance conditions claimed in Theorem 2 may prove to be conservative, being only sufficient. Indeed, with a much lower number ν of off–line solutions, stability and performance are kept for any $x_0 \in \mathcal{X}$. A typical example is

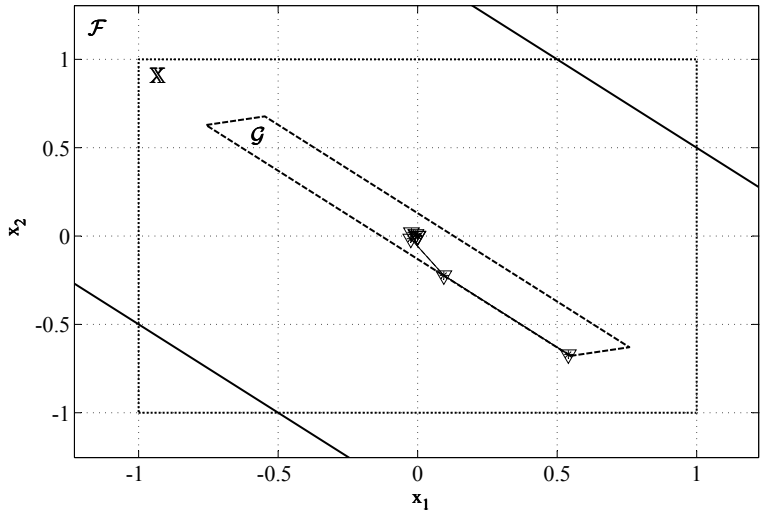

Figure 13.4. Example 1: state trajectories obtained with the nominal (dashed line with triangles) and the approximated (solid line with asterisks) controllers, initial state $x_0 = [0.54, -0.67]^T$. Approximation carried out with OPT approach and $\nu \simeq 1.6\ 10^6$.

reported in Fig. 13.5, which shows the state trajectories in the case $\nu \simeq 10^3$ with initial state $x_0 = [0, -1.45]^T \notin \mathcal{G}$ near the boundary of $\mathcal{X} = \mathcal{F}$. Clearly, a lower number

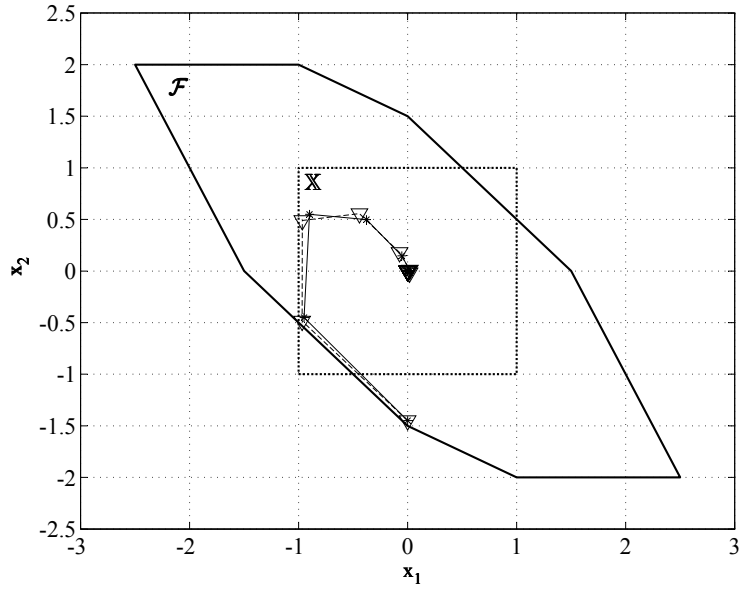

Figure 13.5. Example 1: state trajectories obtained with the nominal (dashed line with triangles) and the approximated (solid line with asterisks) controllers, initial state $x_0 = [0, -1.45]^T$. Approximation carried out with OPT approach and $\nu \simeq 10^3$.

of off–line solutions leads to lower computational efforts and memory usage: to evaluate

the on–line computational times as well as performance degradation obtained with the approximated control law, a number N^{SIM} of simulations have been performed, considering any initial condition x_0^{SIM} computed via uniform gridding over $\mathcal{X}$ with a resolution equal to 0.01 for both state variables. Each simulation lasted 500 time steps. Then, the mean computational time $\overline{t}$ over all the initial conditions and all the time steps of each simulation has been computed, together with the maximum trajectory distance obtained over all the simulations:

$$\Delta^{\text{SIM}} = \max_{x_0^{\text{SIM}}} \left(\max_{t \in [1,500]} \left(\| \phi^{\text{SM}}(t, x_0^{\text{SIM}}) - \phi^0(t, x_0^{\text{SIM}}) \|_2 \right) \right)$$

The following estimate of regulation precision has been also considered:

$$q^{\text{SIM}} = \max_{x_0^{\text{SIM}}} \left(\max_{t \in [301,500]} \left(\| \phi^{\text{SM}}(t, x_0^{\text{SIM}}) \|_2 \right) \right)$$

Finally, also the mean value $\overline{\Delta}_u$ and the maximum value Δ_u^{MAX} of the approximation error $\|\kappa^0(x) - \hat{\kappa}(x)\|_2$ over all time instants of all simulations have been considered. These values have been computed employing different values of ν: the obtained results in the case of OPT approximation are reported in Table 13.1, together with the theoretical values $\Delta(\nu)$, $q(\nu)$ and $\zeta(\nu)$ obtained using the results of Theorems 2 and 5. As it was expected, the obtained estimates of the maximum trajectory distance Δ^{SIM}, regulation precision q^{SIM} and mean and maximum approximation errors $\overline{\Delta}_u$ and Δ_u^{MAX} are bounded by their respective theoretical values, Δ, q and ζ. However, these bounds are not strict, being obtained on the basis of sufficient conditions only. Moreover, note that with any considered value of ν the state trajectory has been always kept inside the set $\mathcal{X}$ for any considered initial condition and inside the constraint set $\mathbb{X}$ for any $t \geq 1$. Finally, variable u always satisfied the input constraints, as it was expected. The obtained computational times depend on the

Table 13.1. Example 1: properties of approximated MPC using OPT approximation.

	$\nu \simeq 1.6\ 10^6$	$\nu \simeq 10^5$	$\nu \simeq 5\ 10^3$	$\nu \simeq 10^3$
$\overline{t}$	$5.4\,10^{-1}$ s	$2.2\,10^{-2}$ s	$7.8\,10^{-4}$ s	$3.8\,10^{-4}$ s
Δ^{SIM}	$1.6\ 10^{-9}$	$1\,10^{-2}$	$3\,10^{-2}$	$9\,10^{-2}$
Δ	$8.5\ 10^{-1}$	1.35	2.5	3.2
q^{SIM}	$1.7\ 10^{-16}$	$4\,10^{-9}$	$4\,10^{-6}$	$1.5\,10^{-4}$
q	$3.7\,10^{-2}$	$1.6\,10^{-1}$	$7.8\,10^{-1}$	1.5
$\overline{\Delta}_u$	$2.4\ 10^{-12}$	$5.9\,10^{-11}$	$4.3\,10^{-7}$	$2.5\,10^{-3}$
Δ_u^{MAX}	$4.5\ 10^{-11}$	$7.4\,10^{-10}$	$8.8\,10^{-6}$	$1\,10^{-2}$
ζ	$1.3\,10^{-3}$	$5.5\,10^{-3}$	$2.7\,10^{-2}$	$5.2\,10^{-2}$

employed calculator and on the algorithm implementation: in this case MATLAB® 7 and

an AMD Athlon(tm) 64 3200+ with 1 GB RAM have been used and no particular effort was made to optimize the numerical computation of $\kappa^{\text{OPT}}(x)$. On the same platform, the mean computational time obtained with on–line optimization (using the MATLAB® `quadprog` function) is about $2.5\,10^{-2}$ s, while the mean computational time obtained with the toolbox developed by [90] for the calculation of the explicit solution is about $2.2\,10^{-3}$ s. As regards input and state constraints satisfaction, in Fig. 13.6 it can be noted

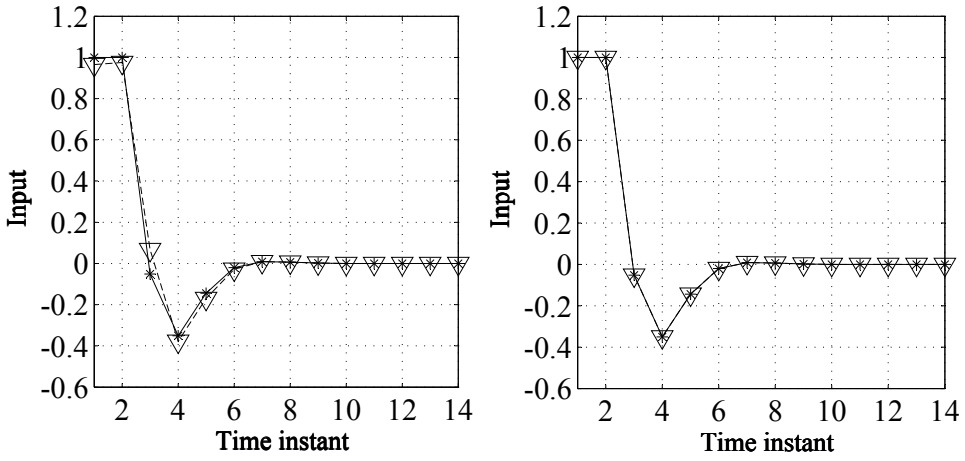

Figure 13.6. Example 1: nominal input variable $u_t = \kappa^0(x_t)$ (dashed line with triangles) and approximated input variable $u_t^{\text{OPT}} = \kappa^{\text{OPT}}(x_t^{\text{OPT}})$ (solid line with asterisks). Approximation carried out with OPT approach and $\nu \simeq 10^3$ (left) and $\nu \simeq 5\ 10^3$ (right). Initial state $x_0 = [0,\ -1.45]^T$

that the input variable is kept inside the set $\mathbb{U}$ for any $t \geq 0$, as it was expected, while Fig. 13.5 shows that the state trajectory is kept inside the constraint set $\mathbb{X}$ for any $t \geq 1$.
In this example, NP approximation has been tested too, using the same off–line computed values of $\kappa^0(\tilde{x}^k)$ employed for the OPT approximation. Table 13.2 contains the estimates of mean computational time, maximum trajectory distance, regulation precision and approximation errors obtained with NP approximation and different values of ν, together with the theoretical values $\Delta(\nu)$, $q(\nu)$ and $\zeta(\nu)$. Finally, Fig. 13.7 shows the growth, as a function of ν, of the mean computational times needed to evaluate OPT and NP approximations. Note that the evaluation times of OPT approximation grow linearly with ν, while those obtained with NP approximation are practically constant: this can be obtained with a suitable storage criterion for the off–line computed data, which leads to computational times that depend on the number of state variables but not on the value of ν. In all the performed simulations, uniform gridding over $\mathcal{X}$ has been used to obtain the set $\mathcal{X}_\nu$ and to compute the corresponding exact control moves $\tilde{u}^k$,$k = 1, \ldots, \nu$. In order to improve the regulation precision of both OPT and NP approximated control laws, it is also possible to employ a more dense gridding of exact MPC solutions near the origin.

Table 13.2. Example 1: properties of approximated MPC using NP approximation.

	$\nu \simeq 1.6\ 10^6$	$\nu \simeq 10^5$	$\nu \simeq 5\ 10^3$	$\nu \simeq 10^3$
$\bar{t}$	$3.5\,10^{-5}$ s	$4\,10^{-5}$ s	$4.5\,10^{-5}$ s	$2.6\,10^{-5}$ s
Δ^{SIM}	$3.4\,10^{-3}$	$1.5\,10^{-2}$	$6.5\,10^{-2}$	$1.3\,10^{-1}$
Δ	1.3	2	3.9	5.4
q^{SIM}	$3.2\,10^{-3}$	$1.3\,10^{-2}$	$4.7\,10^{-2}$	$1.3\,10^{-1}$
q	$7.1\,10^{-2}$	$2.8\,10^{-1}$	1.4	2.9
$\overline{\Delta_u}$	$4.7\ 10^{-4}$	$1.7\,10^{-3}$	$2\,10^{-2}$	$5\,10^{-2}$
Δ_u^{MAX}	$1.3\ 10^{-3}$	$3\,10^{-3}$	$3\,10^{-2}$	$7\,10^{-2}$
ζ	$2.6\,10^{-3}$	$5\,10^{-3}$	$5\,10^{-2}$	$1\,10^{-1}$

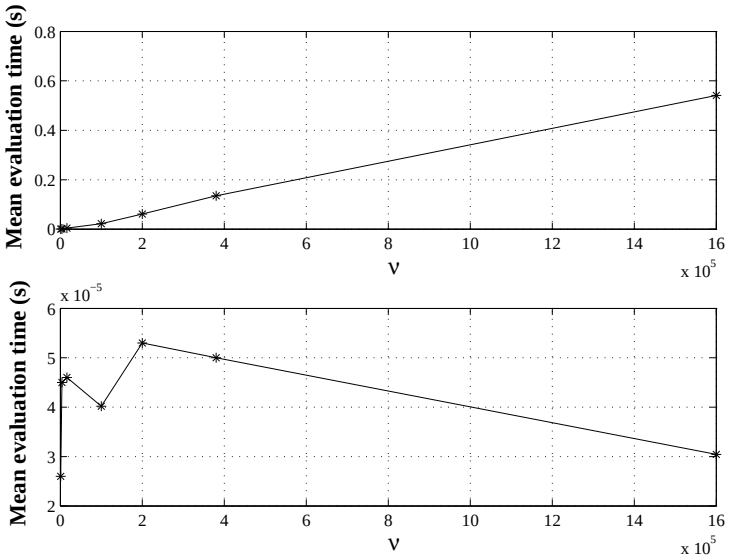

Figure 13.7. Example 1: mean computational time as function of ν for OPT (upper) and NP approximation methodologies.

13.1.2 Example 2: two inputs, two outputs linear system with state contraction constraint

In this example, the following two inputs system, originally introduced in [91], is considered:

$$x_{t+1} = \begin{bmatrix} 0.98 & 0 \\ 0 & 0.98 \end{bmatrix} x_t + \begin{bmatrix} 0.8 & -1 \\ -0.6 & 0.8 \end{bmatrix} u_t$$

State and input constraints are also taken into account:

$$\mathbb{X} = \{x \in \mathbb{R}^2 : \|x\|_\infty \leq 2\},\ \mathbb{U} = \{u \in \mathbb{R}^2 : \|u\|_\infty \leq 1\}$$

The nominal MPC control law has been designed using a quadratic cost function (13.1) with the following parameters

$$Q = \begin{bmatrix} 0.1 & 0 \\ 0 & 0.1 \end{bmatrix}, R = \begin{bmatrix} 1 & 0 \\ 0 & 1 \end{bmatrix}, P = \begin{bmatrix} 0 & 0 \\ 0 & 0 \end{bmatrix}, N = 5$$

Moreover, a state contraction constraint has been added:

$$\|x_{t+1|t}\|_2 \leq \sigma \|x_{t|t}\|_2$$

with $\sigma = 0.96$. The MOSEK© optimization toolbox for MATLAB® [92] has been employed to evaluate the Feasibility set $\mathcal{F}$ and to compute off–line the needed values of $\kappa^0(x)$. The set $\mathcal{X} = \mathcal{F}$ considered for the approximation of κ^0 is reported in Fig. 13.8, together with the level curves of the optimal cost function $J(U^*(x))$. Note that the optimal cost function is not convex, due to the presence of the contraction constraint. Therefore, in this case stability and constraint satisfaction properties cannot be guaranteed with the procedure proposed by [93]. Moreover, $\kappa^0(x)$ results to be continuous

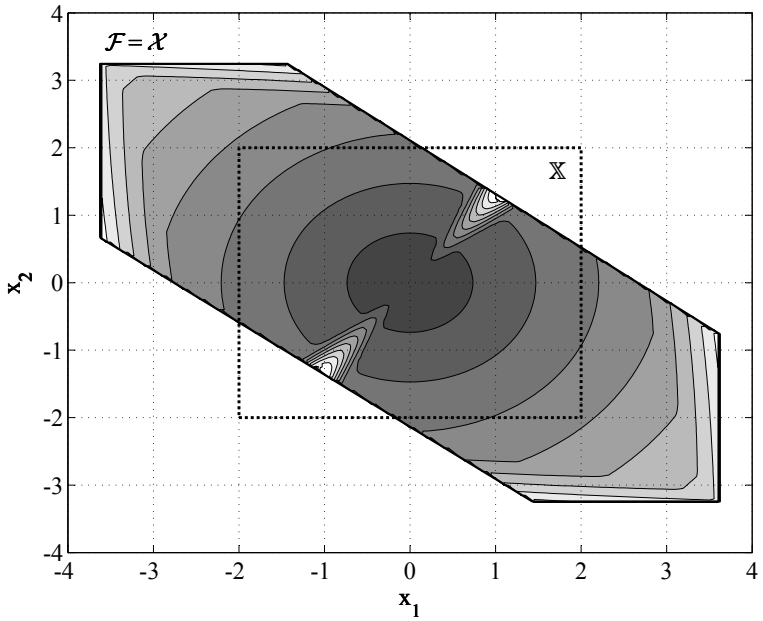

Figure 13.8. Example 2: set $\mathcal{F} = \mathcal{X}$ (solid), constraint set $\mathbb{X}$ (dotted) and level curves of the optimal cost function $J(U^*(x))$.

but it is not piecewise affine. In fact, no explicit solution can be easily obtained in this case. The Lipschitz constants $L_{\kappa^0,1}$ and $L_{\kappa^0,2}$ have been estimated according to (9.6) as $L_{\kappa^0,1} = 5.33, L_{\kappa^0,2} = 4.48$. The resulting value of L_F in (9.11) is $L_F = 12.29$. The Lyapunov function parameters are $b = 1$, $L_V = 1$, $K = 0.04$ (see Remark 7 in Section

9.2). NP approximation has been carried out employing $\nu \simeq 4.3\,10^5$ exact MPC solutions, obtaining $\Delta = 15.04$ and $q = 1.99$. A comparison of the state courses is shown in Fig. 13.9, starting from the initial state $x_0 = [-3, 0.4]^T$, while the trajectory distance is reported in 13.10. The nominal and approximated input values are shown in Fig. 13.11.

The approximated control law has the same properties of the nominal one, i.e. state

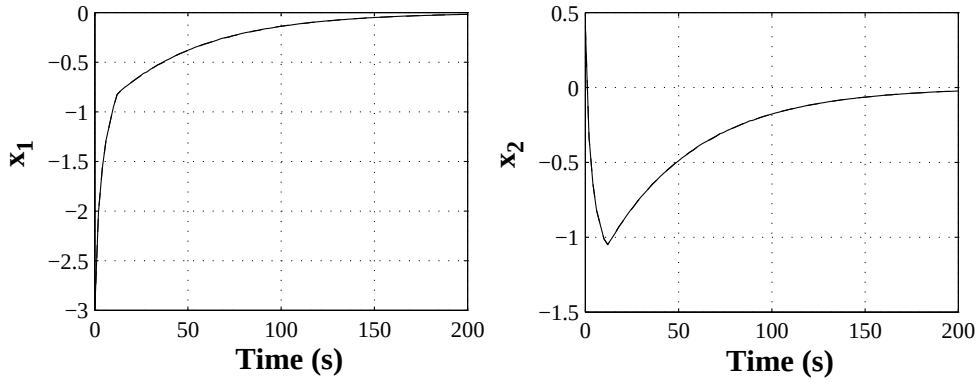

Figure 13.9. Example 2: nominal state course (dashed line) and the one obtained with the approximated control law (solid line). Initial state: $x_0 = [-3, 0.4]^T$. Approximation carried out with NP approach and $\nu \simeq 4.3\,10^5$.

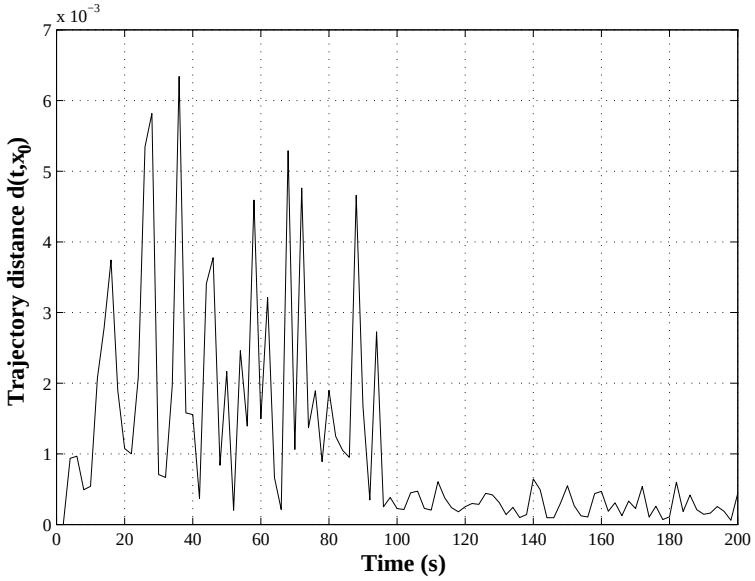

Figure 13.10. Example 2: distance $d(t,x_0)$ between the state trajectories obtained with the nominal and the approximated controllers. Initial state: $x_0 = [-3, 0.4]^T$. Approximation carried out with NP approach and $\nu \simeq 4.3\,10^5$.

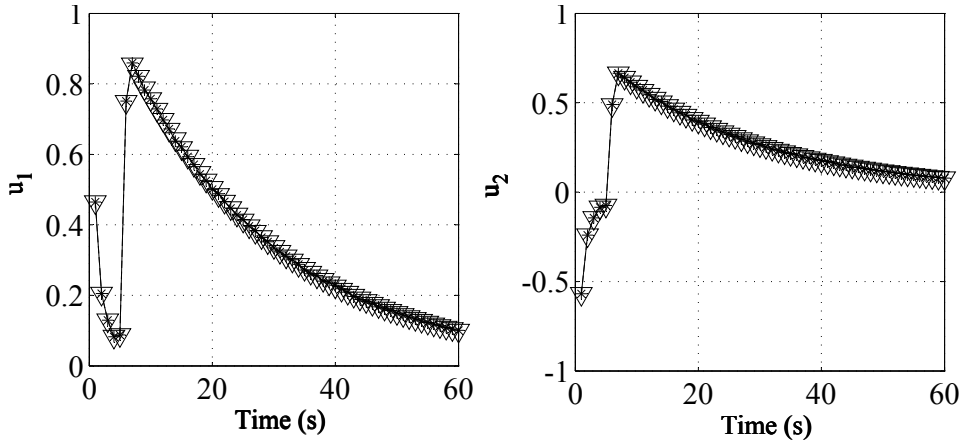

Figure 13.11. Example 2: input courses obtained with the nominal (dashed line with triangles) and the approximated (solid line with asterisks) controllers. Initial state: $x_0 = [-3 \;\; 0.4]^T$. Approximation carried out with NP approach and $\nu \simeq 4.3\,10^5$.

and input constraints are satisfied and the obtained maximum trajectory distance is lower than $7\,10^{-3}$, while the regulation precision is lower than $1\,10^{-3}$. Fig. 13.12 shows the behaviour of the contraction ratio $\|x_{t+1}\|_2/\|x_t\|_2$: note that the two curves match, thus also the contraction constraint is satisfied with the NP approximated control law. As

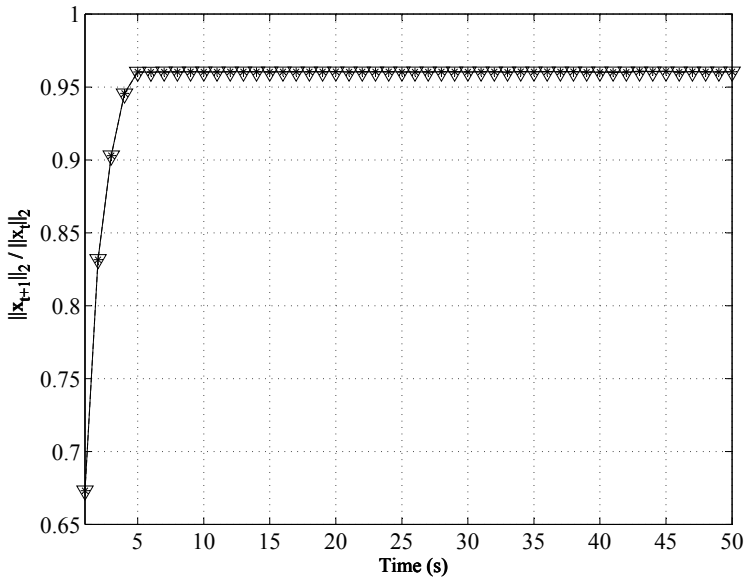

Figure 13.12. Example 2: contraction ratio $\|x_{t+1}\|_2/\|x_t\|_2$ of the nominal state trajectory (dashed line with triangles) and of the one obtained with the approximated control law (solid line with asterisks). Initial state: $x_0 = [-3, 0.4]^T$. Approximation carried out with NP approach and $\nu \simeq 4.3\,10^5$.

regards the evaluation times, the mean computational time obtained with MOSEK© is equal to 0.016 s, while the NP approximation mean computational time is about $3\ 10^{-5}$ s, thus showing the good computational speed improvement obtained with the approximated controller.

13.1.3 Example 3: nonlinear oscillator

Consider the two–dimensional nonlinear oscillator obtained from the Duffing equation (see e.g. [94]):

$$\begin{cases} \dot{x}_1(t) = x_2(t) \\ \dot{x}_2(t) = u(t) - 0.6\, x_2(t) - x_1(t)^3 - x_1(t) \end{cases}$$

where the input constraint set $\mathbb{U}$ is:

$$\mathbb{U} = \{u \in \mathbb{R} : |u| \leq 5\}$$

The following discrete time model to be used in the nominal MPC design has been obtained by forward difference approximation:

$$x_{t+1} = \begin{bmatrix} 1 & T_s \\ -T_s & (1 - 0.6\, T_s) \end{bmatrix} x_t + \begin{bmatrix} 0 \\ T_s \end{bmatrix} u_t + \begin{bmatrix} 0 & 0 \\ -T_s & 0 \end{bmatrix} x_t^3$$

with sampling time $T_s = 0.05$ s. The nominal MPC controller κ^0 is designed according to (8.2) with horizons $N_p = 100$, $N_c = 5$ and the following functions L and Φ:

$$L(x,u) = x^T Q x + u^T R u, \quad \Phi = 0$$

where

$$Q = \begin{bmatrix} 1 & 0 \\ 0 & 1 \end{bmatrix},\ R = 0.5$$

The following linear state inequality constraints define the considered set $\mathbb{X}$:

$$\mathbb{X} = \{x \in \mathbb{R}^2 : \|x\|_\infty \leq 3\}$$

The state prediction has been performed setting $u_{t+j|t} = u_{t+N_c-1|t}$, $j = N_c,...,N_p - 1$. The optimization problem (8.2) employed to compute $\kappa^0(x)$ has been solved using a sequential constrained Gauss–Newton quadratic programming algorithm (see e.g. [95]), where the underlying quadratic programs have been solved using the MatLab® function `quadprog`. The maximum and mean computational times of the on–line optimization were $6\,10^{-1}$ s and $4.3\,10^{-2}$ s respectively, using MATLAB® 7 with an AMD Athlon(tm) 64 3200+ with 1 GB RAM.
Fig. 13.16 shows the obtained feasibility set $\mathcal{F}$ and the set $\mathcal{X}$ considered for the approximation, together with the constraint set $\mathbb{X}$. The level curves of the optimal cost

function$J^*(x) = \min_U J(U,x)$ are reported too: it can be noted that $J^*(x)$ is not convex, thus the technique proposed in [83] cannot be applied without ad–hoc modifications to guarantee closed loop stability and constraint satisfaction properties. On the other hand, the set techniques proposed in this thesis can be systematically employed since κ^0 results to be continuous. A set $\mathcal{X}_\nu$ of $\nu = 1\,10^4$ off–line computed exact control moves has

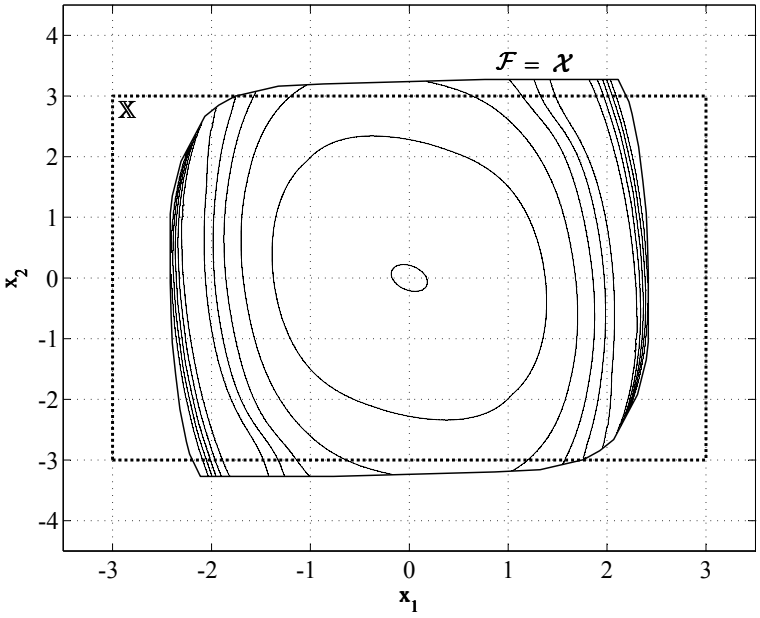

Figure 13.13. Example 3: sets $\mathcal{F}$ and $\mathcal{X}$ (thick solid line), constraint set $\mathbb{X}$ (thick dotted line) and level curves of the optimal cost function $J^*(x)$.

been considered to derive the approximating functions. The values of $\tilde{x} \in \mathcal{X}_\nu$ have been chosen with uniform gridding over $\mathcal{X}$. The following approximating functions have been considered:

I) Neural network approximation, obtained considering the set $\mathcal{X}_\nu$ in the design phase:

$$\hat{\kappa}_{\text{NS}}^{\text{NN}} = \sum_{i=1}^{7} \alpha_i \tanh(\beta_i^1 x_1 + \beta_i^2 x_2 + \gamma_i) + \alpha_0$$

where $\alpha \in \mathbb{R}^8$, $\beta^1 \in \mathbb{R}^7$, $\beta^2 \in \mathbb{R}^7$ and $\gamma \in \mathbb{R}^7$ are suitable weights. To satisfy condition (9.1), function $\hat{\kappa}_{\text{NS}}^{\text{NN}}$ has been then modified as:

$$\hat{\kappa}^{\text{NN}}(x) = \begin{cases} \hat{\kappa}_{\text{NS}}^{\text{NN}}(x) \text{ if } -5 \leq \hat{\kappa}_{\text{NS}}^{\text{NN}}(x) \leq 5 \\ -5 \text{ if } \hat{\kappa}_{\text{NS}}^{\text{NN}}(x) < -5 \\ 5 \text{ if } \hat{\kappa}_{\text{NS}}^{\text{NN}}(x) > 5 \end{cases}$$

II) Function $\tilde{\kappa}^{\text{LOC,NN}}$ obtained by adding to $\hat{\kappa}^{\text{NN}}$ the optimal SM approximation of the residue function $\kappa^0 - \hat{\kappa}^{\text{NN}}$, evaluated off–line at the points $\tilde{x} \in \mathcal{X}_\nu$

III) Global optimal SM approximation κ^{OPT} of κ^0, using the exact control moves computed off–line at the points $\tilde{x} \in \mathcal{X}_\nu$

IV) Nearest point approximation κ^{NP} of κ^0, using the exact control moves computed off–line at the points $\tilde{x} \in \mathcal{X}_\nu$

Fig. 13.14 shows the state trajectories obtained considering the initial condition $x_0 = [1, -3.1]^T$, outside the state constraints. It can be noted that all the approximated controllers are able to regulate the state to the origin and the related trajectories are practically superimposed. Moreover all the approximated controllers satisfy the state constraints. The courses of the input variable u (Fig. 13.15) show that input constraints are always

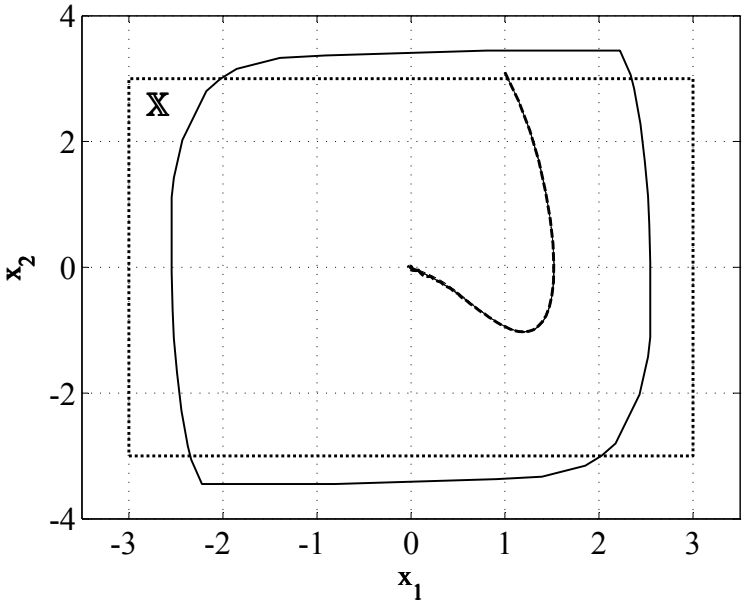

Figure 13.14. Example 3: state trajectories obtained with the nominal NMPC controller (solid), $\hat{\kappa}^{\text{NN}}$ (dashed), $\tilde{\kappa}^{\text{LOC,NN}}$ (dash–dotted), κ^{OPT} (dotted) and κ^{NP} (dashed, thick line). Initial condition: $x_0 = [1, -3.1]^T$

satisfied. To evaluate the performance and computational times of the considered control laws, 300 simulations have been performed starting from different initial conditions chosen with uniform gridding over $\mathcal{X}$. Each simulation lasted 600 time steps. The mean computational time $\bar{t}$, over all time steps of all simulations, obtained with OPT, LOC an NP controllers is reported in Table 13.4. As a measure of control system performance, the Euclidean distance d between the closed loop state trajectories obtained with the nominal controller and any of the approximated ones has been considered at each time step. Then,

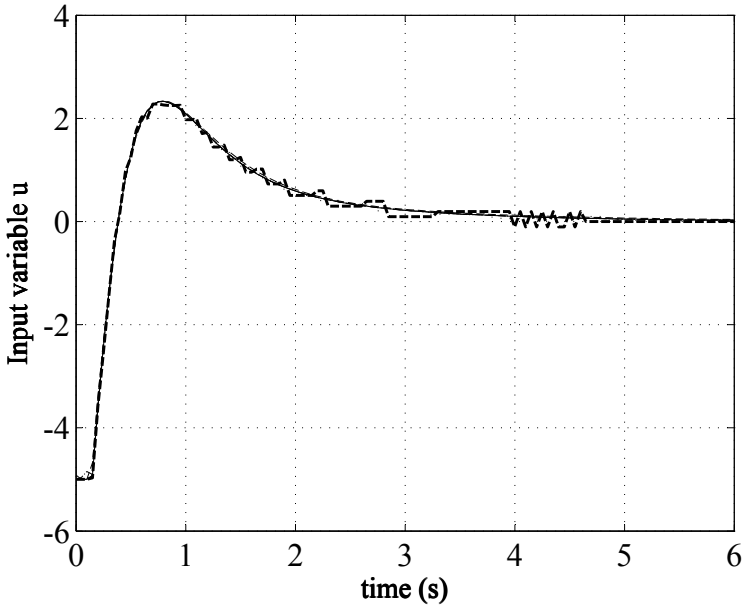

Figure 13.15. Example 3: courses of input variable u obtained with the nominal NMPC controller (solid), $\hat{\kappa}^{\text{NN}}$ (dashed), $\tilde{\kappa}^{\text{LOC,NN}}$ (dash–dotted), κ^{OPT} (dotted) and κ^{NP} (dashed, thick line). Initial condition: $x_0 = [1, -3.1]^T$

the mean distance $\overline{d}$ over all time steps of all simulations has been computed. The values of $\overline{d}$ obtained with OPT, LOC an NP approximated controllers are reported in Table 13.4 too. The values obtained with the neural network approximation are $\overline{d} = 1\,10^{-2}$ and $\overline{t} = 2\,10^{-5}$ s. The mean computational times of the approximated controllers may be up to 4000 times lower than on–line optimization. The NP approximation κ^{NP} achieves the lowest value of $\overline{t}$, which is also independent on ν: again, this can be obtained with a suitable data arrangement. The neural network approximation $\hat{\kappa}^{\text{NN}}$ also achieves a low value of $\overline{t}$, however its performance is poor ($\overline{d} = 1\,10^{-2}$). Functions κ^{OPT} and κ^{LOC} have better precision than κ^{NP} with the same ν value, but also higher computational times, which grow linearly with ν. Note that $\tilde{\kappa}^{\text{LOC,NN}}$ is able either to greatly improve the precision with respect to κ^{OPT}, with the same mean computational time, or, using a lower value of ν, to obtain a precision similar to that of κ^{OPT}, but with faster computational times. Thus, this example shows how the local optimal SM approach is able to improve the performance of a given preliminary approximating function, achieving either the same precision of the global optimal approach, but with faster computation, or better precision with the same computational times.

As regards the memory usage required by the SM approximations, about 90 KBytes, 340 KBytes and 8.4 MBytes were needed with $\nu = 3.5\,10^3$, $\nu = 1.4\,10^4$ and $\nu = 3.5\,10^5$ respectively, without any effort to improve the storage efficiency and using 8 Bytes for all the values contained in the off–line computed data.

Table 13.3. Example 3: mean evaluation times and maximum trajectory distances.

	κ^{OPT}		κ^{NP}		κ^{LOC}	
	$\overline{t}$	$\overline{d}$	$\overline{t}$	$\overline{d}$	$\overline{t}$	$\overline{d}$
$\nu = 3.5\,10^5$	$6\,10^{-2}$ s	$1\,10^{-3}$	$\mathbf{1\,10^{-5}}$ **s**	$3\,10^{-3}$	$6\,10^{-2}$ s	$\mathbf{2\,10^{-4}}$
$\nu = 1.4\,10^4$	$2\,10^{-3}$ s	$4\,10^{-3}$	$\mathbf{1\,10^{-5}}$ **s**	$1.5\,10^{-2}$	$2\,10^{-3}$ s	$\mathbf{6\,10^{-4}}$
$\nu = 3.5\,10^3$	$6\,10^{-4}$ s	$8\,10^{-3}$	$\mathbf{1\,10^{-5}}$ **s**	$3\,10^{-2}$	$6\,10^{-4}$ s	$\mathbf{6\,10^{-3}}$

13.1.4 Example 4: nonlinear system with unstable equilibrium

Consider the following two–dimensional continuous–time nonlinear system (see e.g. [96])

$$\begin{cases} \dot{x}_1(t) = x_2(t) + \dfrac{(1 + x_1(t))}{2}\, u(t) \\ \dot{x}_2(t) = x_1(t) + \dfrac{(1 - 4x_2(t))}{2}\, u(t) \end{cases} \tag{13.2}$$

whose origin is an unstable equilibrium point. The input constraint set $\mathbb{U}$ is:

$$\mathbb{U} = \{u \in \mathbb{R} : |u| \leq 4\}$$

The following discrete time model, to be used in the nominal MPC design, has been obtained by forward difference approximation:

$$x_{t+1} = \begin{bmatrix} 1 & T_s \\ T_s & 1 \end{bmatrix} x_t + \frac{T_s}{2} \left(\begin{bmatrix} 1 \\ 1 \end{bmatrix} + \begin{bmatrix} 1 & 0 \\ 0 & -4 \end{bmatrix} x_t \right) u_t$$

with sampling time $T_s = 0.1$ s. The nominal NMPC controller κ^0 is designed according to (8.2) with horizons $N_p = 30$, $N_c = 30$ and the following functions L and Φ:

$$L(x,u) = x^T Q x + u^T R u, \quad \Phi = 0$$

where

$$Q = \begin{bmatrix} 0.5 & 0 \\ 0 & 0.5 \end{bmatrix},\ R = 0.5$$

The following linear state inequality constraints define the considered set $\mathbb{X}$:

$$\mathbb{X} = \{x \in \mathbb{R}^2 : \|x\|_\infty \leq 3\}$$

Moreover, the following terminal constraint set (see e.g. [45]) has been included to enforce stability of the origin of the nominal discrete–time model:

$$\mathbb{X}_{\text{f}} = \{x \in \mathbb{R}^2 : \|x\|_\infty \leq 0.1\}$$

The origin of the closed–loop system with the linear control law $u_t = -K_{\text{LQR}} x_t$, $K_{\text{LQR}} = [2.1, 2.1]$ is asymptotically stable for any initial state $x_0 \in \mathbb{X}_{\text{f}}$.
The optimization problem (8.2), whose solution defines the control law $\kappa^0(x)$, has been solved using a sequential constrained Gauss–Newton quadratic programming algorithm (see e.g. [95]), where the underlying quadratic programs have been solved using the MatLab® function `quadprog`. The mean computational time of the on–line optimization was between 1 s and $8\,10^{-2}$ s (depending on the actual state value x_t) with a mean value of $1.7\,10^{-1}$ s, using MATLAB® 7 with an Intel® Core™2 Duo @2.4 GHz processor and 2 GB RAM.
Fig. 13.16 shows the set $\mathcal{X}$ considered for the approximation, together with the constraint set $\mathbb{X}$. The level curves of the optimal cost function $J^*(x) = \min_U J(U,x)$ are reported too.
The following approximating functions have been considered:

I) Optimal SM approximation κ^{OPT}

II) Nearest point approximation κ^{NP}

III) Neighborhood SM approximation κ^{NB}, with partitions X_j computed employing a uniform grid on the set $\mathcal{X}$

IV) Linear interpolation κ^{LIN}, with partitions X_j computed applying the Delaunay triangulation (see e.g. [97]) to the set $\mathcal{X}_\nu$

Each of the considered approximations has been computed using different values of ν. An example of simulation results obtained with $\nu = 2.5\,10^3$ and initial condition $x(0) = [2.1, -17]^T$ is reported in Figs. 13.16 and 13.17, in terms of closed–loop state trajectories. It can be noted that the closed–loop trajectories are practically superimposed, except for a quite small neighborhood of the origin (see Fig. 13.17). In particular, it can be noted that control laws κ^0 and κ^{LIN} obtain no steady–state offset, as it can be expected since in the neighborhood of the origin both these controllers are equivalent to a stabilizing linear state feedback law. On the contrary, the SM optimal and neighborhood approximations make the system state converge to an equilibrium point close to the origin. Such a behaviour, which is confirmed by the results of extensive simulation tests reported in Table 13.6 below, is due to the fact that the origin is an unstable equilibrium point and that both κ^{OPT} and κ^{NB} are equal to zero in its proximity (provided that the equilibrium point $\tilde{x} = [0, 0]^T$, $\tilde{u} = 0$ is included in the off–line computed data set $\mathcal{X}_\nu$). The regulation precision obtained with the OPT and NB laws can be improved by using a higher number of off–line computed points near the origin, making the state converge to an arbitrary small neighborhood of $[0, 0]^T$ (see e.g. [59]). Alternatively, a dual–mode controller could be used, switching to a linear stabilizing state feedback control law when the system state enters the related reachable set (or a subset of it).
To evaluate the performance and computational times of the considered control laws, 500

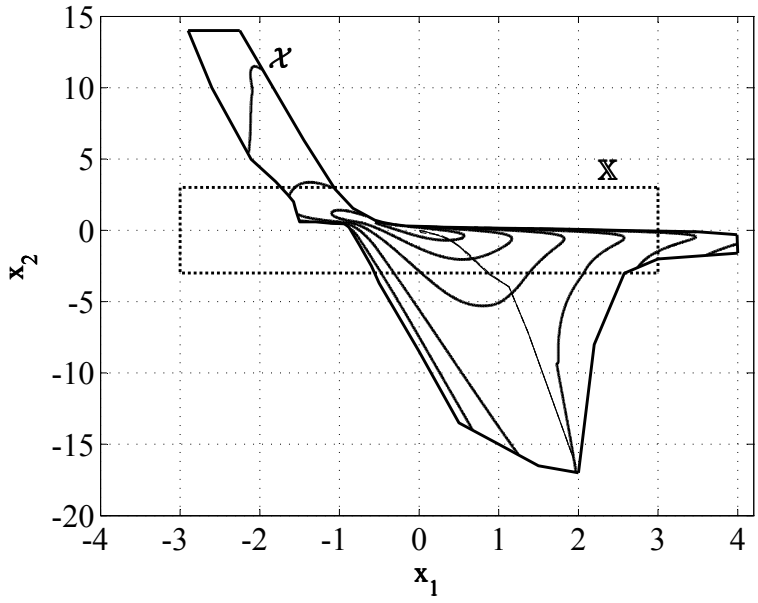

Figure 13.16. Example 4: set $\mathcal{X}$, constraint set $\mathbb{X}$ (thick dotted line) and level curves of the optimal cost function $J^*(x)$ (thick solid lines). Closed loop state trajectories obtained with controllers κ^0 (solid), κ^{OPT} (dotted), κ^{LIN} (dash–dot) and κ^{NB} (dashed). Initial state $x(0) = [2.1,\ -17]^T$, approximations computed using $\nu = 2.5\,10^3$ points.

simulations have been performed starting from different initial conditions, chosen with uniform random gridding over $\mathcal{X}$. Each simulation lasted 300 time steps (i.e. 30 simulation seconds). The mean computational times $\bar{t}$, over all time steps of all simulations, obtained with each controller, are reported in Table 13.4. As a measure of control system performance, the relative Euclidean distance $d^j(t), j = 1, \ldots, 500$ has been considered:

$$d^j(t) = \frac{\|\phi^{0,j}(t) - \phi^j(t)\|_2}{\|\phi^{0,j}(t)\|_2}$$

where $\phi^{0,j}(t)$ and $\phi^j(t)$ are the closed–loop state trajectories obtained in the j–th simulation with the nominal controller and the approximated one respectively, given the same initial state $x^j(0)$. Then, the following definition of transient interval has been considered:

$$t^{\text{TI},j} = \arg\min_t t : \|\phi^j(t)\|_2 \leq 0.1\,\|x^j(0)\|_2$$

and the mean relative distance $\bar{d}$ over the time intervals [0,$t^{\text{TI},j}$] of all the simulations has been computed:

$$\bar{d} = \frac{1}{500}\sum_{j=1}^{500}\left(\frac{1}{t^{\text{TI},j}}\int_0^{t^{\text{TI},j}} d^j(t)\,dt\right)$$

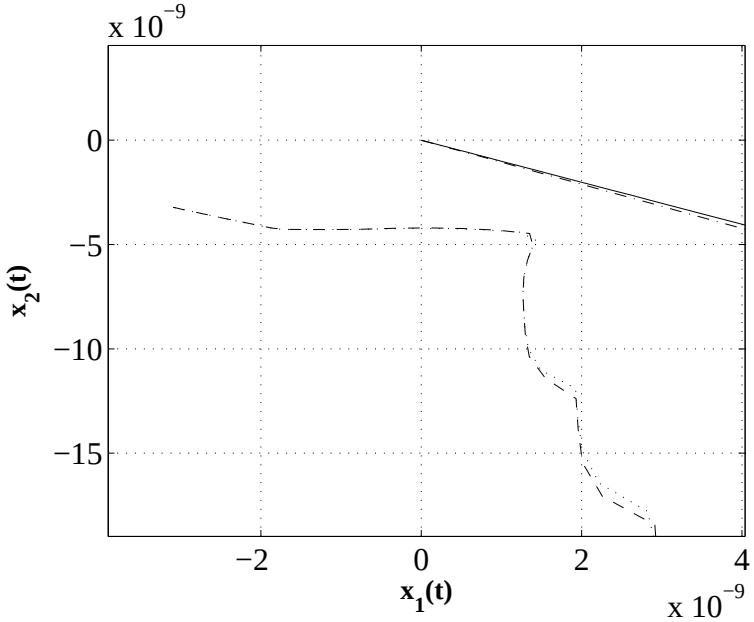

Figure 13.17. Example 4: closed loop state trajectories near the origin, obtained with controllers κ^0 (solid), κ^{OPT} (dotted), κ^{LIN} (dash–dot) and κ^{NB} (dashed). Initial state $x(0) = [2.1, -17]^T$, approximations computed using $\nu = 2.5\,10^3$ points.

Moreover, as a measure of regulation precision, the mean value d^{OR} of the norm of the state trajectory $\|\phi^j(t)\|_2, j = 1, \ldots, 500$ over the last 2 seconds of all the simulations has been also evaluated:

$$d^{\text{OR}} = \frac{1}{500} \sum_{j=1}^{500} \left(\frac{1}{2} \int_{28}^{30} \|\phi^j(t)\|_2 \, dt \right)$$

The values of $\overline{d}$ and d^{OR} obtained with each approximated controller are given in Tables 13.5 and 13.6 respectively. Finally, Table 13.7 shows the memory required by each of the approximated control laws for each value of ν. Indeed, the reported computational times and memory requirements are intended to be used to compare the different control laws in relative terms only. No memory optimization effort has been done on the employed data structures and all the variables have been stored using 4–Byte floating point representation.

From Table 13.4 it can be noted that the NP approximation κ^{NP} achieves the lowest computational values, however its performance (Table 13.5) is also the worst (though quite close to those of OPT and NB approximations) and the memory occupation is high (only LIN technique has higher memory requirements). Function κ^{OPT} has better precision and the lowest memory usage, but also the highest computational times. The best performance

is obtained for any ν value by the linear interpolation κ^{LIN}, at the cost of higher computational time (but still about 250–500 times lower than on–line optimization) and memory usage. In particular, with $\nu = 2.5\,10^3$ points the linear interpolation achieves better performance than the other techniques in most cases, together with asymptotic stability of the origin. Note that the optimal SM approximation has worse performance than LIN technique: this does not contradict the theoretical results since the OPT approximation guarantees the lowest *worst case* error, which does not imply that the average precision in practice is the best. This is also the reason why in some cases (see Table 13.5 for the case $\nu = 2.5\,10^3$) the NB technique (which employs only a subset of the data considered by the OPT approximation) has better average performance than OPT. In fact, the SM neighborhood approximation has performance close to those of OPT and quite fast computational times (slower than the NP technique only, see Table 13.4). This is also put into evidence by the fact that in most cases (93% with $\nu = 2.5\,10^3$ up to 96% with $\nu = 2.5\,10^4$) the input $\kappa^{\text{NB}}(x) = \kappa^{\text{OPT}}(x)$ given the same x value.
Thus, the presented example shows how both LIN and NB techniques can be tuned to achieve a suitable tradeoff between precision, on–line evaluation time, memory usage and off–line computation, providing more degrees of freedom in the control design than the previously introduced OPT and NP approaches.

Table 13.4. Example 4: mean computational times.

ν	κ^{OPT}	κ^{NP}	κ^{NB}	κ^{LIN}
$2.5\,10^3$	$3.3\,10^{-4}$	$\mathbf{9.0\,10^{-5}}$	$1.3\,10^{-4}$	$3.8\,10^{-4}$
$4.9\,10^3$	$1.0\,10^{-3}$	$\mathbf{1.0\,10^{-4}}$	$1.5\,10^{-4}$	$5.9\,10^{-4}$
$9.7\,10^3$	$2.0\,10^{-3}$	$\mathbf{1.1\,10^{-4}}$	$1.7\,10^{-4}$	$8.1\,10^{-4}$
$2.5\,10^4$	$5.0\,10^{-3}$	$\mathbf{7.2\,10^{-5}}$	$1.9\,10^{-4}$	$7.0\,10^{-4}$

Table 13.5. Example 4: mean trajectory distance $\overline{d}$.

ν	κ^{OPT}	κ^{NP}	κ^{NB}	κ^{LIN}
$2.5\,10^3$	7.8%	8.6%	5.9%	**1.6%**
$4.9\,10^3$	2.5%	3.0%	2.7%	**0.7%**
$9.7\,10^3$	1.5%	1.9%	1.5%	**0.2%**
$2.5\,10^4$	1.1%	1.7%	1.3%	**0.1%**

Table 13.6. Example 4: mean regulation precision d^{OR}.

ν	κ^{OPT}	κ^{NP}	κ^{NB}	κ^{LIN}
$2.5\,10^{3}$	$6.0\,10^{-3}$	$6.0\,10^{-3}$	$6.0\,10^{-3}$	$\mathbf{2\,10^{-13}}$
$4.9\,10^{3}$	$4.4\,10^{-9}$	$4.4\,10^{-9}$	$4.4\,10^{-9}$	$\mathbf{2\,10^{-13}}$
$9.7\,10^{3}$	$4.4\,10^{-9}$	$4.4\,10^{-9}$	$4.4\,10^{-9}$	$\mathbf{2\,10^{-13}}$
$2.5\,10^{4}$	$4.4\,10^{-9}$	$4.4\,10^{-9}$	$4.4\,10^{-9}$	$\mathbf{2\,10^{-13}}$

Table 13.7. Example 4: memory usage (KB)

ν	κ^{OPT}	κ^{NP}	κ^{NB}	κ^{LIN}
$2.5\,10^{3}$	$\mathbf{0.6\,10^{2}}$	$0.9\,10^{2}$	$0.7\,10^{2}$	$3.0\,10^{2}$
$4.9\,10^{3}$	$\mathbf{1.2\,10^{2}}$	$1.6\,10^{2}$	$1.3\,10^{2}$	$7.0\,10^{2}$
$9.7\,10^{3}$	$\mathbf{2.3\,10^{2}}$	$3.6\,10^{2}$	$2.8\,10^{2}$	$1.5\,10^{3}$
$2.5\,10^{4}$	$\mathbf{6.0\,10^{2}}$	$1.3\,10^{3}$	$7.5\,10^{2}$	$4.3\,10^{3}$

13.2 Fast NMPC for vehicle stability control using a rear active differential

In this Section, as a further example a NMPC approach to improve vehicle yaw rate dynamics by means of a rear active differential is introduced. In particular, the use of nonlinear predictive controllers is investigated to show their effectiveness in the vehicle stability control context. In order to allow the online implementation of the designed predictive control law, the Nearest Point approach is adopted. Enhancements on stability in demanding conditions such as μ–split braking and damping properties in impulsive maneuvers are shown through simulation results performed on an accurate nonlinear model of the vehicle. Improvements over a well assessed approach which employs an enhanced IMC structure to handle input constraints are obtained too.
This application example shows how the presented techniques for efficient NMPC can be effectively employed in the case of reference tracking problems; moreover, the issue of regressor scaling is also addressed.

13.2.1 Problem description

Vehicle yaw dynamics may show unexpected dangerous behavior in presence of unusual external conditions such as lateral wind force, different left–right side friction coefficients and steering steps needed to avoid obstacles. Moreover, in standard turning manoeuvres understeering phenomena may deteriorate handling performances in manual driving and cause uncomfortable feelings to the human driver. Vehicle active control systems aim to enhance driving comfort characteristics ensuring stability in critical situations. Several solutions to active chassis control have appeared in the last years. All the proposed strategies

modify the vehicle dynamics by means of suitable yaw moments that can be generated in different ways (see e.g. [98], [99], [100], [101], [102], [103]). In particular, the action of active braking systems is employed in Anti Lock Braking System, Vehicle Dynamic Control and Electronic Stability Program strategies; an electronic controlled superposition of an angle to the steering wheel is used in Front Active Steering methodologies; unsymmetrical traction force distributions for left–right sides of the rear axle are imposed by means of active differential devices. Common to all such solutions is the fact that they are able to generate limited values of the yaw moment. The immediate consequence is that the input variable may saturate and this could deteriorate the control performances. Moreover, good damping properties and vehicle safety (i.e. stability) performance can be considered as well by imposing suitable constraints on the on the yaw rate $\dot{\psi}(t)$ and on the sideslip angle $\beta(t)$ values as described in [104]. Therefore, considering the presence of such constraints, the employment of NMPC appears to be an appropriate approach to solve the problem. Indeed, the sampling times required for such kind of application may not allow to perform the NMPC optimization problem online. Nevertheless, predictive control has been successfully employed in vehicle lateral and stability control by means of suitable solutions aimed at improving the online computational times. In particular, in [105], predictive control techniques have been used in active steering control for an autonomous vehicle where online linearization of the vehicle model gave rise to an effective suboptimal solution which allows the online implementation. Moreover, in [106] an interesting contribution to the problem of control allocation in yaw stabilization has been introduced by means of nonlinear multiparametric programming where an approximate solution obtained by means of a piecewise linear function is used for the online implementation of the controller. Here, the problem of efficient MPC implementation is solved using the NP approach presented in Section 12.1. In order to show in a realistic way the effectiveness of the proposed control approach, extensive simulation tests in demanding driving situations are performed using a detailed nonlinear 14 degrees of freedom vehicle model. Finally, improvements over a well assessed approach which employ an enhanced IMC structure to handle input constraints are shown too.

13.2.2 Vehicle modeling and control requirements

Vehicle dynamics can be described using the following single track model (see e.g. [107]):

$$\begin{aligned} &mv(t)\dot{\beta}(t) + mv(t)\dot{\psi}(t) = F_{yf}(t) + F_{yr}(t) \\ &J_z\ddot{\psi}(t) = aF_{yf}(t) - bF_{yr}(t) + M_z(t) \end{aligned} \tag{13.3}$$

In model (13.3) the inputs are the yaw moment M_z and the front steering angle δ. Moreover, m is the vehicle mass, J_z is the moment of inertia around the vertical axis, β is the sideslip angle, ψ is the yaw angle and v is the vehicle speed, a and b are the distances between the center of gravity and the front and rear axles respectively. F_{yf} and F_{yr} are

the front and rear tyre lateral forces which can be expressed as nonlinear functions of the other variables (see [108] and [103] for more details):

$$\begin{array}{l} F_{yf} = F_{yf}(\beta,\dot{\psi},v,\delta) \\ F_{yr} = F_{yr}(\beta,\dot{\psi},v) \end{array} \tag{13.4}$$

Vehicle dynamics can be modified by means of suitable yaw moments generated by exploiting appropriate combinations of longitudinal and/or lateral tyre forces. In this paper, the required yaw moment is supposed to be generated by a Rear Active Differential (RAD) whose clutches are actuated by means of electric valves driven by the current $i(t)$ originated by the control algorithm (see [103] for a detailed description of such device). As a first approximation, the actuator behavior can be described by the model:

$$M_z(t) = K_A i(t - \vartheta) \tag{13.5}$$

where K_A and ϑ are the actuator gain and delay respectively. Equations (13.3), (13.4) and (13.5) can be rearranged in the state equation form:

$$\left[\begin{array}{c} \ddot{\psi}(t) \\ \dot{\beta}(t) \end{array} \right] = f(\dot{\psi}(t),\beta(t),\delta(t),i(t-\vartheta)) \tag{13.6}$$

The input variable $i(t)$ is employed for control purposes, while $\delta(t))$ is not manipulable and describes the driver's maneuvering intention. The control requirements in terms of understeer characteristics improvements can be taken into account by a suitable choice of the reference signal $\dot{\psi}_{\text{ref}}(t)$ generated by means of a nonlinear static map

$$\dot{\psi}_{\text{ref}}(t) = \mathcal{M}(\delta(t),v(t)) \tag{13.7}$$

which uses the current values of the steering angle and of the vehicle speed as inputs. Details on the computation of the map $\mathcal{M}(\cdot)$ can be found in [103]. In order to take into account such reference following requirements, the control strategy can be designed by minimizing the amount of the error variable $e(t)$:

$$e(t) = \dot{\psi}_{\text{ref}}(t) - \dot{\psi}(t)$$

Moreover, good damping properties and vehicle safety (i.e. stability) performance can be considered as well by imposing suitable constraints on the on the yaw rate $\dot{\psi}(t)$ and on the sideslip angle $\beta(t)$ values as described in [104]. However, the amount of the yaw moment generated by the employed active device is subject to its physical limits. In particular, the considered device has an input current limitation of $\pm$ 1 A which correspond to the range of allowed yaw moment $\pm$ 2500 Nm that can be mechanically generated (see [109] and [110]). Thus, saturation aspects of the control input (i.e. the actuator current $i(t)$) have to be carefully taken into account in the control design. Therefore, considering the presence of state and input constraints, the employment of NMPC techniques appears to be an appropriate approach to solve the problem.

13.2.3 NMPC strategy for yaw control

In this Section it is shown how Model Predictive Control strategies (see e.g. [45]) can be effectively employed in vehicle active control. The control move computation is performed at discrete time instants kT_s, $k \in \mathbb{N}$, defined by the sampling period T_s and on the basis of the following state equations obtained by discretization of (13.6) by means of e.g. forward difference approximation (for simplicity, the notation $k+j \triangleq (k+j)T_s$ is used):

$$\begin{bmatrix} \dot{\psi}_{k+1} \\ \beta_{k+1} \end{bmatrix} = \tilde{f}(\dot{\psi}_k, \beta_k, \delta_k, i_{k-r}) \tag{13.8}$$

where r is the input delay of the current i which depends on the value of the actuator delay ϑ. Thus, at each sampling time k, the measured values of the state $\dot{\psi}_k, \beta_k$, supposed to be available, together with the requested value of the yaw rate reference $\dot{\psi}_{\text{ref},k}$, and of the input variables $\delta_k, i_{k-1}, \ldots, i_{k-r}$ are used to compute the control move through the optimization of the following performance index:

$$J = \sum_{k=0}^{N_p-1} e^2_{k+j+1|k} + \rho i^2_{k+j|k} \tag{13.9}$$

where $N_p \in \mathbb{N}$ is the prediction horizon, $e_{k+j|k}$ is j^{th} step ahead prediction of the error variable obtained as

$$e_{k+j|k} \triangleq \dot{\psi}_{\text{ref},k} - \dot{\psi}_{k+j|k}$$

The value of $\dot{\psi}_{\text{ref},k}$ is computed using the current values of δ_k and v_k (see (13.7)). The predicted yaw rate $\dot{\psi}_{k+j|k}$ is obtained via the state equation (13.8), starting from the "initial condition":

$$\begin{bmatrix} \dot{\psi}_k \\ \beta_k \end{bmatrix}$$

and using the following values of the inputs i and δ:

$$\begin{bmatrix} \delta_{k|k} = \delta_{k+1|k} = \ldots = \delta_{k+N_p-1|k} \\ i_{k-r}, \ldots, i_{k-1}, i_{k|k}, \ldots, i_{k+N_c-1|k}, \ldots, i_{k+N_p-1|k} \end{bmatrix}$$

where $N_c \leq N_p$ is the control horizon and the assumption $i_{k+j|k} = i_{k+N_c-1|k}, N_c \leq j \leq N_p - 1$ is made. Thus, since during the prediction horizon the value of the steering angle δ is kept constant at the value $\delta_{k|k}$ measured at time k, the optimization of the index (13.9) is performed with respect to the variables $I = [i_{k|k}, \ldots, i_{k+N_c-1|k}]$. Therefore the performance index J depends on the vector $w_k \in \mathbb{R}^{4+r}$ of the measured variables:

$$w_k \triangleq \left[\dot{\psi}_k, \beta_k, \delta_k, v_k, i_{k-r}, \ldots, i_{k-1}\right]^T \tag{13.10}$$

Thus the predictive control law is computed using the following receding horizon strategy:

1. At time instant k, get w_k.

2. Solve the optimization problem:

$$\min_{I} \quad J(w_k) \tag{13.11a}$$

subject to

$$I \in \mathbb{I} = \left\{ i_{k+j|k} \,:\, |i_{k+j|k}| \leq \bar{i} > 0,\, j \in [0,N_c - 1] \right\} \tag{13.11b}$$

$$|\beta_{k+j|k}| \leq \bar{\beta} > 0,\, j \in [1,N_p - 1] \tag{13.11c}$$

3. Apply the first element of the solution sequence I as the actual control action $i_k = i_{k|k}$.

4. Repeat the whole procedure at the next sampling time $k + 1$.

Note that no constraints have been imposed on $\dot{\psi}$ as their limitation on the basis of criteria similar to the ones introduced in [104] have been implicitly taken into account in the $\dot{\psi}_{\text{ref}}$ computation (see [103]). Besides, the constraint on β accounts for vehicle directional stability.
The predictive controller obtained by the action of current i_k results to be a nonlinear static function of the variable w_k defined in (13.10):

$$i_k = \kappa^0(w_k) \tag{13.12}$$

For a given w_k, the value of the function $\kappa^0(w_k)$ is computed by solving at each sampling time k the constrained optimization problem (13.11). However, such online solution of the optimization problem cannot be performed at the sampling period required for this application, which is of the order of 0.01 s. To overcome this problem the NP approximation $\kappa^{\text{NP}}(w_k) \approx \kappa^0$ is employed here, as discussed in the next Section.

13.2.4 Fast NMPC implementation

Prior information

The a priori knowledge on the nominal control law κ^0 is now introduced. The approximating function κ^{NP} is computed over a compact subset $\mathcal{W} \subset \mathbb{R}^{4+r}$ of the domain of the exact function κ^0. Inside $\mathcal{W}$, a finite number ν of points $\tilde{w}^\ell, \ell = 1, \ldots, \nu < \infty$ is suitably chosen, defining the set: $\mathcal{W}_\nu = \{\tilde{w}^\ell \in \mathcal{W},\ \ell = 1, \ldots, \nu\}$. For each value of $\tilde{w} \in \mathcal{W}_\nu$, the corresponding value $\tilde{i} = \kappa^0(\tilde{w})$ is computed by solving off–line the optimization problem (13.11), so that:

$$\tilde{i} = \kappa^0(\tilde{w}),\ \forall \tilde{w} \in \mathcal{W}_\nu \tag{13.13}$$

Such values of $\tilde{w}$,$\tilde{i}$ are stored to be used for the online computation of κ^{NP}. The set $\mathcal{W}_\nu$ is supposed to be chosen such that the following property holds:

$$\lim_{\nu\to\infty} d_H(\mathcal{W},\mathcal{W}_\nu) = 0 \tag{13.14}$$

where $d_H(\mathcal{W},\mathcal{W}_\nu)$ is defined as:

$$d_H(\mathcal{W},\mathcal{W}_\nu) = \sup_{w\in\mathcal{W}} \inf_{\tilde{w}\in\mathcal{W}_\nu} (\|w-\tilde{w}\|_2) \tag{13.15}$$

Since both $\mathcal{W}$ and $\mathbb{I}$ are compact, the following Lipschitz continuity property holds:

$$\|\kappa^0(w^1) - \kappa^0(w^2)\|_2 \leq L_{\kappa^0}\|w^1 - w^2\|_2,\ \forall w^1, w^2 \in \mathcal{W} \tag{13.16}$$

All this prior information can be summarized by concluding that κ^0 belongs to the following Feasible Function Set (FFS):

$$\kappa^0 \in FFS = \{\kappa \in \mathcal{A}_{L_{\kappa^0}} : \kappa(\tilde{w}) = \tilde{i},\ \forall \tilde{w} \in \mathcal{W}_\nu\} \tag{13.17}$$

where $\mathcal{A}_{L_{\kappa^0}}$ is the set of all continuous functions $\kappa : \mathcal{W} \to \mathbb{I}$, such that (13.16) holds.

Nearest Point approximation

The approximating function κ^{NP} is computed as follows. For any $w \in \mathcal{W}$, denote with $\tilde{w}^{\text{NP}}$ a value such that:

$$\tilde{w}^{\text{NP}} \in \mathcal{W}_\nu : \|\tilde{w}^{\text{NP}} - w\|_2 = \min_{\tilde{w}\in\mathcal{W}_\nu} \|\tilde{w} - w\|_2 \tag{13.18}$$

Then, the NP approximation $\kappa^{\text{NP}}(x)$ is defined as:

$$\kappa^{\text{NP}}(w) = \kappa^0(\tilde{w}^{\text{NP}}) \tag{13.19}$$

As showed in Section 12.1, such approximation has the following properties:

I) the input constraints are always satisfied:

$$\kappa^{\text{NP}}(w) \in \mathbb{I},\ \forall w \in \mathcal{W} \tag{13.20}$$

II) for a given ν, a bound $\zeta^{\text{NP}}(\nu)$ on the pointwise approximation error can be computed:

$$\|\kappa^0(w) - \kappa^{\text{NP}}(w)\|_2 \leq \zeta^{\text{NP}} = L_{\kappa^0}\, d_H(\mathcal{W},\mathcal{W}_\nu),\ \forall w \in \mathcal{W} \tag{13.21}$$

III) $\zeta^{\text{NP}}(\nu)$ is convergent to zero:

$$\lim_{\nu\to\infty} \zeta^{\text{NP}} = 0 \tag{13.22}$$

As regards the computation of the Lipschitz constant L_{κ^0}, which is needed to compute the approximation error bound ζ^{NP}, an estimate $\hat{L}_{\kappa^0}$ can be derived using (9.6).

Variable scaling

In the computation of the NP control law (13.18), (13.19) , the Euclidean norm $\|\tilde{w} - w\|_2 = \sqrt{(\tilde{w} - w)^T(\tilde{w} - w)}$ is considered to measure the distance between $\tilde{w}$ and w. In [57], such choice gives good results on a numerical example. However, in practical applications it is usually needed to scale the variables w to adapt to the properties of data. This is obtained using a weighted Euclidean norm:

$$\|\tilde{w} - w\|_2^M = \sqrt{(\tilde{w} - w)^T M^T M(\tilde{w} - w)} \tag{13.23}$$

where

$$M = \text{diag}(m_i), i = 1, \ldots, 4 + r \tag{13.24}$$

and $m_i \in (0,1) : \sum_{i=1}^{4+r} m_i = 1$ are suitable scalar weights. In [86] the issue of choosing the values of m_i is considered when the function to be approximated is differentiable. A similar approach is now presented in the case of Lipschitz continuous functions. For the sake of notation's simplicity, consider $\kappa^0(w) : \mathbb{R}^{4+r} \to \mathbb{R}$.
Due to the continuity assumption, function κ^0 is Lipschitz continuous with respect to each component w_i of w, $i = 1, \ldots, n$. Thus, for each value of $w \in \mathcal{W}$ there exist Lipschitz constants $L_{\kappa^0,i}(w), i = 1, \ldots, 4 + r$ such that:

$$|\kappa^0([v^1, w_{j\neq i}]) - \kappa^0([v^2, w_{j\neq i}])| \leq L_{\kappa^0,i}(w)|v^1 - v^2|, \forall v^1, v^2 \in \mathcal{V}_i$$

where $\mathcal{V}_i = \{v : [v, w_{j\neq i}] \in \mathcal{W}\}$. Consider now the constants:

$$\Gamma_i = \sup_{w \in \mathcal{W}} L_{\kappa^0,i}(w), i = 1, \ldots, 4 + r$$

Estimates of Γ_i can be computed e.g. by performing a preliminary differentiable approximation $\hat{\kappa} \approx \kappa^0$ (e.g. linear, neural networks…) and evaluating:

$$\Gamma_i \simeq \sup_{w \in \mathcal{W}} |\partial \hat{\kappa}(w)/\partial w_i|$$

Then, the values of m_i can be computed as:

$$m_i = \frac{\Gamma_i}{\sum_{i=1}^{4+r} \Gamma_i} \tag{13.25}$$

equation (13.25) is derived applying normalization to the values given by Lemma 2 in [86].

Design procedure

The overall design procedure for the fast NMPC approach proposed in this paper can be resumed as follows:

1. Design the nominal NMPC control law according to (13.11).

2. Choose the set $\mathcal{W}$ where the approximated control law is defined and collect the values $\tilde{w}^j, \tilde{i}^j, j = 1, \ldots, \nu$ (13.13), e.g. by performing simulations of suitably chosen maneuvers using the closed loop vehicle with the nominal NMPC controller.

3. Derive a preliminary smooth approximated control law $\hat{\kappa} \approx \kappa^0$ using some identification method and evaluate the weight matrix M (13.24) using (13.25).

4. Estimate the Lipschitz constant L_{κ^0} using (9.6), considering the scaled values $\tilde{v}^j = M\tilde{w}^j, j = 1, \ldots, \nu$.

5. Evaluate the guaranteed approximation error $\zeta^{\text{NP}}(\nu)$ using (13.21), computing the Hausdorff distance $d_H(\mathcal{W}, \mathcal{W}_\nu)$ (13.15) with the weighted Euclidean norm $\| \cdot \|_2^M$ (13.23). Eventually tune the weight matrix M and/or increase the number ν of off–line computed values to reduce $\zeta^{\text{NP}}(\nu)$.

6. Implement on–line the NP approximated control law using (13.18) and (13.19) with the weighted Euclidean norm $\| \cdot \|_2^M$ (13.23).

13.2.5 Simulation results

The nominal predictive controller κ^0 has been designed using model (13.3), (13.4) with the following nominal parameter values:
$m = 1715\,\text{kg} \quad J_z = 2700\,\text{kgm}^2 \quad a = 1.07\,\text{m} \quad b = 1.47\,\text{m}$
$\vartheta_A = 20\,\text{ms}\ K_A = 2500\,\text{Nm/A}$
To be used in the optimization algorithm, the vehicle model has been discretized using forward difference approximation, with sampling time $T_s = 0.01$ s. Therefore, since the nominal actuator delay value is $\vartheta = 20\text{ms} = 2T_s$, at the generic time step k the past input values i_{k-1}, i_{k-2} (i.e. the number r of the current delay is 2) have to be used to compute the predicted vehicle behavior. The weight ρ in cost function (13.9) has been chosen as $\rho = 10^{-6}$, and the employed state and input constraints are $\overline{\beta} = 5^\circ$ and $\overline{i} = 1\,\text{A}$. The chosen prediction and control horizons are $N_p = 100$ and $N_c = 5$ respectively. The nominal control move computation has been performed using a sequential constrained Gauss–Newton quadratic programming algorithm (see e.g. [95]), where the underlying quadratic programs have been solved using the MatLab® optimization function `quadprog`. Thus, the nominal control law at sampling time k results to be a static function of the variables

$w_k = [\dot{\psi}_k\, \beta_k\, \delta_k\, v_k\, i_{k-1}\, i_{k-2}]^T \in \mathbb{R}^6$. Note that the reference yaw rate $\dot{\psi}_{\text{ref}},k$ is not explicitly considered in the regressor vector w_k, since it is computed using a static function of δ_k and v_k (see [103]), which are already included in w_k. The values of $\tilde{w}, \tilde{i}$ in (13.13) have been computed performing simulations involving an extensive set of handwheel steps and sinusoids maneuvers. In this way, a number $\nu = 5.5\,10^5$ of values was collected in the set:

$$\mathcal{W} = \left\{ w : \begin{bmatrix} -0.5 \\ -0.1 \\ -0.1 \\ 22 \\ -1 \\ -1 \end{bmatrix} \preceq w \preceq \begin{bmatrix} 0.5 \\ 0.1 \\ 0.1 \\ 33 \\ 1 \\ 1 \end{bmatrix} \right\}$$

where the symbol $\preceq$ indicates element–wise inequalities.

The weights $m_i, i = 1, \ldots, 6, \sum_{i=1}^{6} m_i = 1$ (13.25) for the NP control approximation have been initially computed on the basis of a preliminary linear approximation of κ^0 (see [86]) and they have been tuned through simulations. The chosen values are $m_{1\div 6} = [0.107, 0.539, 0.352, 1.9 \cdot 10^{-7}, 2.6 \cdot 10^{-4}, 2.6 \cdot 10^{-4}]$.

In order to test the performances obtained by the considered yaw control approach, simulations have been performed using a detailed nonlinear 14 degrees of freedom Simulink model, which gives an accurate description of the vehicle dynamics as compared to actual measurements and includes nonlinear suspension, steer and tyre characteristics, obtained on the basis of measurements on the real vehicle. The following open loop (i.e. without driver's feedback) maneuvers have been chosen to test the control effectiveness:

- steer reversal test with handwheel angle of 50° performed at 100 km/h, with a steering wheel speed of 400°/s. This test aims to evaluate the controlled car transient and steady state performances: the employed handwheel course is showed in Fig. 13.18.

- $\mu --$split braking maneuver performed at 100 km/h with dry road on one side and icy road on the other, with braking pedal input corresponding to a deceleration value of 0.5 g on dry road. The objective of this test is to evaluate the system response in presence of strong disturbances. Note that the μ–split maneuver implies a differential left–right change in the tyre–road friction coefficients, which was not taken into account in NMPC design, since the maneuvers considered in the off–line computation of the control moves were performed with a single track model.

- steering wheel frequency sweep performed at 90 km/h in the frequency range 0–7 Hz with steering wheel angle amplitude of 30°.

The performance obtained with the NP approximation technique have been compared to those of the uncontrolled vehicle, of the nominal MPC control law and of the enhanced IMC structure proposed in [103] for the same application, which proved to give quite good results.

The results of the 50° steer reversal test are reported in Fig. 13.19–13.22. In Fig. 13.19

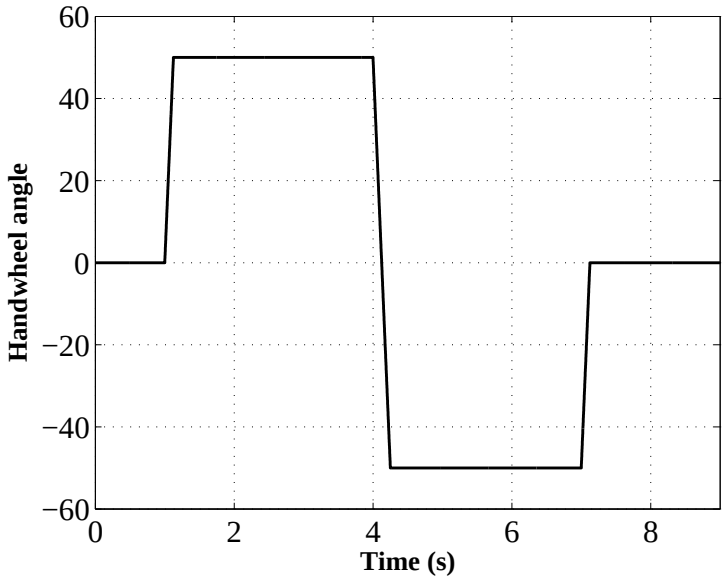

Figure 13.18. Handwheel angle course for the 50° steer reversal test maneuver.

it can be noted that the approximated MPC controller (solid line) and the nominal one (dashed–dotted) show a very similar behavior, with only a slight difference in the second part of the maneuver (see Fig. 13.19 at about $t = 6\,\mathrm{s}$). Moreover, the transient performances obtained with the proposed fast NMPC technique are better than those of the IMC controller (dashed line, see Fig. 13.20 at $t = 1\,\mathrm{s}$, $t = 4\,\mathrm{s}$ and $t = 7\,\mathrm{s}$), which already showed very good performance with respect to the uncontrolled vehicle (Fig. 13.20, dotted line). The steady state yaw rate reference is reached and, according to the reference map (see e.g. [103]), it is higher than the uncontrolled vehicle yaw rate, thus improving car maneuverability. The obtained sideslip angle $\beta(t)$ is kept inside the considered constraint (see Fig. 13.21, solid line), as well as the input variable u (Fig. 13.22, solid line). Note that some chattering of the input variable occurs with the NP approximated control law: such phenomenon can be mitigated by increasing the number ν of off–line computed control moves (see [57]), at the expense of higher memory usage. Another possibility would be the use of a "local" set membership approximation, as described in [86], which can practically lead to good approximation accuracy with low values of ν. Indeed, the choice of the regressor values is a key point in the approximated controller design, especially if the regressor dimension is relatively high, like in the considered application. A higher value of ν leads to better accuracy, but also to higher memory requirements and computational costs. With the employed NP approximation, the on–line computational time can be greatly reduced by suitably arranging the collected data and, in the case of uniform gridding of $\mathcal{W}$, the computational burden is independent on ν (see [57] for details). However, uniform gridding of $\mathcal{W}$ may lead to excessively high ν values and is not

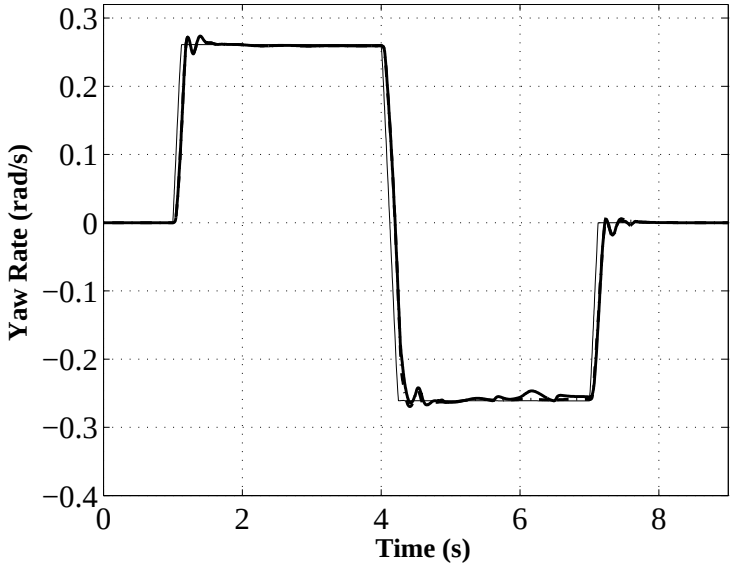

Figure 13.19. 50° steer reversal test at 100 km/h. Comparison between the reference (thin solid line) vehicle yaw rate course and those obtained with the nominal NMPC (dash–dotted) and NP approximation (solid) controlled vehicles.

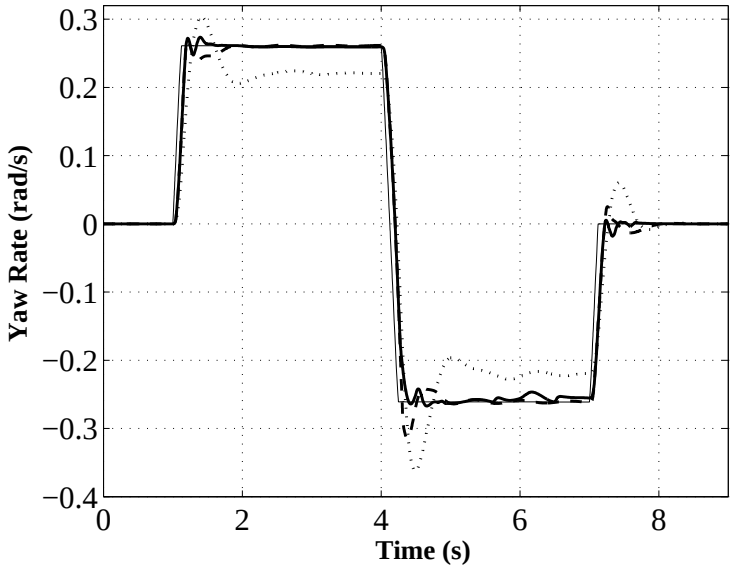

Figure 13.20. 50° steer reversal test at 100 km/h. Comparison between the reference (thin solid line) vehicle yaw rate course and those obtained with the uncontrolled (dotted) and the IMC (dashed) and NP approximation (solid) controlled vehicles.

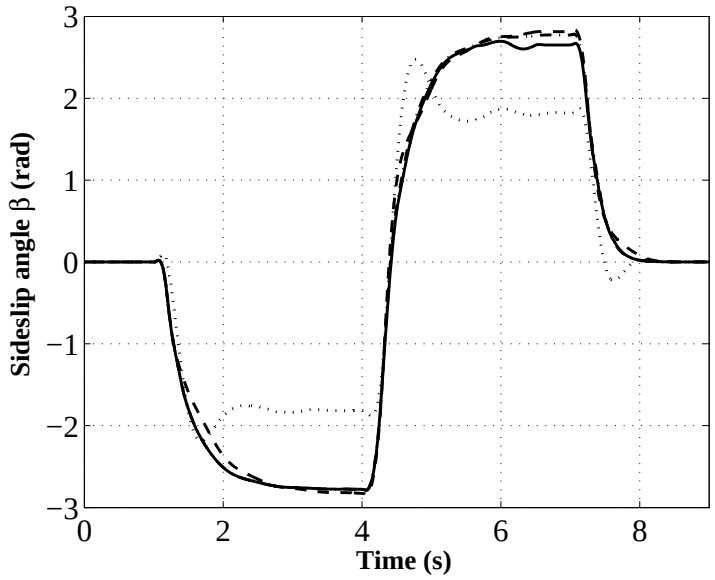

Figure 13.21. 50° steer reversal test at 100 km/h. Comparison between the sideslip angle courses obtained with the uncontrolled (dotted) and the IMC (dashed) nominal NMPC (dash–dotted) and NP approximation (solid) controlled vehicles.

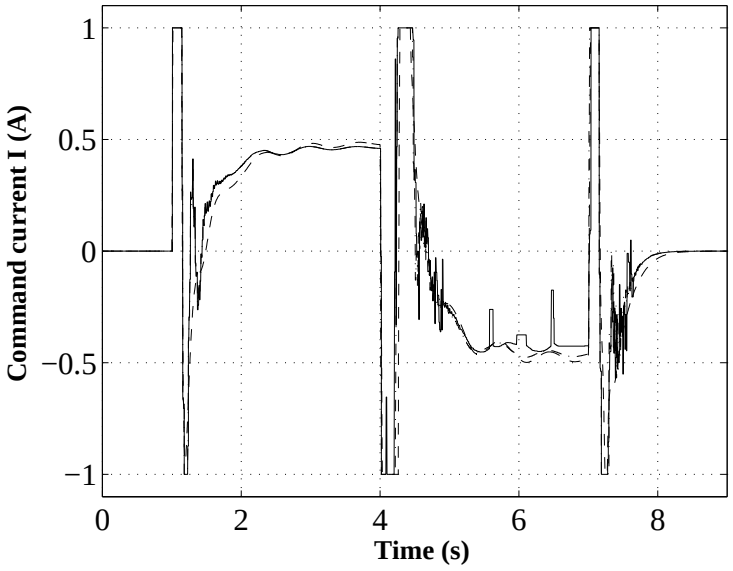

Figure 13.22. 50° steer reversal test at 100 km/h. Comparison between the input variable u obtained with the IMC (dashed), nominal NMPC (dash–dotted) and NP approximation (solid).

adopted in this application. The obtained mean computational time for the approximated control law is 1 ms, using MatLab® 7 under MS Windows XP and an Intel® Core(tm)2 Duo T7700@2.4 GHz processor with 2 GB RAM. On the same machine, the mean computational time for the online optimization is 35 ms.
As regards the considered μ–split braking maneuver, Fig. 13.23 shows the vehicle trajectories obtained in the uncontrolled case (black), with the IMC controller (white) and with the NP approximated controller (gray). It can be noted that the NP approximated predictive control law achieves the best performance, since the effects of the disturbance on the vehicle path is lower than the other cases, while the uncontrolled vehicle is not stable. Finally, the steering wheel frequency sweep maneuver aims to evaluate the improvement

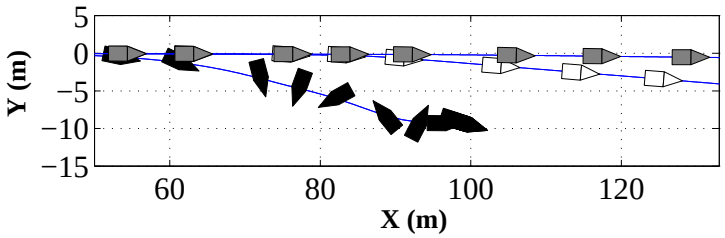

Figure 13.23. μ–split braking maneuver at 100 km/h. Comparison between the trajectories obtained with the uncontrolled vehicle (black) and the IMC (white) and NP approximated (gray) controlled ones.

achieved by the controlled vehicle with NP approximation in terms of resonance peak reduction and bandwidth increase. Fig. 13.24 shows the frequency course of the transfer ratio:

$$T_m(\omega) = \frac{\overline{\dot{\psi}}(\omega)}{\overline{\dot{\psi}}(0)}$$

where $\overline{\dot{\psi}}(\omega)$ is the steady state yaw rate amplitude obtained in presence of the sinusoidal 30° handwheel input at frequency ω, and $\overline{\dot{\psi}}(0)$ is the steady state yaw rate in presence of a constant handwheel input of 30°. It can be noted that the NP approximated controlled vehicle has a slightly lower resonance peak with respect to the case of IMC control, and a higher bandwidth. Note that the enhanced IMC controller of [103] also employs a feedforward control contribution to enhance the system transient response, which is not needed in the case of NMPC.

13.2.6 Conclusions

A Model Predictive Control approach to vehicle yaw control has been introduced. In the proposed approach the predictive controller has been realized by means of a Nearest Point approximation using a finite number of exact offline solutions. Simulation results

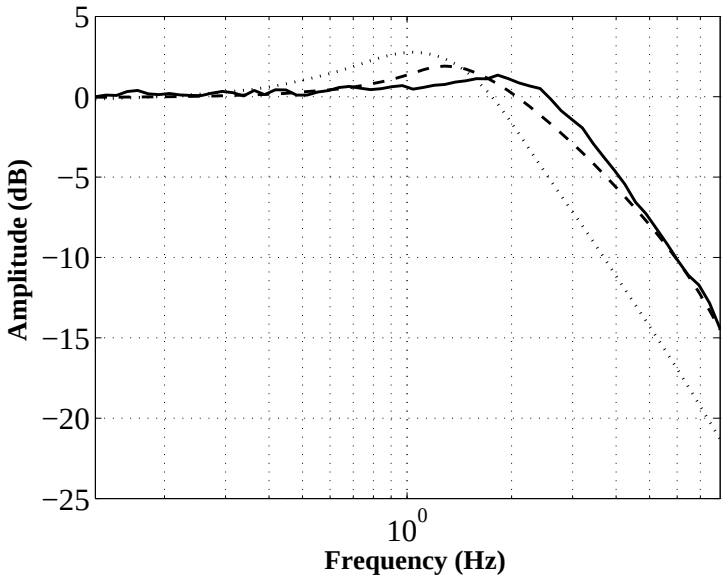

Figure 13.24. Frequency response obtained from the handwheel sweep maneuver at 90 km/h, with handwheel amplitude of 30°. Comparison between the uncontrolled vehicle (dotted) and the IMC (dashed) and approximated NMPC (solid) controlled ones.

performed on an accurate model of the considered vehicle demonstrate the effectiveness of the considered approach. In particular, it has been shown that a highly damped behaviour in reversal steer maneuvers has been obtained; stability is guaranteed in presence of demanding driving conditions like μ–split braking and resonance peak has been significantly reduced in the frequency response. Finally, improvements over a well assessed approach which employ an enhanced IMC structure to handle input constraints have been shown too.

Chapter 14

Concluding remarks

This Chapter summarizes the main contributions of Part II of this dissertation and indicates possible further research directions.

14.1 Contributions

The second Part of this dissertation focused on the use of approximated NMPC laws to avoid on–line optimization and allow one to employ NMPC also with systems with "fast" dynamics. The approximation is performed on the basis of the prior information given by a finite number ν of exact control moves computed off–line and stored. The main given contributions are the following:

I) analysis of the closed loop properties of stability, constraint satisfaction and performance degradation obtained using an approximated NMPC law (Chapter 9).
The main theoretical result states that if the approximated control law enjoys three *key properties*, then guaranteed closed loop stability and performance can be obtained. Namely, such properties are satisfaction of input constraints, boundedness of the pointwise approximation error and its convergence to an arbitrary small value, as ν increases. The obtained guaranteed closed loop properties regard the boundedness and convergency of the controlled state trajectories, satisfaction of state constraints and a bound on the maximum distance between the closed loop state trajectories obtained with the exact and with the approximated control laws.

II) Analysis of the guaranteed accuracy obtained by a generic approximating function (Chapter 10).
A general framework has been considered, where the approximation is obtained with any technique (e.g. polynomial curve fitting, interpolation, neural networks,

etc.), and sufficient conditions have been derived for the approximated controller to satisfy the above–mentioned key properties.

III) Derivation of novel approaches to approximate a given NMPC law (Chapters 11–13).
Five different approaches have been described, which satisfy the considered key properties and can be therefore employed to obtain approximating functions with guaranteed closed loop stability and performance. Such approaches are able to achieve different tradeoffs between accuracy, computational efficiency, memory usage and off–line computational effort (required to derive the approximating function). Several numerical examples have been also given, together with an application example in the field of vehicle yaw control.

14.2 Directions for future research

Some possible future developments of the presented work regard the choice of the off–line computed control moves, employed to compute the approximating function, the use of control approaches that mix on–line optimization and function approximation techniques and finally further improvements of the optimal SM approaches described in Chapter 11.

I) Optimal choice of the off–line computed data.
The results given in this dissertation do not concern how the off–line computed data are chosen, i.e. the choice of the set $\mathcal{X}_\nu = \{\tilde{x}^k, k = 1, \ldots, \nu\}$, apart from the assumption (8.10). An interesting research direction is to find out an optimal choice of $\mathcal{X}_\nu$, which minimizes the number of off–line computed control moves to obtain a given accuracy level. It would be also of interest to develop an algorithm able to increase ν iteratively to improve the obtained guaranteed accuracy, choosing the "new" data in an optimal way.

II) Generalization of the theoretical results.
The stability and performance results presented in this dissertation assume continuity of the MPC control law over the compact subset where the approximation is carried out. Though sufficient conditions that guarantee satisfaction of this assumption exists [64], they are in general difficult to verify with nonlinear systems. Thus, removing the continuity assumption would lead to more general and powerful results.

III) Mixed on–line/off–line approximation approaches.
In order to add further degrees of freedom in the design of an approximated NMPC law achieving a tradeoff between accuracy and memory usage, it would be interesting to mix on–line optimization (using a simplified system model and/or shorter

control horizons) and off–line NMPC approximation. In this context, the local optimal SM approach seems to be well suited to be employed together with a simple on–line optimization procedure.

IV) Improvements of the optimal SM approaches.

The optimal SM approaches described in Chapter 11 give the minimal worst–case accuracy, according to the considered prior information, however their computational time grows linearly with ν, since all of the off–line computed data are considered for their evaluation. Indeed, for a given state value x, the values of the optimal bounds (whose computation is required to obtain the optimal SM approximation) depend only on few of the memorized data.

An interesting research direction is the improvement of the evaluation efficiency of the optimal SM approaches, via the off–line partitioning of the set $\mathcal{X}$, over which the approximation is carried out. Then, for each of such partitions, a subset of the overall memorized data can be computed, containing only the off–line computed data which give useful information for the computation of the optimal bounds. This way, the on–line evaluation would firstly require a search for the active partition and then the computation of the optimal bounds, using the reduced number of memorized data related to that partition. The obtained guaranteed accuracy would be the same as the optimal approaches described in this thesis, with improved on–line efficiency (similar to that of the NB approximation of Section 12.3)

Appendix A

Regional definitions and country groupings

The regional definitions employed in Part I of this dissertation correspond to those of [1]. In particular, six basic groups are considered (see Figure A.1), with a further subdivision of the OECD group:

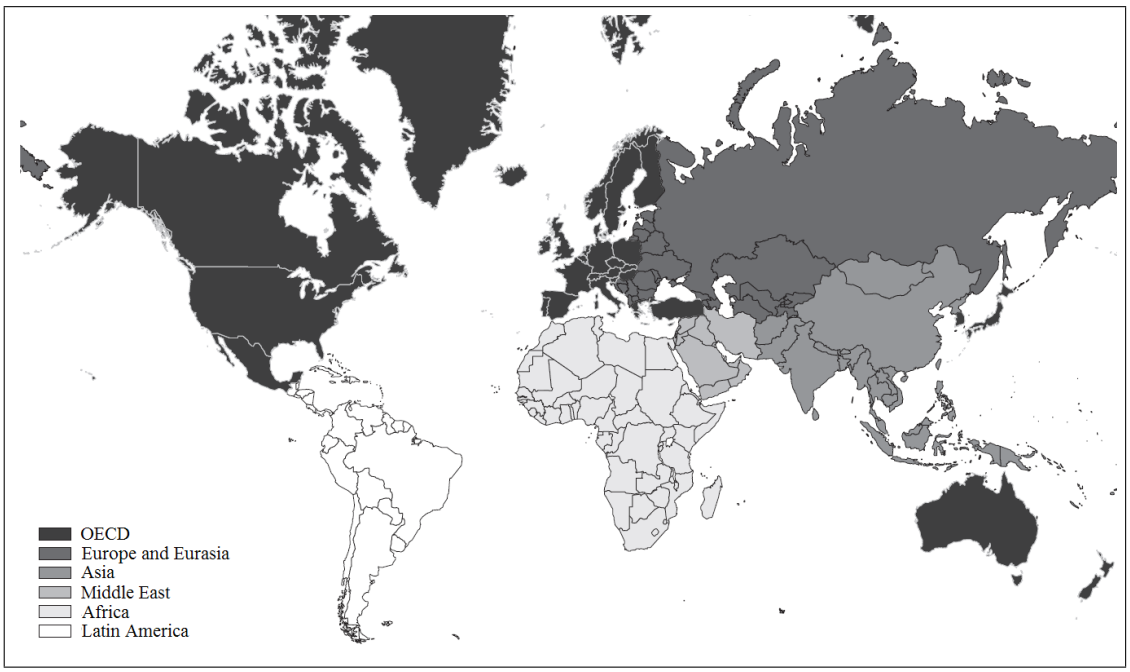

Figure A.1. Map of the six basic country groupings. Image taken from [2]

1. **OECD**

OECD North America: Canada, Mexico and the United States.

OECD Europe: Austria, Belgium, the Czech Republic, Denmark, Finland, France, Germany, Greece, Hungary, Iceland, Ireland, Italy, Luxembourg, the Netherlands, Norway, Poland, Portugal, the Slovak Republic, Spain, Sweden, Switzerland, Turkey and the United Kingdom.

OECD Pacific: Australia, Japan, Korea and New Zealand)

2. **Europe and Eurasia:** Albania, Armenia, Azerbaijan, Belarus, Bosnia-Herzegovina, Bulgaria, Croatia, Cyprus, Estonia, Serbia, Montenegro, the former Yugoslav Republic of Macedonia, Gibraltar, Georgia, Kazakhstan, Kyrgyzstan, Latvia, Lithuania, Malta, Moldova, Romania, Russia, Slovenia, Tajikistan, Turkmenistan, Ukraine and Uzbekistan.

3. **Asia:** Afghanistan, Bangladesh, Bhutan, Brunei, Cambodia, China, Chinese Taipei, Fiji, French Polynesia, India, Indonesia, Kiribati, the Democratic PeopleŠs Republic of Korea, Laos, Macau, Malaysia, Maldives, Mongolia, Myanmar, Nepal, New Caledonia, Pakistan, Papua New Guinea, the Philippines, Samoa, Singapore, Solomon Islands, Sri Lanka, Thailand, Tonga, Vietnam and Vanuatu.

4. **Middle East:** Bahrain, Iran, Iraq, Israel, Jordan, Kuwait, Lebanon, Oman, Qatar, Saudi Arabia, Syria, the United Arab Emirates and Yemen.

5. **Africa:** Algeria, Angola, Benin, Botswana, Burkina Faso, Burundi, Cameroon, Cape Verde, Central African Republic, Chad, Comoros, Congo, Democratic Republic of Congo, Côte d'Ivoire, Djibouti, Egypt, Equatorial Guinea, Eritrea, Ethiopia, Gabon, Gambia, Ghana, Guinea, Guinea-Bissau, Kenya, Lesotho, Liberia, Libya, Madagascar, Malawi, Mali, Mauritania, Mauritius, Morocco, Mozambique, Namibia, Niger, Nigeria, Reunion, Rwanda, Sao Tome and Principe, Senegal, Seychelles, Sierra Leone, Somalia, South Africa, Sudan, Swaziland, United Republic of Tanzania, Togo, Tunisia, Uganda, Zambia and Zimbabwe

6. **Latin America:** Antigua and Barbuda, Aruba, Argentina, Bahamas, Barbados, Belize, Bermuda, Bolivia, Brazil, Chile, Colombia, Costa Rica, Cuba, Dominica, the Dominican Republic, Ecuador, El Salvador, French Guyana, Grenada, Guadeloupe, Guatemala, Guyana, Haiti, Honduras, Jamaica, Martinique, Netherlands Antilles, Nicaragua, Panama, Paraguay, Peru, St. Kitts and Nevis, Saint Lucia, St. Vincent and Grenadines, Suriname, Trinidad and Tobago, Uruguay and Venezuela.

Appendix B

Fuel definitions

The following fuel definitions are adopted in this thesis (see [1] for more details):

Oil: includes crude oil, condensates, natural gas liquids, refinery feedstocks and additives, other hydrocarbons (including emulsified oils, synthetic crude oil, mineral oils extracted from bituminous minerals such as oil shale, bituminous sand and oils from coal liquefaction), and petroleum products (refinery gas, ethane, LPG, aviation gasoline, motor gasoline, jet fuels, kerosene, gas/diesel oil, heavy fuel oil, naphtha, white spirit, lubricants, bitumen, paraffin waxes and petroleum coke).

Coal: coal includes both primary coal (including hard coal and lignite) and derived fuels (including patent fuel, brown–coal briquettes, coke–oven coke, gas coke, coke–oven gas, blast–furnace gas and oxygen steel furnace gas). Peat is also included in this category.

Nuclear: primary heat equivalent of the electricity produced by a nuclear plant with an average thermal efficiency of 33%.

Hydropower: refers to the energy content of the electricity produced in hydropower plants, assuming 100% efficiency. It excludes output from pumped storage plants.

Biomass and waste: solid biomass, gas and liquids derived from biomass, industrial waste and the renewable part of municipal waste.

Other renewables: includes geothermal, solar PV, solar thermal, wind, tide and wave energy for electricity generation and heat production.

Appendix C

Estimated capacity factor in 25 sites around the world

Table C.1. Average wind speed, in the ranges 50–150 m and 200–800 m above the ground, and estimated Capacity Factors of a 2–MW, 90–m diameter wind turbine and of a 2–MW, 500–m^2 HE–yoyo for 25 sites around the world. Data collected daily form January 1st, 1996 to December 31st, 2006.

	Average wind speed		Estimated CF	
Site	**50–150 m**	**200–800 m**	**Wind tower**	**HE–yoyo**
Buenos Aires (Argentina)	5.7 m/s	9.1 m/s	0.18	0.63
Melbourne (Australia)	5.2 m/s	8.7 m/s	0.15	0.56
Porto Alegre (Brazil)	4.9 m/s	7.5 m/s	0.13	0.52
Nenjiang (China)	2.7 m/s	5.2 m/s	0.04	0.30
Taipei (China–Taiwan)	1.5 m/s	5.6 m/s	0.02	0.32
St. Cristobal (Ecuador)	6.0 m/s	6.5 m/s	0.15	0.44
Nice (France)	4.5 m/s	5.8 m/s	0.09	0.33
Calcutta (India)	2.8 m/s	5.6 m/s	0.02	0.31
Brindisi (Italy)	7.2 m/s	8.5 m/s	0.31	0.60
Cagliari (Italy)	7.2 m/s	8.2 m/s	0.31	0.56
Linate (Italy)	0.7 m/s	5.9 m/s	0.006	0.33
Pratica di Mare (Italy)	6.2 m/s	7.4 m/s	0.23	0.49
Trapani (Italy)	7.1 m/s	8.3 m/s	0.30	0.56
Udine (Italy)	1.5 m/s	5.6 m/s	0.02	0.32
Bandar Abbas (Iran)	1.5 m/s	5.6 m/s	0.02	0.32
Misawa (Japan)	4.4 m/s	7.8 m/s	0.11	0.50
Casablanca (Morocco)	2.4 m/s	7.0 m/s	0.03	0.45
De Bilt (The Netherlands)	8.0 m/s	10.7 m/s	0.36	0.71
Bodø (Norway)	6.9 m/s	8.7 m/s	0.28	0.56

Table C.2. Average wind speed, in the ranges 50–150 m and 200–800 m above the ground, and estimated Capacity Factors of a 2–MW, 90–m diameter wind turbine and of a 2–MW, 500–m^2 HE–yoyo for 25 sites around the world. Data collected daily form January 1st, 1996 to December 31st, 2006 (continued).

	Average wind speed		Estimated CF	
Site	**50–150 m**	**200–800 m**	**Wind tower**	**HE–yoyo**
Leba (Poland)	8.1 m/s	10.1 m/s	0.38	0.71
St. Petersburg (Russian Federation)	4.1 m/s	8.5 m/s	0.1	0.59
Port Elizabeth (South Africa)	7.5 m/s	8.9 m/s	0.20	0.58
Murcia (Spain)	2.6 m/s	5.9 m/s	0.03	0.35
Nottingham (United Kingdom)	1.3 m/s	5.3 m/s	0.01	0.31
Point Barrow (Alaska, U.S.)	6.6 m/s	8.8 m/s	0.25	0.59

Bibliography

[1] International Energy Agency (IEA), *World Energy Outlook 2008*. Paris, France: IEA PUBLICATIONS, 2008.

[2] U. S. Energy Information Administration (EIA), "International Energy Outlook 2008," September 2008, available online: http://www.eia.doe.gov/oiaf/ieo/index.html.

[3] Organization for Economic Cooperation and Development (OECD), *OECD Environmental Outlook to 2030*, 2008.

[4] ——, "Climate change mitigation – what do we do?" 2008, available online: http://www.oecd.org/dataoecd/31/55/41751042.pdf.

[5] "An energy policy for europe," January 2007, communication from the Commission to the European Council and the European Parliament of 10 January 2007 (COM(2007) 1, available online: http://europa.eu/scadplus/leg/en/lvb/l27067.htm).

[6] C. L. Archer and M. Z. Jacobson, "Evaluation of global wind power," *J. Geophys. Res.*, vol. 110, D12110, 2005.

[7] R. Thresher, M. Robinson, and P. Veers, "To capture the wind," *IEEE Power & Energy Magazine*, vol. 5, no. 6, pp. 34–46, 2007.

[8] M. L. Loyd, "Crosswind kite power," *Journal of Energy*, vol. 4, no. 3, pp. 106–111, 1980.

[9] M. Canale, L. Fagiano, and M. Milanese, "Power kites for wind energy generation," *IEEE Control Systems Magazine*, vol. 27, no. 6, pp. 25–38, December 2007.

[10] ——, "Kitegen: A revolution in wind energy generation," *Energy*, vol. 34, pp. 355–361, 2008, doi:10.1016/j.energy.2008.10.003.

[11] ——, "High altitude wind energy generation using controlled power kites," *IEEE Transactions on Control Systems Technology*, 2009, provisionally accepted.

[12] M. Canale, L. Fagiano, M. Milanese, and M. Ippolito, "Control of tethered airfoils for a new class of wind energy generator," in *45^{th} IEEE Conference on Decision and Control*, San Diego, CA, 2006, pp. 4020–4026.

[13] ——, "Kitegen project: control as key technology for a quantum leap in wind energy generators," in *26^{th} American Control Conference*, New York City, 2007, pp. 3522–3528.

[14] M. Canale, L. Fagiano, and M. Milanese, "Kitegen: a revolution in wind energy generation," in *5th Biennal international workshop "Advances in energy studies: perspectives on energy future"*, Portovenere, Italy, September 2006.
[15] International Energy Agency (IEA), "Key World Energy Statistics 2008," 2008, available online: http://www.iea.org/textbase/nppdf/free/2008/key_stats_2008.pdf.
[16] Britsh Petroleum (BP) company, "BP Statistical Review of World Energy," June 2008, available online: http://www.bp.com/statisticalreview.
[17] B. G. Miller, *Coal energy systems*. Academic Press, Boston, NY (US), 2004.
[18] S. Peter and H. Lehmann, "Renewable energy outlook 2030 – Energy Watch Group global renewable energy scenarios," 2008, available online: http://www.energywatchgroup.org.
[19] V. Utgikar and J. Scott, "Energy forecasting: Predictions, reality and analysis of causes of error," *Energy Policy*, vol. 34, pp. 3087–3092, 2005.
[20] U.S. Department of Commerce – Bureau of Economic Analysis, http://www.bea.gov/.
[21] IPCC, *Climate Change 2007 – The Physical Science Basis*, 2007, contribution of Working Group I to the Fourth Assessment Report of the IPCC.
[22] ——, *Climate Change 2007 – Impacts, Adaptation and Vulnerability*, 2007, contribution of Working Group II to the Fourth Assessment Report of the IPCC.
[23] ——, *Climate Change 2007 – Mitigation of Climate Change*, 2007, contribution of Working Group III to the Fourth Assessment Report of the IPCC.
[24] T. Burton, D. Sharpe, N. Jenkins, and E. Bossanyi, *Wind Energy: Handbook*. John Wiley and Sons, 2001.
[25] G. M. Masters, *Renewable and Efficient Electric Power Systems*. Wiley, 2004.
[26] Vestas Wind Systems A/S website: http://www.vestas.com.
[27] National Oceanic & Atmospheric Administration – Earth System Research Laboratory, NOAA/ESRL Radiosonde Database Access: http://raob.fsl.noaa.gov/.
[28] M. Ippolito, "Smart control system exploiting the characteristics of generic kites or airfoils to convert energy," European patent ♯ 02840646.
[29] M. Milanese and M. Ippolito, "Sistema e procedimento di controllo automatico del volo di profili alari di potenza," Patent n. TO2006A000372, May 2006.
[30] A. Ilzhöfer, B. Houska, and M. Diehl, "Nonlinear MPC of kites under varying wind conditions for a new class of large-scale wind power generators," *International Journal of Robust and Nonlinear Control*, vol. 17, pp. 1590–1599, 2007.
[31] P. Williams, B. Lansdorp, and W. Ockels, "Optimal crosswind towing and power generation with tethered kites," *Journal of guidance, control, and dynamics*, vol. 31, pp. 81–93, 2008.
[32] B. W. Roberts, D. H. Shepard, K. Caldeira, M. E. Cannon, D. G. Eccles, A. J. Grenier, and J. F. Freidin, "Harnessing high–altitude wind power," *IEEE Transactions on Energy Conversion*, vol. 22, no. 1, pp. 136–144, 2007.
[33] Sky Wind Power Corporation, http://www.skywindpower.com.

[34] SkySails GmbH & Co., http://www.skysails.com.

[35] "World Nuclear Association, *The Nuclear Renaissance*," May 2007, available online: http://world-nuclear.org/info/inf104.html.

[36] "World Nuclear Association, *Plans For New Reactors Worldwide*," March 2008, available online: http://world-nuclear.org/info/inf17.html.

[37] W. Zittel and J. Schindler, "Uranium resources and nuclear energy," December 2006, energy Watch Group report N. 01/2006. Available online: http://www.energywatchgroup.org/fileadmin/global/pdf/EWG_Report_Uranium_3-12-2006ms.pdf.

[38] "U. S. Energy Information Administration (EIA), *Solar Thermal and Photovoltaic Collector Manufacturing Activities 2006*," October 2007, available online: http://www.eia.doe.gov/cneaf/solar.renewables/page/solarreport/solar.html.

[39] F. Allgöwer and A. Zheng, *Nonlinear model predictive control*. New York: Wiley, 2000.

[40] M. Milanese, C. Novara, K. Hsu, and K. Poolla, "Filter design from data: direct vs. two-step approaches," in *American Control Conference*, Minneapolis, MN, 2006, pp. 4466–4470.

[41] M. Milanese, C. Novara, and F. Ruiz, "Direct design of optimal filters from data," in *17^{th} IFAC World Congress*, Seoul, Korea, 2008, pp. 462–467.

[42] B. Houska and M. Diehl, "Optimal control for power generating kites," in *9^{th} European Control Conference*, Kos, GR, 2007, pp. 3560–3567.

[43] B. Lansdorp, R. Ruiterkamp, and W. Ockels, "Towards flight testing of remotely controlled surfkites for wind energy generation," in *AIAA Atmospheric Flight Mechanics Conference and Exhibit*, Hilton Head, CA, August 2007.

[44] B. Houska and M. Diehl, "Optimal control of towing kites," in *45^{th} IEEE Conference on Decision and Control*, San Diego, CA, 2006, pp. 2693–2697.

[45] D. Q. Mayne, J. B. Rawlings, C. V. Rao, and P. Scokaert, "Constrained model predictive control: Stability and optimality," *Automatica*, vol. 36, pp. 789–814, 2000.

[46] M. Diehl, "Real-time optimization for large scale nonlinear processes," Ph.D. dissertation, University of Heidelberg, Germany, 2001.

[47] G. M. Maneia, "Aerodynamic study of airfoils and wings for power kites applications," Master's thesis, Politecnico di Torino, October 2007, http://lorenzofagiano.altervista.org/MasterThesisManeia.pdf.

[48] Vestas Wind Systems A/S, "Vestas v90 brochure," available online: http://www.vestas.com.

[49] B. Houska, "Robustness and stability optimization of open-loop controlled power generating kites," Master's thesis, University of Heidelberg, 2007.

[50] D. Piga, "Analisi delle prestazioni del sistema kitegen: eolico di alta quota," Master's thesis, Politecnico di Torino, 2008, (in Italian).

[51] M. Z. Jacobson and G. M. Masters, "Exploiting wind versus coal," *Science*, vol. 293, p. 1438, 2001.

[52] HAWE project, experimental test movie, January 2008. Available on–line: http://lorenzofagiano.altervista.org/movies/Casale_test.wmv.

[53] HAWE project, experimental test movie, September 2006. Available on–line: http://lorenzofagiano.altervista.org/movies/Sardinia_test.wmv.

[54] T. Wizelius, *Developing Wind Power Projects: Theory and Practice*. Earthscan, 2007.

[55] H. Takatsu and T. Itoh, "Future needs for control theory in industry - report of the control technology survey in japanese industry," *IEEE Transactions on Control Systems Technology*, vol. 7, no. 3, pp. 298–305, 1999.

[56] M. Canale, L. Fagiano, and M. Milanese, "Fast implementation of predictive controllers using SM approximation methodologies," in *46th IEEE Conference on Decision and Control*, 2007, pp. 1361–1367.

[57] ——, "Fast nonlinear model predictive control using Set Membership approximation," in *17th IFAC World Congress*, Seoul, Korea, 2008, pp. 12 165–12 170.

[58] ——, "On the use of approximated predictive control laws for nonlinear systems," in *47th IEEE Conference on Decision and Control*, Cancun, Mexico, 2008.

[59] ——, "Set Membership approximation theory for fast implementation of model predictive control laws," *Automatica*, vol. 45, no. 1, pp. 45–54, 2009.

[60] M. Canale, L. Fagiano, M. Milanese, and C. Novara, "Set Membership approximations of predictive control laws: the tradeoff between accuracy and complexity," in *10th European Control Conference*, Budapest, Hungary, 2009, submitted.

[61] M. Canale, M. Milanese, and C. Novara, "Semi-active suspension control using "fast" model-predictive techniques," *IEEE Transactions on Control System Technology*, vol. 14, no. 6, pp. 1034–1046, November 2006.

[62] M. Canale and L. Fagiano, "Vehicle yaw control using a fast NMPC approach," in *47th IEEE Conference on Decision and Control*, Cancun, Mexico, 2008.

[63] G. C. Goodwin, M. Seron, and J. D. Dona, *Constrained Control and Estimation: An Optimisation Approach*. Springer, 2005.

[64] D. Q. Mayne and H. Michalska, "Receding horizon control of nonlinear systems," *IEEE Transactions on Automatic Control*, vol. 35, no. 7, pp. 814–824, 1990.

[65] E. Meadows, "Stability and continuity of nonlinear model predictive control," Ph.D. dissertation, University of Texas, December 1994.

[66] J. Spjøtvold, P. Tøndel, and T. A. Johansen, "Continuous selection and unique polyhedral representation of solutions to convex parametric quadratic programs," *Journal of Optimization Theory and Applications*, vol. 134, pp. 177–189, 2007.

[67] Y. Wang and S. Boyd, "Fast model predictive control using online optimization," in *17th IFAC World Congress*, Seoul, Korea, 2008, pp. 6974–6979.

[68] D. Leineweber, A. Schäfer, H. Bock, and J. Schlöder, "An efficient multiple shooting based reduced SQP strategy for large-scale dynamic process optimization. part

ii: Software aspects and applications," *Computers and Chemical Engineering*, vol. 27, pp. 167–174, 2003.

[69] M. Diehl, R. Findeisen, H. G. Bock, J. P. Schlöder, and F. Allgöwer, "Nominal stability of the real-time iteration scheme for nonlinear model predictive control," *IEE Control Theory Applications*, vol. 152, no. 3, pp. 296–308, 2005.

[70] T. Ohtsuka, "A continuation/gmresmethod for fast computation of nonlinear receding horizon control," *Automatica*, vol. 40, no. 4, pp. 563–574, 2004.

[71] M. Alamir, *Stabilization of Nonlinear Systems by Receding-Horizon Control Schemes: Parametrized Approach for Fast Systems*. Springer, 2006.

[72] A. Bemporad, M. Morari, V. Dua, and E. Pistikopoulos, "The explicit linear quadratic regulator for constrained systems," *Automatica*, vol. 38, pp. 3–20, 2002.

[73] M. Seron, G. Goodwin, and J. D. Doná, "Characterization of receding horizon control for constrained linear systems," *Asian Journal of Control*, vol. 5, no. 2, pp. 271–286, 2003.

[74] D. Muñoz de la Peña, A. Bemporad, and C. Filippi, "Robust explicit MPC based on approximate multiparametric convex programming," *IEEE Transactions on Automatic Control*, vol. 51, no. 8, pp. 1399–1403, August 2006.

[75] A. Bemporad, F. Borrelli, and M. Morari, "Piecewise linear optimal controllers for hybrid systems," in *American Control Conference*, Chicago, IL, 2000, pp. 1190–1194.

[76] A. Grancharova and T. Johansen, *Survey of Explicit Approaches to Constrained Optimal Control*, ser. Lecture notes in Computer Science, R. Murray-Smith and R. Shorten, Eds. Springer Berlin / Heidelberg, 2005, vol. Switching and Learning in Feedback Systems, no. 3355/2005, doi: 10.1007/b105497.

[77] A. Alessi and A. Bemporad, "A survey on explicit model predictive control," in *Int. Workshop on Assessment and Future Directions of NMPC*, Pavia, Italy, 2008.

[78] P. Tondel, T. Johansen, and A. Bemporad, "Computation and approximation of piecewise linear affine control laws via binary search trees," in *41st IEEE Conference Decision an Control*, Las Vegas, Nevada, December 2002, pp. 3144–3149.

[79] T. Johansen, I. Petersen, and O. Slupphaug, "Explicit suboptimal linear quadratic regulation with state and input constraints," *Automatica*, vol. 38, pp. 1099–1111, 2002.

[80] A. Bemporad and C. Filippi, "Suboptimal explicit receding horizon control via approximate multiparametric quadratic programming," *Journal of Optimization Theory and Applications*, vol. 117, no. 1, pp. 9–38, 2003.

[81] T. Parisini and R. Zoppoli, "A receding-horizon regulator for nonlinear systems and a neural approximation," *Automatica*, vol. 31, no. 10, pp. 1443–1451, 1995.

[82] M. Canale and M. Milanese, "FMPC: A fast implementation of model predictive control," in *16th IFAC World Congress*, July 2005.

[83] T. Johansen, "Approximate explicit receding horizon control of constrained nonlinear systems," *Automatica*, vol. 40, pp. 293–300, 2004.

[84] A. Ulbig, S. Olaru, D. Dumur, and P. Boucher, "Explicit solutions for nonlinear model predictive control: A linear mapping approach," in *9^{th} European Control Conference*, 2007, pp. 3295–3302.

[85] E. Polak and T. Yang, "Moving horizon control of linear systems with input saturation and plant uncertainty-part 1: robustness," *International Journal of Control*, vol. 58, no. 3, pp. 613–638, 1993.

[86] M. Milanese and C. Novara, "Set Membership identification of nonlinear systems," *Automatica*, vol. 40, pp. 957–975, 2004.

[87] J. Traub and H. Woźniakowski, *A General Theory of Optimal Algorithms*. New York: Academic Press, 1980.

[88] L. Wang, P. Heng, and K. Leung, "Global exponential asymptotic stability in nonlinear discrete dynamical systems," *Journal of Mathematical Analysis and Applications*, vol. 258, no. 1, pp. 349–358, 2001.

[89] M. Milanese and C. Novara, "Computation of local radius of information in SM–IBC identification of nonlinear systems," *Journal of Complexity*, vol. 4, no. 6, pp. 937–951, August 2007.

[90] M. Kvasnica, P. Grieder, and F. Christophersen, "Multi-parametric toolbox - ver. 2.6.2," 2006, http://control.ee.ethz.ch/∼mpt.

[91] A. Zheng, M. Kothare, and M. Morari, "Anti-windup design for internal model control," *International Journal of Control*, vol. 60, no. 5, pp. 1015–1022, 1994.

[92] MOSEK ApS, "Mosek optimization toolbox - ver. 4.0," 2006, http://www.mosek.com.

[93] T. Johansen and A. Grancharova, "Approximate explicit constrained linear model predictive control via orthogonal search tree," *IEEE Transactions on Automatic Control*, vol. 48, no. 5, pp. 810–815, May 2003.

[94] D. W. Jordan and P. Smith, *Nonlinear ordinary differential equations*. Oxford University Press, 1987.

[95] J. Nocedal and S. Wright, *Numerical Optimization*. Springer, 2006.

[96] H. Chen and F. Allgöwer, "A quasi-infinite horizon nonlinear model predictive control scheme with guaranteed stability," *Automatica*, vol. 34, pp. 1205–1217, 1998.

[97] C. B. Barber, D. Dobkin, and H. Huhdanpaa, "The quickhull algorithm for convex hulls," *ACM Transactions on Mathematical Software*, vol. 22, no. 4, pp. 469–483, 1996.

[98] J. Ackermann and W. Sienel, "Robust yaw damping of cars with front and rear wheel steering," *IEEE Trans. on Control Systems Technology*, vol. 1, no. 1, pp. 15–20, 1993.

[99] A. T. V. Zanten, R. Erhart, and G. Pfaff, "VDC, the vehicle dynamics control system of bosch," in *SAE Technical Paper No. 95759*, 1995.

[100] J. Ackermann, J. Guldner, R. Steinhausner, and V. I. Utkin, "Linear and nonlinear design for robust automatic steering," *IEEE Transactions on Control System*

Technology, vol. 3, no. 1, pp. 132–143, 1995.

[101] P. Kohen and M. Ecrick, "Active steering - the BMW approach towards modern steering technology," in *SAE Technical Paper No. 2004-01-1105*, 2004.

[102] B. A. Güvenç, T. Bünte, and L. Güvenç, "Robust two degree-of-freedom vehicle steering controller design," *IEEE Trans. on Control System Technology*, vol. 12, no. 4, pp. 627–636, 2004.

[103] M. Canale, L. Fagiano, M. Milanese, and P. Borodani, "Robust vehicle yaw control using an active differential and IMC techniques," *Control Engineering Practice*, vol. 15, pp. 923–941, 2007.

[104] U. Kienke and L. Nielsen, *Automotive Control Systems*. Springer Verlag, 2000.

[105] M. Falcone, F. Borrelli, H. C. Tseng, and D. Hrovat, "Predictive active steering control for autonomous vehicle systems," *IEEE Transactions on Control System Technology*, vol. 15, no. 3, pp. 566–580, May 2007.

[106] P. Tøndel and T. Johansen, "Control allocation for yaw stabilization in automotive vehicles using multiparametric nonlinear programming," in *American Control Conference*, June 2005.

[107] R. Rajamani, *Vehicle Dynamics and Control*. Springer Verlag, 2005.

[108] E. Bakker, L. Lidner, and H. Pacejka, "A new tyre model with an application in vehicle dynamics studies," in *SAE Paper 890087*, 1989.

[109] L. Ippolito, G. Lupo, and A. Lorenzini, *System for controlling torque distribution between the wheels of a common vehicle axle*. EU Patent no. 92121621.4, Applicant Centro Ricerche Fiat, 1992.

[110] S. Frediani, R. Gianoglio, and F. Giuliano, *System for the active control of a motor vehicle differential*. Patent no. US 2002/0016661 A1, Applicant Centro Ricerche Fiat, 2002.